FLORIDA STATE UNIVERSITY

COLLEGE OF ARTS AND SCIENCES

SEARCH FOR NEW AND UNUSUAL STRANGEONIA STATES USING $\gamma p \to p\phi\eta$ WITH GLUEX AT THOMAS JEFFERSON NATIONAL ACCELERATOR FACILITY

By

BRADFORD EMERSON CANNON

A Dissertation submitted to the
Department of Physics
in partial fulfillment of the
requirements for the degree of
Doctor of Philosophy

2019

Bradford Emerson Cannon defended this dissertation on April 12, 2019.
The members of the supervisory committee were:

Paul Eugenio

Professor Directing Dissertation

Ettore Aldrovandi

University Representative

Simon Capstick

Committee Member

Horst Wahl

Committee Member

Volker Crede

Committee Member

Alexander Ostrovidov

Committee Member

The Graduate School has verified and approved the above-named committee members, and certifies that the dissertation has been approved in accordance with university requirements.

This thesis is dedicated to Warren Palmeira. Without him, this journey would never have happened.

ACKNOWLEDGMENTS

It has taken a great many people in my life to get to where I am now. The first and most obvious people to start with are my parents, Karin and Len, and my brother Ian. They have always been there for me and have always believed in me. It was a difficult decision to leave my home in the north for so long, but I feel it was a necessary one. Being away has given me perspective on life, and I am happy to say that I plan to move back to be closer to all of you. I would also like to thank all of the teachers that have inspired me in the past. The most important being Warren Palmeira, whom this thesis is dedicated to. Warren Palmeira was always a kind and brilliant high school physics teacher; and without him I certainly would never have considered physics as a major in college. To put it in the words of one of my favorite quotes, "the journey of a thousand miles begins with one step". In retrospect, I have absolutely no idea what I would have done with my life had I not been inspired by Warren Palmeira at such a young age.

Upon graduating from high school, I had the great fortune to attend the Physics Department at the University of New Hampshire. If there is one thing that I would like to say about the University of New Hampshire, it is that the Physics Department provided me a world class education. Much like my time in high school, this had everything to do with the professors that are in the department. Dawn Meredith, James Connell, Lynn Kistler, David Mattingly, James Ryan, and Roy Torbert; thank you for all of the wonderful lectures that you had given to me while I was an undergraduate. A special shout out to Professor Adam Boucher in the Math Department. You were instrumental in building the math skills which allowed me to acquire a great understanding of physics. Lastly, the greatest acknowledgement from my time as an undergraduate goes to my adviser, mentor, and friend, Charles W. Smith. It goes without saying that I learned the most from him, including how to program, research, and most importantly, how to be a better person. I am not sure if I would have gone to graduate school if it were not for him.

After I graduated from the University of New Hampshire, I immediately joined the PhD program at Florida State University. Since joining the department, I have had the great pleasure of meeting some of the most amazing people in my life. The first of these would have to be my classmates and friends that I have made. Thank you all for helping me along the way. Graduate school was a long and grueling experience and you all made it tolerable, and on several occasions, very

enjoyable. I also want to thank Professors Laura Reina, Todd Adams, Andrew Askew, Hanwei Gao, Stephen Hill, Alexander Volya, and especially Jorge Piekarewicz. You were all amazing teachers and mentors for me. Thank you for expanding my understanding of physics to a level that I did not think was possible. It would not be an appropriate acknowledgement section if I did not mention some of the support staff in the Physics Department, Jonathan Yeargan, Johnathan Henry, Brian Wilcoxon, Lynn Lacombe, and Felicia Youngblood. You guys made my life so much easier, and I really appreciate all of the hard work that each of you did on my behalf.

While in graduate school, I was given the wonderful opportunity to be in residency at Thomas Jefferson National Accelerator Facility for one year. I had many fantastic experiences, including the daily spades game that took place in the cafeteria with Thomas Britton, Alex Austregesilo, and Paul Mattione. The daily sports activities of street hockey and pickup soccer were a blast as well. I especially want to thank staff scientists Mark Ito and Beni Zihlmann for all of the time that they had spent with me, and the work that we accomplished together on the Time of Flight detector. The GlueX collaboration is filled with many talented professors and staff scientists including Justin Stevens, Matthew Sheppard, Dave Lawrence, Mark Dalton, Richard Jones, and Curtis Meyer; all of which were excellent mentors during my time at GlueX. I cannot wait to read the news one day and find out that this collaboration has discovered exotic mesons.

I would also like to thank all members of my PhD committee, Ettore Aldrovandi, Horst Wahl, Simon Capstick, Volker Crede, and especially Alexander Ostrovidov, and my adviser, Paul Eugenio. It goes without saying that obtaining a PhD is not possible without support from research faculty and an adviser. Luckily for me, I had exceptional support from both Alexander Ostrovidov and Paul Eugenio. Thank you both for the countless hours which took place in the nuclear conference room. Thank you, Dr. Eugenio, for all of the support and opportunities that you have given me throughout my graduate education. With your guidance I have become a better programmer, researcher, and physicist. I cannot wait to find out where all of it will take me. Lastly, I want to thank the girl of my dreams and the love of my life, Golnaz. It goes without saying that we both did not expect to come to graduate school and find each other, but we did. I know I tell you this all the time, but I really could not have accomplished this impossible dream with out you by my side.

TABLE OF CONTENTS

LIST OF TABLES

LIST OF FIGURES

GLOSSARY OF ACRONYMS

ADC	An analog/amplitude to digital converter.
BCAL	Barrel Calorimeter.
CDC	Central Drift Chamber.
CEBAF	Continuous Electron Beam Accelerator Facility.
DIRC	Detector of Internally Reflected Cherenkov Radiation.
FCAL	Forward Calorimeter.
FDC	Forward Drift Chamber.
GEANT4	The fourth version of GEANT, which is a collection of simulation softwares designed to describe the passage of elementary particles through matter, using Monte Carlo methods.
genr8	An event generator used to generate event four-vectors
GlueX	The name of the experiment and detector located in Hall D of Jefferson Lab.
JLAB	Thomas Jefferson National Accelerator Facility.
Linac	Linear Accelerator; or the linear section of the accelerator track at JLAB.
OZI	Okubo-Zweig-Iizuka Suppression.
QCD	Quantum Chromodynamics.
PS	Pair Spectrometer.
RF	Radio Frequency. More specifically, the frequency at which the electron beam oscillates about the acclerator track.
ST	Start Counter.
TDC	Time to digital converter.
TOF	Time of Flight detector.
TPOL	Triplet Polarimeter.

ABSTRACT

We perform an analysis dedicated to the search for new and unusual strangeonium states produced in the reaction $\gamma p \to p\phi\eta$. The data used for this analysis was recorded during the Spring 2017 physics run for Hall D of Thomas Jefferson National Accelerator Facility, where the GlueX experiment is located. The GlueX experiment uses a linearly polarized coherent bremsstrahlung beam of up to 12 GeV in energy. This photon beam interacts with a stationary liquid hydrogen target located inside the GlueX detector. The subsequent photoproduction will provide final states ideal for studying both exotic and non-exotic $s\bar{s}$ mesons. After all cuts, a total of four different selection methods were used to study the $\phi\eta$ parent state. Three of these methods used an event by event probabilistic weighting method in order to separate signal from background, and the fourth method was simply an elliptical subtraction which did not utilize probabilistic weighting. After comparing the $\phi\eta$ invariant mass spectra for all selection methods, two structures were consistently observed. One of the structures was found to have a mass of $(m_{Peak1} = 1.657 \pm 0.008)\frac{GeV}{c^2}$ and a width of $(\sigma_{Peak1} = 0.190 \pm 0.024)\frac{GeV}{c^2}$; and the second structure was found to have a mass of $(m_{Peak2} = 1.879 \pm 0.004)\frac{GeV}{c^2}$ and a width of $(\sigma_{Peak2} = 0.042 \pm 0.014)\frac{GeV}{c^2}$.

CHAPTER 1

A BRIEF INTRODUCTION TO PARTICLE PHYSICS

1.1 Early Discoveries

One of the most important questions in all of particle physics is "what is matter made of?" That is to say, what are the fundamental building blocks for which all things are comprised of. This question dates all the way back to ancient Greece where philosophers postulated the existence of an atom; something that is indivisible. This idea resonated throughout time, with the eventual discovery of the electron by J.J Thomson in 1897. Thomson discovered the electron by testing the properties of cathode rays, where he subjected the rays to a magnetic field. When the rays were shown to bend due to the presence of the magnetic field, it was known that the rays must be charged particles with mass. He then applied an external electric field in the opposite direction of the bent particles. Adjusting the electric field strength allowed him to measure the velocity of the particles (approximately ninety percent the speed of light) and to also measure the amount of charge per mass, e/m.

Upon measuring this quantity, Thomson realized that the particle had an e/m of 1.7×10^7, or a quantity 1700 times that of hydrogen. This meant that the particle either had an extremely large electrical charge and similar mass in comparison to hydrogen, or the particle had similar charge and an extremely small mass. Thomson correcly determined that the particle possessed the properties of similar charge and an extremely small mass. At the time, Thomson refered to his new discovery as a 'corpuscle'; and indeed he knew that this particle of mass and charge was fundamental. "The corpuscle appear to form a part of all kinds of matter under the most diverse conditions; it seems natural therefore to regard it as one of the bricks of which atoms are built up." [1]. Joseph John Thomson would eventually win the 1906 Nobel Prize in Physics for "recognition of the great merits of his theoretical and experimental investigations on the conduction of electricity by gases".

The mysteries surrounding the nature of matter were nowhere near settled, however. If Thomson was correct in that electrons were everywhere in nature, then why was so much ordinary matter

electrically neutral? Thomson attempted to explain this phenomena with his famous 'plum pudding' model. In his plum pudding model, he envisioned the electrons were attached to a paste that was electrically positive, but with no internal structure. This hypothesis would eventually be shown inaccurate by Ernest Rutherford's gold foil experiment. Rutherford conducted this experiment by shooting charged helium particles towards a stationary sheet of gold foil. The idea of the experiment was simple. If matter is made of pudding as Thomson suggested, then the helium particle will pass through the gold foil slightly perturbed, but in no way greatly deviated from its original direction of motion. However, Rutherford discovered the exact opposite. Most of the time the helium passed through the gold foil completely unscathed. Yet, a small fraction of interactions showed the helium deflecting off of the gold foil at large angles. These discoveries provided a number of interesting insights. First off, that matter was most certainly not made of a paste or a pudding; but instead matter was comprised of compact and heavy objects with vast amount of empty space between them. Additionally, since Thomson had shown that the electron had to be extremely light, it must be the case that the helium particles were bouncing off an entirely different particle; what Rutherford postulated as the proton.

But the proton could not be the final answer to everything that existed inside the nucleus. The structure of organized matter still had one last void to fill which was now the problem of the periodic table of the elements. Considering the first three elements, we know that hydrogen has one proton and one electron. The next element is Helium, which is four times the weight of the proton, but only has two electrons. Then there is Lithium, seven times larger that the proton but only has three electrons. If each fundamental element in nature has an electron that matches a proton to make it electrically neutral, then why are the masses of the elements not equal to the number of electrons or protons inside the nucleus? This question would be answered in 1932 by the physicist James Chadwick. Chadwick had a similar experimental setup as Rutherford - firing Helium particles towards a stationary target; only this time the target was Berillium. The interaction of the Helium beam with the Berillium target subsequently produced a Carbon-12 and some electrically neutral radiation. Using kinematics and the conservation of momentum, Chadwick was able to determine that the mass of the electrically neutral radiation was almost exactly the same as that of a proton. He would eventually win the 1935 Nobel Prize in physics for his discovery of the neutron. [2]

Once the neutron had been discovered, many physicists believed that all of matter was organized with three fundamental particles - the proton, the neutron and the electron. However, there were still some questions that had not been answered about organized matter such as "how do protons and neutrons remain in a bound state inside the nucleus"? The first significant theory to describe the bound states of protons and neutrons was done by Hideki Yukawa in 1934. He postulated the existence of a particle that had a mass between the proton and the electron which he named the pion. The pion would eventually be discovered but not without confusion. Multiple charged particles with masses between the proton and electron had been observed in experimentation, especially with cosmic rays. The amount of charged and neutral particles with masses between the proton and electron continued to grow to an absurd amount. This led physicists to wonder if there were different fundamental building blocks of matter other than the proton, the neutron, and the electron. [3]

1.2 The Standard Model of Particle Physics

To date, there are only a handful of what physicists would label as 'fundamental particles'. We typically organize these particles into groups depending on the properties that they possess. The first group of fundamental particles that will be discussed are the neutrinos. Currently there are three species of neutrinos - the electron neutrino, the muon neutrino, and the tau neutrino; or ν_e, ν_μ, and ν_τ, respectively. For each neutrino there exists a corresponding antineutrino as well ($\bar{\nu}_e$, $\bar{\nu}_\mu$, and $\bar{\nu}_\tau$). Neutrinos are unique particles due to the fact that they have no electromagnetic charge, have an extremely small mass, and they can only interact by means of the weak nuclear force. Neutrinos can also oscillate between the three different *flavor* states mentioned above and have an interesting history in the realm of particle physics. However, in order to keep this discussion short, we will not delve into those details.

You may have thought the names of the neutrino species listed above as somewhat random; but in fact, they are not. These names are chosen because they are grouped with three more particles, all of which share the same names - the electron, the muon, and the tau; or e, μ, and τ, respectively. Just like the neutrinos, these particles all have associated antiparticles ($\bar{e}$, $\bar{\mu}$, and $\bar{\tau}$). The differences between this set of particles and the neutrinos is the fact that they all have much higher masses, possess one unit of negative electromagnetic charge, and can therefore interact

both weakly and electromagnetically. All six of these particles and their associated antiparticles are classified as *leptons* or 'light weights'.

The next set of particles that I would like to discuss are the most important particles for the subject of this thesis: the quarks. Just like the leptons, there are six quarks with mass, electromagnetic charge, and they all have corresponding anti-particles as well. There are six *flavors* of quarks: up, down, charm, strange, top, bottom; or u, d, c, s, t, b. You may notice that the names are grouped in pairs of names that seem to be opposite of one another. This naming scheme has some historical significance, but the most important thing to take away is that the 'up' quarks (u,c,t) have a positive electromagnetic charge of +2/3, and the 'down' quarks (d,s,b) have a negative electromagnetic charge of -1/3. Lastly, the quarks can interact by means of three different forces: the weak nuclear force, the electromagnetic force, and the strong nuclear force.

All of the aforementioned quarks and leptons have one very important characteristic in common between them; they are all spin 1/2 particles or *fermions*. There are other fundamental particles that exist which are not fermions. These particles are referred to as *gauge bosons*, or spin 1 particles. All of these particles are described as 'mediators' since they are the particles responsible for communicating force between other fermions. There are currently four mediators known - the W and Z bosons, the photon, and the gluon. The W and Z gauge bosons are the only particles with mass and are responsible for mediating the weak nuclear force. There are two W bosons, one that has a positive electromagnetic charge and one that has a negative electromagnetic charge. There is only one Z boson and that simply has a neutral electromagnetic charge. Since the Z and W bosons mediate the weak nuclear force, they can interact with all of the fermions mentioned in the previous paragraphs. The photon is the most well known of the four gauge bosons and is responsible for mediating the electromagnetic force. Unlike the W bosons, the photon has no mass or electromagnetic charge and can interact with all of the fermions mentioned before except the neutrinos (because they have no electromagnetic charge). Lastly there is the gluon, which much like the photon, has no mass or electromagnetic charge. However, the gluon is special in that it has a charge that is not completely obvious. We call this the *color* charge and it is the way that we explain the interaction of the strong nuclear force between quarks and gluons in the Standard Model. The gluon does not interact with any of the fermions except for the quarks.

There is one last particle which is the Higgs Boson. The Higgs may sound familiar to the reader due to its recent discovery on July 4th, 2012 [4]. Although this particle is arguably the most important discovery in particle physics for quite some time, we will not go into details about its nature here. All that the reader needs to know is that it is the particle responsible for giving mass to all of the fundamental particles. Having said this, all of the previously mentioned particles are parts to something that we like to call The Standard Model of Particle Physics. A depiction of these particles in a nicely organized fashion is given in Figure 1.1 below.

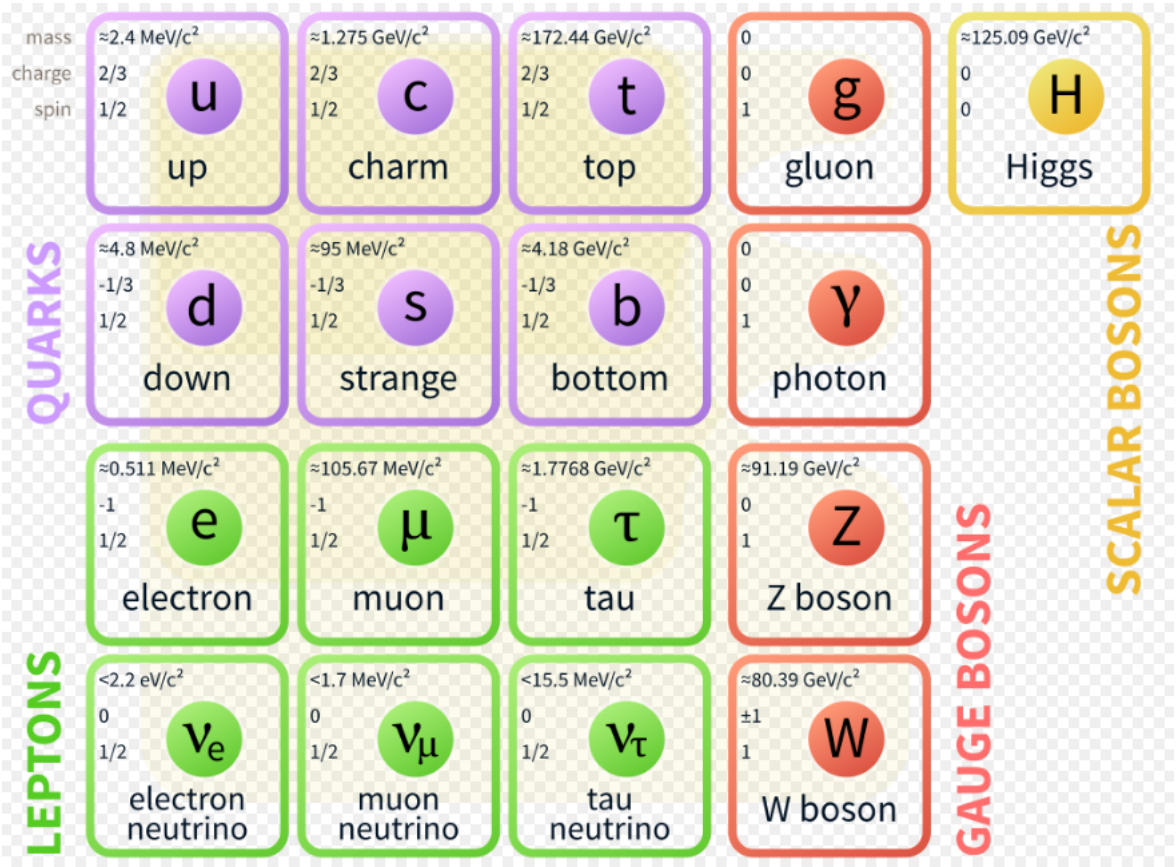

Figure 1.1: An illustration of The Standard Model of Particle Physics. The bottom left (green) boxes contain the six flavors of leptons, and the top left (purple) boxes contain the six flavors of quarks. The middle vertical column (red) displays all of the gauge bosons or mediators in the same row as the particles with which they interact. The far right box (yellow) box contains the Higgs Boson.

1.3 Meson Spectroscopy

We spent a great deal of time describing what we know as the fundamental building blocks of nature in the previous section. However, one thing that I did not mention was that quarks cannot exist individually in nature. That is to say, it is impossible to observe a single quark by itself, it must be in some type of bound state. So the next question that I would like to address is how exactly these quarks can combine to create the plethora of particles that we can observe in our every day world.

To date, there are only two ways that quarks can exist inside bound states. One of the ways that they can combine is in groups of three, with three quarks (qqq) or three antiquarks ($\bar{q}\bar{q}\bar{q}$). These groups of three quarks are called *baryons* or 'heavy weights'; and they are called *antibaryons* when they have three antiquarks. Two well known examples of baryons are protons and neutrons where the proton is comprised of two up quarks and one down quark (uud) and the neutron is comprised of one up quark and two down quarks (udd). It should be easy enough to realize then that the anti-proton and anti-neutron have the same composition as the proton and neutron except all of the quarks are antiquarks ($\bar{u}\bar{u}\bar{d}, \bar{u}\bar{d}\bar{d}$). The second way that quarks can exist inside a bound state is when they combine in groups of two, where one is a quark and the other is an antiquark, or $q\bar{q}$. These composite particles are given the name *mesons*, or 'middle weights'. Since there are six quarks and two different primary ways in which they can organize with both matter and antimatter, one quickly realizes that there is an abundant amount of possible hadronic combinations. A fair question that one may have is 'how do particle physicists organize baryons and mesons into groups?'

This question would eventually be answered with the creation of the Eightfold Way by Murray Gell-Mann circa 1961 [5]. Gell-Man introduced a way of organizing all of the known mesons and baryons into groups that shared patterns of strangeness, charge, and isospin. These diagrams helped to show that hadronic matter is comprised of six different quarks and antiquarks which are held together by their interaction via the strong nuclear force. Examples of baryon and meson multiplets are depicted in Figure 1.2 below [6].

The strong nuclear force is described by Quantum Chromodynamics (QCD), which is a theory that predicts the behaviour of particles and their coupling to the color field. These particles include all quarks, antiquarks, and gluons which are the quantized mediators of the strong force. When a quark and an antiquark are in a bound state (ie - a meson) their individual quantum numbers

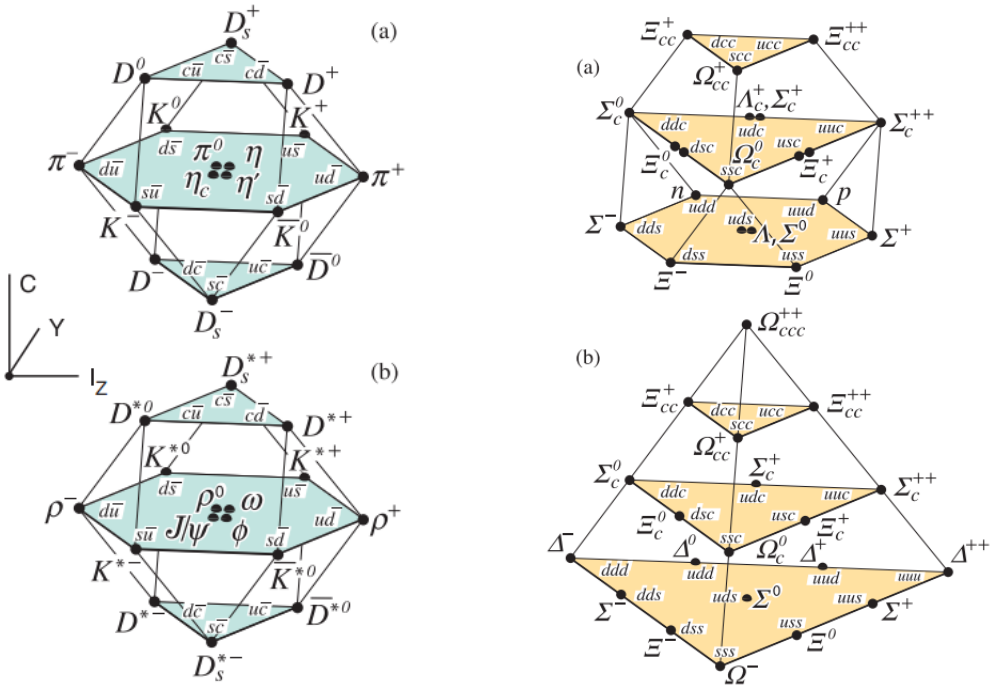

Figure 1.2: (upper-left) $J^{PC} = 0^{-+}$ pseudoscalar meson multiplet. (upper-right) $J^{PC} = 1/2^{+}$ baryon multiplet. (lower-left) $J^{PC} = 1^{--}$ vector meson multiplet. (lower-right) $J^{PC} = 3/2^{+}$ baryon multiplet

combine to make a total bound state with a given J^{PC}; where J is the quantum number for total angular momentum, P is the quantum number for parity, and C is the quantum number for charge conjugation. Knowing that quarks and antiquarks are fermions and therefore have 1/2 spins, it is easy to investigate the allowed quantum mechanical bound states of all $q\bar{q}$ mesons, regardless of their quark-antiquark flavor combination. A list of good quantum numbers for all mesons is given below in Table 1.1. If you take a closer look at the resulting J^{PC} states in Table 1.1, you should notice that certain states are missing; such as 0^{--}, 0^{+-}, 1^{-+}, and 2^{+-}. These states are known as *exotic* J^{PC} meson states, or exotic quantum number states. In addition to exotic quantum number states of mesons, QCD allows other exotic states such as $q\bar{q}q\bar{q}$ (four quark), $qqqq\bar{q}$ (pentaquark), and $q\bar{q}g$ (gluonically excited meson). Interestingly, some experiments have observed structures which resembles some of these exotic states [7]. However, more evidence needs to be provided in order to identify these resonances as undisputed exotic states. Having said that, the primary goal of the GlueX experiment is to unambiguously map all light quark exotic meson multiplets. Discussion of

Table 1.1: List of quark model quantum numbers for mesons, where s represents the spin of the meson and l represents the relative orbital angular momentum between the quark and antiquark. $Constraints: |l-s| <= J <= |l+s|, P=(-1)^{l+1}, C=(-1)^{l+s}$

s	$l=0$	$l=1$	$l=2$
$s=0$	0^{-+}	1^{+-}	2^{-+}
$s=1$	1^{--}	0^{++},1^{++},2^{++}	1^{--},2^{--},3^{--}

the GlueX experiment will be presented in Chapter 2.

1.4 Motivation

At this point in history, there are no universally accepted non $q\bar{q}$ meson states; only observed exotic meson candidates. The primary reason for this is the absence of an established $q\bar{q}g$ nonet. The purpose of the GlueX experiment at Jefferson Lab is to unambiguously map exotic meson states. In order to establish exotic nonets, we need to first understand non exotic meson states. An example of a non exotic state that is poorly understood is $s\bar{s}$, or *strangeonia*. Out of the twenty-two expected $s\bar{s}$ resonances below 2.2 GeV/c^2, only seven probable resonances exist : $\eta\eta'$, $\phi(1020)$, $h_1(1386)$, $f_1(1426)$, $f_2'(1525)$, $\phi(1680)$, and $\phi_3(1850)$; where $\eta\eta'$ is counted as one resonance [8]. Of these seven resonances, only three of them are considered pure $s\bar{s}$ states - $\phi(1020)$ $f_2'(1525)$, and $\phi_3(1850)$. Due to the heavy nature of the strange quark in comparison to the up and down quarks, one would expect more pure $s\bar{s}$ states to exist in nature. Historically, there has been some controversy over the identification of $s\bar{s}$ states in the 1600-2200 MeV mass range; specifically the $\phi(1680)$, the $X(1750)$, and the $Y(2175)$ meson states.

1.4.1 $\phi(1680)$

The first observation of $\phi(1680)$ came from the DM1 collaboration at DCI in 1981. The experiment analysed the $K_s^o K_L^o$ final state and observed a small enhancement in the cross section between 1.6-1.8 GeV center of mass energy [9]. Research on the $\phi(1680)$ continued to be done by many collaborations [6], however there is one particular study that stands out due its large sampling of statistics and the fact that it includes $\phi\eta$ as a final state topology.

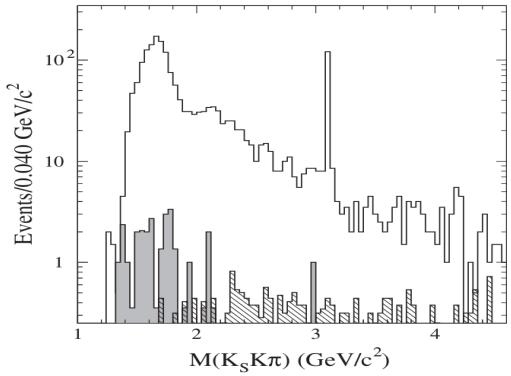

(a) Invariant Mass Spectrum for the $K_sK\pi$ final state.

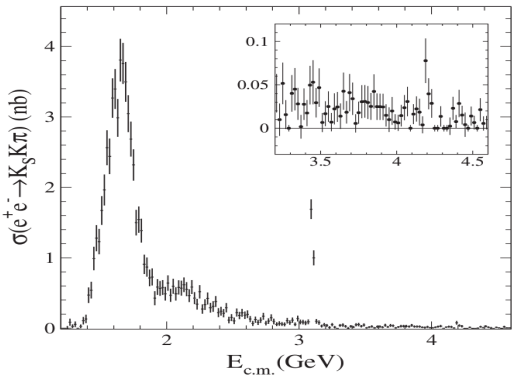

(b) Measured cross section for the $K_sK\pi$ final state.

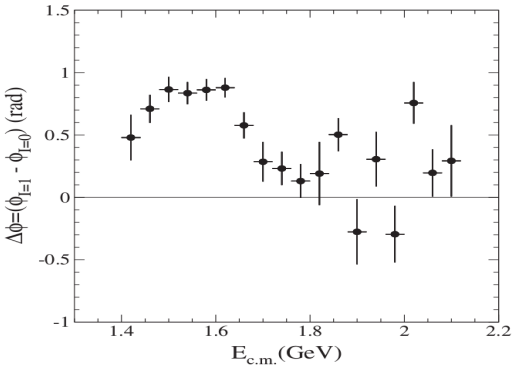

(c) Relative phase difference between the isoscalar and isovector components of the $KK^*(892)$ final state.

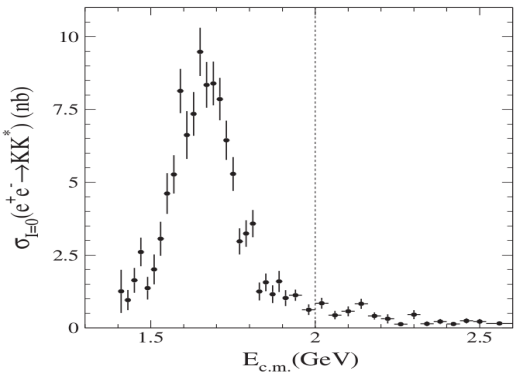

(d) Measured cross section of the isoscalar component of the $KK^*(892)$ final state.

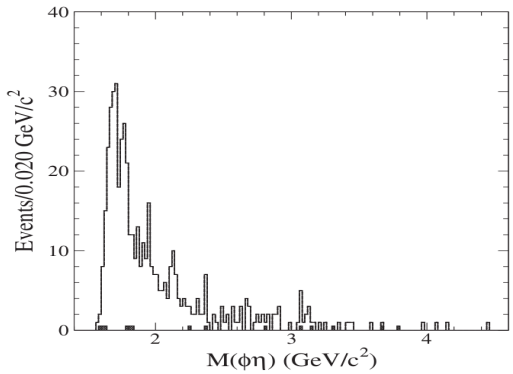

(e) Invariant mass spectrum for the $\phi\eta$ final state.

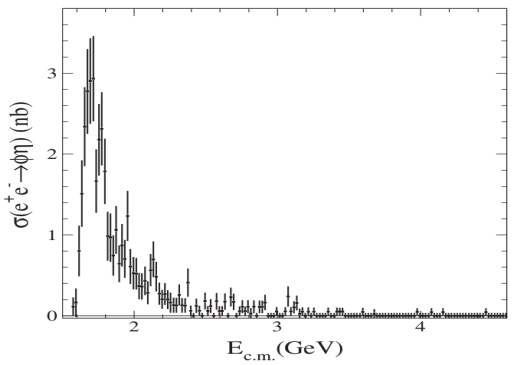

(f) Measured cross section for the $\phi\eta$ final state.

Figure 1.3: Highlighted results from the BaBar detector and collaboration where there is significant evience to suggest that a $\phi(1680)$ has been observed from both $KK^*(892)$ and $\phi\eta$ final states by means of electron positron annihilation.[10]

In 2008, the BABAR collaboration published a study containing many different topologies arising from electron-positron annihilation; most notably: $e^+e^- \to KK^*(892)$ and $e^+e^- \to \phi\eta$. The $KK^*(892)$ signal was studied by means of a Dalitz plot analysis and then showing the isovector and isoscalar components of the cross section (Figure 1.3d), as well as the phase difference plot between the two components (Figure 1.3c). The results strongly suggested that an isoscalar resonance exists at 1.7 GeV/c in the center of mass frame. The paper also provided an invariant mass plot (Figure 1.3a) and a measured cross section (Figure 1.3b) of the $K_sK\pi$ final state, which was the final state of the $KK^*(892)$ parent state. Once again, both plots provided evidence of a resonance at 1.7 GeV/c.

The $\phi\eta$ analysis provided far fewer statistics in comparison to the $K_sK\pi$ final state. However, the same plots were shown and provided the same conclusion (Figures 1.3e and 1.3f). Furthermore, since the resonance was thought to be an isoscaler that decayed to $\phi\eta$ and $K_sK\pi$, it was concluded that the parent state must have been $s\bar{s}$; more specifically, the radially excited version of the $\phi(1020)$. This enhancement was eventually observed to have a dominant decay into a neutral KK^* final state. An odd feature of the $\phi(1680)$ is that it has only been observed in electron-positron annihilation experiments, and has never been observed in photoproduction [11].

1.4.2 X(1750)

Six months after the discovery of the $\phi(1680)$, the X(1750) meson was observed by the Omega Photon collaboration at CERN [12]. The experiment analysed a K^+K^- final state from photoproduction and found an enhancement in the invariant mass spectrum of the K^+K^- pair. To be clear, the statistics of this study were very low and only produced 100 events in the peak region. The same collaboration produced another paper four years later which provided many more statistics and a matching result [13]. A clear resonance at 1760 MeV/c was observed, however the spin and parity of this state were not well described by angular distributions and therefore could not be confirmed as the radially excited version of the $\phi(1020)$. Significant evidence would eventually become available in the year 2002, when the FOCUS collaboration performed another photoproduction study on a K^+K^- final state [14]. There were three significant findings from this analysis, the first being an observation of a resonance after performing a transverse momentum cut on the K^+K^- system (Figure 1.4a). Second, a study was performed on the same final state as BaBar ($K_sK\pi$) where no significant resonances were found in any invariant mass spectra (Figure 1.4b). Finally,

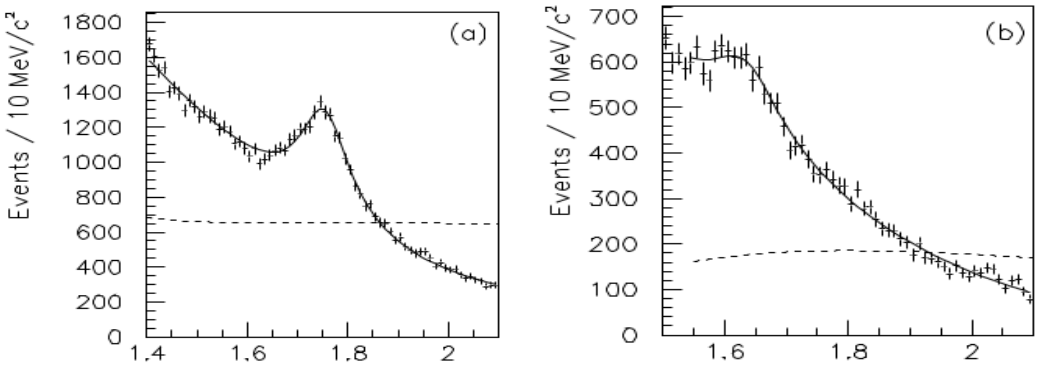

(a) Invariant Mass Spectrum for the K^+K^- final state after transverse momentum cut.

(b) Invariant Mass Spectrum for the K^*K final state after transverse momentum cut.

Figure 1.4: Highlighted results from the FOCUS collaboration where there is significant evidence to suggest that an $X(1750)$ has been observed in the K^+K^- invariant mass sepctrum. Additionally, no resonance is found inside the K^*K invariant mass spectrum.[14]

using these two results, branching ratios of $X(1750) \to K^*K$ were compared to $X(1750) \to K^+K^-$. It was found that these ratios were both less that 0.183 with a 90 percent confidence level. The observation of the $X(1750)$ raises many questions and a lot of confusion. In all likelihood, the $\phi(1680)$ probably is the radially excited form of the $\phi(1020)$ since the masses of the other radially excited vector mesons are $\omega(1650)$ and $\rho(1700)$. However, it is a complete mystery as to why the $\phi(1680)$ is seen so clearly in electron positron annihilation with no sign of a resonance at 1750 MeV/c^2; yet we see a clear $X(1750)$ resonance from photoproduction and no observable structure near 1680 MeV/c^2. To quote the final line from the FOCUS publication "The interpretation of the $X(1750)$ remains uncertain".

1.4.3 Y(2175)

Lastly, the BaBar collaboration at SLAC discovered a structure at 2175 MeV/c^2 in the reaction $e^+e^- \to \phi f_0(980) \to K^+K^-\pi\pi$ [15]. Since the $f_0(980)$ decays to a neutral and charged pion final state, both the $\pi^+\pi^-$ and $\pi^0\pi^0$ topologies were studied in the analysis. In each instance, a resonance was obseved inside the cross sections of the charged and neutral final states. Additionally, the $K^+K^-\pi^{+,0}\pi^{-,0}$ final state invariant mass distributions showed a clear enhancement around 2175 MeV/c^2. Due to the fact that the structure came from the $\phi f_0(980)$ intermediate state, one can easily deduce that the parent state is both isosinglet and has quantum numbers equivalent to 1^{--}.

Furthermore, it has been suggested that this resonance may be a four quark strangeonium or hybrid strangeonium state for serveral reasons. One of the reasons is the fact that no isosinglet vector mesons have been seen to have an invariant mass this large. A second reason is the possibility that this state is analogous to the $Y(4260)$ state which is belived to be either a $c\bar{c}g$ or $cs\bar{c}\bar{s}$ exotic state. It follows naturally that the $Y(2175)$ could either be an $s\bar{s}g$ or an $ss\bar{s}\bar{s}$ exotic state. What makes this resonance even more enticing for this dissertation is that its quantum numbers forbid decay into $\eta\eta^{'}$, $\eta^{'}\eta^{'}$, and $\phi\phi$ final states due to C-parity and G-partiy violations. However, the $\phi\eta$ and $\phi\eta^{'}$ final states are quantum mechanically allowed. Assuming the $Y(2175)$ is a four quark $ss\bar{s}\bar{s}$ resonance, many theoretical models view this bound state as an ss $\bar{s}\bar{s}$ 'diquark' molecule. If this is true, then the primary decays of the $Y(2175)$ should be to the $\phi\eta$ and $\phi\eta^{'}$ final states [16].

The underlying issue with all of the observations previously described is that the production of final state kaons does not necessarily confirm the existence of an $s\bar{s}$ state. The observation of the $Y(2175)$ may be evidence of an $s\bar{s}$ exotic state. However, this cannot be officially resolved due to the fact that the valence quarks for the $f_0(980)$ are not known or well understood. Therefore, the only way to ensure that a state has $s\bar{s}$ content is to choose an intermediate state in which the parent $u\bar{u}$ / $d\bar{d}$ content is suppressed. One channel that will resolve this ambiguity is $\phi\eta$. If a state is shown to have a significant branching fraction to $\phi\eta$, it will be good evidence that the state is an $s\bar{s}$ state. Furthermore, if a state is not seen in the $\phi\eta$ channel, it will be good evidence that the state has little to no $s\bar{s}$ content. The reason for this will be described in more detail below.

1.5 Proposed Analysis

The purpose of this research is to accomplish at least one out of two goals. The first is to provide a spectrum of excited $s\bar{s}$ states using the $\phi\eta$ channel. The $\phi\eta$ channel is a unique final state to study because it can only be produced from a parent state that is dominantly comprised of $s\bar{s}$ quarks. The reason for this is due to a few different characteristics of the $\phi\eta$ final state. One characteristic is due to the fact that the ϕ meson is almost pure $s\bar{s}$, and that the η meson has a super position of $u\bar{u}$, $d\bar{d}$, and $s\bar{s}$ quark content. Since quark flavor is conserved in hadronic decays, having a strange and anti-strange particle in the final state is an absolute must. Another characteristic that makes $\phi\eta$ a desirable channel to study is because the daughter states are both isosinglet and relatively light in mass. The conservation of isospin in strong decays ensures that the

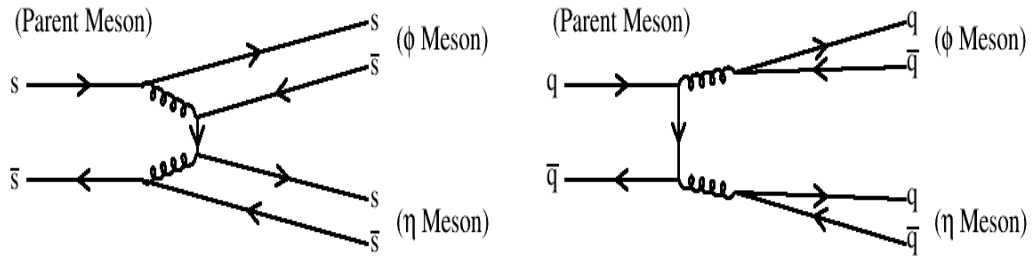

(a) Feynman Diagram for OZI allowed process.

(b) Feynman Diagram for OZI suppressed process.

Figure 1.5: (Figure 1.5a) Feynman Diagram depicting the decay of a parent $s\bar{s}$ state into $\phi\eta$ strangeonia. (Figure 1.5b) Feynman Diagram depicting the decay of an arbitrary $q\bar{q}$ parent state into $\phi\eta$ quarkonia.

parent state of an exclusive $\gamma p \to p\phi\eta$ reaction must be isosinglet as well. The last characteristic is that the $\phi\eta$ channel is Okubo-Zweig-Iizuka (OZI) suppressed from $u\bar{u}$ and $d\bar{d}$ parent states. The easiest way to understand OZI suppression is by considering Figure 1.5a and Figure1.5b, where Figure 1.5a is an OZI allowed process, and Figure 1.5b is an OZI suppressed process. Essentially, nature does not prefer to have a flavorless $q\bar{q}$ bound state spontaneously annihilate, then radiate into gluons which then need to carry enough energy to hadronize into mesons. It is more likely that the quarks from the parent state are passed to the daughter states.

Evidence of OZI suppression can be summarized with two examples, the branching fraction of $\phi(1020) \to \pi^+\pi^-\pi^0$, and the lifetime of the J/ψ. The branching fraction of $\phi(1020) \to \pi^+\pi^-\pi^0$ is small as compared to the branching fraction to two kaons, even though the three pion final state is more energetically favorable (two kaons have a mass of 990 MeV/c^2, whereas three pions have a mass of 415 MeV/c^2). The reason that the three pion branching fraction is small as compared to the two kaon branching fraction is due to OZI suppression. Since the $\phi(1020)$ is considered to be a pure $s\bar{s}$ bound state, the quark and anti-quark would have to annihilate and radiate into three gluons which would then become a three pion final state. Whereas, the two kaon final state can simply have the initial $s\bar{s}$ quarks passed by means of an OZI allowed decay.

Another nice example of OZI suppression comes from the fact that the J/ψ has an abnormally long lifetime. The J/ψ is a 1^{--} $c\bar{c}$ bound state, analogous to the $\phi(1020)$ vector meson which is

$s\bar{s}$. Due to OZI suppression, we would expect the J/ψ to decay into a pair of D mesons, much like the $\phi(1020)$ decays into a pair of kaons. However, the J/ψ is kinematically forbidden to decay into a pair of D mesons because the sum total of two D meson masses is greater than the J/ψ. This forces the J/ψ to annihilate and radiate into gluons, causing its lifetime to be much longer [17] [18] [19].

As previously stated, an observation of a parent state that has a large branching fraction to $\phi\eta$ will be good evidence of a dominant $s\bar{s}$ excited state. Conversely, if there is an absence of a state into $\phi\eta$, it should have little to no $s\bar{s}$ content. Understanding and establishing dominant $s\bar{s}$ states is an important aspect to meson spectroscopy because there are only three well known states to date; the $\phi(1020)$, the $f_2'(1525)$, and the $\phi_3(1854)$. The second goal of this research will be to search for exotic mesons using the $\phi\eta$ channel. Knowing that the ϕ meson has $J^{PC} = 1^{--}$, and that the η meson has $J^{PC} = 0^{-+}$, it is easy to derive what parent states can produce $\phi\eta$ with different relative orbital angular momentum. A table of possible parent states is given in Table 1.2.

Table 1.2: List of good quantum numbers (J^{PC}) for the parent stare of $\phi\eta$, where l represents the relative orbital angular momentum between the ϕ meson and the η meson.

l	J^{PC}
$l = 0$	1^{+-}
$l = 1$	0^{--}, 1^{--}, 2^{--}
$l = 2$	1^{+-}, 2^{+-}, 3^{+-}
$l = 3$	2^{--}, 3^{--}, 4^{--}

There are three states in Table 1.2 that are of particular interest, the most obvious being the 0^{--} and the 2^{+-} quantum states since they are inherently J^{PC} exotic for mesons. The other state of interest is the 2^{--} since it is not well understood for $s\bar{s}$ bound states [6].

CHAPTER 2

GLUEX

The data in this thesis came from the Spring 2017 run period which was recorded by the GlueX experiment located at Thomas Jefferson National Accelerator Facility in Newport News, Virginia (Figure 2.1). The Spring 2017 run started on January 23rd, 2017 and ended on March 13th, 2017. The conditions for this run were fairly stable and the only major change was increasing the beam current by 50% on February 24th, 2017. The run consisted of five different radiator settings including an amorphous radiator, and four different orientations of the linear polarization vector. The four different diamond radiator orientations included an angle of 0°, 45°, 90°, and 135° relative to the lab floor. There were two reasons for choosing these four different diamond orientations. The first reason is that we need to have a set of data which is perpendicular in photon polarization relative to another set of data. Therefore, the data set which was measured at 0° is perpendicular to the data set which was measured at 90°. Similarly, the 45° data set is perpendicular to the 135° data set. The second reason for choosing four different diamond orientations was to make sure the acceptance inside the spectrometer remained the same for different photon polarization angles.

Over the course of the entire Spring 2017 run, there were 10.4×10^9 physics triggers recorded for the 0° diamond orientation, 11.0×10^9 physics triggers recorded for the 90° diamond orientation, 10.0×10^9 physics triggers recorded for the 45° diamond orientation, 10.2×10^9 physics triggers recorded for the 135° diamond orientation, and 8.0×10^9 physics triggers recorded for the amorphous radiator. Therefore, a total of 50 billion physics triggers were recorded for the Spring 2017 run, resulting in 120 TB of reconstructed event files. In addition, there was a trigger rate of roughly 50 kHz for the diamond and amorphous radiators. The run conditions were initially set to a "low intensity" beam current of 100 nA for the diamond radiator, and 150 nA for the amorphous radiator. As previously mentioned, the beam current was then increased to 150 nA for the diamond radiator and 200 nA for the amorphous radiator. For the entirety of this run, a 5 mm collimator hole was used for the beam line and a 75 μm Beryllium converter was used to measure photon polarization. As of this date, the Spring 2017 run is the most successful reconstructed physics run period for

GlueX. It should be noted, however, that the Spring 2018 run should have even more statistics once the data is reconstructed and analyzed.

Figure 2.1: A picture taken from inside Hall D. From this angle, the photon beam would be coming towards the viewer, and eventually interact with the liquid hydrogen target located inside the apparatus. One can easily identify the shell of the superconducting barrel-shaped solenoid as well as the back side of the forward calorimeter and some photomultiplier tubes attached to the time of flight detector. [20]

2.1 Jefferson Lab

Thomas Jefferson National Accelerator Facility (JLab) is a U.S. Department of Energy Office of Science national laboratory which has 1,500 scientists from 30 different countries and a total of 230 institutions worldwide (Figure 2.2). The lab has also completed nearly 200 experiments from all of its halls (not counting the new Hall D) and has graduated more than 500 Ph.D's due to the exceptional research conducted there. The primary mission of JLab is to understand the atomic nucleus by utilizing the Continuous Electron Beam Accelerator Facility (CEBAF) and the four experimental halls which receive its electrons. In addition, JLab also contains advanced computing resources, theoretical, and applied research which will help to educate future generations of scientists. The lab recently received over three hundred million dollars to upgrade the CEBAF

from 6 GeV to 12 GeV in energy. The upgrade included many new features of the CEBAF such as ten new superconducting radio-frequency (SRF) accelerating elements; or five per linear section of the accelerator. There were also ten new RF stations to power the ten new cryomodules (SRF) which required doubling the refrigeration capacity at JLab. Modifications to the magnets in the recirculation arcs and their power supplies were also an obvious necessity in order to keep the higher energy beam confined to the existing beam path. There was also a tenth magnetic arc added to the curved section of the CEBAF. This extra arc allows us to send beam towards the north linac which will then boost the electron beam to 12 GeV, the amount necessary to accommodate the experimental program in Hall D. All in all, this upgrade will allow scientists and researchers at Jefferson Lab to explore a greater amount of detail that may be hidden within the atomic nucleus. This upgrade was also coupled with the construction and creation of a new experimental Hall D, which houses the GlueX experiment and is the ultimate source for the data contained within this thesis [21].

Figure 2.2: A picture taken of the Thomas Jefferson National Accelerator Facility (JLab) in Newport News, Virginia. In this picture, the electron beam from the Continuous Electron Beam Accelerator Facility (CEBAF) will travel in a clockwise motion. The two linear accelerator sections of the CEBAF are near the two parallel lab roads which run towards and away from the picture view. Three circular grass mounds can be observed in the lower part of this picture which represent the locations of Hall A, Hall B, and Hall C. Hall D is located diagonally across the CEBAF from those three halls and somewhat visible in this picture. [20]

2.2 CEBAF

CEBAF is an acronym which stands for Continuous Electron Beam Accelerator Facility (Figure 2.3). The beam is created by shining laser light onto a gallium-arsenide wafer that is roughly

the size of a postage stamp. The laser light forces the bound electrons to fly off of the surface of the wafer and towards magnets which confine the electrons into a stream of particles the width of a human hair. These electrons are then passed into the linear accelerator region of the CEBAF. The linear accelerator contains a series of accelerator cavities called Radio Frequency (RF) cavities which are responsible for increasing the energy and momentum of the electron beam. These cavities are superconducting and cooled by a central helium liquefier which contains approximately 16,500 gallons of liquid helium and also keeps the RF cavities at -456 degrees Fahrenheit, or 2 degrees Kelvin. Attached to the two linear accelerator regions of the CEBAF are two arc regions. These regions contain large magnets responsible for steering and focusing the electron beam between the two linear accelerators. In total, the CEBAF is 7/8 of a mile in distance, or 1400 meters long, and is 25 feet below ground. The accelerator tunnel itself is 13.5 feet wide and 10 ft tall with 2 feet of concrete for its walls. Electrons travel through the straight section of the track up to 5.5 times which allow them to obtain energies as high as 11.5 GeV for Halls A, B, and C; and up to 12 GeV for Hall D. The CEBAF can also deliver beam to all four of the experimental halls simultaneously, allowing a wide variety of research to be done concurrently at Jefferson Lab. [22]

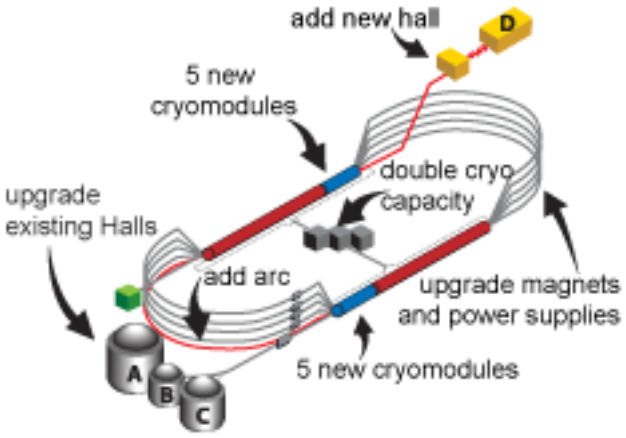

Figure 2.3: An illustration of the 12 GeV CEBAF upgrade at Jefferson Lab. This depiction shows where many of the aforementioned upgrades were physically placed within CEBAF and JLab. [20]

2.2.1 Injector

The CEBAF injector is a unique piece of equipment because it provides beam to the main accelerator at JLab while having to work in sync with two recirculating linear accelerators operating at 1497 MHz. The beam can be delivered to each experimental hall at 499 MHz, one third of the linear accelerator's frequency. This allows simultaneous operation of three halls at JLab; where the three beams are typically at 499 MHz with 120 degrees phase separation. Figure 2.4 shows the general layout of the injector [23]. The beam is created by using one of the 100 keV photo cathodes, the other gun being a hot spare.

Figure 2.4: An illustration of the injector at CEBAF, showing components for photo-producing, bunching and accelerating the beam electrons up to the point where they are ready to be injected into the linear section of the accelerator. [23]

The next element in the injector is the pre-buncher cavity, followed by emittance limiting apertures A1, A2, and then the three beam chopper system. The three beam chopper system is in charge of initial timing and longitudinal structure of the beam. Just like the three halls that will eventually receive the electron beam, this system operates at 499 MHz with three independently variable slits to define a phase acceptance from 0 to 110 ps for each beam. This part of the apparatus is important because it assures that any beam outside this window would not go correctly through the bunching and acceleration process, and therefore is stopped at the choppers. After the chopper is a device called the buncher which starts the main bunching of the beams. The capture section follows this which simply provides acceleration of the beams to 500 keV in energy. The phase and amplitude of buncher and capture cavities are crucial to the beam bunch length and energy spread.

Following the buncher and capture is the bunch length cavity which is a diagnostic system used to tune the beam bunch length by measuring the beam timing. Next are a series of superconducting radio frequency (SRF) cavities which ultimately accelerate the electrons to a final energy or 23 to 68 MeV. There are also three Faraday cups in the injector to measure the beam current at different stages; as well as some magnetic elements which provide transverse focusing and steering of the beam.

2.2.2 RF Cavities

After the electrons leave the injector, they receive a boost in energy due to several RF cavities that are located inside the linear section of the accelerator. The RF cavities are made with superconducting niobium material and are maintained at 2K using liquid Helium. The cavities have a cycloid geometry in the direction that the electrons travel, and are azimuthally symmetric. The specific design of these cavities are depicted below in Figure[2.5].

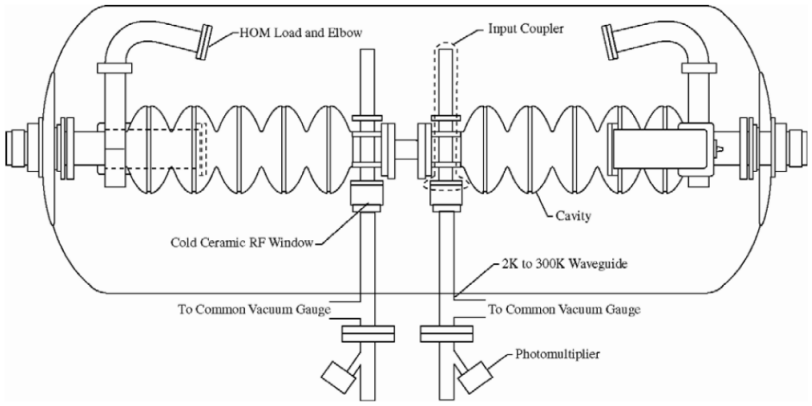

Figure 2.5: An example of the RF cavity design at CEBAF. The electrons would enter the cavity from the left hand side nozzle that is sticking out of the main cavity. Upon entering the cavity, the electrons will have their linear momentum increased inside the cycloid section of the RF cavity. After an increase in linear momentum, the electrons will exit the main cavity to the right. [20]

The electrons will have their linear momentum increased inside the cavities due to a standing radio frequency (RF) electromagnetic wave. The standing waves are kept in phase with the electron beam bunches that are sent from the injector. The acceleration of the electrons is possible due to the changing electric field inside the RF cavities. Once the electrons are inside one of the cavities,

the electron is accelerated forward due to an electric field. This field is created by a negative charge collection behind the electron beam bunch, and a positive electric charge ahead of the electron beam bunch. Since the negative charge will repel the electrons and the positive charge will attract the electrons, there is an overall force applied to the beam bunch, causing its linear momentum to increase. An example of this is illustrated in Figure[2.6] below.

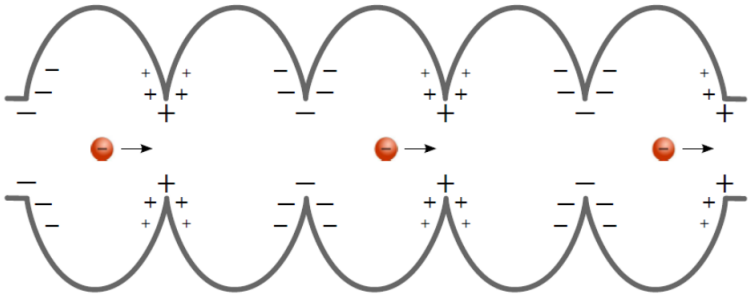

Figure 2.6: An example of how electrons are accelerated inside the CEBAF at Jefferson Lab. The electron beam bunches enter the RF cavities from the right and are immediately repelled away from the negative charge collection on the cavity, while simultaneously attracted to the positive charge collection farther down stream. As the electrons travel from one cell to the next, the charges will alternate, causing the electron to always maintain a positive acceleration from left to right. [20]

2.2.3 Linac

After the electron beam bunches are accelerated by the RF cavities, they must then turn around by 180° to be accelerated by the other linear section of the accelerator and to ultimately complete one full pass. The steering of the electrons is accomplished by several magnets which are precisely positioned throughout the east and west arcs of the accelerator. The first magnet is responsible for separating the beam into five different mono-energetic beam bunches. Since the linear accelerators will boost the energy of the electrons discretely, the first magnet can be tuned to bend the lower energy electrons more abruptly, while barely affecting the motion of more energetic electrons. This means that the less energetic electrons will bend upward towards the ceiling of the beam tunnel, while the more energetic electrons will stay relatively level with respect to the beam tunnel floor (Figure[2.7]). In order to turn the beam, a series of magnets are placed along the beam pipes for

the different energy levels. After the electron beam has done five passes, it will enter its last turn until it enters Hall D where the GlueX experiment will convert it into a photon beam.

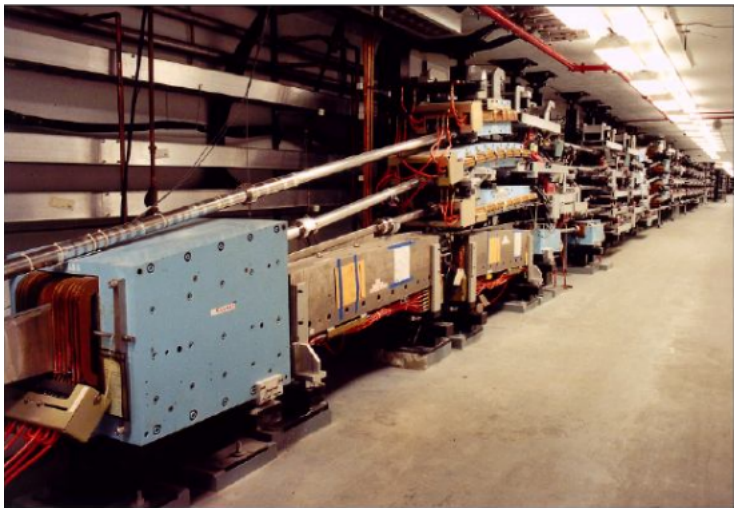

Figure 2.7: A picture inside the acclerator tunnel at Thomas Jefferson National Accelerator Facility; specifically the North Linac section of the accelerator which houses the magnets used to turn the electron beam. The blue box located in the lower left portion of the picture is the magnet responsible for splitting the electron beam into the monoenergetic beam bunches which will eventually continue into one of the five beam pipes in the picture. Farther down stream are several magnets used to steer the beam around the accelerator. Image source [20]

2.3 Hall D

After an electron beam bunch has made 5.5 passes around the JLab accelerator ring and reaches an energy of 12 GeV, it will be passed towards Hall D. This section will follow the electron beam towards the diamond radiator where it will produce linearly polarized coherent Bremsstrahlung radiation. This radiation will then continue down the beam pipe and into the GlueX spectrometer where it will interact with a stationary liquid hydrogen target. All of the relevant sub detectors inside the beam pipe, as well as inside the GlueX spectrometer will be described in the subsections below.

2.3.1 Diamond Radiator

There are four different experimental halls at Jefferson Lab; Hall A, Hall B, Hall C, and Hall D. Halls A, B, and C are located at the south-west section of the accelerator oval, whereas Hall D is located unaccompanied at the opposite end of the accelerator oval. When electrons are approaching the direction of Halls A, B, and C, they can either continue straight into those halls or continue around the track towards Hall D. Once inside the Hall D, the electron beam will collide into a diamond radiator.

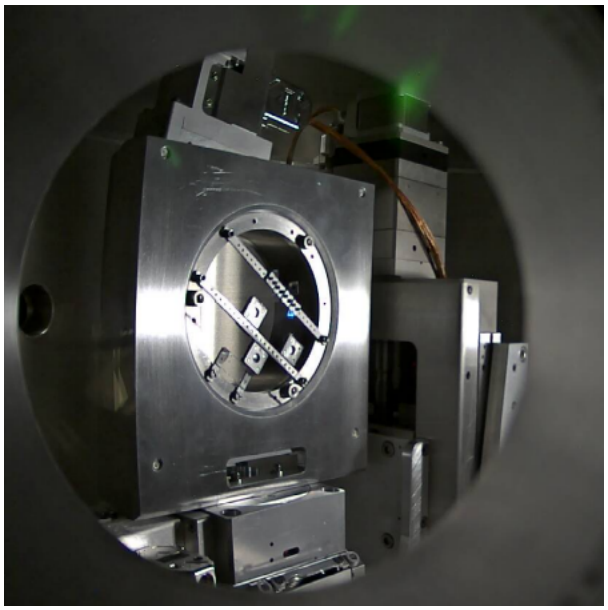

Figure 2.8: A photograph taken from a monitoring camera located inside the beam tunnel. The photograph shows the goniometer which is the disk shaped metal mount in the middle of the square object. Located inside this disk is the diamond radiator which can be seen due to a faint blue light being emitted from its surface. [24]

The diamond radiator is a synthetic material with a nearly perfect lattice structure in order to produce highly polarized photons. It is roughly sixty microns thick and has a square cross sectional area, with each size having a length of 5.6 millimeters. The diamond radiator is mounted onto a goniometer which allows the GlueX experiment to change its orientation relative to the incident electron beam (Figure[2.8]). The orientation of the diamond radiator plane with respect to the electron beam can change two properties of the coherent Bremsstrahlung radiation. The first

property is the energy of the coherent peak, which can be changed by adjusting the transverse angle of the normal of the radiator plane with respect to the beam direction. The second property is the polarization direction of the coherent Bremsstrahlung radiation, which can be adjusted by rotating the radiator in the azimuthal direction with respect to the normal of the radiator plane. Since it is desirable to keep the energy of the coherent peak a constant throughout an experimental run period, the only property of the beam that will consistently change is the polarization direction.

It should be noted that there is an additional radiator used to collect data at GlueX which does not produce coherent Bremsstrahlung radiation. This radiator is amorphous and is used intermittently between runs with different diamond radiator orientations. [25]

2.3.2 Photon Beam

Once the linearly polarized photon beam is created by the diamond radiator, it continues straight towards the GlueX detector. Before reaching Hall D, the beam travels through a series collimators which only allow photons traveling with a particular direction to pass. This reduces the amount of noise from the Bremsstrahlung radiation and ensures that the beam is traveling towards the proton target. In addition, the scattered electrons that are left over from the interaction with the diamond radiator are bent by a magnetic field and are ejected towards a tagger which measures their energy. Knowing the initial energy of the incident electron beam, and then measuring the recoiled energy of the electrons allows us to get an idea of the energy of the photons that are about to enter Hall D. In addition to the energy, the photon tagger can also provide timing information for the photons that arrive into the hall. As previously mentioned, there are two radiators that are used for GlueX; a diamond radiator and an amorphous radiator. The biggest difference between these two radiators is the presence of an organized lattice structure. Since the amorphous radiator has a homogeneous distribution, the photon polarization will be uniform in all directions, while a lattice distribution will only allow photon polarization in one direction. The difference in atomic structure between the two radiators will result in different beam energy distributions. Additionally, the photons contained within the coherent peak will be highly polarized. In the case of GlueX, our radiator is designed to produce a fourty percent linear photon polarization at the edge of the coherent peak. These effects are most easily understood by referencing Figure[2.9], which is from the first GlueX physics publication [26].

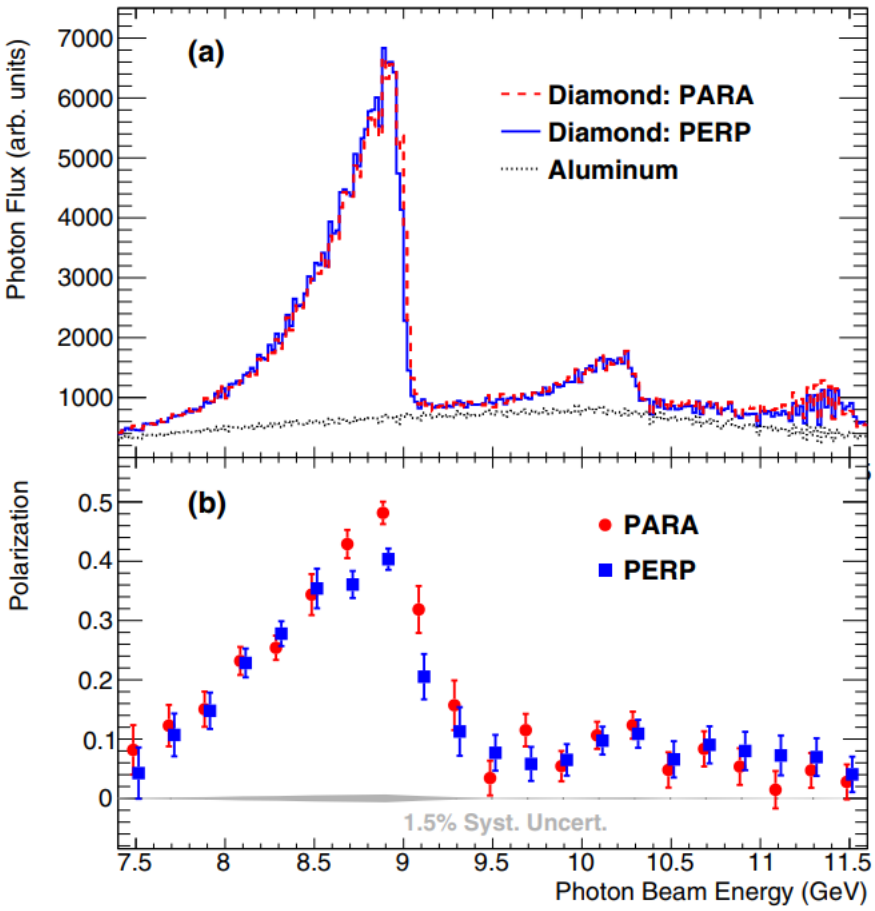

Figure 2.9: (a) Photon beam intensity versus energy as measured by the pair spectrometer (not corrected for instrumental acceptance). (b) Photon beam polarization as a function of beam energy, as measured by the triplet polarimeter, with data points offset horizontally by 0.015 GeV for clarity. [26]

2.3.3 Triplet Polarimeter (TPOL)

The triplet polarimeter (Figure [2.10]) is responsible for measuring the degree of polarization from the coherent Bremsstrahlung radiation created by the diamond radiator. The triplet polarimeter measures the degree of photon polarization using the triplet photoproduction process. When an incident photon interacts with the electromagnetic field of a bound state electron, the incident photon can spontaneously convert into an electron-positron pair, in addition to kicking the bound

state electron out of its orbital. Since the recoil electron will have a very large polar scattering angle with respect to the incident beam direction, the triplet polarimeter is responsible for measuring the azimuthal distribution of the recoil electron. Conversely, the electron-positron pair will carry most of the longitudinal momentum from the incident photon, therefore causing them to travel farther down stream and eventually detected by the pair spectrometer. The azimuthal angular distribution of the recoil electron will provide information on the polarization of the incident photon. The determination of photon polarization in the triplet polarimeter is similar to the study of beam asymmetries, such that the triplet cross section is proportional to the total cross section multiplied by a factor which involves the cosine of the recoil electron. Measuring the coefficient from a fit of the recoil electron angle will allow GlueX to determine the degree of polarization of photons as a function of beam energy. [27]

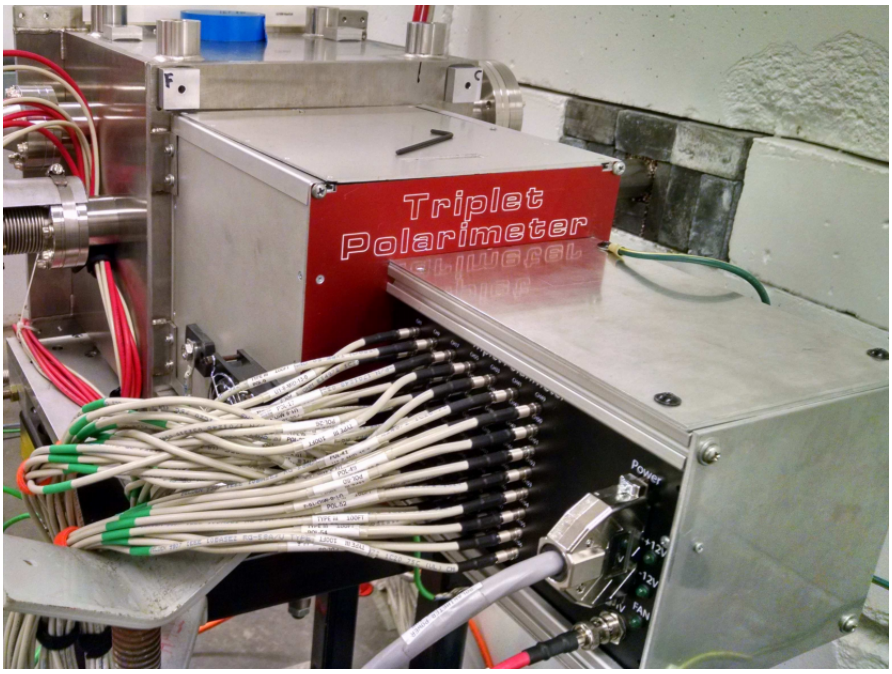

Figure 2.10: A picture of the triplet polarimeter inside the Hall D beamline. The photon beam will enter the triplet polarimeter from the upper left part of the picture and travel to the right. After interaction with the triplet polarimeter, an electron-positron pair will travel beyond the wall on the right portion of the photograph, where the pair spectrometer is located; as well as the GlueX spectrometer. [27]

2.3.4 Pair Spectrometer (PS)

After a photon interacts with the thin converter of the triplet polarimeter, an electron-positron pair are immediately produced with high longitudinal momentum, causing them to travel downstream. A dipole magnet of 1.8 Tesla is located after the triplet polarimeter in order to separate the photoproduced electron and positron and to not affect neutral particles such as the beam photons. Upon separation, the electron and positron will eventually be detected by scintillators on the pair spectrometer (Figure[2.11]).

Figure 2.11: A picture of the pair spectrometer. [28]

The scintillation array on the pair spectrometer consists of sixteen course counters, as well as an additional layer containing a high-granularity hodoscope. Since the electrons and positrons will travel in opposite directions due to the dipole magnetic field, there are two arms on the pair spectrometer, each of which can measure an electron/positron energy between 3 GeV and 6.25 GeV. This electron/positron energy range corresponds to a photon energy between 6 GeV to 12 GeV. The addition of the pair spectrometer allows GlueX to measure two important features about the incident photon beam, the energy and the flux (Figure [2.9a]). As previously mentioned, the pair spectrometer has the ability to reconstruct the energy of the pair produced electron and positron, thus allowing us to measure the energy of the incident photon. Additionally, knowing the radiation length of the diamond or amorphous radiator in conjunction with the amount of hits per beam bunch that the pair spectrometer sees, allows us to estimate the photon flux entering the GlueX

spectrometer. Accurately measuring the beam energy is obviously important for determining the amount of energy allowed in a final state, and measuring the beam flux is important for determining cross sections of final states as well. [29] [25]

2.3.5 Target

As the photon beam travels down the beam pipe and enters the GlueX detector, it will eventually interact with the target. The target at GlueX is a proton, so therefore the target chamber is filled with liquid Hydrogen (LH_2) which is stored at roughly 18 degrees Kelvin and at a pressure of 16 psiA. The entrance and exit of the target chamber are made from the polymide film material Kapton [30], and are 75 μm thick. The liquid hydrogen is insulated from the start counter by five layers of aluminized mylar and cerex material. The length of the target is aligned in the direction of the photon beam in order to increase the likelihood of observing an interaction with one of the protons at rest. [31] [25]

2.3.6 Start Counter (ST)

The start counter is the first detector located outside of the target chamber. The purpose of the start counter is to record the time of the photon-proton interaction which took place inside the target chamber, and to ultimately identify which beam bucket caused an event. Due to this, the start counter is designed to handle photon intensities up to $10^8 \frac{\gamma}{s}$, and must also have the ability to differentiate between beam buckets which can be separated by as little as 2 nanoseconds, or 500 MHz. The detector consists of thirty scintillators which are uniformly distributed around the target chamber in the azimuthal direction, which can be seen in the schematic given in Figure [2.12]. The scintillators contain silicon photomultipliers in order to record when the detector fires and to ultimately create a signal. Another important aspect of the start counter is the fact that its components and are not affected by the superconducting solenoid magnet which produces a strong magnetic field where the apparatus is located. The start counter has a timing resolution which ranges from 450 to 700 picoseconds and can correctly identify beam buckets up to a 94 percent accuracy. It also provides a ninety percent solid angle coverage around the target chamber, with the exception of highly back scattered angles with respect to the beam direction, and a hole in the forward direction due the beam halo. [32] [25]

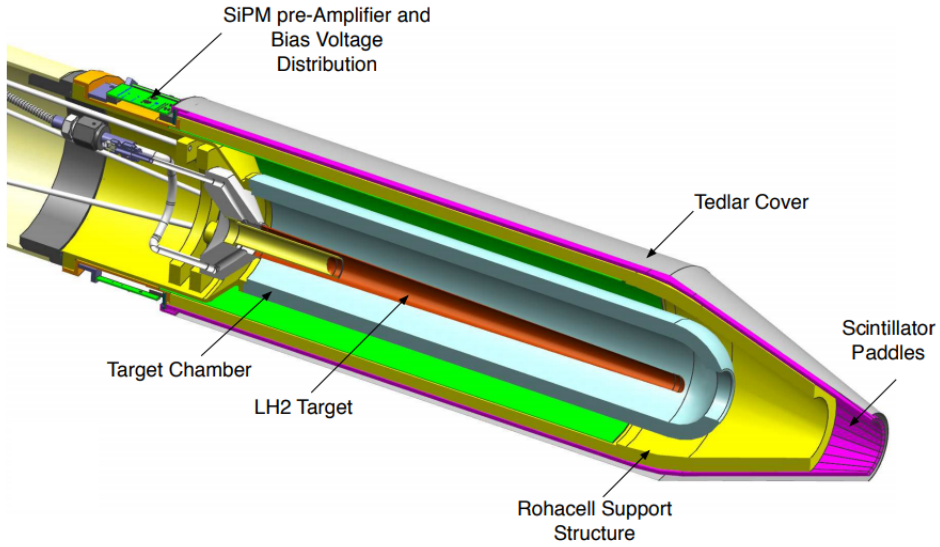

Figure 2.12: A schematic of the start counter located at the center of the GlueX spectrometer. The photon beam enters the detector from the upper left hand corner of the schematic and will exit the lower right hand corner of the schematic, out of the nozzle of the device. The start counter encapsulates the target chamber and makes its measurements using the scintillator paddles labeled on the diagram. [32]

2.3.7 Superconducting Solenoid/Magnet

The superconducting solenoid/magnet is the outer most part of the barrel portion of the GlueX detector. It was originally built and used by the Stanford Linear Accelerator (SLAC) in the 1970's for the LASS detector; and was even used for the E-135 experiment in the early 80's. In 1985, the solenoid was moved to Los Alamos National Laboratory (LANL) in order to be used for the MEGA experiment. Eventually, the superconducting magnet was moved to Hall D of Jefferson Lab during April of 2000, and has been housed there ever since. The superconducting solenoid has a diameter of 1.85 meters, and is 4.8 meters in length and can be seen in Figure [2.13]. This barrel shaped geometry contains four separate superconducting toroidal coils connected in series, as well as four cryostats, which all contribute to produce a magnetic field. When operating at the maximum GlueX current, the magnet can produce a magnetic field inside the spectrometer of roughly two Tesla in the direction of the beam direction. The operating current is 1360 Amperes, which produces an inductance of 26.3 Henry and a stored energy of 24 mega joules inside the coil. In order for the coil

of the solenoid to be superconducting, there is a common liquid Helium reservoir located on top of the barrel in order to cool the system. Part of the cooling apparatus can be seen in Figure[2.13]. The purpose of the superconducting solenoid/magnet is to produce a magnetic field responsible for bending charged particles inside the detector. The existence of this magnetic field allows us to determine both the charge of a particle as well as its momentum. The momentum of a charged particle is proportional to the radius of curvature around a magnetic field line. Having the ability to measure both the charge and momentum of charged particles is crucial for any physics analysis at GlueX. [33] [25]

Figure 2.13: A picture taken of the solenoid located inside Hall D. [33]

2.3.8 Central Drift Chamber (CDC)

There are two subdetectors inside the GlueX spectrometer which are responsible for tracking charged particles; one of them is the forward drift chamber, and the other is the central drift chamber. The central drift chamber has a cylindrical/barrel geometry, much like the superconducting solenoid, with the exception that the central drift chamber surrounds the target and start counter,

and is inside of the barrel calorimeter. The large cylindrical chamber is 1.5 m long and has an inner radius of 10 cm and an outer radius of 54 cm. Located within the central drift chamber are twenty four layers of 1.6 cm diameter straw tubes, containing a total of 3522 anode wires made of gold-plated tungsten at their centroid (Figure[2.14]).

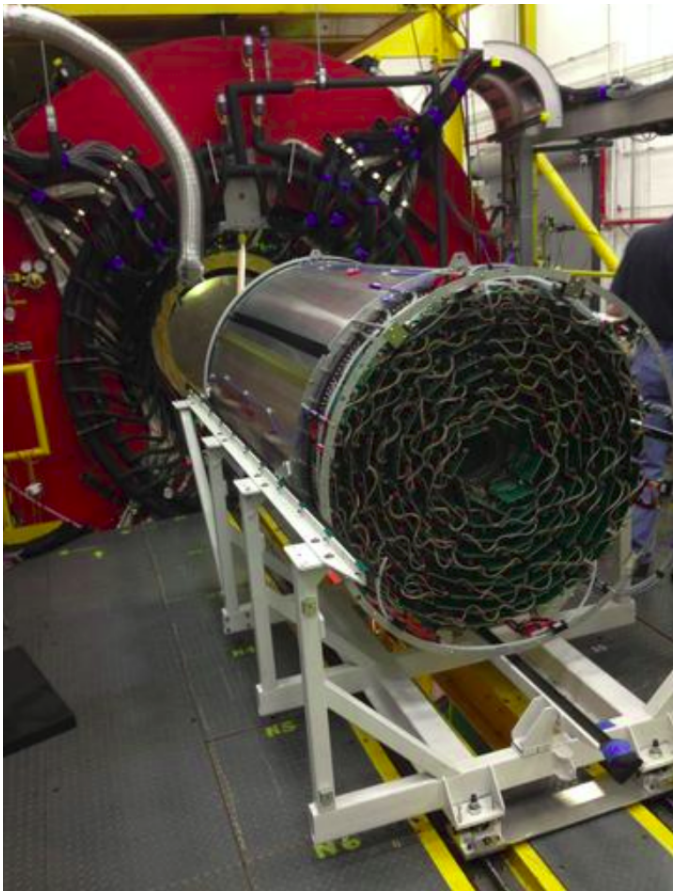

Figure 2.14: A picture taken of the central drift chamber before being installed into the GlueX spectrometer inside Hall D. [28]

Between the anode wires and the walls of the straw tubes is a mixture of carbon dioxide and Argonne gas at atmospheric pressure. The purpose of this gas is to become ionized when a charged particle has passed through it. This ionized gas is then attracted to the gold-plated tungsten wires due to the fact that they have a voltage. The charge deposited onto the wire will induce a current inside the anode which will then be read out by electronics in order to record the geometric path

that a charged particle has taken within the central drift chamber. This chamber is optimized for charged tracks with highly transverse momentum and therefore covers a polar angle range between 6 and 165 degrees with respect to the beam direction. In addition, the barrel shaped geometry of the central drift chamber provides a full angular coverage in the azimuthal direction. The detector has been optimized for a position resolution perpendicular to the wires of 150 micrometers, and can also provide information on the loss of energy per unit distance. This measurement allows the GlueX spectrometer to separate positively charged pions from protons with momentum as high as 450 MeV/c. In addition to energy loss, the central drift chamber is also responsible for measuring momentum of charged particles by utilizing the path that a charged particle has taken inside the magnetic field of the spectrometer. Knowing the momentum of charged particles is another crucial measurement for performing physics analyses at GlueX. [25] [34]

2.3.9 Forward Drift Chamber (FDC)

The forward drift chambers (FDC) are located downstream of the central drift chamber and are encapsulated by the superconducting solenoid/magnet and barrel calorimeter. The purpose of the detector is to track charged particles originating from the target chamber with shallow angles relative to the beam direction. Since it is in the downstream direction, the forward drift chamber is designed to provide a large number of measurements in a short amount of time due to high momentum and the high multiplicity of tracks. Much like the central drift chamber, it must also have good spatial resolution of charged particle paths in order to accurately reconstruct their momentum. To perform these tasks, the forward drift chamber uses two planes comprised of cathode strips which face a wire plane. The cathode strips are analogous to the argon-carbon dioxide gas inside the straws of the central drift chamber; when struck by a particle, a charge is induced onto the strips. This excess of charge is measured by the detector and with timing information, can properly reconstruct the path of a charged particle. The FDC detector includes four separate but identical 62 disk-shaped packages. Each of the disk shaped packages contains six independent planar drift chambers with separate gas volumes. Contained within these gas volumes are an anode wire frame with two cathode strip planes. There are also aluminized mylar planes which act as ground between the electrically charged strips. The four sets of electrical planes with six gas volumes can easily bee seen in Figure[2.15]. [25]

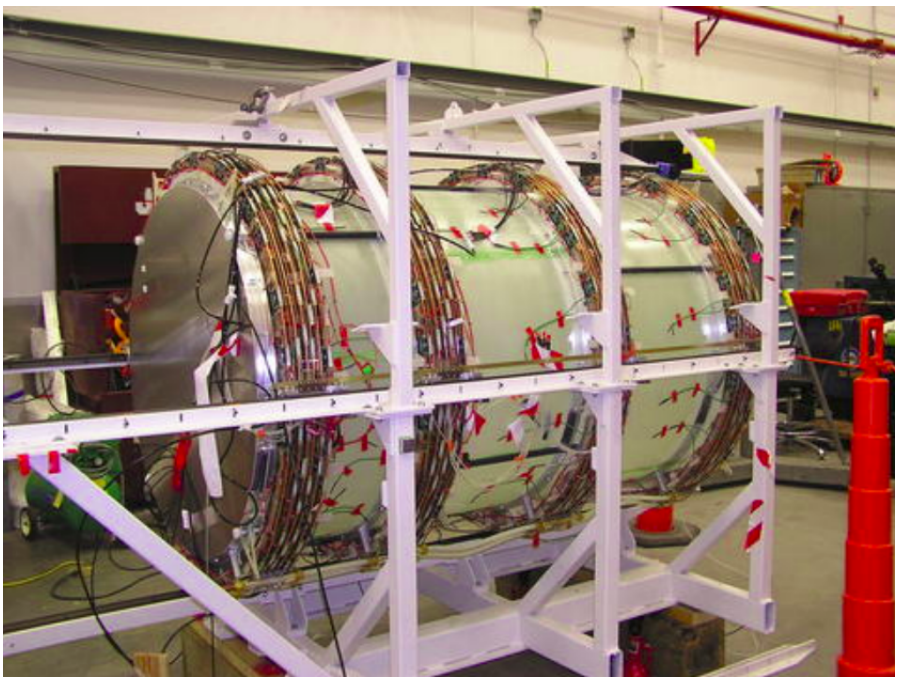

Figure 2.15: A picture taken of the forward drift chamber being surveyed on the floor of Hall D before installation. [28]

2.3.10 Barrel Calorimeter (BCAL)

At this point, a lot has been said about the detection of charged particles, but not a lot has been said about the detection of neutral particles, specifically, photons. One of the devices that is designed to detect photons is the barrel calorimeter. Originally constructed at the University of Regina, the BCAL is a lead scintillating fiber matrix, located immediately inside the super conducting solenoid. This sub detector has an outer radius of 90 cm, an inner radius of 65 cm, and is 390 cm in length, as seen in Figure[2.16]. The primary goal of the barrel calorimeter and the forward calorimeter is to measure photons which originated from the decays of π^0 and η; both of which produce two photons as a decay mode.

When a particle enters the BCAL, it excites several electrons inside the scintillation material, which then radiate energy in the form of photons. The photons travel down the scintillation fibers until they reach the endpoints of the barrel where they are then collected by light guides which then leads to silicon photo multipliers (SiPM). The SiPMs collect the light signals and convert

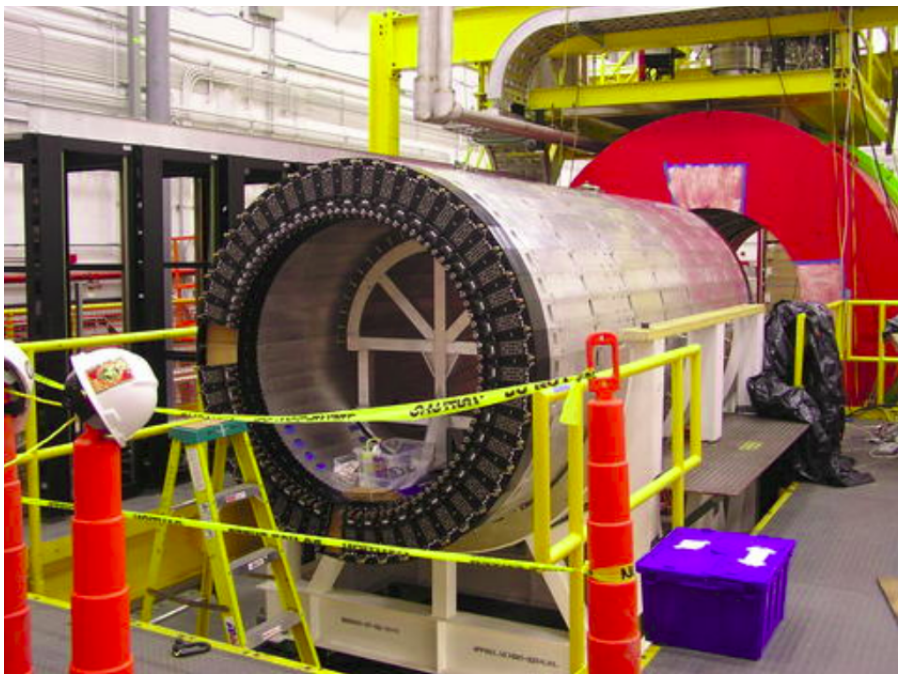

Figure 2.16: A picture of the barrel calorimeter before assembly into the superconducting solenoid. [28]

them into amplified electrical pulses. The barrel calorimeter performs this duty by accurately reconstructing the positions and energies of photons within the GlueX spectrometer. The BCAL can measure individual photon energies as low as 60 MeV and as high as 2.5 GeV, and additionally can provide timing information for photons and charged tracks originating from the target chamber. The timing, energy, and position resolution for the barrel calorimeter is somewhat tricky to define, as many of these parameters are a function of the incident photons energy and angle with respect to the lead scintillating blocks. As an example, the energy resolution of the BCAL depends on the number of photo-electrons detected by the photo sensors at the end of the scintillators. The number of photo electrons produced within a lead block is directly proportional to the energy deposited by the incident photon. The photon position is determined by the time difference at upstream and downstream fiber ends. [25] [35] [36]

2.3.11 Forward Calorimeter (FCAL)

Much like the barrel calorimeter, the forward calorimeter is designed to detect photons which were radiated by either π^0 or η mesons; only this detector is placed in the forward direction rather than a direction more transverse to the beam direction. The forward calorimeter is comprised of an array of lead glass blocks which collectively form a circular pattern to cover the end of the barrel segment of the GlueX spectrometer, as seen in Figure[2.17].

Figure 2.17: A picture of the forward calorimeter with no cover in front of it. One can clearly see the lead blocks used to reconstruct photons in the forward direction. [28]

The lead glass blocks detect high energy photons because of their tendency to spontaneously pair produce into an electron-positron pair upon entering the lead glass medium. The resulting electron-positron pairs emit bremsstrahlung radiation, which can then spontaneously pair produce into another electron-positron pair. This process will continue until all of the energy from the original photon has been completely absorbed by the lead glass in a process which is known as showering. When the electron-positron pair travel through the lead glass material at a high enough velocity, they can produce Cherenkov radiation which is collected and measured by photomultiplier tubes

attached to the end of the lead blocks. The amound of Cherenkov radiation that is detected by the absorbing lead block is directly proportional to the amount of energy deposited into it. Therefore, knowing the position, energy, and timing of the electromagnetic shower allows us to perform particle identification on photons traveling in the forward direction. The forward calorimeter has a circular lead glass array with a diameter of 2.4 m and has 2800 lead glass blocks. The front face of the forward calorimeter is 560 cm down stream from the center of the target chamber. Each lead glass block has a rectangular geometry, with a (4x4) cm square base and a height of 45 cm. In addition, a 3x3 square array of lead block located near the beam hole were removed from the detector due to the high rates inherent within that region of the detector. [25] [37]

2.3.12 Time of Flight Detector (TOF)

Unlike the aforementioned detectors, the time of flight (TOF) is square in shape and is (252 x 252) cm in size. The sub detector has two layers of scintillator paddles, one layer that is parallel to the floor of Hall D, and a second layer that is perpendicular to the floor of Hall D. Each layer contains 38 'standard' paddles, 4 'half width' paddles, and 4 'half length' paddles. The dimensions of the standard paddles are (2.54 x 6 x 252) cm, while the half width paddles are (2.54 x 3 x 252) cm, and the half length paddles are (2.54 x 6 x 120) cm. The purpose of the half width paddles is to compensate for the higher rates that take place closer to the beam hole, and the purpose of the half length paddles is to allow the beam to pass through the beam hole. All of these different paddles can be seen by closely inspecting Figure[2.18].

The time of flight is located downstream of the cylindrical portion of the GlueX detector and is before the forward calorimeter. The time of flight is comprised of transparent scintillating bars that are wrapped in highly reflective material so that no light can escape. The scintillation material in the TOF is similar to the scintillation material in the BCAL. When a particle hits the time of flight, the electrons inside the scintillation material become excited and radiate photons which travel down the material and are eventually collected by a photomultiplier tube. The purpose of the time of flight is to deduce how long it took a particle to travel from the interaction vertex inside the target chamber, all the way to the wall of the time of flight. Since the distance travelled by a charged particle is known from the reconstructed drift chamber paths, we can divide this by the flight time in order to calculate a velocity. In addition to the path of a charged particle, the momentum of it can also be measured since that it is proportional to its radius of curvature with

respect to the magnetic field within the spectrometer. Measuring the momentum of a charged particle and calculating its velocity within the chamber allows us to approximate the mass of the particle which ultimately leads to a particle identification. [25]

Figure 2.18: A picture of the time of flight after sucessful assembly inside Hall D. [28]

CHAPTER 3

MONTE CARLO

3.1 Monte Carlo Features of $\gamma p \to p\phi\eta$

In order to better understand the acceptance of the $\gamma p \to p\phi\eta$ topology in the GlueX spectrometer, a generated Monte Carlo sample was analyzed. More specifically, the exact sample that was produced was $\gamma p \to pX; X \to \phi\eta; \phi \to K^+K^-; \eta \to \gamma\gamma$. This Monte Carlo sample consisted of 1,666,667 generated events for each of the run numbers 030408, 030620, 030699, 030802, 030900, and 031029. The run numbers were chosen because two have beam polarizations in the PARA/PERP directions at low intensity (030408 and 030620), two have PARA/PERP orientations at high intensity (030802 and 031029), and two of the run numbers are from amorphous radiators (030699 and 030900). The total number of generated $\phi\eta$ events is therefore 10 million. The events were generated using a combination of a coherent and an incoherent bremsstrahlung beam energy spectrum ranging from 3 GeV to 12 GeV. These events were also generated with a t-slope of 2.5 $(GeV/c^2)^2$. To be more clear, the thrown beam particles were not polarized in this sample; only the beam energy spectrum matched that of a polarized beam spectrum plus an incoherent beam spectrum (Figure [3.1]). All final state particle kinematics were generated using the GlueX Monte Carlo generator (genr8). The generated final state phase space did not include any spin information from parent or daughter states. The $\gamma, K^+, K^-, \phi, \eta$, and p particles were generated using the invariant mass values and widths provided in the PDG. The photo-produced X mass was distributed between the lower kinematic limit $m_\phi + m_\eta$ and the upper kinematic limit which is a function of the momentum transfer t, and the thrown beam energy.

An example of what the generated beam energy distribution looks like for this Monte Carlo sample is given in Figure [3.1]. It should be noted that this particular Monte Carlo sample includes both coherent and incoherent beam structures, where the peaks in the image come from coherent Monte Carlo. The lower energy region of the beam energy spectrum comes primarily from the incoherent data. It should also be noted that the slow rise of the beam energy in this region is due to Lorentz factor weighting, or phase space.

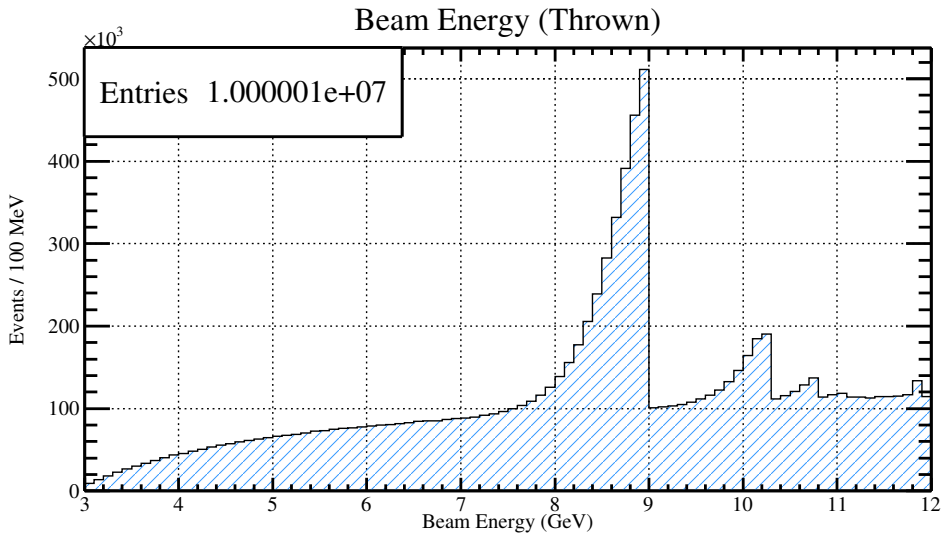

Figure 3.1: A histogram which includes the thrown beam statistics from the generated Monte Carlo example. In the figure one can easily see the coherent peak which maximizes at 9 GeV. Additionally, one can also see other secondary peaks at higher energy.

Momentum versus θ distributions are also provided in Figures [3.2], [3.3], [3.4], and [3.5]. These figures are generated Monte Carlo and represent the distributions of final state particles in the lab frame before running hdgeant, mcsmear, and `hd_root`. Still, the figures provide some insight into the expected kinematic distributions of the final state particles. For example, Figure [3.2] displays the momentum versus theta distribution for the recoil proton. This figure shows that we should expect the proton to have a very low momentum and high recoil angle relative to the beam direction for this final state.

Additionally, Figures [3.3][3.4] seem merely identical in shape and contour. This is expected and the reason for this is that both kaons are decaying from the ϕ meson, and the K^+ and K^- are anti-particles. In these figures, it is clear that Kaons will preferentially travel towards the TOF/FCAL and with a momentum that should include a lot of pion contamination (see Figures [4.18][4.26] for more information on pion contamination at high momentum).

Lastly, Figure [3.5] shows that the final state photons will be mostly forward going and therefore we should expect to see the majority of them interacting with the FCAL rather than the BCAL. It is not surprising that the Monte Carlo has generated photons and kaons that favor the forward direction, while the recoil proton has low momentum and a highly transverse direction. This is

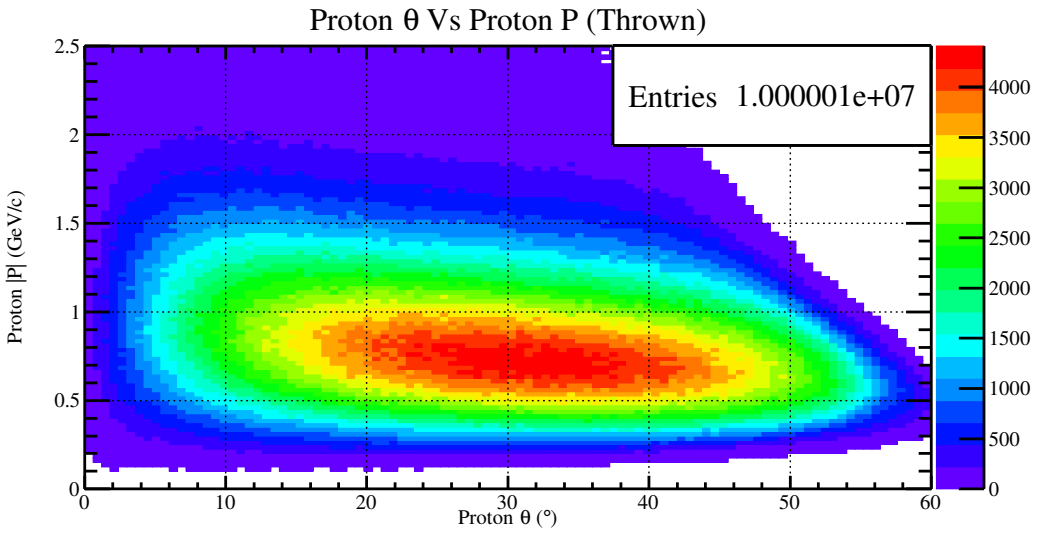

Figure 3.2: A two dimensional histogram which includes the thrown kinematic information of the recoil proton. In the histogram, the horizontal axis represents the generated θ angle in the lab frame, and the vertical axis represents the generated momentum magnitude in the lab frame. One interesting feature of this Monte Carlo data is that the kinematics of the recoil proton appear to be constrained between $[0.2 - 2.0] GeV/c$ in momentum, and $[0.0 - 60.0]^\circ$ in angle.

simply a consequence of the fact that a low t interaction was programmed into the Monte Carlo, resulting in Figure [3.6].

The last few figures to be discussed in this section involve the study of invariant mass spectra. The first of which is the invariant mass of $\phi\eta$ (Figure [3.7]) which shows a phase space distribution between the values of 1.5 to 3.2 GeV/c^2; then the slope of the distribution changes drastically from 3.3 to 4 GeV/c^2. These features may seem incorrect at first glance since the generated Monte Carlo mass is supposed to just show phase space. However, upon further inspection, it is clear that these features manifest themselves within the Monte Carlo data because of the shape of the beam spectra. The best way to see this behavior is by considering Figure [3.8]. This figure shows the generated beam energy on the vertical axis, and the generated $\phi\eta$ mass on the horizontal axis. Since the primary peak from the coherent bremsstrahlung will dominate most of the statistics in this generated sample, the $\phi\eta$ invariant mass range which it couples too will be most dominant as well. Inspecting Figure [3.8], one can clearly see the coherent peak at 9 GeV, and the corresponding $\phi\eta$ invariant mass ranging from 1.5 to 3.2 GeV/c^2.

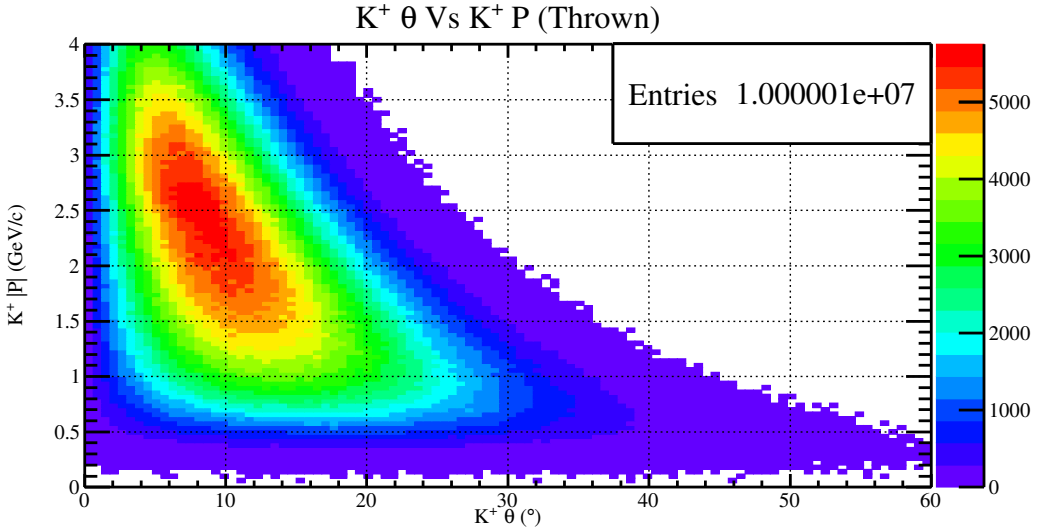

Figure 3.3: A two dimensional histogram which includes the thrown kinematic information of the generated K^+. In the histogram, the horizontal axis represents the generated θ angle in the lab frame, and the vertical axis represents the generated momentum magnitude in the lab frame.

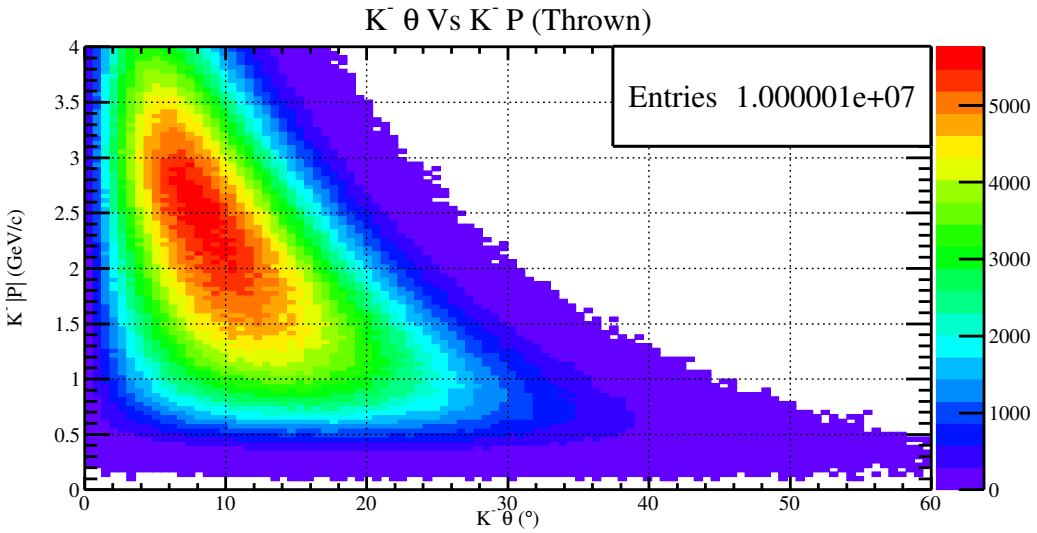

Figure 3.4: A two dimensional histogram which includes the thrown kinematic information of the generated K^-. In the histogram, the horizontal axis represents the generated θ angle in the lab frame, and the vertical axis represents the generated momentum magnitude in the lab frame.

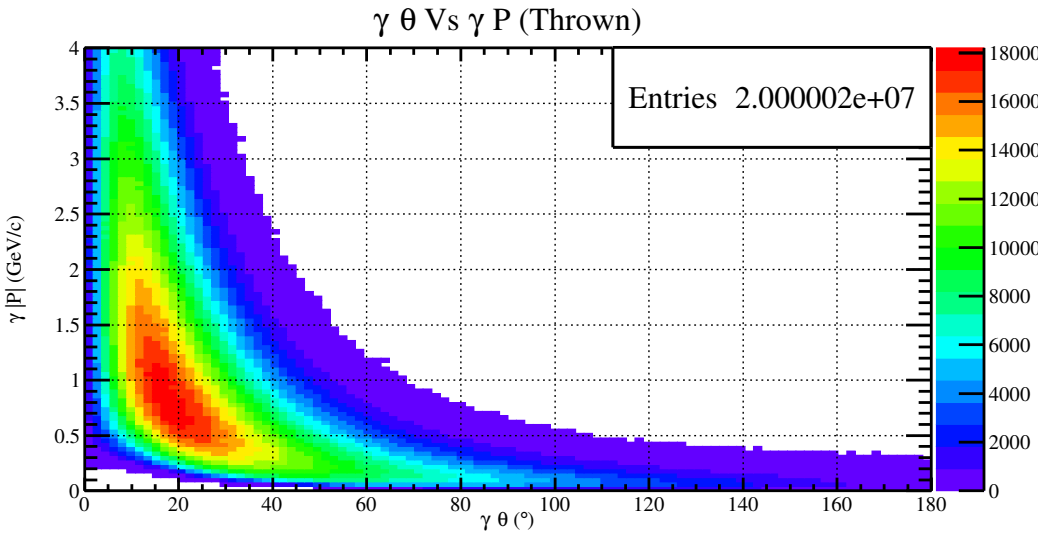

Figure 3.5: A two dimensional histogram which includes the thrown kinematic information of the generated photons. In the histogram, the horizontal axis represents the generated θ angle in the lab frame, and the vertical axis represents the generated momentum magnitude in the lab frame. The reason that the statistics are doubled in this histogram is due to both final state photon measurements being included in the plot.

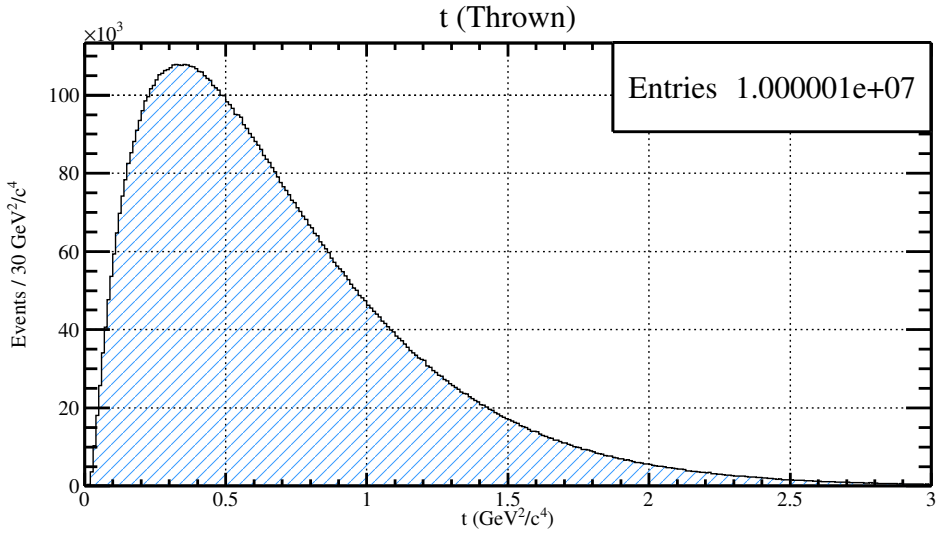

Figure 3.6: A histogram which includes the generated spectrum for the Mandelstam variable, t. The t-slope for the Monte Carlo presented here is 2.5 $\frac{GeV^2}{c^4}$

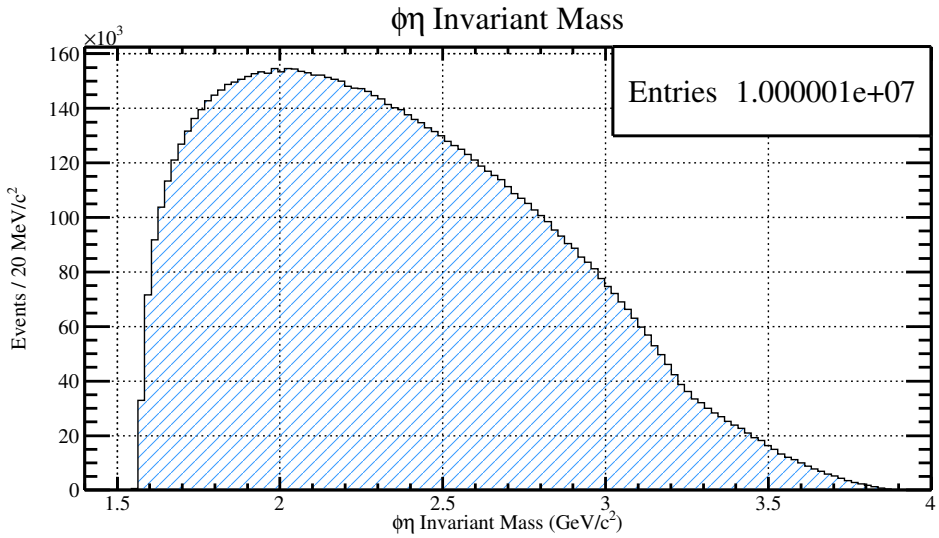

Figure 3.7: A histogram which includes the generated $\phi\eta$ invariant mass. In the figure one can easily see that the invariant mass of the $\phi\eta$ has the shape of phase space until it reaches ~ 3.2 GeV/c^2. From that point, the invariant mass falls less sharply until ~ 4.0 GeV/c^2. This feature of the invariant mass is directly related to the fact that a coherent bremsstrahlung beam energy spectrum was used. The abrupt change in the invariant mass range of $3.3 - 4.0$ GeV/c^2 is caused by the primary coherent peak at $9.0GeV$. To visualize this in two dimensions, see Figure [3.8].

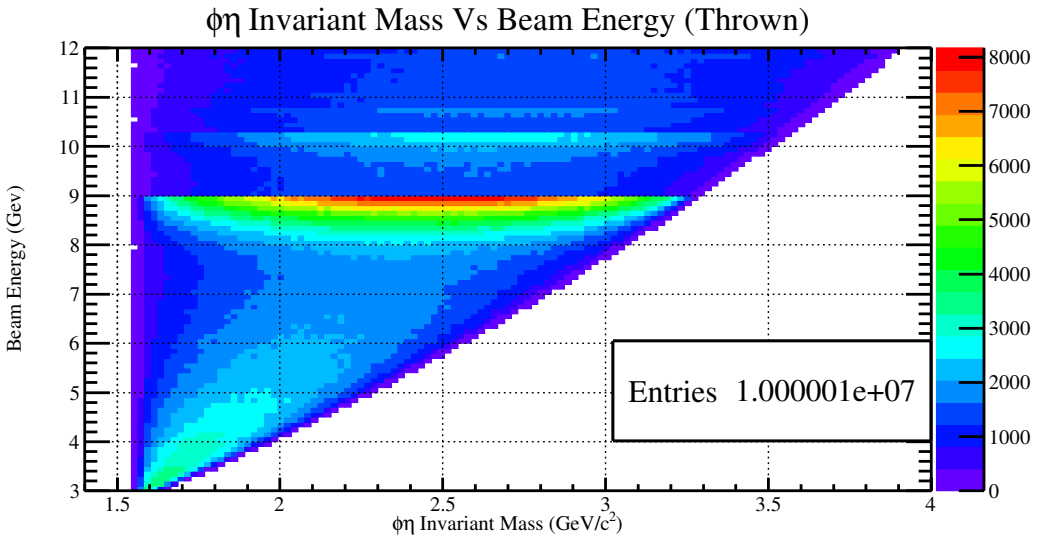

Figure 3.8: A two dimensional histogram which includes the generated $\phi\eta$ invariant mass on the horizontal axis and the Beam Energy on the vertical axis. In the figure one can easily see the effect that the coherent peak has on the shape of the phase space.

CHAPTER 4

DATA SELECTION

4.1 Identification of $\gamma p \to pK^+K^-\gamma\gamma$ Events at GlueX

In order to study potential states of bound strangeonia, it is essential to properly identify all final and initial state particles. The final state topology that will be studied for this thesis is $\gamma p \to pK^+K^-\gamma\gamma$, where the K^+K^- pair are daughter states of the ϕ meson, and the $\gamma\gamma$ pair are daughter states of the η meson. Therefore, the beginning of this analysis section will focus on the particle identification of the proton, kaons, and final state photons, as well as the incident beam and target proton. Once identification of all particles has been well established, this analysis will then provide evidence that the final event sampling enforces exclusivity.

4.1.1 Spring 2017 Run Period

The data presented here is the result of the successful Spring 2017 run period. The Spring 2017 run period spanned from January 23rd to March 13th and accumulated roughly 50 billion physics events. The maximum electron beam energy used was 12 GeV, and the accelerator ran at 250 MHz while in low intensity (beam every 4 ns), and later ran at 500 MHz while in high intensity (beam every 2 ns). Upon entering Hall D, the electron beam was incident upon a radiator. During this run period, both amorphous and diamond radiators were used to produce either incoherent or coherent polarized bremsstrahlung radiation. The diamond radiator was experimentally set up to produce linear photon polarization at four different angles relative to the lab floor - 0°(parallel with floor), 45°, 90°(perpendicular with floor), and 135°. These directions were chosen in order to provide the detector with a uniform sampling of linear polarization in the transverse direction to the incident beam. In order to yield roughly the same amount of statistics for an amorphous radiator run as compared to a diamond radiator run, a beam current of 150 nA was incident upon the amorphous radiator, while a beam current of 100 nA was incident upon the diamond radiator. Farther downstream, a 5 mm collimator hole was used for all radiator configurations. Lastly, the

collimated photon beam was incident upon a stationary liquid hydrogen target. This resulted in one petabyte of files and 16 pb^{-1} of integrated luminosity.

4.1.2 Identification of Initial State Particles

Photon Beam. The first step in identifying the initial state beam photon is to select the correct beam bunch. Since the electron beam is delivered from the accelerator every four nanoseconds, the timing of when the beam particles arrive into the hall is well known and we call this the Radio Frequency (RF) time.

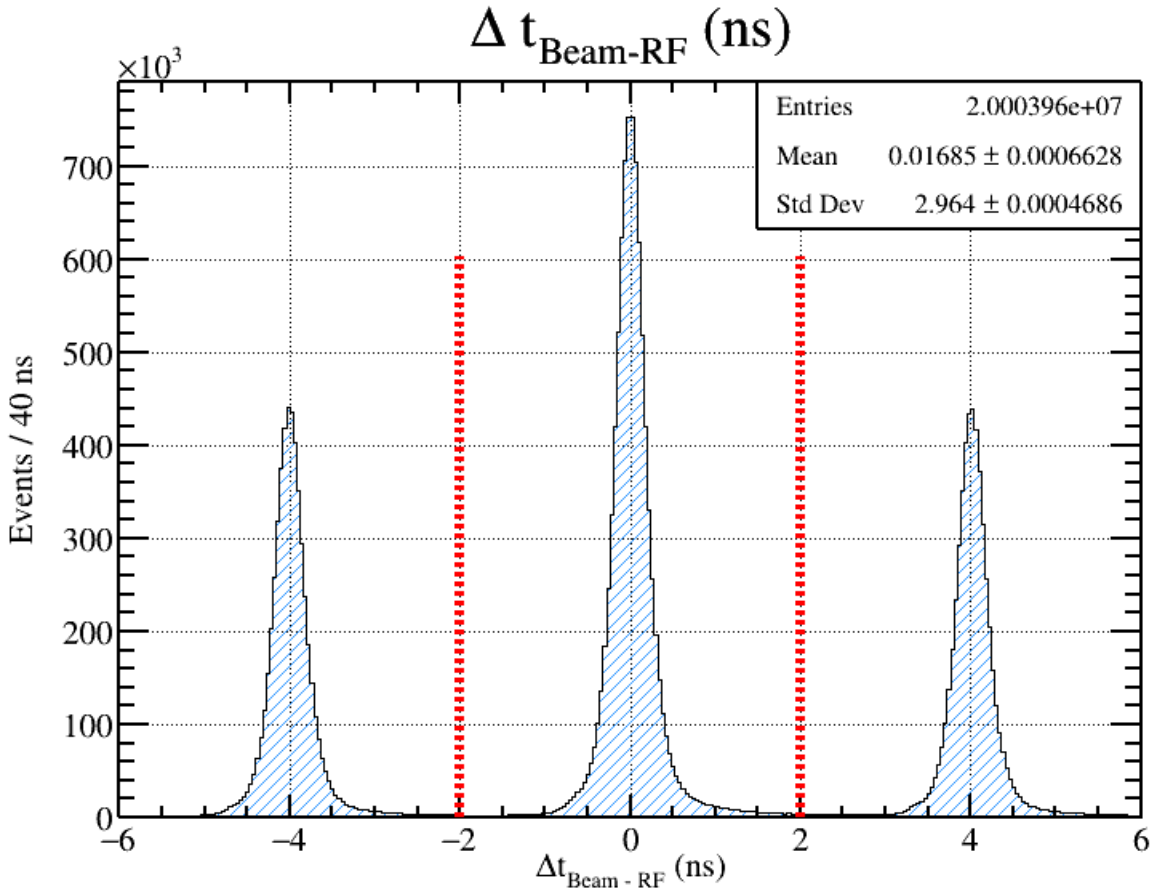

Figure 4.1: An example histogram of beam time as compared to the reported Radio Frequency (RF) time. In the plot there are three peaks, all of which are separated by four nanoseconds. Also included in the plot are two red dashed cut lines at ±2 ns. These cut lines represent the values used to perform an accidental subtraction on the data.

In addition to the RF time, we also have the beam time. The beam time is defined as the time which the reconstruction converged upon a common vertex time. The common vertex time is found by using the final state charged tracks and their timing, and back tracking them to a common point in space and time. Comparing the beam time with the RF time provides the experiment with the correct beam bunch which should be centered at zero. An example of what this distribution looks like and the cut used for it is given in Figure 4.1. It should be noted that this analysis will enforce a beam timing cut of ± 6ns in order to allow 3 beam bunches to pass. Once all cuts are made on the data and the final set of events is known, the additional side peaks will be used for accidental subtraction. An accidental subtraction is necessary in this analysis due to the high volume of accidental beam photons in the primary peak at zero. The accidental subtraction will be performed on all final plots shown in this analysis and can be executed by assigning a weight of 1 for any event with a beam timing of $\pm 2ns$, and a weight of -0.5 for any event from the side peaks. The purpose of assigning a weight of -0.5 for the side peaks is simply because there are twice as many side peaks (2) as primary peaks (1).

Target Proton. There are two cuts needed to select the initial state proton. Both of these cuts enforce the reconstructed vertex for all final state particles to be within the geometric volume of the target chamber. Since this analysis does not contain a particle lifetime which would result in a detached vertex, it is imperative to reduce backgrounds from other channels that may have this feature, such as excited baryons with a strange quark. Examples of what the reconstructed vertex for the final state photons looks like in the beam direction and in the transverse beam direction, is given in Figure [4.2a] and Figure [4.2b], respectively.

4.1.3 Identification of Final State Particles

Recoil Proton. There are three cuts that were used to identify the recoil proton and remove background. One of the cuts is a standard dE/dX cut, which separates some of the slow moving protons from other particles of positive charge such as e^+, π^+, and K^+. Due to the higher mass of the proton in comparison to the other particles with positive charge, the proton will tend to lose more energy inside of the Central Drift Chamber. This cut is highlighted in the first GlueX paper [26], and can be seen in Figure [4.3].

The second cut is to enforce the reconstructed vertex position of the charged proton track came from inside the target chamber. This cut is used to reduce any background from particles that

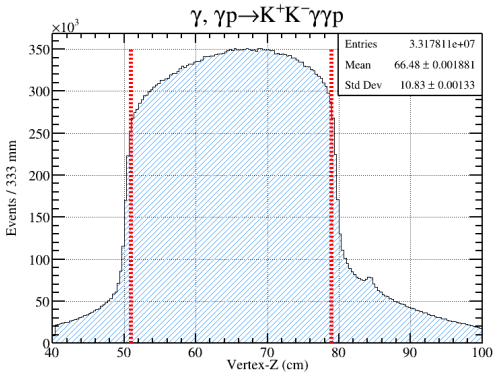

(a) Reconstructed vertex position along the beam direction with cut lines at 51 and 79 cm.

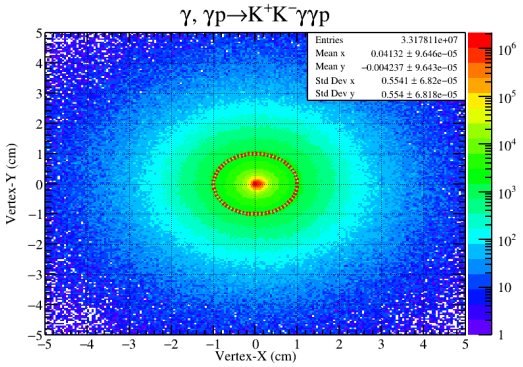

(b) Reconstructed vertex position transverse to the the beam direction with cut a line at 1 cm in the radial direction.

Figure 4.2: An example of what a reconstructed vertex distribution looks like for a final state γ in the reaction $\gamma p \to pK^+K^-\gamma\gamma$. The upper image is the reconstructed vertex position along the beam line, or z axis; and the lower image is the reconstructed vertex position in the directions transverse to the beam line. Both figures contain red dashed lines which represent the cut values for all reconstructed final state particles. In the z direction the cut values are 51 cm $\leq V_z \leq$ 79 cm, and in the transverse direction the cut values are $V_r \leq 1$ cm. The z direction cut values are established from Log Entry 3456336 from a Spring 2017 empty target run. The transverse cuts are simply established by considering the geometric size of the target chamber.

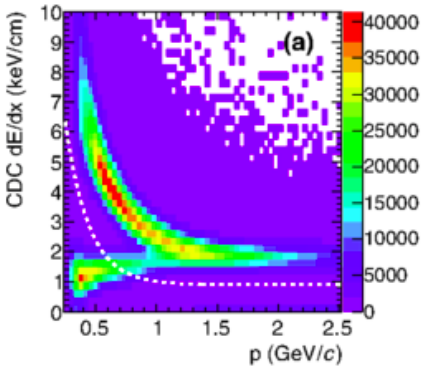

Figure 4.3: A figure which shows the energy lost in the Central Drift Chamber on the vertical axis, and the reconstructed momentum on the horizontal axis. At lower momentum, a proton band can be seen rising sharply towards higher energy loss values. Also contained within the figure is a white dashed line which represents the cut value used to identify slower moving protons. The horizontal band which deviates from the proton band at low momentum comes from positively charged pions and kaons.

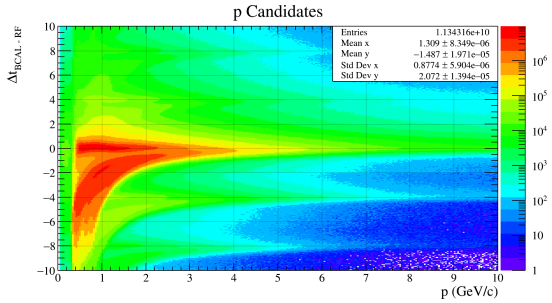

(a) Δ tVs P for Proton candidates that have the Barrel Calorimeter as the timing detector in data.

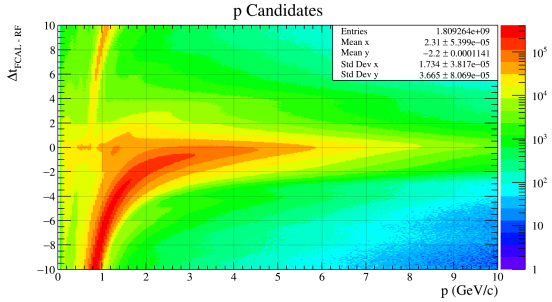

(b) Δ tVs P for Proton candidates that have the Forward Calorimeter as the timing detector in data.

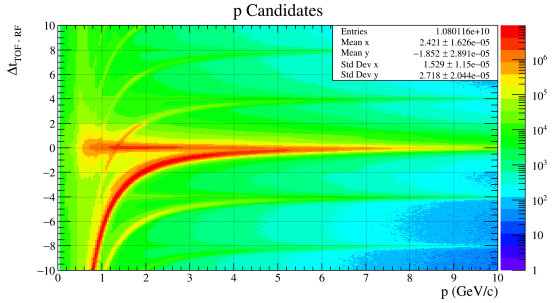

(c) Δ tVs P for Proton candidates that have the Time of Flight as the timing detector in data.

Figure 4.4: Timing plots for recoil proton candidates during the Spring 2017 run period for GlueX. Protons are identified by selecting the horizontal band centered about $\Delta T = 0$. The curved line deviating below the horizontal proton line comes from miss identified π^+ tracks. The additional curved lines above and below $\Delta T = 0$ come from π^+ tracks that are associated with the wrong RF bunch.

may have a detached vertex. The cut used is identical to those found and described in the Target section, specifically Figure [4.2a] and Figure [4.2b]. The third and final cut that is used to identify the recoil proton is the timing difference (Δ T) from the BCAL, FCAL, and TOF. Δ tis defined as the difference between the reconstructed vertex time for the particle and the time when the photon beam arrived. An example of what these distributions look like in data, as a function of momentum, is given in Figure [4.4]. Since the data has a lot of pion background in these plots, it is difficult to determine what the proper timing cuts should be for all of the sub detectors. Due to this, a Monte Carlo sample of $\gamma p \to pX; X \to \phi\eta; \phi \to K^+K^-; \eta \to \gamma\gamma$ was generated, simulated, and then reconstructed. This greatly reduces the background that is present in the timing plots and therefore can be used to estimate a proper timing cut for the proton and the sub detectors used to measure its time. Examples of these distributions and their associated projections onto the timing axis are given in Figure [4.5] through Figure [4.10]. A summary of all of the timing cuts used for the recoil proton as well as all other final state particles is given in Table [4.1].

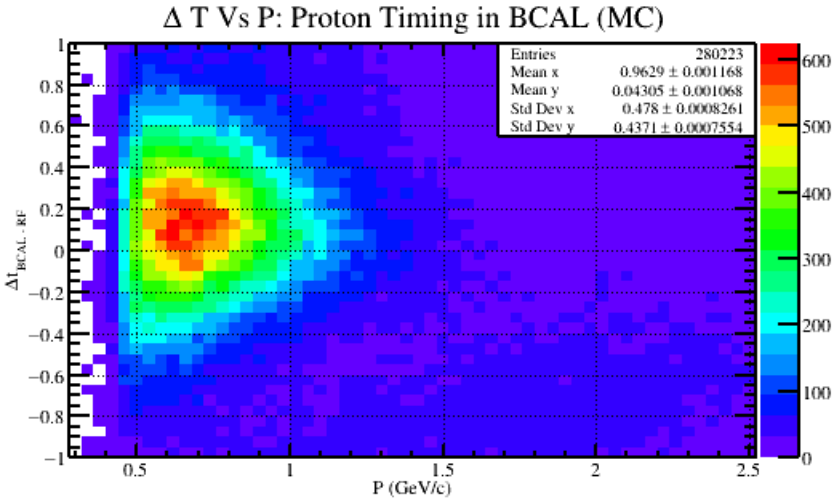

Figure 4.5: A timing plot for accepted recoil protons from the generated reaction $\gamma p \to pX; X \to \phi\eta; \phi \to K^+K^-; \eta \to \gamma\gamma$. The horizontal axis is the reconstructed momentum of the recoil proton and the vertical axis is the timing difference between the BCAL and RF. The enhancement of statistics in the lower right portion of the plot comes from miss identified kaons that are also present in the accepted Monte Carlo.

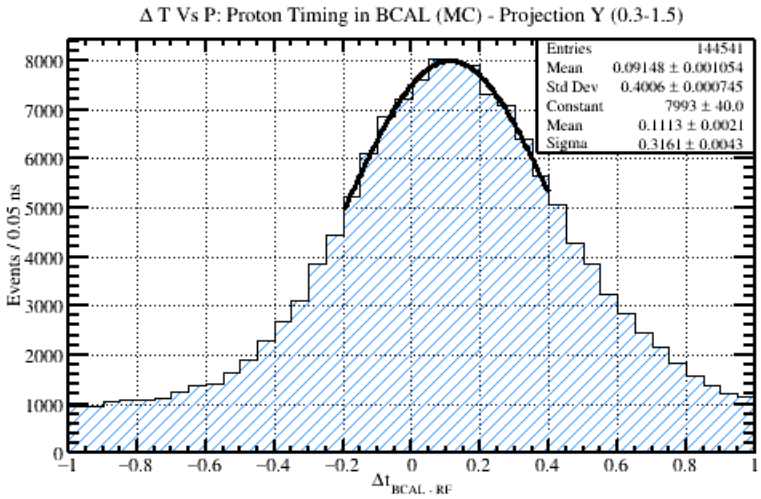

Figure 4.6: A projection of the statistics from Figure [4.5] onto the vertical (timing) axis between the momentum range of 0.3-1.5 GeV/c. This projection range was chosen so that the distortion from the lower kaon band was minimized. A Gaussian fit was performed and is included in the figure where the mean and width of the distribution are given in the legend.

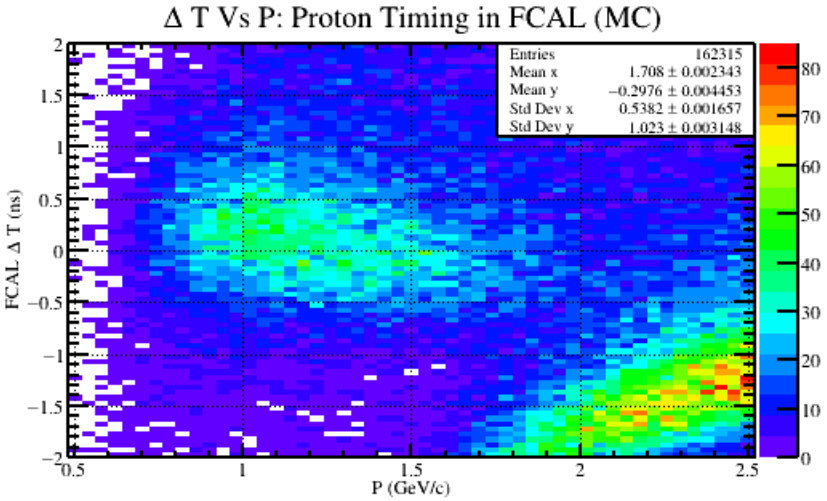

Figure 4.7: A timing plot for accepted recoil protons from the generated reaction $\gamma p \to pX; X \to \phi\eta; \phi \to K^+K^-; \eta \to \gamma\gamma$. The horizontal axis is the reconstructed momentum of the proton and the vertical axis is the timing difference between the FCAL and RF. The enhancement of statistics in the lower right portion of the plot comes from miss identified kaons that are also present in the accepted Monte Carlo.

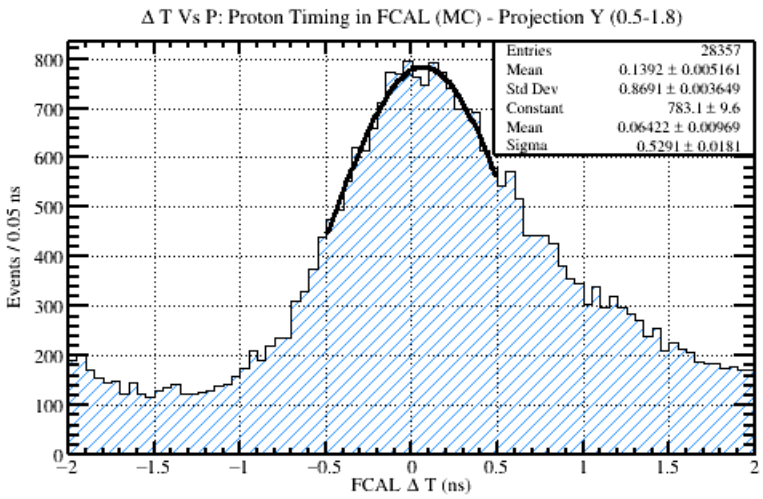

Figure 4.8: A projection of the statistics from Figure [4.7] onto the vertical (timing) axis between the momentum range of 0.5-1.8 GeV/c. This projection range was chosen so that the distortion from the lower kaon band was minimized. A Gaussian fit was performed and is included in the figure where the mean and width of the distribution are given in the legend.

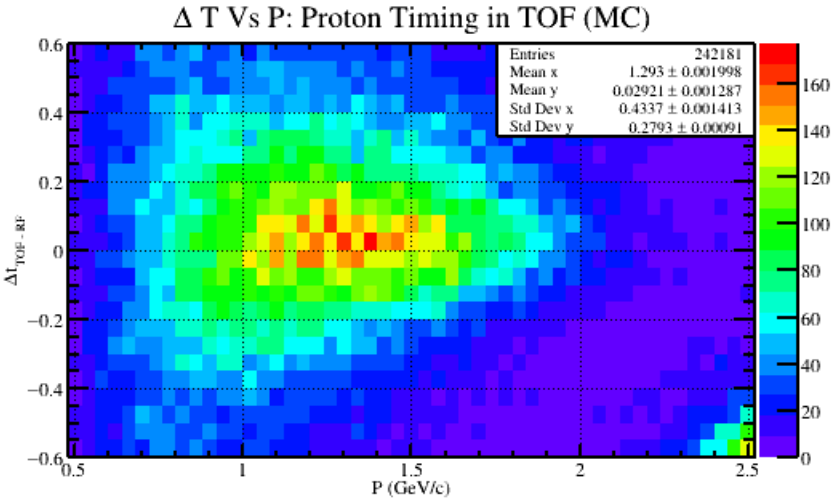

Figure 4.9: A timing plot for accepted recoil protons from the generated reaction $\gamma p \to pX; X \to \phi\eta; \phi \to K^+K^-; \eta \to \gamma\gamma$. The horizontal axis is the reconstructed momentum of the proton and the vertical axis is the timing difference between the TOF and RF. The enhancement of statistics in the lower right portion of the plot comes from miss identified kaons that are also present in the generated Monte Carlo.

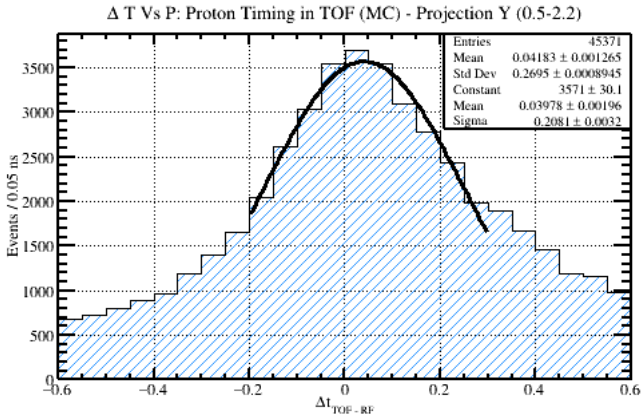

Figure 4.10: A projection of the statistics from Figure [4.9] onto the vertical (timing) axis between the momentum range of 0.5-1.8 GeV/c. This projection range was chosen so that the distortion from the lower kaon band was minimized. A Gaussian fit was performed and is included in the figure where the mean and width of the distribution are given in the legend.

K^+. There are two cuts that were used to identify the final state K^+ and remove background. The first cut is to enforce the reconstructed vertex position of the K^+ track came from inside the target chamber. This cut is used to reduce any parent state of the K^+ that may have a longer lifetime and therefore a detached vertex. The cut used is identical to those found and described in the Target section, specifically Figure [4.2a] and Figure [4.2b]. The other cut that is used to identify the K^+ is the timing (Δ T) from the BCAL, FCAL, and TOF. Δ tis defined as the difference between the reconstructed vertex time for the particle and the time when the photon beam arrived. An example of what these distributions look like in data, as a function of momentum, is given in Figure [4.11]. Since the data has a lot of pion and proton background in these plots, it is difficult to determine what the proper timing cuts should be for all of the sub detectors. Due to this, a Monte Carlo sample of $\gamma p \to pX; X \to \phi\eta; \phi \to K^+K^-; \eta \to \gamma\gamma$ was generated, simulated, and then reconstructed. This greatly reduces the background that is present in the timing plots and therefore can be used to estimate a proper timing cut for the K^+ and the sub detectors used to measure its time. Examples of these distributions and their associated projections onto the timing axis are given in Figure [4.12] through Figure [4.17]. It should be noted that in many of the Monte Carlo plots, there appears to be an additional band from a particle with less mass. This is a consequence of using the *hdgeant* simulator, which will decay particles while in flight. Therefore, the band inside the Monte Carlo plots arises from the weak decay of a kaon to a muon

and a neutrino. A summary of all of the timing cuts used for the K^+ as well as all other final state particles is given in Table [4.1].

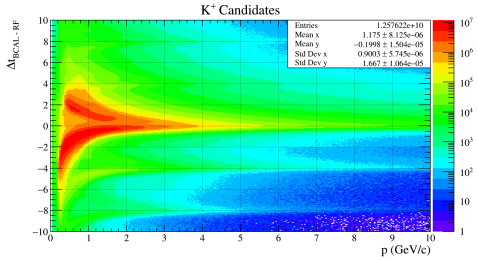

(a) Δ tVs P for K^+ candidates that have the Barrel Calorimeter as the timing detector in data.

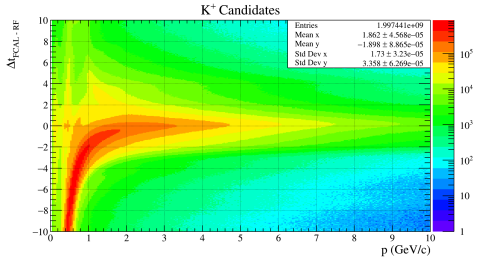

(b) Δ tVs P for K^+ candidates that have the Forward Calorimeter as the timing detector in data.

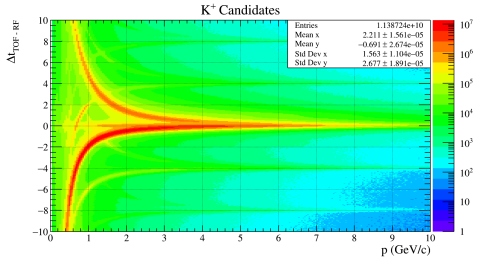

(c) Δ tVs P for K^+ candidates that have the Time of Flight as the timing detector in data.

Figure 4.11: Timing plots for K^+ candidates during the Spring 2017 run period for GlueX. K^+ are identified by selecting the horizontal band centered about $\Delta T = 0$. The curved line deviating below the horizontal K^+ line comes from miss identified π^+ tracks, and the curved line deviating above the horizontal K^+ line comes from miss identified proton tracks. The additional curved lines above and below $\Delta T = 0$ come from π^+ and proton tracks that are associated with the wrong RF bunch.

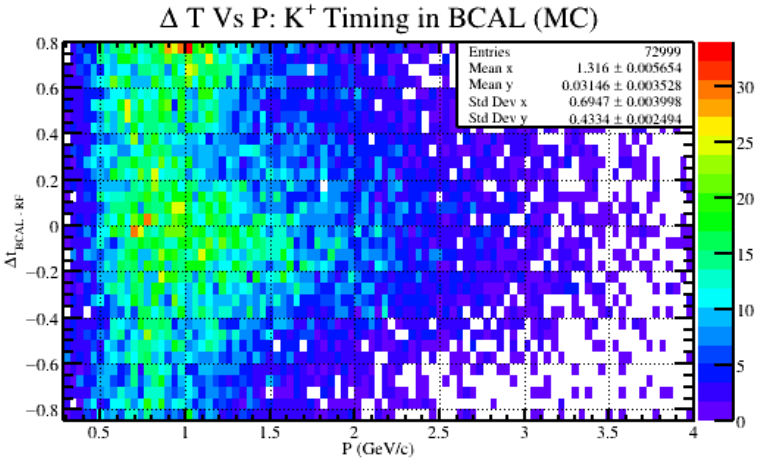

Figure 4.12: A timing plot for accepted K^+ from the generated reaction $\gamma p \to pX; X \to \phi\eta; \phi \to K^+K^-; \eta \to \gamma\gamma$. The horizontal axis is the reconstructed momentum of the K^+ and the vertical axis is the timing difference between the BCAL and RF. It should be noted that the statistics in this sampling are smaller than other plots. This is due to the fact that the kinematics of the generated channel prefer to have the kaons moving in the forward direction; and therefore provide few timing hits in the BCAL. Additionally, the extra statistics present in the upper left portion of the graph are due to protons that are also present in the accepted Monte Carlo.

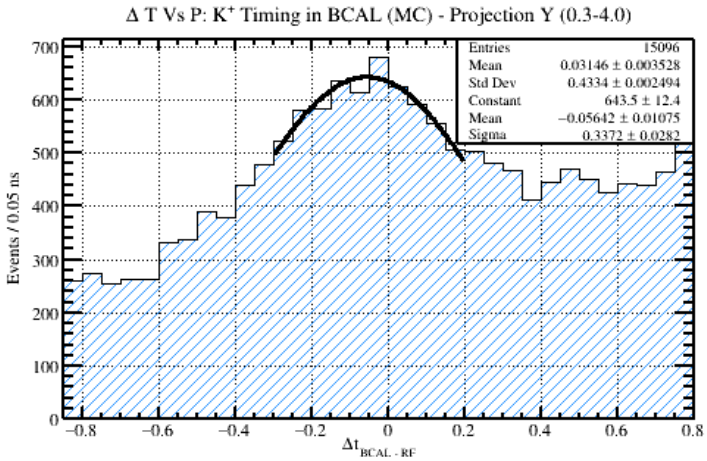

Figure 4.13: A projection of the statistics from Figure [4.12] onto the vertical (timing) axis between the momentum range of 0.3-4.0 GeV/c. A Gaussian fit was performed and is included in the figure where the mean and width of the distribution are given in the legend. The distortion of statistics towards the higher timing differences is due to protons that are also present in the generated Monte Carlo.

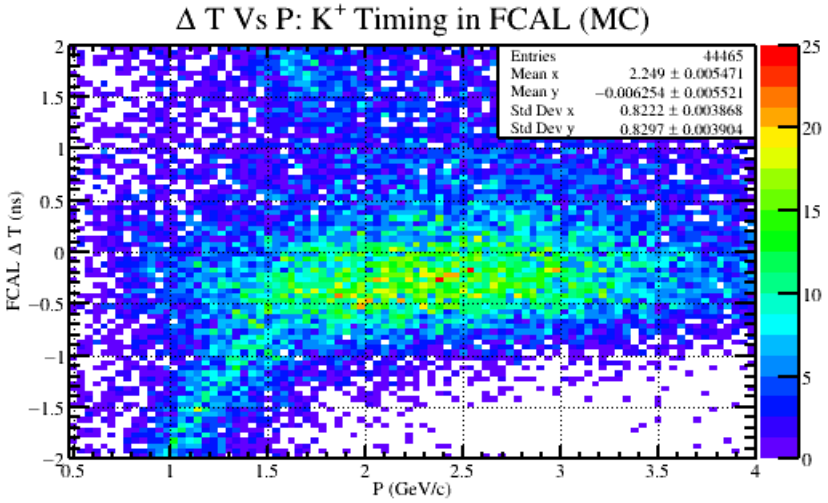

Figure 4.14: A timing plot for accepted K^+ from the generated reaction $\gamma p \to pX; X \to \phi\eta; \phi \to K^+K^-; \eta \to \gamma\gamma$. The horizontal axis is the reconstructed momentum of the K^+ and the vertical axis is the timing difference between the FCAL and RF. The curved band that appears below the K^+ band around 1.5 GeV/c and lower comes from μ^+. Although muons were not explicitly generated, the computer program hdgeant (derived from geant) allows for some fraction of kaons to decay weakly while in flight; resulting in observed muons.

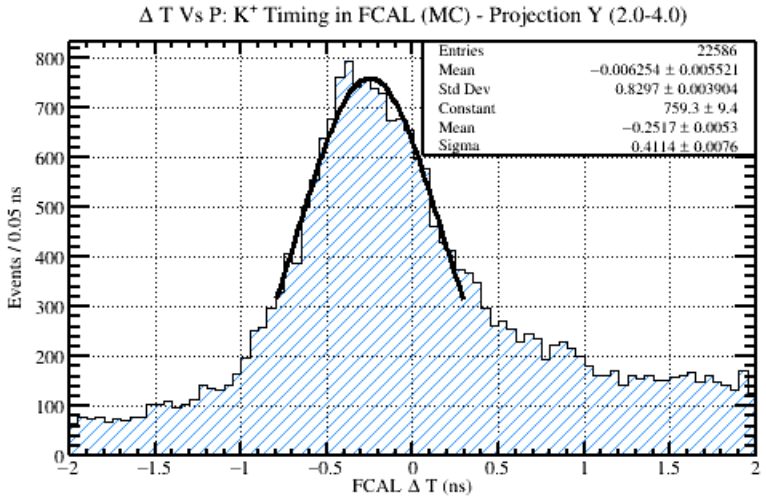

Figure 4.15: A projection of the statistics from Figure [4.14] onto the vertical (timing) axis between the momentum range of 2.0-4.0 GeV/c. This projection range was chosen so that the distortion from the lower muon band and upper proton band was minimized. A Gaussian fit was performed and is included in the figure where the mean and width of the distribution are given in the legend.

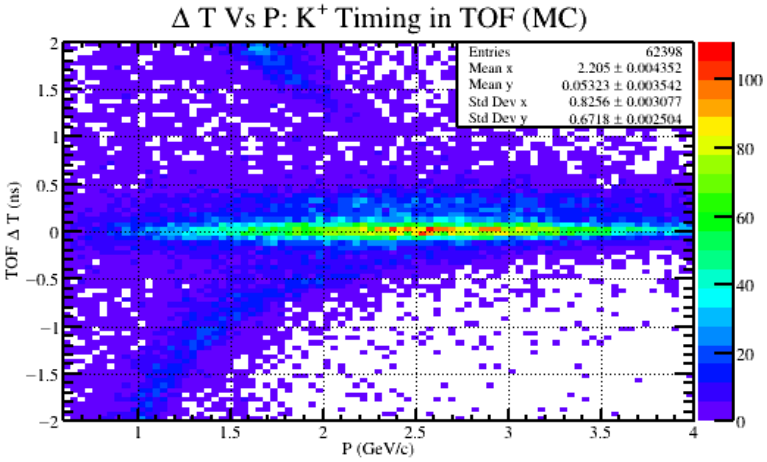

Figure 4.16: A timing plot for accepted K^+ from the generated reaction $\gamma p \to pX; X \to \phi\eta; \phi \to K^+K^-; \eta \to \gamma\gamma$. The horizontal axis is the reconstructed momentum of the K^+ and the vertical axis is the timing difference between the TOF and RF. The curved band that appears below the K^+ band around 2.5 GeV/c and lower comes from μ^+; and the band near the top of the plot comes from protons. Although muons were not explicitly generated, the computer program hdgeant (derived from geant) allows for some fraction of kaons to decay weakly while in flight; resulting in an observed muon.

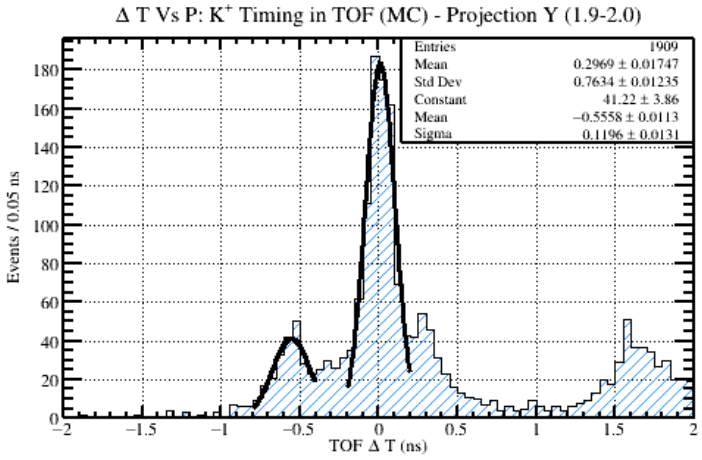

Figure 4.17: A projection of the statistics from Figure [4.16] onto the vertical (timing) axis between the momentum range of 1.9-2.0 GeV/c. This projection range is one out of many that were studied from Figure [4.16]. The purpose of this study is to determine the amount of muon contamination in the kaon band as a function of momentum. The results of this study are provided in Figure [4.18]. Lastly, two Gaussian fits were performed on this data. The mean and width of these Gaussian fits are recorded in Figure [4.18] for each momentum range.

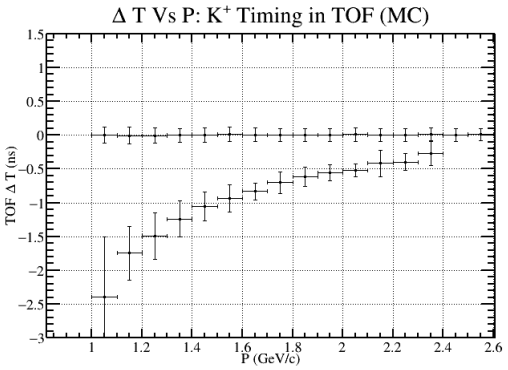

Figure 4.18: The image above is the result of the timing study performed on Figure [4.16]. Using that figure, a number of projection histograms were fit using different momentum ranges. An example of one of these fits is given in Figure [4.17]. The data points close to 0 ΔT correspond to the Gaussian fits performed on the kaon signal, and the data points that approach that band from the bottom correspond to the Gaussian fits performed on the muon signal. The horizontal position of each point is in the middle of the projection range, and the vertical position of each point was assigned based on the mean value of the Gaussian fit for each particle. The horizontal error bars are the size of the projection range, which is always 0.1 GeV/c. The vertical error bars are determined by the width of the Gaussian fits. The average of the widths of the kaon peaks is 0.1 ns which is the value used to determine the timing cut in Table 4.1.

K^-. Just like its antiparticle, the K^- has two cuts; the vertex and timing cuts. The vertex cut is used to eliminate any parent state of the K^- that may have a longer lifetime and therefore a detached vertex. The cut used is identical to those found and described in the Target section, specifically Figure [4.2a] and Figure [4.2b]. The timing cuts (Δ T) for the K^- are for the BCAL, FCAL, and TOF sub detectors. Δ tis defined as the difference between the reconstructed vertex time for the particle and the time when the photon beam arrived. Since the timing distributions from data (Figure [4.19]) have too much background in them, a Monte Carlo sample of $\gamma p \to pX; X \to \phi\eta; \phi \to K^+K^-; \eta \to \gamma\gamma$ was generated, simulated, and then reconstructed. This greatly reduces the background that is present in the timing plots and therefore can be used to estimate a proper timing cut for the K^- and the sub detectors used to measure its time. Examples of these distributions and their associated projections onto the timing axis are given in Figure [4.20] through Figure [4.25]. It should be noted that in many of the Monte Carlo plots, there appears to be an additional band from a particle with less mass. This is a consequence of using the *hdgeant* simulator, which will decay particles while in flight. Therefore, the band inside the Monte Carlo

plots arises from the weak decay of a kaon to a muon and a neutrino. A summary of all of the timing cuts used for the K^- as well as all other final state particles is given in Table [4.1].

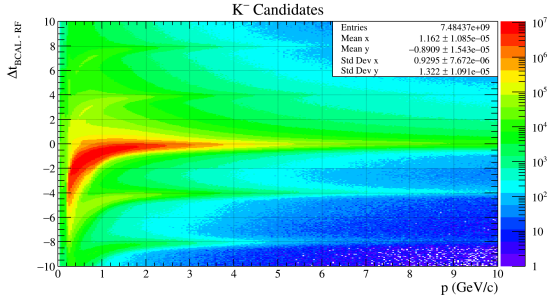

(a) Δ tVs P for K^- candidates that have the Barrel Calorimeter as the timing detector in data.

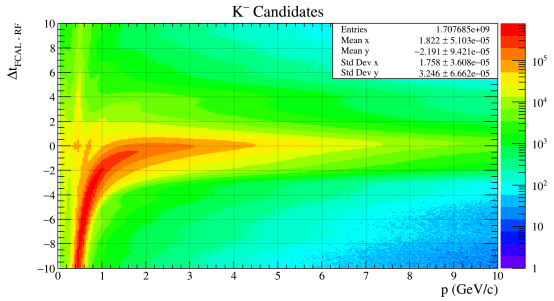

(b) Δ tVs P for K^- candidates that have the Forward Calorimeter as the timing detector in data.

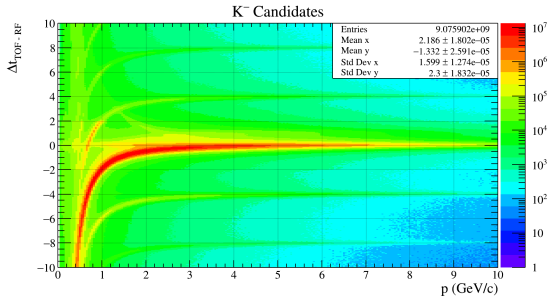

(c) Δ tVs P for K^- candidates that have the Time of Flight as the timing detector in data.

Figure 4.19: Timing plots for K^- candidates during the Spring 2017 run period for GlueX. K^- are identified by selecting the horizontal band centered about $\Delta T = 0$. The curved line deviating below the horizontal K^- line comes from miss identified π^- tracks. The additional curved lines above and below $\Delta T = 0$ come from π^- tracks that are associated with the wrong RF bunch.

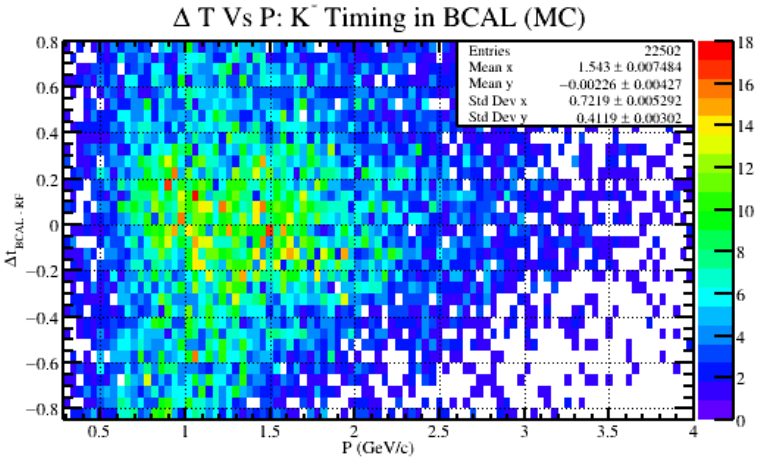

Figure 4.20: A timing plot for accepted K^- from the generated reaction $\gamma p \to pX; X \to \phi\eta; \phi \to K^+K^-; \eta \to \gamma\gamma$. The horizontal axis is the reconstructed momentum of the K^- and the vertical axis is the timing difference between the BCAL and RF. It should be noted that the statistics in this sampling are smaller than other plots. This is due to the fact that the kinematics of the generated channel prefer to have the kaons moving in the forward direction; and therefore provide few timing hits in the BCAL. Additionally, the extra statistics present in the lower left portion of the graph are due to muons. Although muons were not explicitly generated, the computer program hdgeant (derived from geant) allows for some fraction of kaons to decay weakly while in flight; resulting in observed muons.

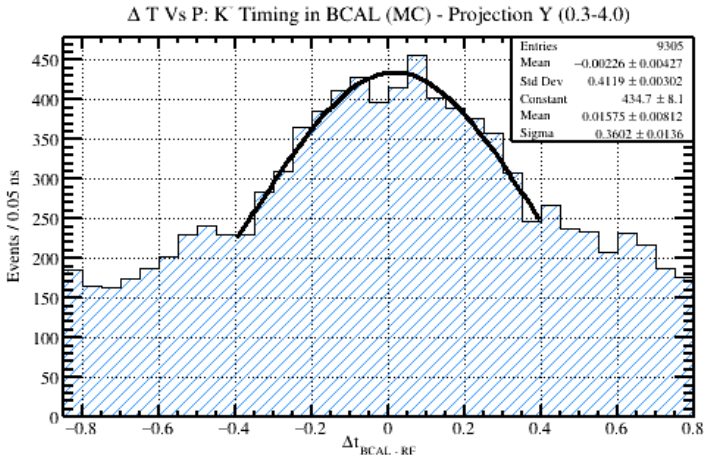

Figure 4.21: A projection of the statistics from Figure [4.20] onto the vertical (timing) axis between the momentum range of 0.3-4.0 GeV/c. A Gaussian fit was performed and is included in the figure where the mean and width of the distribution are given in the legend.

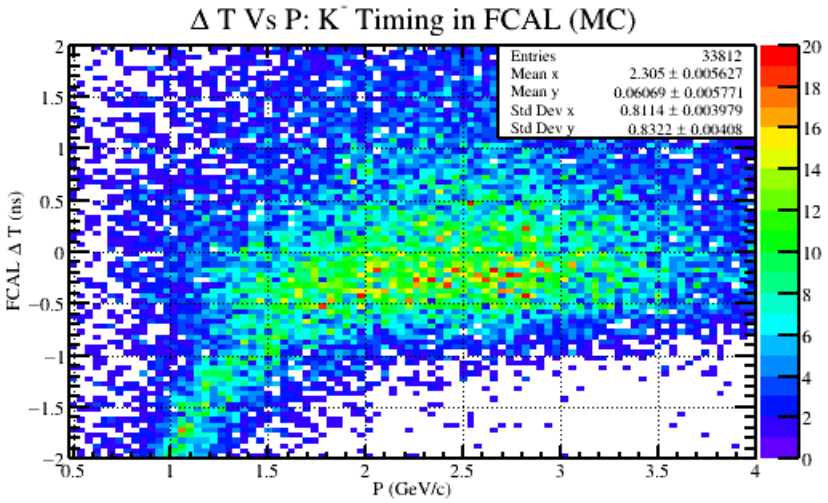

Figure 4.22: A timing plot for accepted K^- from the generated reaction $\gamma p \to pX; X \to \phi\eta; \phi \to K^+K^-; \eta \to \gamma\gamma$. The horizontal axis is the reconstructed momentum of the K^- and the vertical axis is the timing difference between the FCAL and RF. The curved band that appears below the K^- band around 1.5 GeV/c and lower comes from μ^-. Although muons were not explicitly generated, the computer program hdgeant (derived from geant) allows for some fraction of kaons to decay weakly while in flight; resulting in an observed muon.

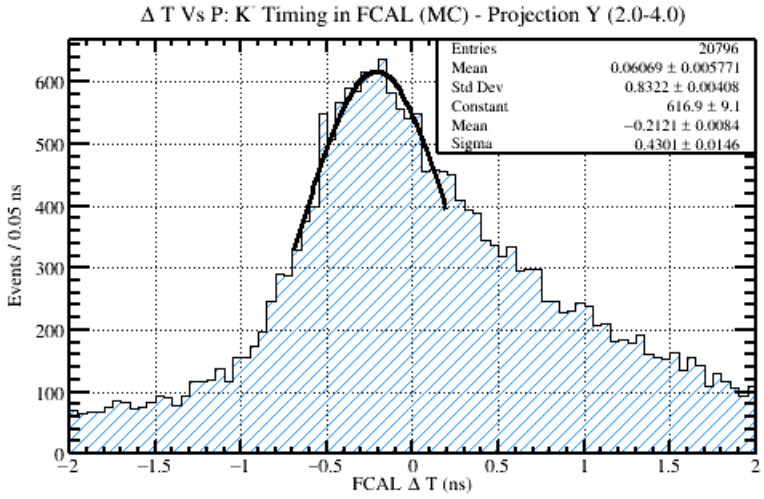

Figure 4.23: A projection of the statistics from Figure [4.22] onto the vertical (timing) axis between the momentum range of 2.0-4.0 GeV/c. This projection range was chosen so that the distortion from the lower muon band was minimized. A Gaussian fit was performed and is included in the figure where the mean and width of the distribution are given in the legend.

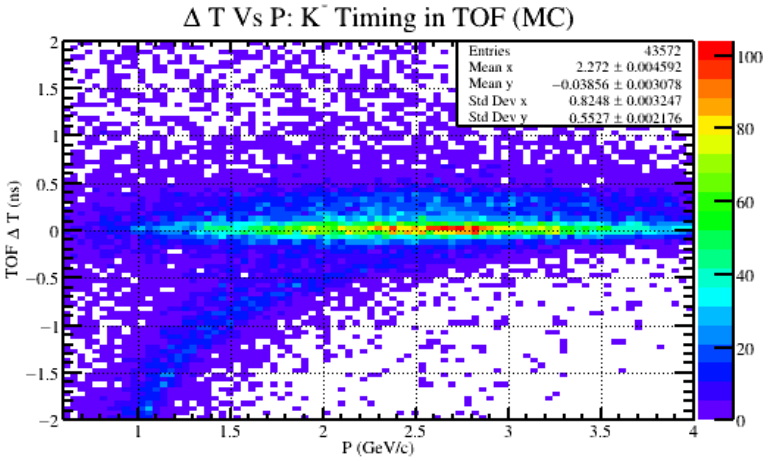

Figure 4.24: A timing plot for accepted K^- from the generated reaction $\gamma p \to pX; X \to \phi\eta; \phi \to K^+K^-; \eta \to \gamma\gamma$. The horizontal axis is the reconstructed momentum of the K^- and the vertical axis is the timing difference between the TOF and RF. The curved band that appears below the K^- band around 2.5 GeV/c and lower comes from μ^-. Although muons were not explicitly generated, the computer program hdgeant (derived from geant) allows for some fraction of kaons to decay weakly while in flight; resulting in an observed muon.

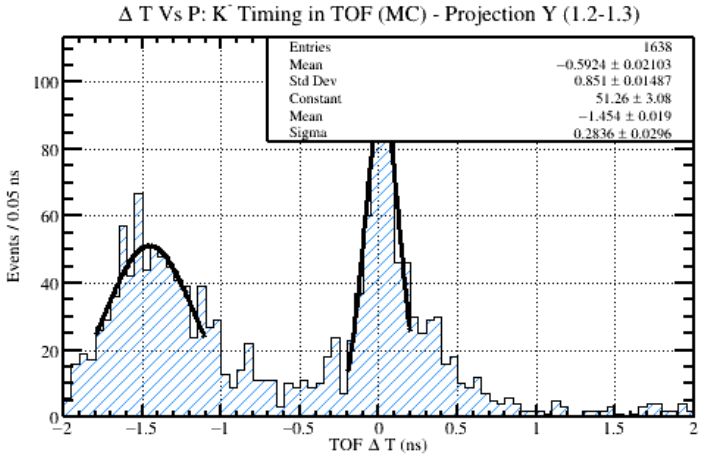

Figure 4.25: A projection of the statistics from Figure [4.24] onto the vertical (timing) axis between the K^- momentum range of 1.2-1.3 GeV/C. This projection range is one out of many that were studied from Figure [4.24]. The purpose of this study is to determine the amount of muon contamination in the kaon band as a function of momentum. The results of this study are provided in Figure [4.26]. Lastly, two Gaussian fits were performed on this data. The mean and width of these Gaussian fits are recorded in Figure [4.26] for each momentum range.

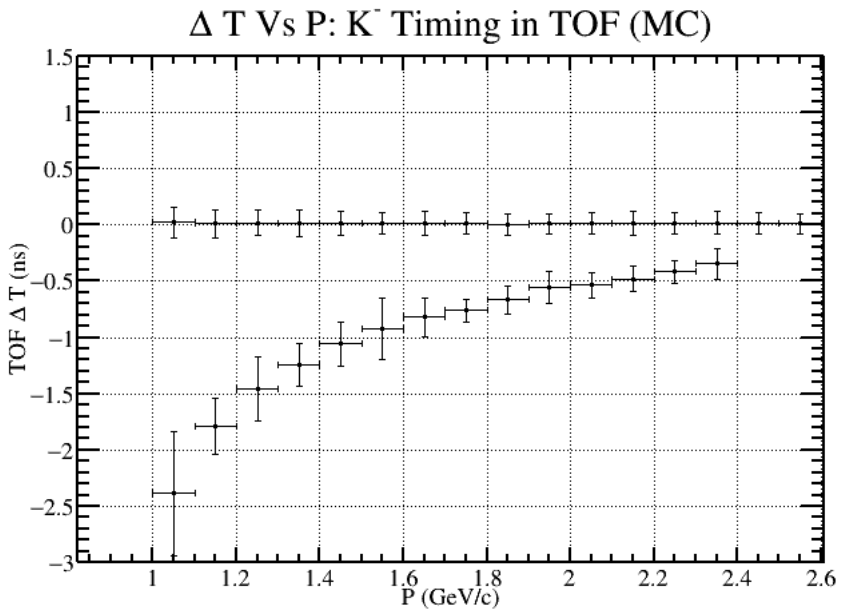

Figure 4.26: The image above is the result of the timing study performed on Figure [4.24]. Using that figure, a number of projection histograms were fit using different momentum ranges. An example of one of these fits is given in Figure [4.25]. The data points close to 0 ΔT correspond to the Gaussian fits performed on the kaon signal, and the data points that approach that band from the bottom correspond to the Gaussian fits performed on the muon signal. The horizontal position of each point is in the middle of the projection range, and the vertical position of each point was assigned based on the mean value of the Gaussian fit for each particle. The horizontal error bars are the size of the projection range, which is always 0.1 GeV/c. The vertical error bars are determined by the width of the Gaussian fits. The average of the widths of the kaon peaks is 0.1 ns which is the value used to determine the timing cut in Table 4.1.

γ. Unlike the other final state particles, the neutral final state photons do not leave a charged track. Therefore, the reconstruction requires at least one charged particle in the event to be used as a reference trajectory towards the event vertex. In the case of this study, there are three charged tracks used to determine the event vertex position. Once the vertex position of the event is known, it is assigned to all neutral particles in the final state. Therefore, the final state photons have a vertex distribution. These distributions and their associated cuts are given in the Target section, specifically Figure [4.2a] and Figure [4.2b]. It should also be mentioned that final state photons do not have a timing cut for the TOF. This is due to the fact that the time of flight can only interact with charged particles, and therefore cannot interact with photons. The timing cuts (Δ T) for the γ only come from the BCAL, FCAL. Δ tis defined as the difference between the reconstructed vertex

time for the particle and the time when the photon beam arrived. Since the timing distributions from data (Figure [4.27]) have too much neutron background in them, a Monte Carlo sample of $\gamma p \to pX; X \to \phi\eta; \phi \to K^+K^-; \eta \to \gamma\gamma$ was generated, simulated, and then reconstructed. This greatly reduces the background that is present in the timing plots and therefore can be used to estimate a proper timing cut for the γ and the sub detectors used to measure its time. Examples of these distributions and their associated projections onto the timing axis are given in Figure [4.28] through Figure [4.31]. A summary of all of the timing cuts used for the photon as well as all other final state particles is given in Table [4.1].

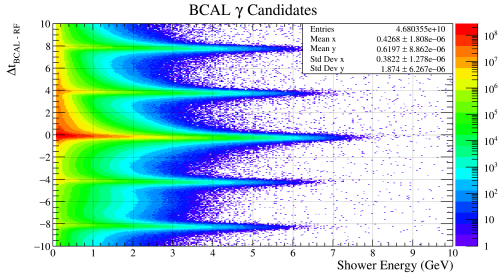

(a) Δ tVs Shower Energy for γ candidates that have the Barrel Calorimeter as the timing detector in data.

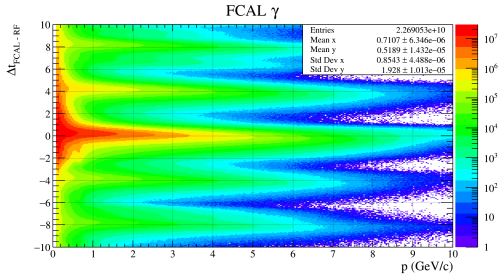

(b) Δ tVs Shower Energy for γ candidates that have the Forward Calorimeter as the timing detector in data.

Figure 4.27: Timing plots for γ candidates during the Spring 2017 run period for GlueX. γ are identified by selecting the horizontal band centered about $\Delta T = 0$. Large enhancement in statistics at low momentum and out of time with the γ line comes from slow moving and poorly timed neutrons. The additional horizontal lines above and below $\Delta T = 0$ come from γ showers that are associated with the wrong RF bunch.

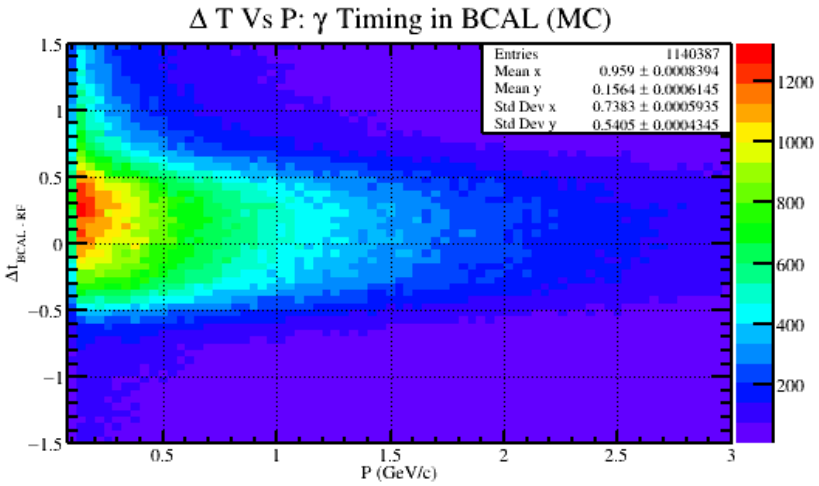

Figure 4.28: A timing plot for accepted γ from the generated reaction $\gamma p \to pX; X \to \phi\eta; \phi \to K^+K^-; \eta \to \gamma\gamma$. The horizontal axis is the reconstructed momentum of the γ and the vertical axis is the timing difference between the BCAL and RF.

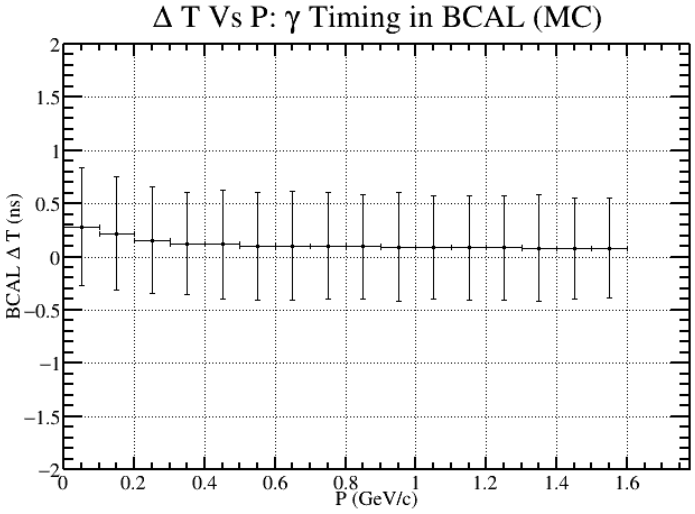

Figure 4.29: The image above is the result of the timing study performed on Figure [4.28]. Using that figure, a number of projection histograms were fit using different momentum ranges. The horizontal position of each point is in the middle of the projection range, and the vertical position of each point was assigned based on the mean value of the Gaussian fit. The horizontal error bars are the size of the projection range, which is always 0.1 GeV/c. The vertical error bars are determined by the width of the Gaussian fit. The average of the widths of the photon peaks is ~ 0.5 ns which is the value used to determine the timing cut in Table [4.1].

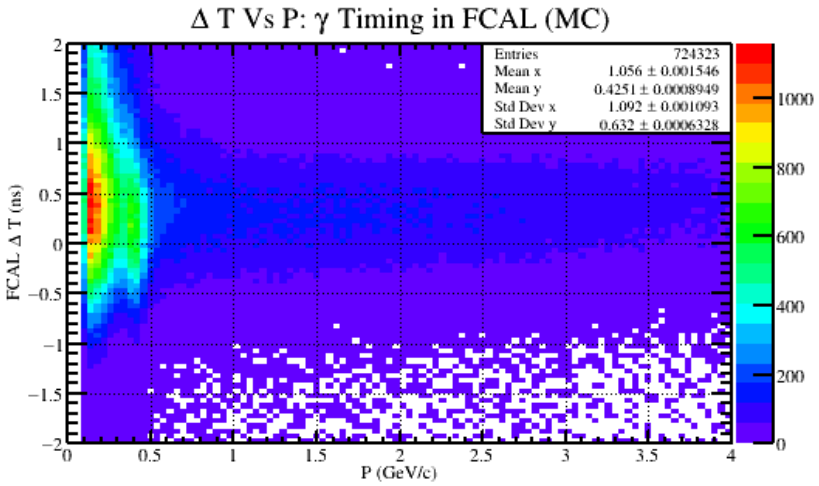

Figure 4.30: A timing plot for accepted γ from the generated reaction $\gamma p \to pX; X \to \phi\eta; \phi \to K^+K^-; \eta \to \gamma\gamma$. The horizontal axis is the reconstructed momentum of the γ and the vertical axis is the timing difference between the FCAL and RF.

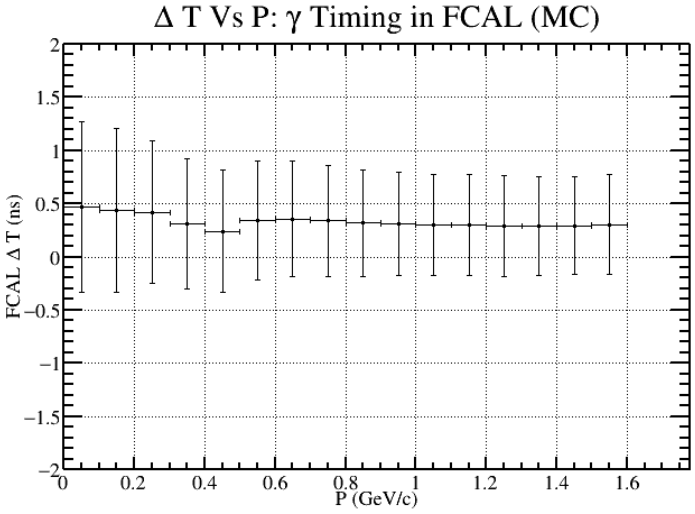

Figure 4.31: The image above is the result of the timing study performed on Figure [4.30]. Using that figure, a number of projection histograms were fit using different momentum ranges. The horizontal position of each point is in the middle of the projection range, and the vertical position of each point was assigned based on the mean value of the Gaussian fit. The horizontal error bars are the size of the projection range, which is always 0.1 GeV/c. The vertical error bars are determined by the width of the Gaussian fit. The average of the widths of the photon peaks is ~ 0.55 ns which is the value used to determine the timing cut in Table [4.1].

4.2 Additional Cuts for $\gamma p \to pK^+K^-\gamma\gamma$

4.2.1 Kaon Selection and Pion Rejection from TOF

One key aspect to performing a $\phi\eta$ analysis is to both identify the ϕ and the η mesons while also reducing the amount of background in each of their invariant mass spectra. One of the issues with the K^+K^- invariant mass spectra is that it contains misidentified pions. This background causes a peak in the K^+K^- invariant mass around 1.2 GeV/c^2. This peak is a manifestation of a ρ^0 which can decay to a $\pi^+\pi^-$ final state. An example of this background is illustrated nicely in Figure 4.32. It should be noted that all of the data used in this subsection is only 20 percent of the total data set.

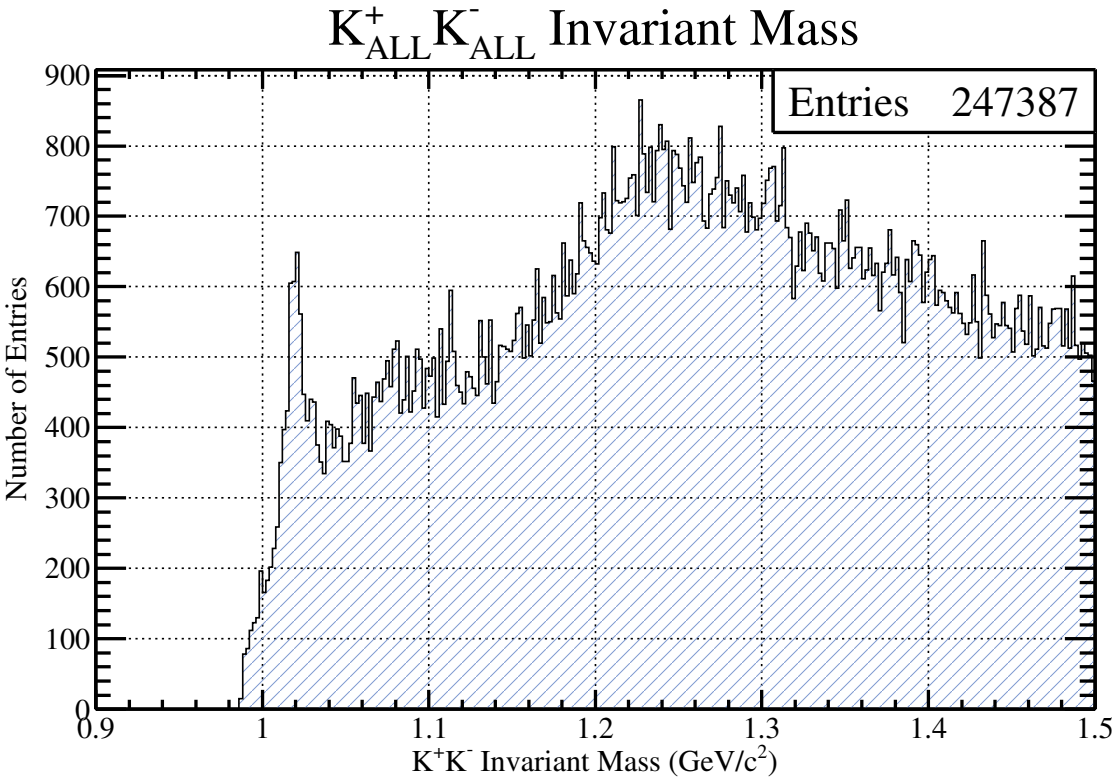

Figure 4.32: An example K^+K^- invariant mass histogram without pion removal from the Time of Flight. A rho peak can be seen around roughly 1.25 GeV/c^2.

One important aspect of QCD and the quark model is the conservation of quark flavor in hadronic decays, or decays which involve the interaction of the strong nuclear force. Conservation of quark flavor states that the initial number flavored quarks minus the initial number of anti-quarks

of the same flavor, must be conserved. An example of this can be any strong or electromagnetic interaction which is being studied with the GlueX spectrometer. The GlueX experiment has an initial state photon which has no net quark content, plus a proton which has two up quarks and one down quark. Since the GlueX experiment is designed to study hadronic interactions, the final state must have a net quark flavor of two up quarks and one down quark. Considering the $\gamma p \rightarrow p\phi\eta$ interaction, it is clear that this requirement is met. The initial and final state proton are identical in quark flavor, and the ϕ and η mesons have no net quark flavor to them. Moreover, since the K^+K^- decay of the ϕ meson is being considered, the overall strangeness of this decay needs to be conserved as well. To state this more explicitly, the K^+ meson consists of a $u\bar{s}$ composite state, while the the K^- meson consists of a $s\bar{u}$ composite state. Since each kaon carries either a strange or anti-strange quark, it is only necessary to observe one kaon well. The method is based on strangeness conservation.

Strangeness conservation is used to both preserve good $\phi\eta$ statistics, while also reducing the amount of background under the ϕ peak (Figure 4.32). Since the Time of Flight detector has the best timing resolution out of all subdetectors in the GlueX spectrometer, it will be used as an example in this section. In order to understand how strangeness conservation is implemented in this analysis, Figure 4.33 is provided. Contained within this figure is the timing versus momentum plot for the K^+, identical to Figure 4.18. Also contained within this diagram is a red line which represents the cut that will be used to separate particles with 'good strangeness' as opposed to particles that 'do not have good strangeness'. This red line is derived from simple equations of physics in the following way:

The flight time it takes for any relativistic particle to travel a distance δX at a velocity V in the lab frame, can be expressed using Equation 4.1.

$$t = \frac{\delta X}{V} = \frac{\delta X}{\beta c} \tag{4.1}$$

Furthermore, it is well known from Special Relativity that $\beta = P/E$. Using the relativistic equation for invariant mass, we can rewrite Equation 4.1 as Equation 4.2.

$$t = \frac{\delta X}{c} \frac{\sqrt{m_i^2 + P^2}}{P} \tag{4.2}$$

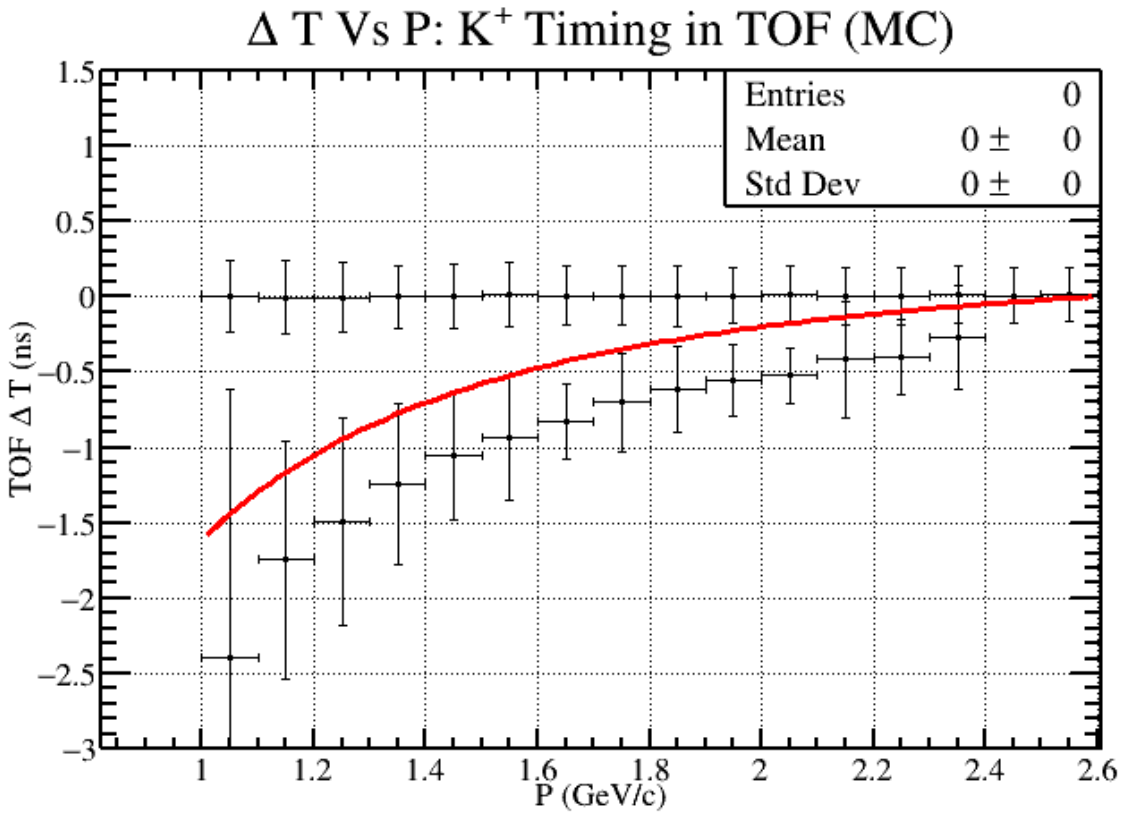

Figure 4.33: A graph which provides the strangeness conservation cut used for kaons that are detected by the Time of Flight detector. This is identical to Figure 4.18, except that the vertical error bars have been multiplied by a factor of 2 in order to visualize a 2σ uncertainty. The graph also contains Equation 4.3, with a timing shift of 0.2 ns.

Since Equation 4.2 is true for any particle, we can then use it to describe the timing difference between pions and kaons in the lab frame, as measured by the Time of Flight. This final equation will take the form of Equation 4.3.

$$\delta t = \frac{\delta X}{c} \frac{\sqrt{m_\pi^2 + P^2} - \sqrt{m_K^2 + P^2}}{P} \tag{4.3}$$

The parameters δX, c, m_π, and m_K are known for Equation 4.3 since one is the speed of light, two are invariant masses, and the other is the distance that the charged particle traveled from the target chamber to the Time of Flight wall; which is a measured quantity in our experiment for all

charged tracks. Therefore, the only two variables left over are δt and P which serve as the vertical and horizontal axis variables, respectively.

One last modification of Equation 4.3 is needed in order to take the form seen in Figure 4.33. If the equation is left the way that it is, the red line would simply bisect the pion curve, and would therefore not work well as a background cut. Therefore, Equation 4.3 is shifted up by 0.2 ns. This parameter was chosen based on the timing study that was performed on the Monte Carlo and is therefore a 2σ timing shift. It should be noted that since the K^+ and K^- mesons are anti-particles, as well as the π^+ and π^-, the same equation can be used to separate background for both kaons.

Given Equation 4.3 and Figure 4.33, strangeness conservation can now be addressed. In order to enforce strangeness conservation, it is imperative to identify one 'good kaon'. Good kaons will have one characteristic to them which is that they need to be positively identified by the Time of Flight detector. A positive identification will be defined as any kaon candidate that has timing above or to the left of the red line given in Figure [4.33]. Any particle that is to the right or below the red line is not guaranteed to be a kaon, and is therefore 'unknown'. Strangeness conservation allows us to preserve more statistics because all that is needed to justify the observation of a final state which includes a K^+K^- is one 'good kaon'. Therefore, any combination that the has either a K^+ or a K^- with the characteristic mentioned above will be accepted. The only combinations that will be rejected are those which both kaon candidates fail the characteristic mentioned above. To emphasize the importance and effectiveness of this cut, one should see what the K^+K^- invariant mass looks like without strangeness conservation (Figure 4.32), and then compare it to the K^+K^- invariant mass with strangeness conservation (Figure 4.38c).

4.2.2 Kaon Timing Selection Cut

After the particle identification cuts and the kaon selection from the Time of Flight, it was found that there was still a large amount of background in the K^+K^- invariant mass plot. This background was in all likelihood due to misidentified pions that were mistaken for kaons from detectors other than the Time of Flight. This can happen because of the timing and momentum resolutions inherent in any particle physics experiment. Furthermore, as can be seen in many of the timing plots provided, charged particles are in fact indistinguishable at high momentum. An example of the K^+K^- invariant mass histogram can be seen in Figure 4.34.

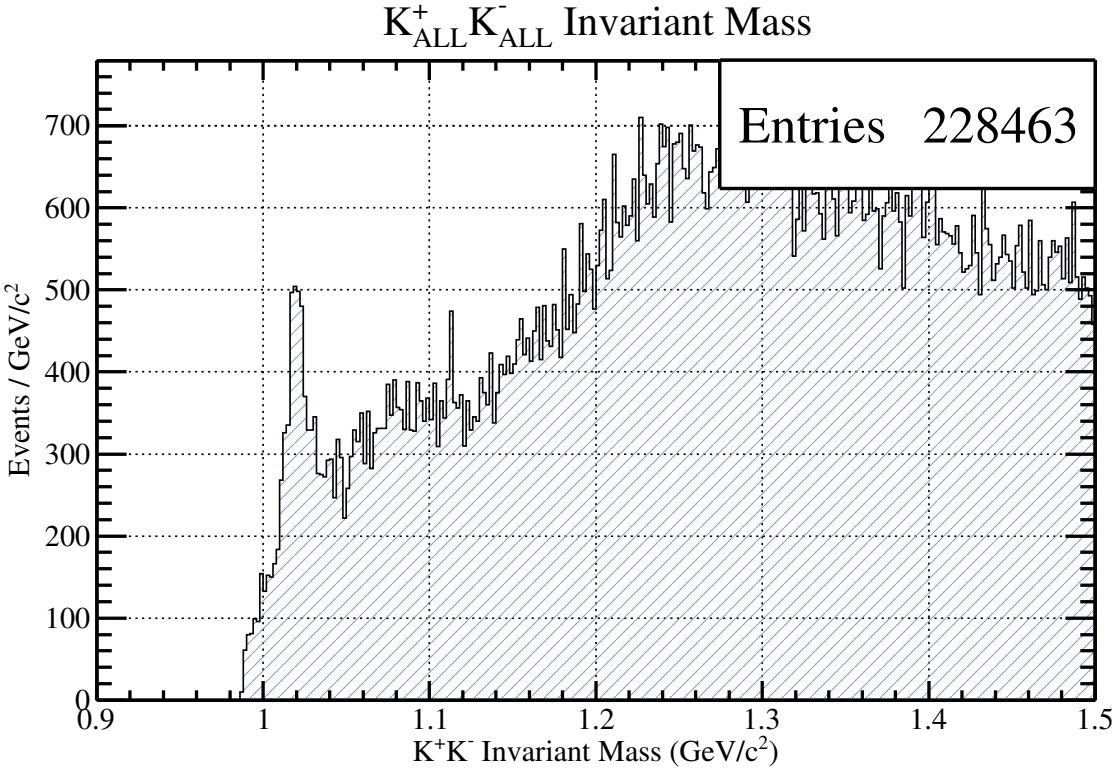

Figure 4.34: A histogram showing the K^+K^- invariant mass after particle identification cuts and the Equation 4.3 cut from the Time of Flight. The figure clearly shows a large amount of background at masses higher than the ϕ. This is due to the misidentification of pions for kaons from detectors other than the Time of Flight.

Due to this background, a study was performed over 5 percent of the data in order to understand where it may be coming from. The answer to this question was found by splitting up the K^+K^- invariant mass into different sub detectors which are responsible for the timing of the kaons. At GlueX, the three sub detectors which are responsible for providing timing and particle identification for charged particles are the Barrel Calorimeter, the Forward Calorimeter, and the Time of Flight. Since both the K^+ and the K^- can interact with any three of these sub detectors, there are nine total possible timing combinations that need to be considered. In order to properly understand these combinations, a two dimensional color histogram was provided to show how the K^+K^- invariant mass changes as a function of sub detector timing for the kaons (Figure 4.35).

There are three important observations that can be made from Figure 4.35. One observation is that there is an overwhelming amount of background which comes from the Barrel Calorimeter

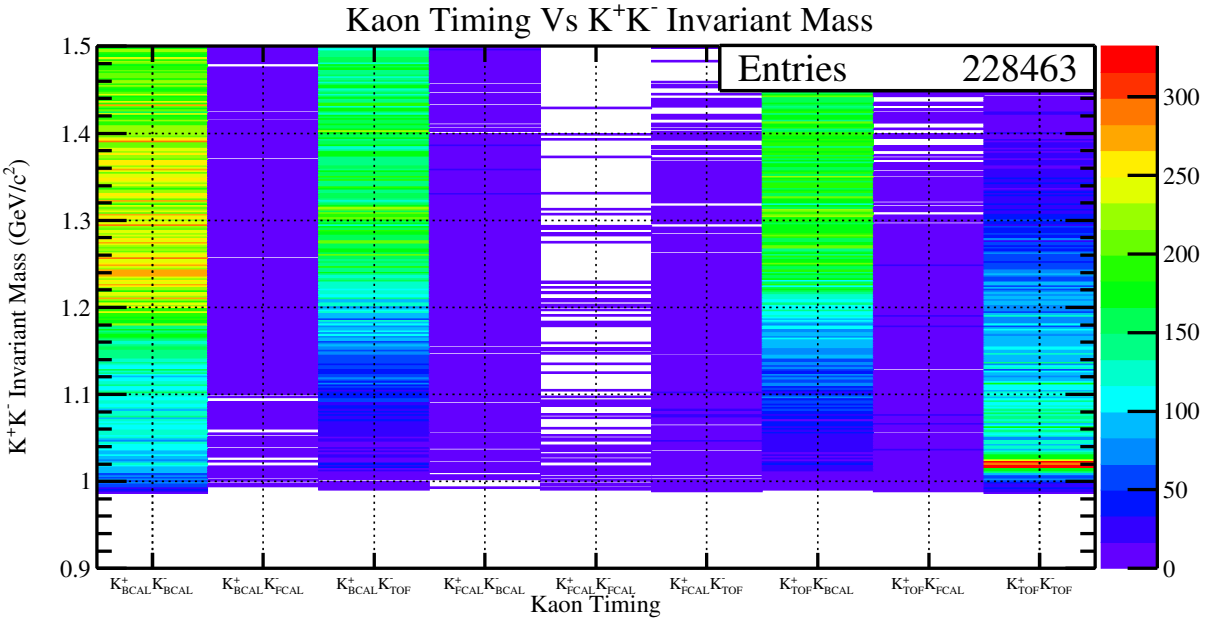

Figure 4.35: A two dimensional color histogram of the K^+K^- invariant mass versus the timing detectors for the kaons.

timing for both K^+ and K^-. The second observation is that the Forward Calorimeter has little to no statistics what so ever. This is because the GlueX reconstruction algorithm prefers timing from sub detectors that have the best timing resolution. Since the Time of Flight and the Forward Calorimeter are in the same geometric direction, they tend to provide timing information for the same charged tracks. Since the timing resolution of the Time of Flight detector is better than the Forward Calorimeter, the majority of forward going charged tracks have timing from the Time of Flight. The last observation of Figure 4.35 is that nearly all of the events which appear to have a ϕ meson reconstructed in them only exist in the last bin which is the TOF/TOF timing bin. More specifically, it appears that most of the relevant $\phi\eta$ events will only have kaon timing that came from the Time of Flight detector. Therefore, all other timing sub detectors for the kaons can be thrown out. To further emphasize this point, projections of all nine bins contained within Figure 4.35 have been provided in Figure [4.36], Figure [4.37], and Figure [4.38]. These figures clearly show K^+K^- invariant mass spectra which contain all background and no sign of a ϕ meson; with the exception of the TOF/TOF projection.

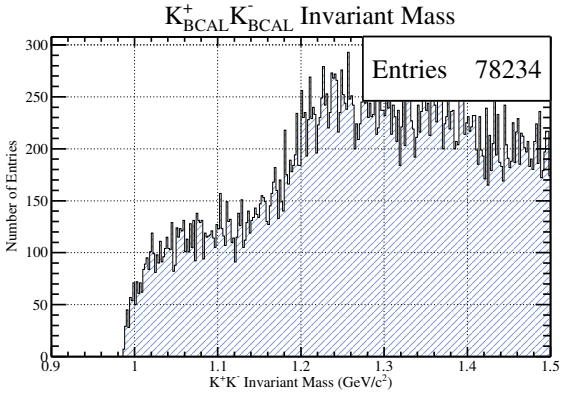

(a) Projection of $K^+_{BCAL}K^-_{BCAL}$ bin from Figure 4.35.

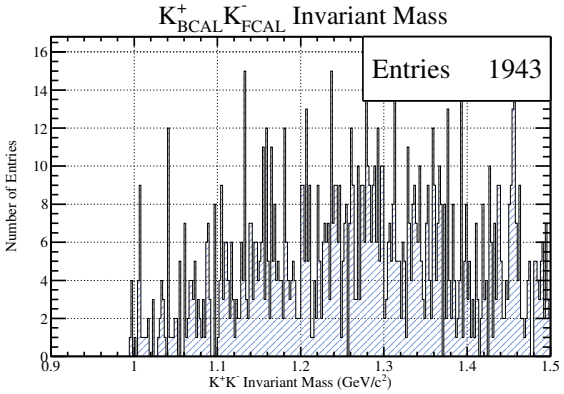

(b) Projection of $K^+_{BCAL}K^-_{FCAL}$ bin from Figure 4.35.

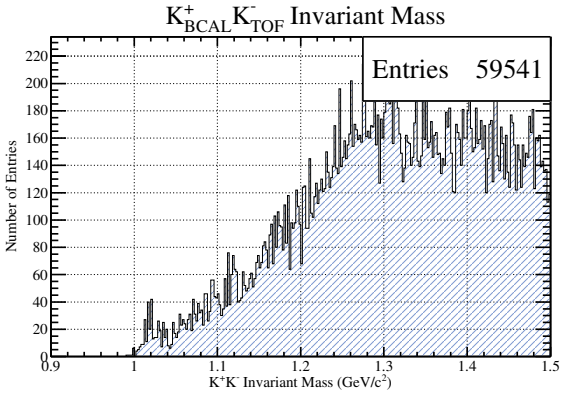

(c) Projection of $K^+_{BCAL}K^-_{TOF}$ bin from Figure 4.35.

Figure 4.36: Projections of $K^+_{BCAL}K^-_X$ bins from Figure 4.35.

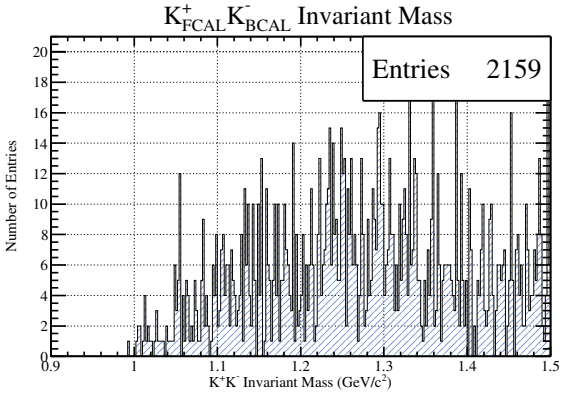

(a) Projection of $K^+_{FCAL}K^-_{BCAL}$ bin from Figure 4.35.

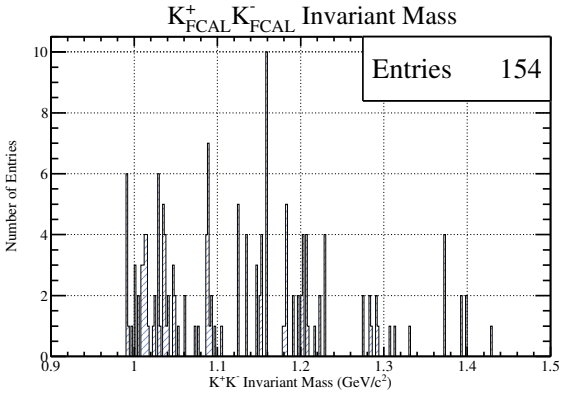

(b) Projection of $K^+_{FCAL}K^-_{FCAL}$ bin from Figure 4.35.

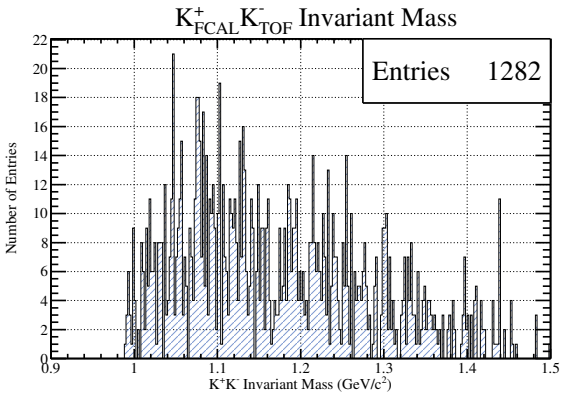

(c) Projection of $K^+_{FCAL}K^-_{TOF}$ bin from Figure 4.35.

Figure 4.37: Projections of $K^+_{FCAL}K^-_X$ bins from Figure 4.35.

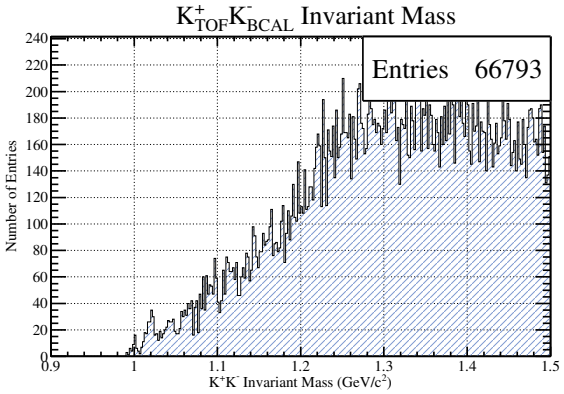

(a) Projection of $K^+_{TOF}K^-_{BCAL}$ bin from Figure 4.35.

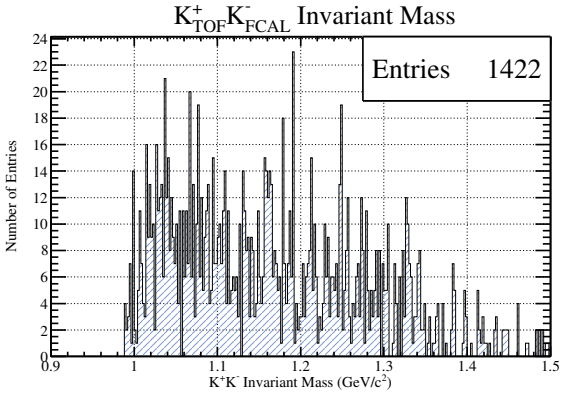

(b) Projection of $K^+_{TOF}K^-_{FCAL}$ bin from Figure 4.35.

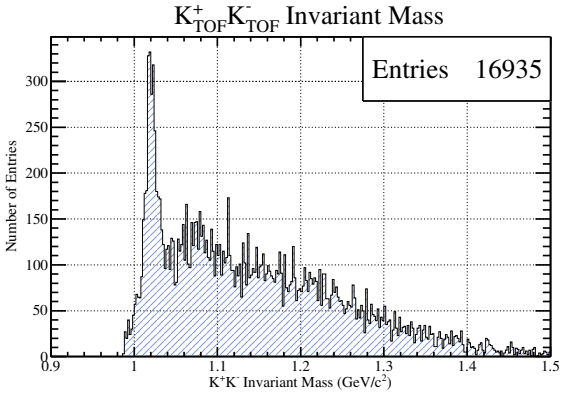

(c) Projection of $K^+_{TOF}K^-_{TOF}$ bin from Figure 4.35.

Figure 4.38: Projections of $K^+_{TOF}K^-_X$ bins from Figure 4.35.

4.2.3 Fiducial Photon Cut and Two Photon Cut

Before performing the $\gamma p \to p\phi\eta$ Monte Carlo study, it was well known that there was a lot of photon background seen in the data. After studying the data for quite some time, it was found that a two photon cut would destroy most of the background associated with photons and would also result in an observed η resonance in a $\gamma\gamma$ invariant mass plot. At the time, it was unknown why the cut appeared to throw out a lot of photon background while simultaneously appearing to enhance signal. After carefully studying accepted Monte Carlo, background generated Monte Carlo (`bggen`), and data, it was found that much of this background is attributed to secondary photons. A secondary photon should be thought of as a photon that did not originate from any photoproduction reaction, nor from any expected decay of parent states. Therefore, a secondary photon can be thought of as a photon that arose from an interaction within the GlueX spectrometer from a final state particle. An example of a secondary photon that would be present in $\gamma p \to p\phi\eta$ data can be explained by means of high momentum and forward going kaons (Figures [3.3][3.4]). Since it is very likely that most of the kaons in this channel will interact with either the Time of Flight detector or the Forward Calorimeter, it is expected that these particles will deposit a lot of energy in this region of the spectrometer. These high momentum particles will cause a signal in one or both of these detectors and will also cause a hadronic shower in the FCAL. These hadronic showers will be much wider and irregular in comparison to an electromagnetic shower. In addition to hadronic showers, another source of secondary photons are delta-electrons which are knocked out by charged tracks or beam halo anywhere in the downstream direction where they cannot be tracked by the FDC. These additional backgrounds create low energy electromagnetic showers in the FCAL but cannot be vetoed due to an absence of a reconstructed track. The additional reconstructed photons will therefore cause the number of photons reconstructed in an event to be fictitiously higher than what was actually present within the detector. To first order, this perhaps explains why doing a two photon cut on data will both greatly reduce background and enhance a signal. However, many important questions will still remain about this cut. How much signal do we lose by simply performing a two photon cut? Furthermore, is there a better way to cut out the background and preserve as many signal events as possible? This subsection will show that this effect does in fact manifest itself in both Monte Carlo and data; and will perform an analysis on Monte Carlo and data to show the best way of reducing secondary photons.

The first evidence that suggests the existence of secondary photons in $\gamma p \to p\phi\eta; \phi \to K^+K^-; \eta \to \gamma\gamma$ accepted Monte Carlo can be seen by simply plotting the invariant mass of a reconstructed $\gamma\gamma$ pair (Figure [4.39]). The data which went into this plot was created by throwing $\gamma p \to p\phi\eta; \phi \to K^+K^-; \eta \to \gamma\gamma$ into the GlueX detector and then simulating its behavior with `hdgeant` and `mcsmear`. The invariant mass spectrum in Figure [4.39] shows a clear peak from the generated η meson on top of a background that spans to low mass. If this sample initially only threw two photons exactly equal to the η meson invariant mass, then why are there so many low mass photon combinations that appear to be in the shape of background? To answer this question, we can separate our reconstructed Monte Carlo particles into two categories: particles that were generated and particles that were not generated. In doing so, we can see where this background comes from and also how to possibly reduce it.

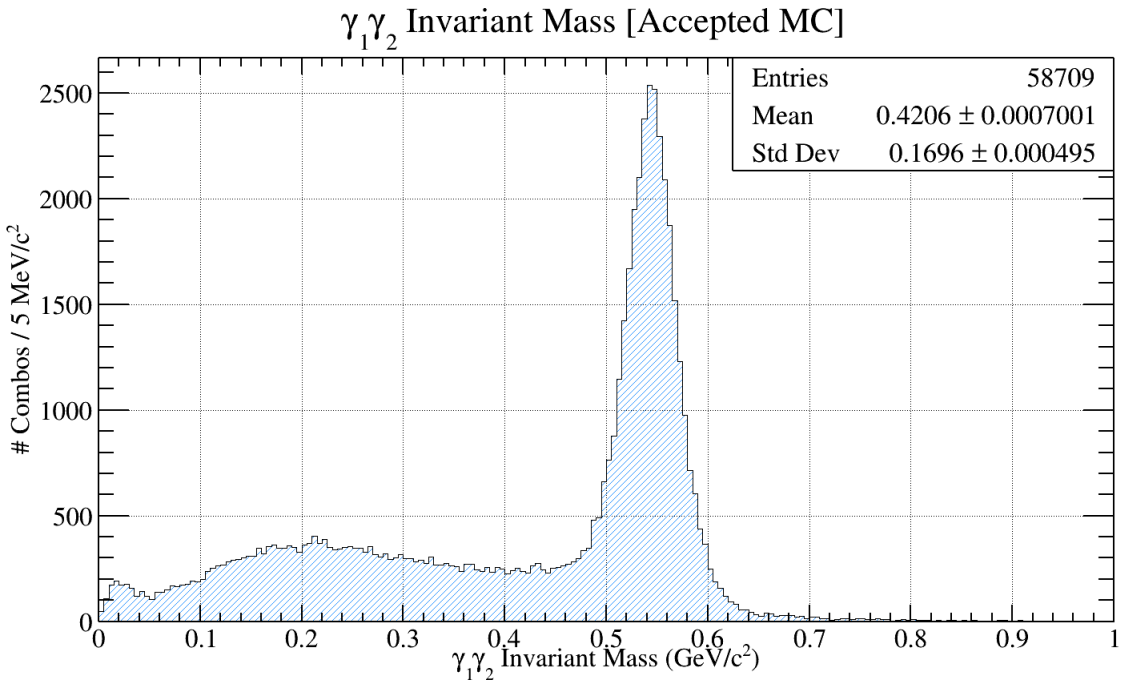

Figure 4.39: Invariant mass of the reconstructed $\gamma\gamma$ pair from accepted Monte Carlo. This Monte Carlo data originally came from a $\gamma p \to p\phi\eta; \phi \to K^+K^-; \eta \to \gamma\gamma$ generated topology. An interesting feature of this invariant mass spectra is that it shows a clear η peak, but also contains a background as well. The source of this background is thoroughly studied in subsection 4.2.3.

The signal and background seen in Figure [4.39] can be studied by displaying P Vs θ and ϕ Vs θ plots for the thrown photons and the secondary photons in Figure [4.40]. The most important

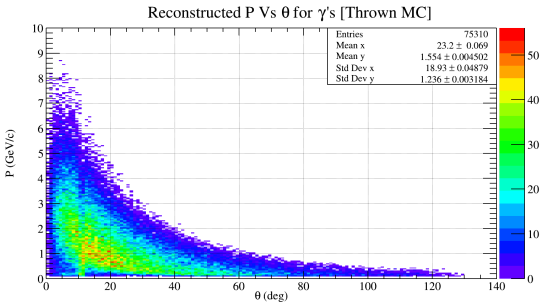

(a) P Vs θ distribution for thrown Monte Carlo photons.

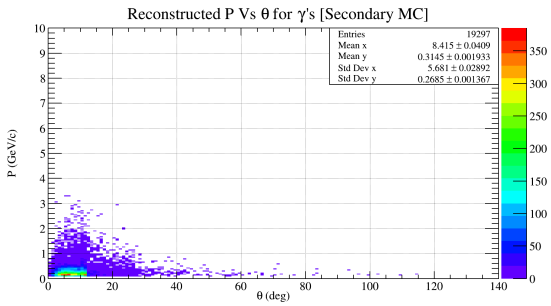

(b) P Vs θ distribution for secondary Monte Carlo photons.

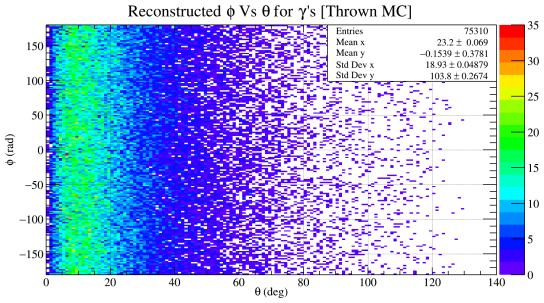

(c) ϕ Vs θ distribution for thrown Monte Carlo photons.

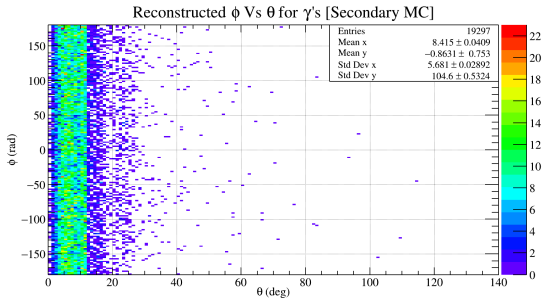

(d) ϕ Vs θ distribution for secondary Monte Carlo photons.

Figure 4.40: P Vs θ and ϕ Vs θ distributions for thrown (left column) and secondary (right column) photons inside accepted Monte Carlo data.

feature to take away from these plots is the tendency for secondary photons to be at a shallow angle relative to the beam direction (below 12°) while also having a low three momentum magnitude (below 500 MeV/c). Simply knowing the distribution of these photons gives us some insight into where they came from. Since neutral photons can only be detected by either the Forward Calorimeter or the Barrel Calorimeter and most of these photons appear in the forward direction, it is clear that FCAL showers are causing these photons to appear.

The reconstructed invariant mass for a given $\gamma\gamma$ combination within an event as a function of the number of photons reconstructed within an event can also be shown. By using our Monte Carlo samples, we can also separate these plots into thrown and secondary photons, identical to what we did in Figure [4.40]. The reconstructed invariant mass of two photons versus the number of reconstructed photons in an event is given in Figure [4.41]. There is one important observation

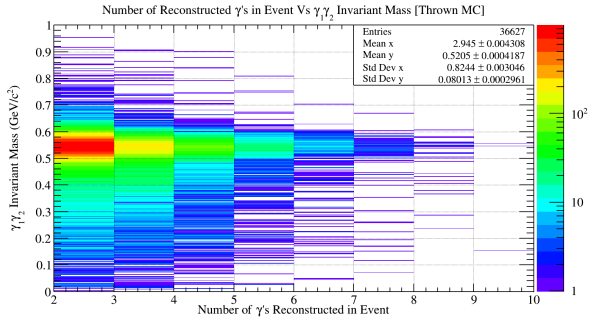

(a) Number of photons reconstructed in an event versus $\gamma\gamma$ Invariant Mass for thrown photons.

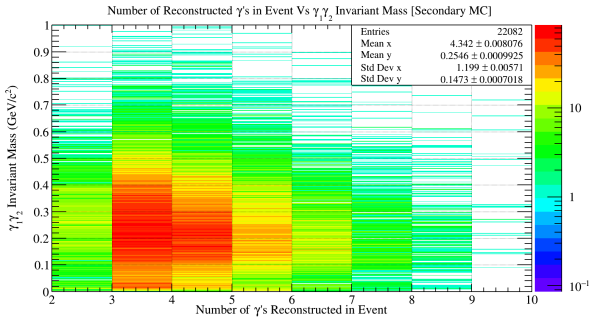

(b) Number of photons reconstructed in an event versus $\gamma\gamma$ Invariant Mass for secondary photons.

Figure 4.41: Comparing how the invariant mass for a given $\gamma\gamma$ pair changes depending on the number of reconstructed photons in an event and whether or not the photons were thrown or secondary photons.

that should be taken away from the two sub figures. In Figure 4.41a a clear η resonance can be seen which spans a large number of reconstructed photons per event. This sub figure indicates that performing a two photon cut on the signal data is not good for signal events at this stage.

In fact, after fitting a Gaussian function to the η peaks between 3 and 10 reconstructed photons, it was found that ∼8,000 combinations would be lost out of a total of ∼30,000; resulting in a 26 percent loss of events. Therefore, it is imperative to perform a P vs θ cut *before* a two photon cut.

Seeing that there is a non negligible amount of secondary photons left in accepted Monte Carlo, the next cut that will be applied to all of the data is a P Vs θ cut, where $P < 500MeV/c$ and $\theta < 12°$. After enforcing these cuts on all photons, the distribution of number of photons reconstructed in an event versus $\gamma\gamma$ invariant mass is shown once again in Figure [4.42]. It is easy to see that most of the η signal has migrated to the two photon bin and simultaneously much of the secondary background has been reduced in the accepted Monte Carlo data set. Due to this, a two photon cut is now necessary to do in order to reduce some of the left over background at higher number of reconstructed photons per event.

In this section it was shown that it is necessary to perform a P Vs θ cut of $P < 500MeV/c$ and $\theta < 12°$ and a two photon cut. After completing this sequence of cuts, it was found that 94 percent of background data was cut, while preserving 93 percent of signal data.

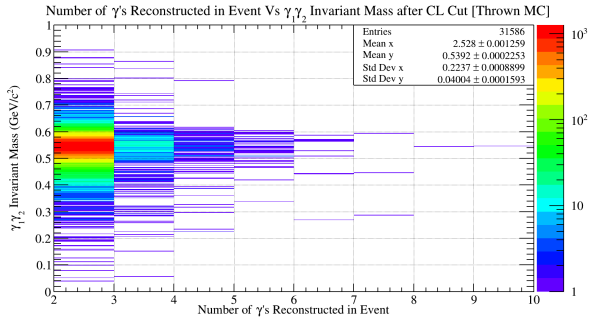

(a) Number of photons reconstructed in an event versus $\gamma\gamma$ Invariant Mass for thrown photons after a $P < 500$ MeV/c and $\theta < 12°$ cut.

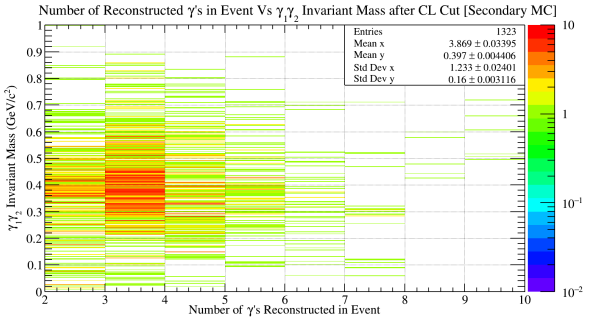

(b) Number of photons reconstructed in an event versus $\gamma\gamma$ Invariant Mass for secondary photons after a $P < 500MeV/c$ and $\theta < 12°$ cut.

Figure 4.42: Number of photons reconstructed in an event versus $\gamma\gamma$ Invariant Mass for thrown photons and secondary photons after a $P < 500MeV/c$ and $\theta < 12°$ cut.

4.2.4 Exclusivity

The last cuts that need to take place in order to observe $\gamma p \to p\phi\eta$ are two; one which reduces the number of photons from the beam, and the other which cuts on the missing mass squared of the system. After all cuts had been made, it was found that there were still residual combinations from events which came directly from the beam photons and not the final state particles. After the proper beam timing cut, the event selection will then loop over available combinations in order to select the best available beam photon. This is done by selecting the beam photon which reconstructs the missing mass squared that is closest to zero. After enforcing this criteria, it is guaranteed that only one combination per event will survive. After this selection of events, an additional cut is placed on the data which enforces exclusivity. This is done by only allowing events with a missing mass squared between -0.02 GeV$^2/c^4 \leq MM^2 \leq 0.02$ GeV$^2/c^4$ (Figure 4.43). The enforcement of exclusivity removes any background that did not properly conserve the measured four momentum from the $\gamma p \to pK^+K^-\gamma\gamma$ reaction. To finalize this section Table 4.2 is a summarized list of all cuts performed by this analysis.

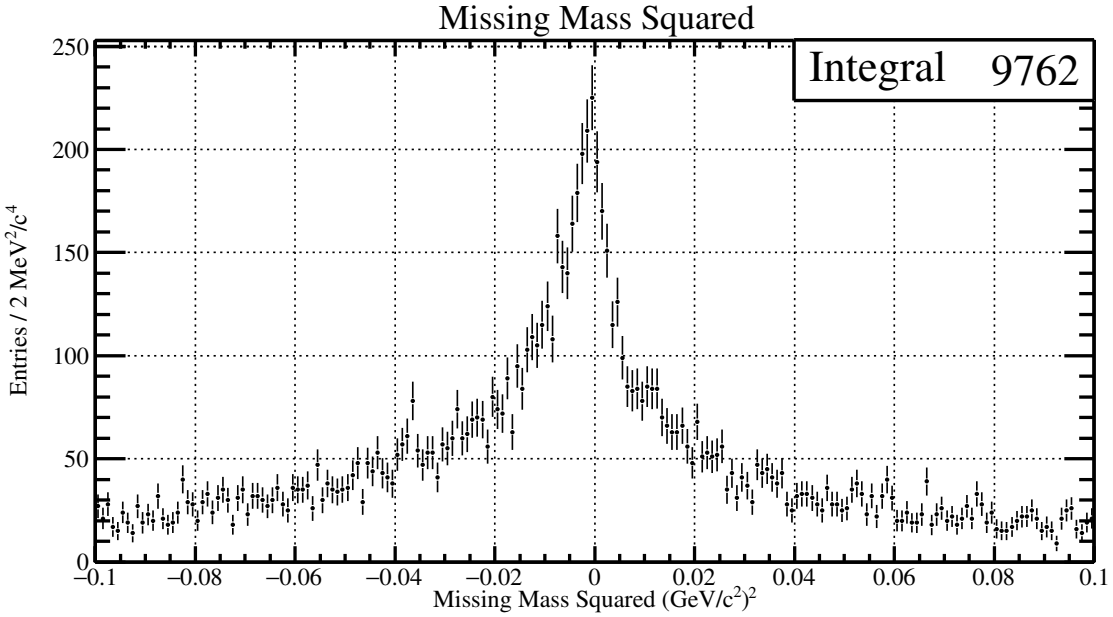

Figure 4.43: A plot of the final missing mass square after all cuts described in this chapter.

4.2.5 Tabular Summary of Particle Identification Cuts

Table 4.1: A table with timing cut values for all final state particles in the reaction $\gamma p \to pK^+K^-\gamma\gamma$. The values of the timing cuts change depending on both the particle species and detector system resolution. It should be noted that the final state photons only have the calorimeters as possible timing detectors. This is due to the fact that they do not interact with the TOF detector.

Particle	Detector	ΔT Cut [ns] (2σ)
Proton	BCAL	$\pm$ 0.6
Proton	FCAL	$\pm$ 1.0
Proton	TOF	$\pm$ 0.4
K^+	BCAL	$\pm$ 0.7
K^+	FCAL	$\pm$ 0.8
K^+	TOF	$\pm$ 0.2
K^-	BCAL	$\pm$ 0.7
K^-	FCAL	$\pm$ 0.8
K^-	TOF	$\pm$ 0.2
γ	BCAL	$\pm$ 1.0
γ	FCAL	$\pm$ 1.1

Table 4.2: A list which summarizes all cuts used to identify $\gamma p \to pK^+K^-\gamma\gamma$.

#	Description of Cut	Reference
1	Timing cuts for all final state particles	Table 4.1
2	Vertex cuts for all final state particles	Figures 4.2a, 4.2b
3	Beam timing cut	Figure 4.1
4	Proton dE/dX cut	[26]
5	P vs θ Cut for photons	Subsec: 4.2.3
6	Two Photon Cut	Subsec: 4.2.3
7	Kaon Selection	Subsec: 4.2.1
8	Kaon Timing Selection	Subsec: 4.2.2
9	$-0.02GeV^2/c^4 \leq MM^2 \leq 0.02GeV^2/c^4$	Subsec: 4.2.4
10	γ_{Beam} with MM^2 closest to zero	Subsec: 4.2.4

CHAPTER 5

ANALYSIS

5.1 Investigation of $\phi\eta$ correlation by means of K^+K^- Vs $\gamma\gamma$ Invariant Mass Plot

The image illustrated in Figure 5.1 is the data in question. On the vertical axis is the K^+K^- invariant mass and on the horizontal axis is the $\gamma\gamma$ invariant mass. To be absolutely clear, this is a plot of invariant mass versus invariant mass and is therefore not a Dalitz Plot. Some interesting features contained within the image are the clear vertical bands for the π^0 and η resonances which have large decay modes to $\gamma\gamma$ final states. In addition, one can also observe a horizontal band slightly above 1 $\frac{GeV}{c^2}$ which corresponds to the ϕ meson decaying to a K^+K^- final state. This analysis will focus on the region where the ϕ meson and η meson bands cross in order to determine if their intersection region contains some type of correlation.

5.1.1 Cuts on the 2D Invariant Mass Plot

In order to analyze the $\phi\eta$ region of this data, only events which fall within $\pm 10\sigma_\phi$ away from the ϕ peak and $\pm 10\sigma_\eta$ away from the η peak will be considered. This was done by taking different slices of either the $\gamma\gamma$ or K^+K^- data, then projecting the invariant mass distribution onto the opposite axis. For example, there were five different ϕ mass regions studied in this analysis. Each fit corresponds to a different $\gamma\gamma$ mass range. The $\gamma\gamma$ mass ranges are all $4\sigma_\eta$ in width, and span a total mass range of $m_\eta - 10\sigma$ to $m_\eta + 10\sigma$. An example with labeled cut lines is provided in Figure 5.2. It should be noted that the analysis of the η mass was not studied symmetrically about the ϕ due to the K^+K^- threshold.

5.1.2 Projections and Fits for ϕ and η

Once the data had been cut and projected in the ten different mass regions, the ϕ and η peaks were fit. In the instance of the ϕ meson, the signal plus background events were fit with a Gaussian plus a second degree polynomial. The fit range used in each histogram projection for the ϕ meson spans from $m_\phi - 6\sigma_\phi$ to $m_\phi + 30\sigma_\phi$. The unusually large fit range was necessary in order to properly

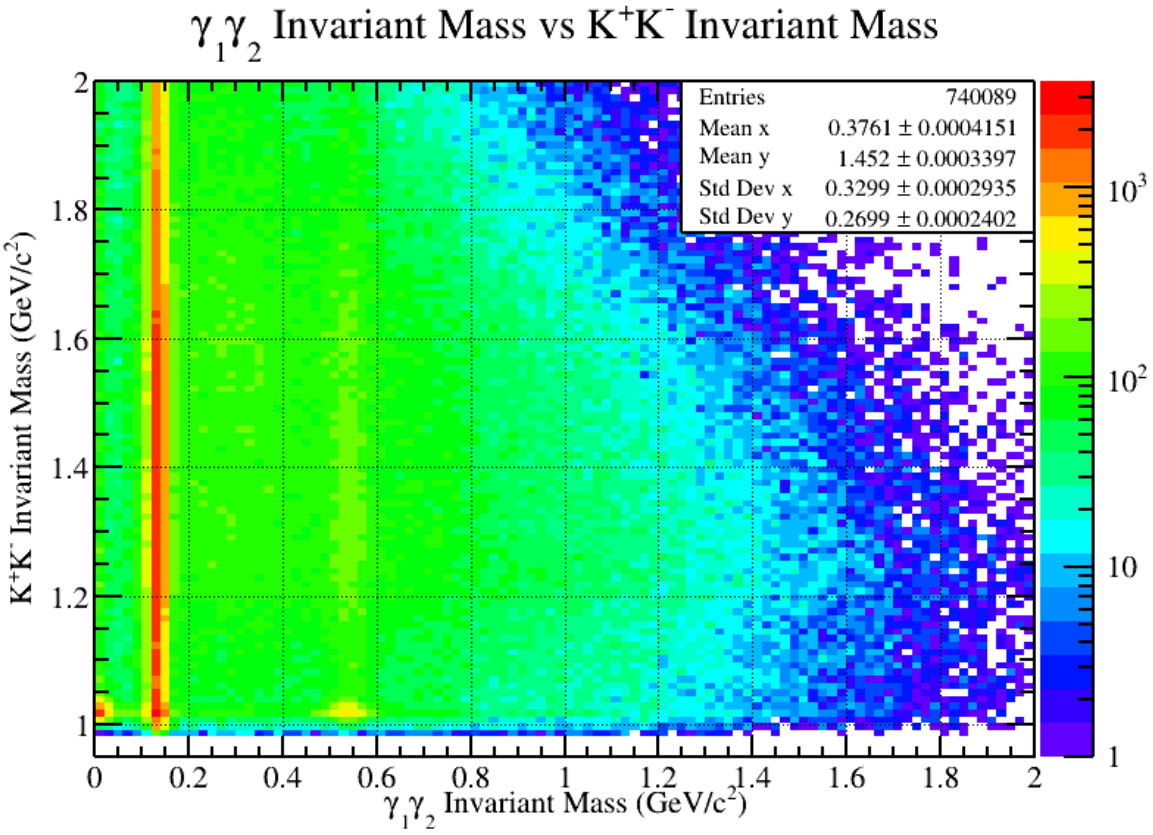

Figure 5.1: A two dimensional invariant mass plot with the K^+K^- invariant mass on the vertical axis, the $\gamma\gamma$ invariant mass on the horizontal axis, and a logarithmically scaled z axis. Some interesting features contained within the image are the clear vertical bands for the π^0 and η resonances which have large decay modes to $\gamma\gamma$ final states. In addition, one can also observe a horizontal band slightly above 1 $\frac{GeV}{c^2}$ which corresponds to the ϕ meson decaying to a K^+K^- final state.

estimate the background surrounding the ϕ mass. In the instance of the η meson, the signal plus background events were fit with a Gaussian plus a first degree polynomial due to the relatively flat background surrounding the η peak. The fit range used for the η meson spans $m_\eta \pm 6\sigma_\eta$ $\frac{GeV}{c^2}$. The resulting fits are provided in Figures 5.3 and [5.4], where the blue line represents the fit for all events (signal plus background), the green line represents the Gaussian fit (signal events), and the red line represents the polynomial fit (background events). Each histogram contains a title with brackets at the end. The arguments encapsulated by the brackets is the cut range that was used for that particular projection sample.

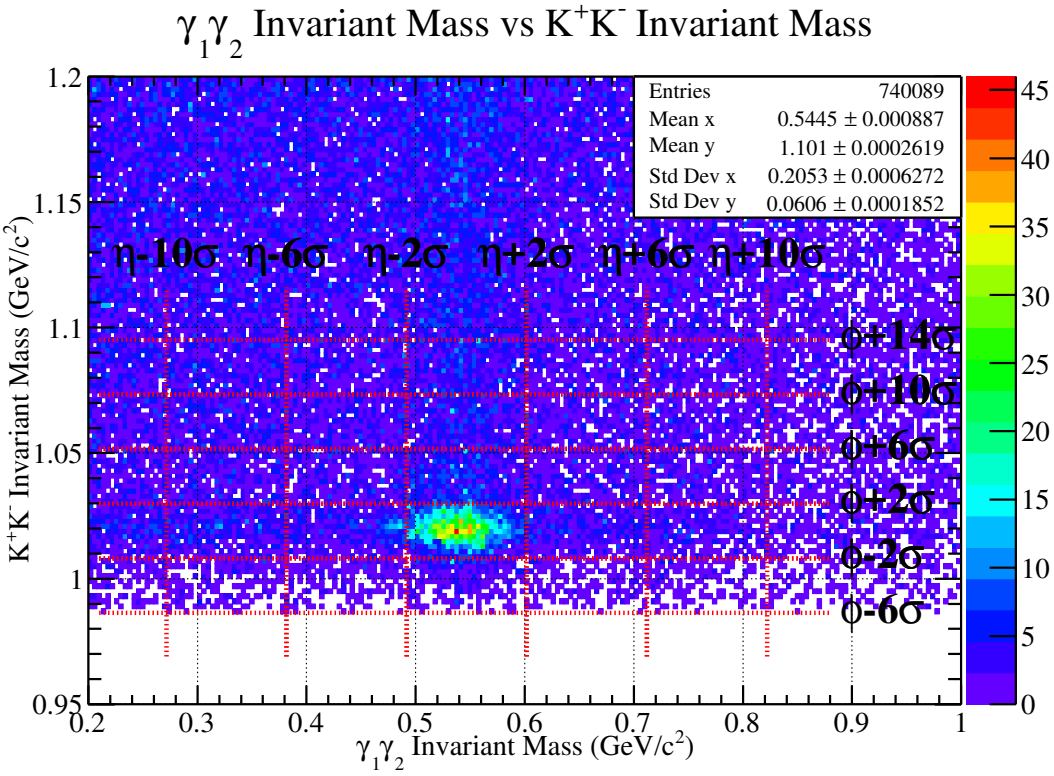

Figure 5.2: An illustrated example of the cuts used for studying the correlation of $\phi\eta$. The figure above is a two dimensional invariant mass plot which clearly shows an η band spanning the vertical direction at ~ 0.547 GeV/c^2 and a ϕ band spanning the horizontal direction at ~ 1.02 GeV/c^2. The red vertical and horizontal cut lines provide the ranges used to study $\phi\eta$ correlation. Examples of what the projected ranges look like are provided in Figures [5.3][5.4].

5.1.3 Integration Results for ϕ and η

After obtaining accurate fits for all regions, integration of the Gaussian fit functions was performed. Each Gaussian fit was integrated in the range of $m \pm 2\sigma_m$, where m represents either m_ϕ or m_η mass coupled with the addition or subtraction of two standard deviations in each direction. Integration of the Gaussian fits provides an accurate estimate for the number of signal events that exists for that particular sampling of $\gamma\gamma$ Vs K^+K^- phase space. The estimated number of signal events have been added to Figure [5.5], with the exception of the $\phi\eta$ intersection region which will be discussed in more detail in the Conclusion section.

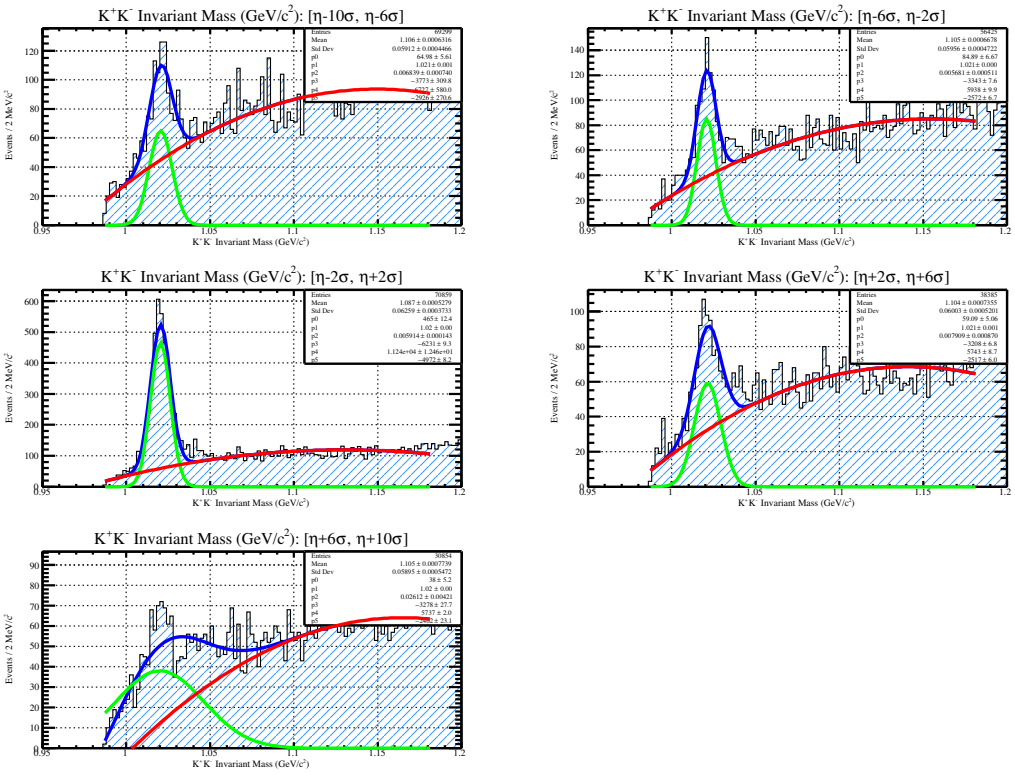

Figure 5.3: A collection of different K^+K^- invariant mass projections as a function of $\gamma\gamma$ invariant mass cut range. Each sub figure includes a red line which is a second degree polynomial used to estimate the shape of the background, a green line which is a Gaussian used to estimate the ϕ signal peak, and a blue line which the sum total of the polynomial fit and Gaussian fit. Lastly, each sub figure also includes the $\gamma\gamma$ invariant mass cut range used to produce the projected figure. This information is in the title of the histogram, inside the brackets.

5.1.4 Additional Statistics Study

In addition to the analysis mentioned above, an alternative study has been included which simply samples the phase space and records the number of events within that sample. To do this, the same cut ranges as before were used. The only difference is that this approach only considers the 3x3 grid surrounding the $\phi\eta$ intersection region. Each region is a box cut which is exactly $4\sigma_\phi$ x $4\sigma_\eta$ in area. Each area is given an index to denote the specific region of phase space that is being sampled and an illustration is provided in Figure [5.6].

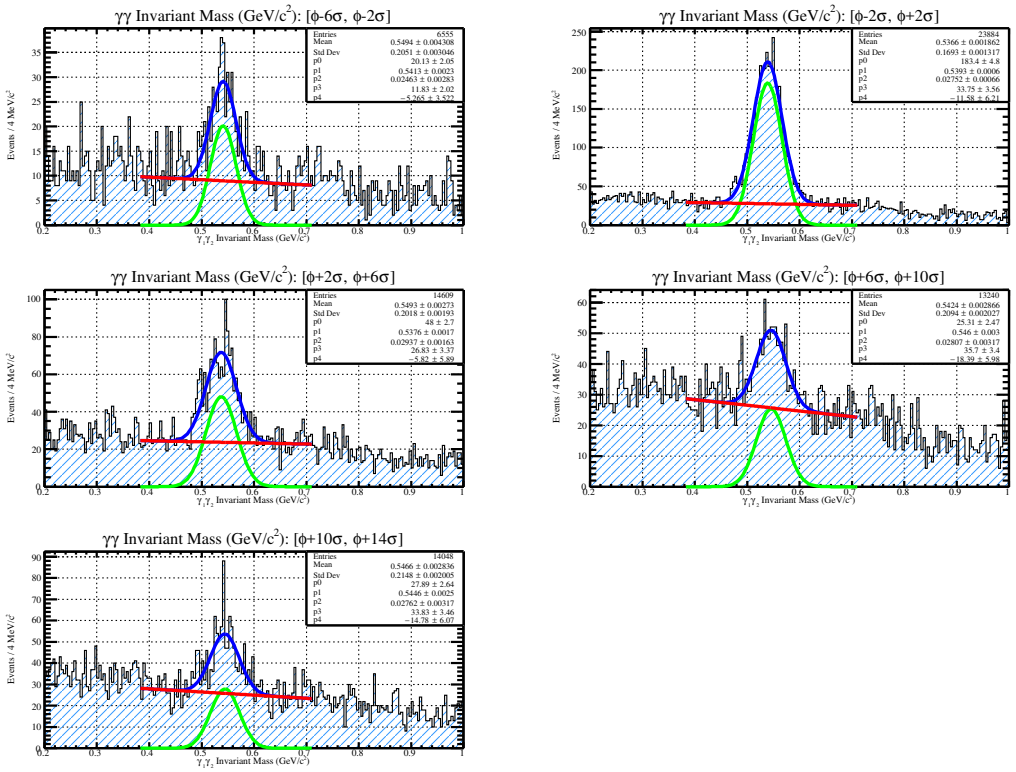

Figure 5.4: A collection of different $\gamma\gamma$ invariant mass projections as a function of K^+K^- invariant mass cut range. Each sub figure includes a red line which is a first degree polynomial used to estimate the shape of the background, a green line which is a Gaussian used to estimate the η signal peak, and a blue line which the sum total of the polynomial fit and Gaussian fit. Lastly, each sub figure also includes the K^+K^- invariant mass cut range used to produce the projected figure. This information is in the title of the histogram, inside the brackets.

Using the diagram as a reference, it is easy to see that the average number of background events within this phase space can be calculated using the formula $N_{BG} = (A_1 + A_3 + A_7 + A_9)/4$. Additionally, the average number of ϕ and η events plus background can be calculated using $N_{BG} + N_\phi = (A_4 + A_6)/2$ and $N_{BG} + N_\eta = (A_2 + A_8)/2$, respectively. Lastly, quantification of the number of correlated events in region 5 is possible by using $N_{BG} + N_\phi + N_\eta + N_{correlated} = A_5$. The number of events contained within each region of phase space is given in Figure [5.7].

The first step of this simplistic analysis is to determine what the average number of background

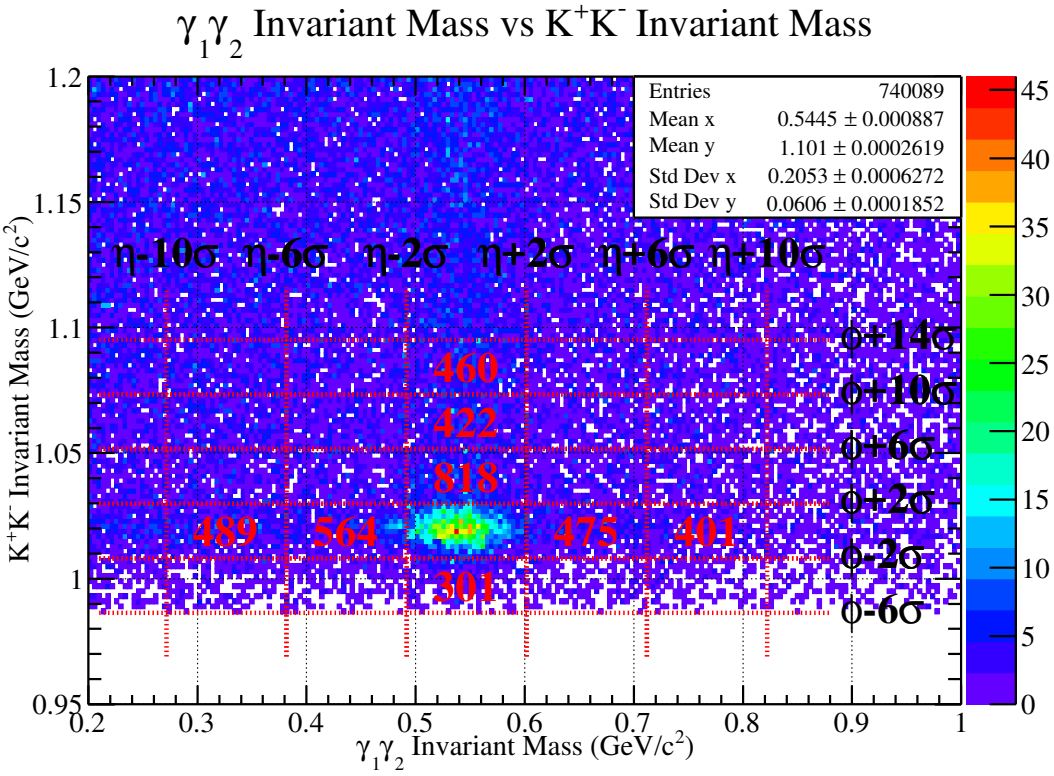

Figure 5.5: The above figure provides the number of events for each projection range studied. These numbers were calculated by means of integrating the Gaussian fit for either the ϕ or η between $\pm 2\sigma$. The vertical column of numbers represents the number of η events for a given K^+K^- invariant mass, and the horizontal row of numbers represents the number of ϕ events for a given $\gamma\gamma$ invariant mass. The number of events observed in the intersection region was not included in the figure due to the amount of space available. There numbers can be found in the Conclusion section.

events is, which is calculated to be 453. Knowing this, the number of ϕ and η events can now be determined by using the equations $N_{BG} + N_\phi = (A_4 + A_6)/2$ and $N_{BG} + N_\eta = (A_2 + A_8)/2$, and then subtracting the average number of background events. Upon doing this, it was found that N_ϕ is 423 and N_η is 433. To complete this analysis, the number of correlated events can now be estimated by using the equation $N_{BG} + N_\phi + N_\eta + N_{correlated} = A_5$, and subtracting N_{BG}, N_ϕ, and N_η. The total number of correlated events is 2446. This calculation shows once again that there is an overflow of events within the $\phi\eta$ intersection region that cannot be explained by the presence

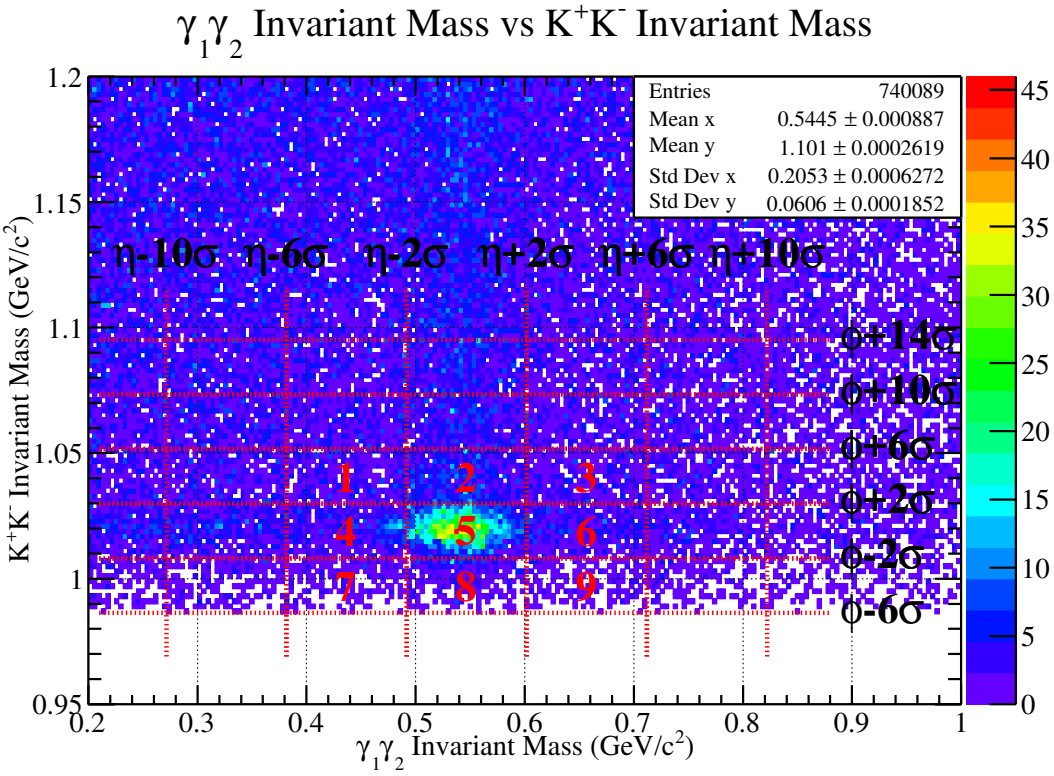

Figure 5.6: An illustration to provide the reader with an idea of how the second statistics study is performed. All of the cut ranges are identical to the first statistics study. The numbers provided in the figure do not represent events, but simply indicate the index associated with a certain area of $\phi\eta$ phase space.

of background or the addition of events from the ϕ and η bands.

5.1.5 Conclusion of K^+K^- Vs $\gamma\gamma$ Invariant Mass Plot Study

Figure [5.5] provides the estimated number of signal events for the ϕ and η bands near the $\phi\eta$ intersection region. If there is no correlation between ϕ and η events, the total number of signal events in the intersection region should be equal to the sum of an η peak plus a ϕ peak. Taking the numbers from Figure [5.5], the average number of signal events in the ϕ band is $\overline{\phi_{events}} \sim 482$, and the average number of signal events in the η band is $\overline{\eta_{events}} \sim 500$. Therefore, it is estimated that the number of signal events within the $\phi\eta$ intersection region should be just shy of 1000 events

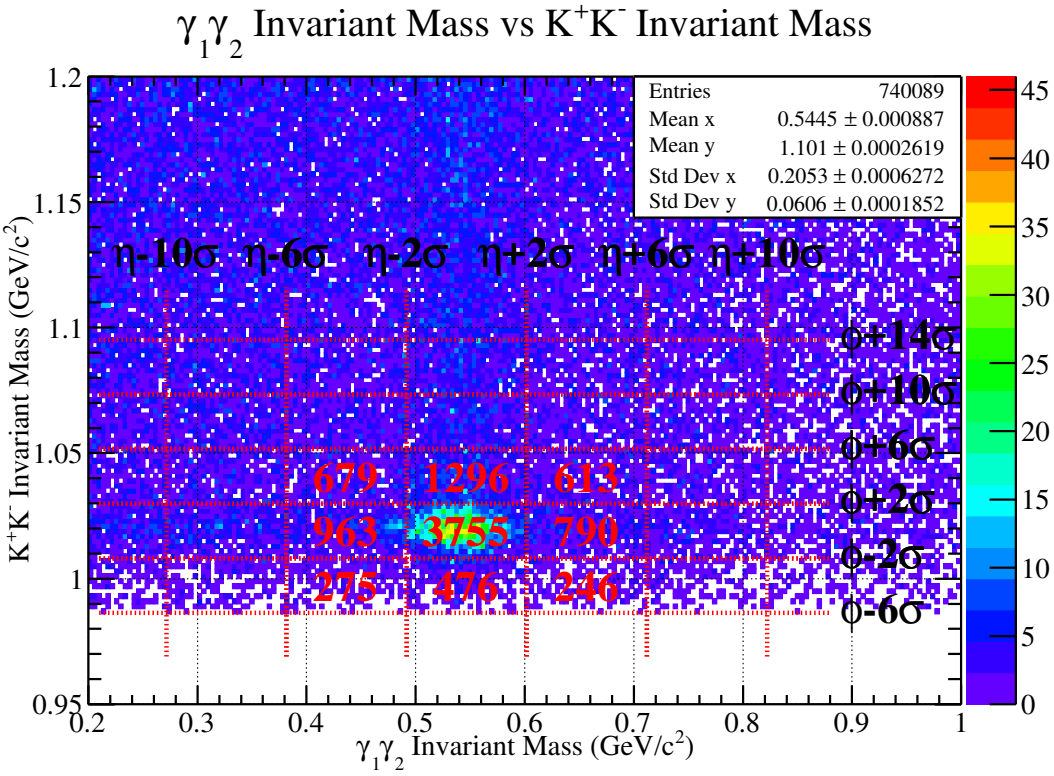

Figure 5.7: This figure shows the total number of counts in each box. To be clear, the numbers in each box do not represent the total number of events, but rather the precise amount of statistics contained within the cut lines. Upon inspection, one can see evidence of $\phi\eta$ correlation, which is explained in the Conclusion section.

if there is no correlation present. After integrating the Gaussian fit for the ϕ and η mesons in the intersection region, it was found that there were 3194 events corresponding to the ϕ fit, and 2993 events corresponding to the η fit. Both of these fits not only yield roughly the same number of events, but they also produce an event estimate which is a factor of three higher than what would have been there from the ϕ and η bands alone. The large increase in event statistics within the $\phi\eta$ intersection region strongly suggests that some type of correlation is present within this area of K^+K^- $\gamma\gamma$ phase space. It should be clearly noted that the nature of this correlation is not identified at this time. Moreover, it is unclear if this $\phi\eta$ enhancement corresponds to a $\phi\eta$ bound state, or comes from some other topology such as $\gamma p \to N^*\phi$ and $\gamma p \to N^*\eta$.

5.2 Probabilistic Weightings for $\phi\eta$ Events

Throughout the course of history, physicists have tried clever ways of reducing the amount of background that is present under a given signal, or resonance. An example of this may be the classic side band subtraction, where the signal region will be defined by some average mass value, plus or minus a well defined width. If one were to perform a cut about this region after particle identification and cuts, there still may be background underneath the peak. In order to eliminated the background under the signal, one thing to do is use the background near the peak as reference for subtraction. To do this, one would use background events that are located at both higher and lower mass values far away from the signal, so long as the total mass range used is equal to the mass range for selecting the signal region. The side band subtraction method works well for some physics analyses, but not all. Side band subtraction is an issue with this analysis because the primary purpose is to observe structures in the $\phi\eta$ invariant mass spectra. Performing a side band subtraction is problematic because it allows events well below the $\phi\eta$ threshold to exist in the background spectra. Subtracting off these events from the primary signal region results in a final $\phi\eta$ invariant mass spectra which has negative event counts at low $\phi\eta$ mass values. Therefore, it is imperative to seek alternative background subtraction methods. The method that will be presented in this analysis uses a probabilistic weighting procedure which will be explained in this section.

5.2.1 Introduction to Probabilistic Event Weightings

One of the issues with a side band subtraction method is that it treats all events with a relative weight of one. The purpose of this section is to describe and propose a new method which does not treat all events with a value of one, but instead assigns a fractional weight to an event based on a quality factor, or Q-factor. The quality value idea was first introduced in 2008 by M. Williams, M. Bellis, and C. A. Meyer in a paper titled "*Separating Signals from Non-Interfering Backgrounds using Probabilistic Event Weightings.*" [38]. The paper considers a generic situation in which there is a data set of n total events described by m coordinates, which will be written as $\vec{\xi}$. Within the data set, there exists n_s total signal events and n_b total background events, and therefore $n = n_s + n_b$. In addition, both the signal and the background distributions are functions of the coordinates, such that $S(\vec{\xi})$ can be thought of as a signal distribution and $B(\vec{\xi})$ can be thought of as a background distribution. Contained within the set of coordinates $\vec{\xi}$, there exists a *reference*

coordinate (ξ_r) with which we know the functional form of $S(\xi_r)$ and $B(\xi_r)$ *a priori*. The reference coordinate that is used in this thesis as well as in the paper mentioned above is the invariant mass of a final state. For many invariant mass distributions, the functional form of the signal distribution, $S(\xi_r)$ can be represented with a well known signal function. Some examples of well known signal functions are Gaussian, Voigtian, and Breit-Wigner distributions. In addition, the background distribution, $B(\xi_r)$, can be represented with an n^{th} degree polynomial function.

Since the signal and background distributions are not necessarily known *a priori* for the other coordinates, we use them to calculate a kinematic distance on an event by event basis. This is done by using the Equation (5.1).

$$d_{ij}^2 = \sum_{k \neq r} \left[\frac{\xi_k^i - \xi_k^j}{R_k} \right]^2 \tag{5.1}$$

In Equation(5.1), the total kinematic distance is calculated between some event i, as compared to another event j. This is done by taking the sum of the squared difference over all of the coordinates ξ_k, except for the reference coordinate ξ_r. The difference between coordinates is then normalized by the parameter R_k. The parameter R_k is the total maximum difference for a given coordinate ξ_k. An example of this may be the measurement of an azimuthal angle which spans from 0 to 2π. Therefore, the R_k for an azimuthal angle would be 2π. Upon closer inspection, one should realize that Equation(5.1) is simply a representation of the Pythagorean Theorem in a normalized $m-1$ dimensional kinematic space.

After calculating all of the kinematic distances for an event i, as compared to all other events within the data set $1...j...n$, it is then necessary to only keep the *nearest neighbors*. The nearest neighbors, by definition, are a subset of the n events which have the smallest kinematic distance with respect to the i^{th} event that is being considering. The purpose of only keeping the nearest neighbors stems from the assumption that a signal or background events will share similar kinematic measurements with other signal or background events. The number of nearest neighbors for a set of events n is an arbitrary amount, and does not greatly effect the quality factor calculation; so long as the amount is a small fraction of the total events n. Once the list of nearest neighbors is known for the i^{th} event, it is then necessary to plot their reference coordinate, ξ_r, onto a histogram. This histogram should contain a well understood signal distribution $S(\xi_r, \vec{\alpha})$, and background distribution $B(\xi_r, \vec{\alpha})$, as mentioned above; where $\vec{\alpha}$ is the set of known/unknown fit parameters

used to describe the signal or background distribution. The histogram will then be fit by the sum of the signal and background distributions such that $F(\xi_r, \vec{\alpha}) = S(\xi_r, \vec{\alpha}) + B(\xi_r, \vec{\alpha})$. The quality factor can then be calculated by using the reference coordinate value for the i^{th} event and plugging it into the signal and background functions by using Equation(5.2), where $\hat{\alpha}$ is the set of fitted parameters for the signal or background distribution.

$$Q_i = \frac{S(\xi_r^i, \hat{\alpha}_i)}{S(\xi_r^i, \hat{\alpha}_i) + B(\xi_r^i, \hat{\alpha}_i)} \tag{5.2}$$

Once the quality factor is known for an event i, it can be recorded, and then the analysis can consider the next event and repeat the sequence all over again. Once all events have been run over, the quality factors for each event are used as a weight for plotting inside histograms. If the quality factor is correctly calculated for each event, the method should be able to separate signal from background. More specifically, if a histogram of the K^+K^- invariant mass is plotted with Q_i as the weight for the i^{th} event, one should see a 'pure' ϕ peak with absolutely no background. In addition, if the K^+K^- invariant mass is plotted with $1 - Q_i$ as the weight for the i^{th} event, one should see all background and absolutely no ϕ peak. Therefore, the sum of the signal histogram plus the background histogram should be equal to the K^+K^- invariant mass with all events having a weight of 1.

Determining the Number of Nearest Neighbors. After the kinematic distances are calculated for all events with respect to the i^{th} event, they are sorted in order from smallest kinematic distance to largest kinematic distance. Only the the nearest neighbors, or the set of events with the smallest kinematic distance, will be used to determine the quality factor of a given event. For this analysis, there were a total of 16,981 events after selection cuts, and the number of nearest neighbors used was 500. This number was chosen somewhat arbitrarily; it is important to pick the smallest number possible such that the events used truly are those which share the most similar kinematic features to the event that is being considering. If the number was extremely large with respect to the total number of events, the analysis will not work properly. Events that are background will have some nearest neighbors that are signal, and vice versa. Furthermore, the number of nearest neighbors needs to be large enough such that a fit can converge with the filled histogram. If the number of nearest neighbors is too small, ROOT will fail to provide any signal or background information inside the histogram, and therefore calculation of a quality factor will be

impossible. Considering these two constraints and testing with different values, it was found that the smallest number which did not result in *any* fitting failures was 500.

Fitting the K^+K^- Invariant Mass. Upon determining the nearest neighbors of the i^{th} event, the next step is to plot and fit the set of K^+K^- and $\gamma\gamma$ invariant mass distributions. As mentioned above, it is extremely difficult to model the invariant mass distribution for the K^+K^- final state. Simply picking a signal distribution plus a polynomial background is not enough to properly parameterize the K^+K^- invariant mass near or around the ϕ peak. After attempting several different combinations of signal and background functions, it was found that the best way to accurately describe both the ϕ and the background near it is to use convoluted functions. A convolution is the operation between two functions which expresses how the shape of one function is modified by the other. The purpose for utilizing a convoluted function when attempting to fit an invariant mass histogram is to describe both the shape of the distribution as well as the inherent resolution of the data. Since both the ϕ peak and the background surrounding it contain similar resolutions, it is appropriate to fit the K^+K^- invariant mass distribution with the summation of a signal function plus a background function, both of which are then convoluted by a third function which manages the resolution.

The signal function chosen to describe the ϕ peak is a relativistic Breit-Wigner (Equation 5.3).

$$|Q_1(m)|^2 = A * |F_1(m) * \Delta_1(m)|^2 \tag{5.3}$$

Contained within this equation is a fit parameter, A, which simply scales the function in order to match the distribution. Also contained in this equation are two functions of mass, the Blatt-Weisskopf centrifugal-barrier factor for a spin 1 particle (Equation 5.4),

$$F_1(m) = \sqrt{\frac{2\sqrt{m^2/4 - m_K^2}}{\sqrt{m^2/4 - m_K^2} + p_R/c}} \tag{5.4}$$

and a standard Breit-Wigner (Equation 5.5) for a particle with spin 1.

$$\Delta_1(m) = \frac{m_o * \Gamma_o}{m_o^2 - m^2 - i m_o \Gamma_1(m)} \tag{5.5}$$

The Blatt-Weisskopf function plays an important role in the fit since it forces the signal function to be equal to zero when the K^+K^- mass is at threshold. It should be noted that $\sqrt{m^2/4 - m_K^2}$

appears throughout many of the equations mentioned. This smaller function represents the magnitude of the breakup momentum for either the K^+ or K^- daughter particle, given some parent mass m, in the rest frame of the parent particle. Additionally, the mass dependent width (Equation 5.6) also helps to describe the changing width of the ϕ due to the K^+K^- mass near threshold.

$$\Gamma_1(m) = \Gamma_o \frac{m_o}{m} \frac{\sqrt{m^2/4 - m_K^2}}{\sqrt{m_o^2/4 - m_K^2}} \frac{F_1^2(m)}{F_1^2(m_o)} \tag{5.6}$$

Finally, in many of the equations, m_K is the mass of a $K^{+/-}$, m_o is the ϕ mass value as determined by the fit, and Γ_o is the natural width of the ϕ. The value chosen for this parameter was taken from the PDG and is $\Gamma_o = 0.004266 \frac{GeV}{c^2}$.

Plotted along with the signal function is the background function which is simply a third degree polynomial, given by Equation (5.7).

$$b(m) = C_1 * (m - C_0)^3 + C_2 * (m - C_0)^2 + C_3 * (m - C_0) \tag{5.7}$$

The background equation has three free parameters and one fixed parameter. The free parameters are the coefficients in front of the powered terms of m; specifically C_1, C_2, and C_3. Since the background shape can drastically change due to the event and its nearest neighbors, these parameters are not given any restriction on their values (Table 5.1). The one fixed parameter is C_0 which is set to $0.987354 \frac{GeV}{c^2}$. This value is the smallest possible mass which can produce the K^+K^- final state, and is easily derived by simply performing the calculation $m_{K^+} + m_{K^-} = 2 * m_{K^\pm} = 0.987354 \frac{GeV}{c^2}$. The purpose of fixing this parameter is force the polynomial background to have a root at the K^+K^- threshold. While attempting different fit functions to describe the K^+K^- invariant mass, it was found that the polynomial function often exaggerated, or over fit the area near the K^+K^- threshold. This caused an effect which resulted in weighted histograms that took away good events near the low mass side of the ϕ peak. Forcing the background function to be equal to zero at the K^+K^- threshold fixed this issue.

To complete the fit of the K^+K^- invariant mass, the signal and background function are added together, then convoluted by a Gaussian in order to compensate for the kaon momentum resolution of the GlueX spectrometer. Although the signal and background functions mentioned above had to be programmed by hand, the convolution of these functions with a Gaussian could be fed into

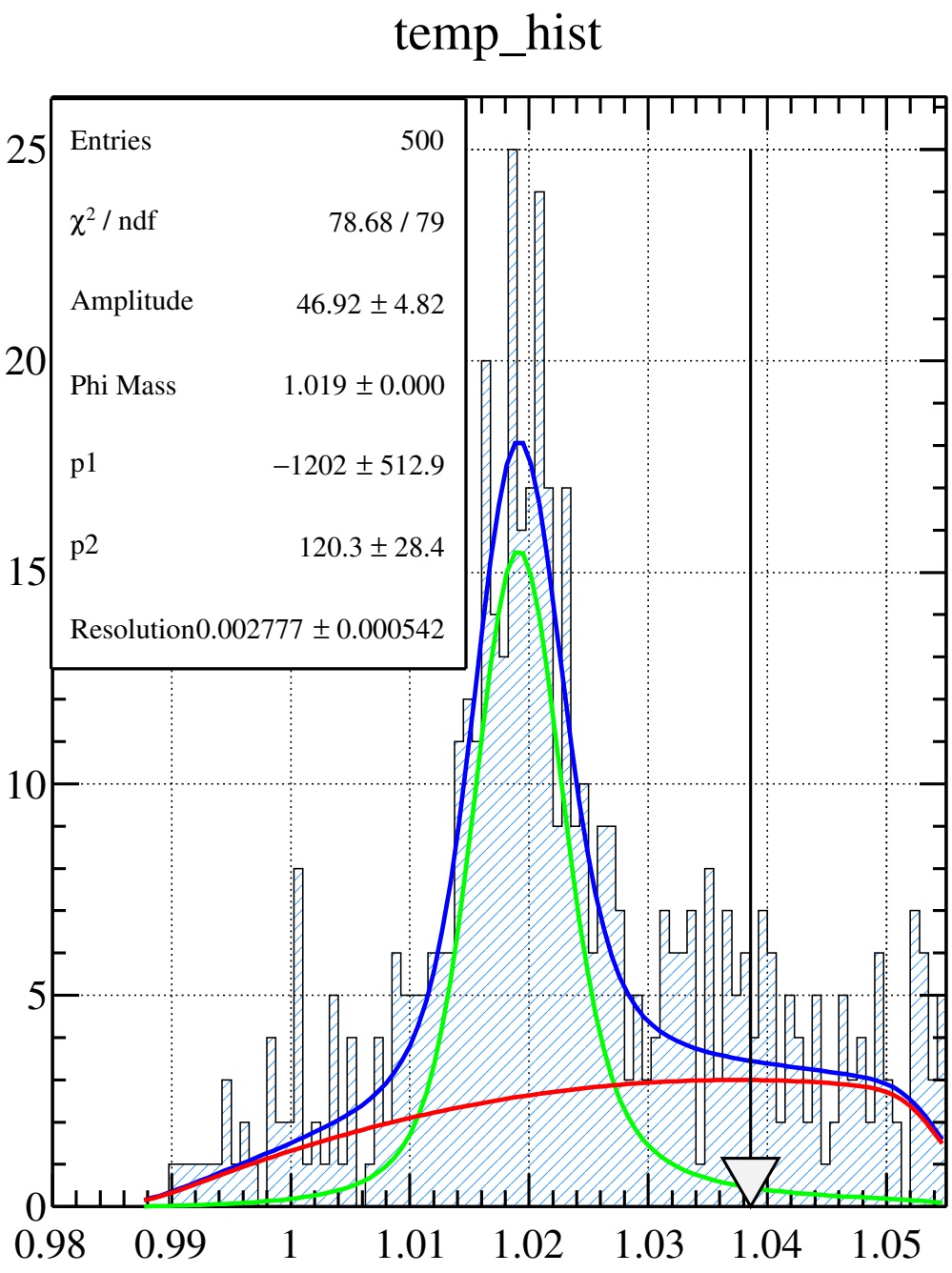

Figure 5.8: A fit which will result in an extremely low quality factor due to the very few signal events in comparison to background events at the location of the arrow, or invariant mass of the event being considered.

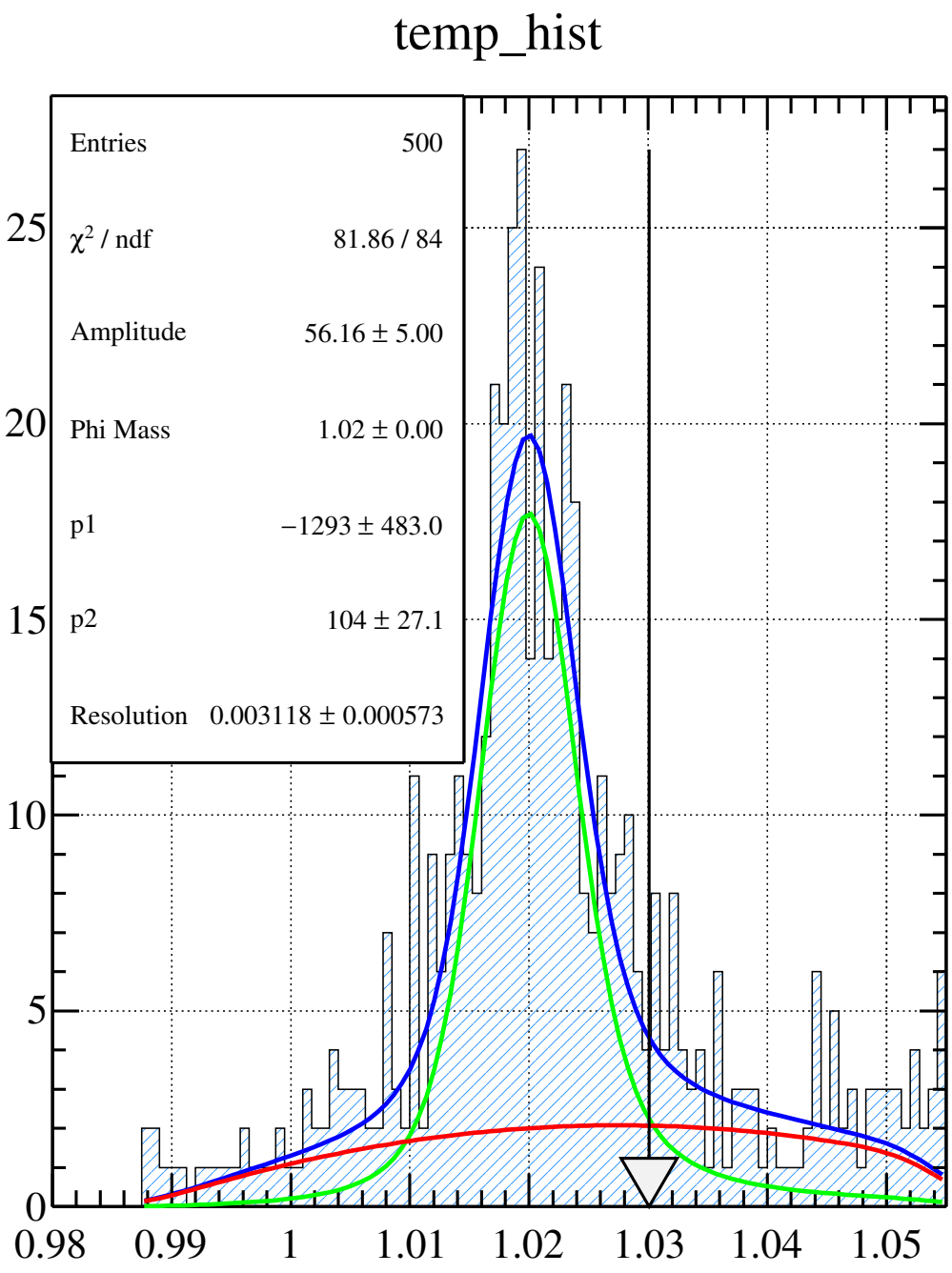

Figure 5.9: A fit which will result in a quality factor around 0.5, due to the fact that there are roughly the same signal and background events at the location of the arrow, or invariant mass of the event being considered.

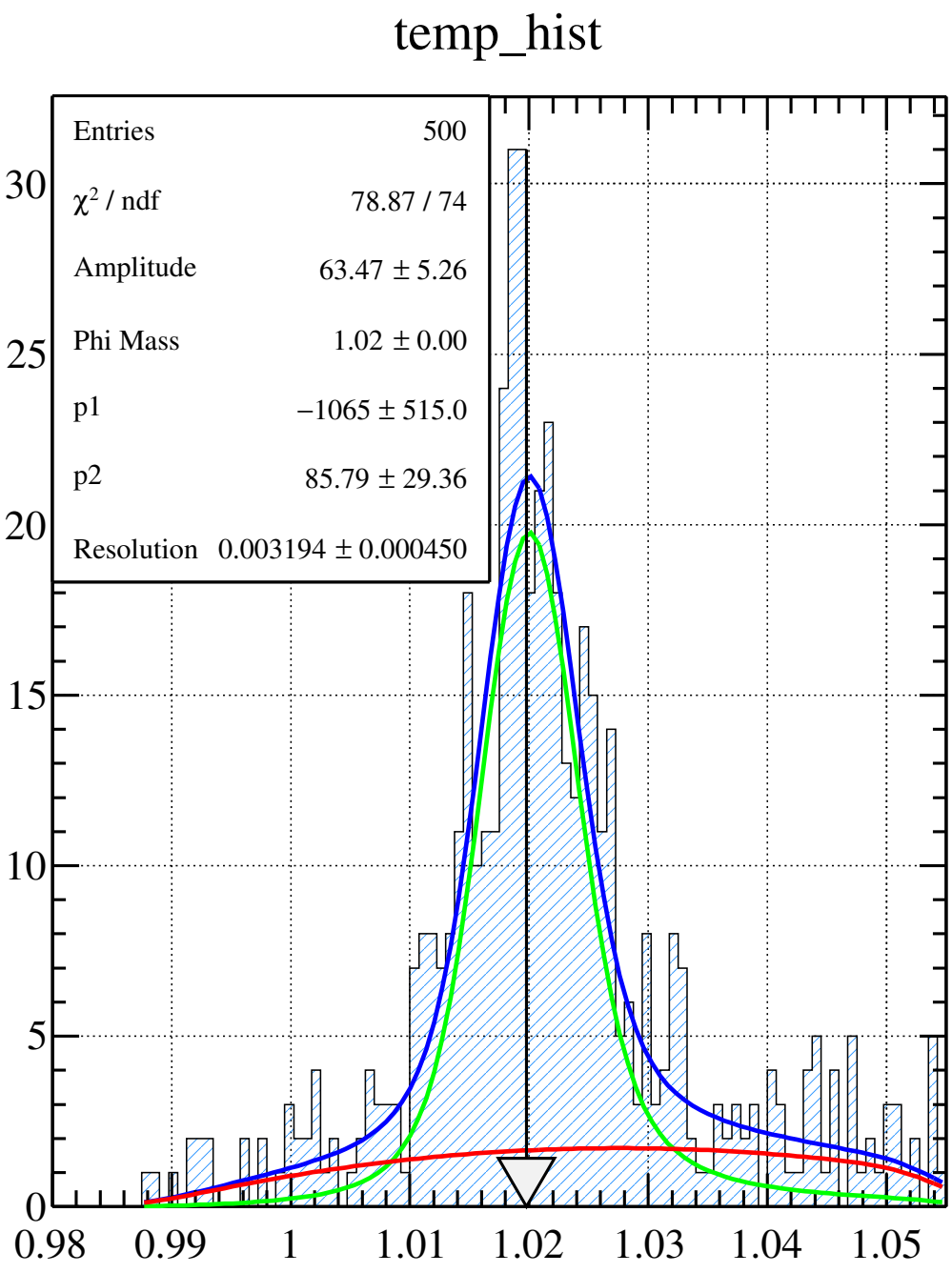

Figure 5.10: A fit which will result in a very high quality factor due to the large number signal events in comparison to background events at the location of the arrow, or invariant mass of the event being considered.

the ROOT library using the TF1Convolution object. More precisely, the total function used to describe the K^+K^- invariant mass for all events is given in Equation (5.8).

$$T(m) = \int \left[s(m') + b(m') \right] G(m - m') dm' \tag{5.8}$$

In the equation above, m' is simply a dummy variable for integration, and m represents the K^+K^- invariant mass. The function $s(m')$ is a relativistic Breit-Wigner (Equation 5.3), and the $b(m')$ is the polynomial background function referenced in Equation (5.7). Finally, $G(m - m')$ is the Gaussian function which is responsible for describing the resolution. This particular Gaussian function has one free parameter, and one fixed parameter. The free parameter is the width of the Gaussian, and the fixed parameter is the mean of the Gaussian which is simply set to zero. Because the Gaussian is being convoluted over the range of the fit, the value of the mean in this instance does not matter. Adding all things together, the total function listed in Equation (5.8) has one independent variable, two fixed parameters, and six free parameters, half of which are restricted (Table 5.1). Once a fit has converged, the parameters of the total function can be extracted and used to plot a signal function and a background function. This procedure is mathematically allowed due to the distributive property of convolutions; and therefore the final background and signal function can be written in Equation (5.9) and Equation (5.10), respectively.

$$B(m) = \int b(m') G(m - m') dm' \tag{5.9}$$

$$S(m) = \int s(m') G(m - m') dm' \tag{5.10}$$

Examples of different fits of the K^+K^- invariant mass distributions have been provided in Figures[5.8][5.9][5.10]. Each figure contains a blue line which represents the total fit of the data (Equation 5.8), a green line which represents the signal portion of the fit (Equation 5.10), and a red line which represents the background portion of the fit (Equation 5.9). Located within each plot is also a vertical arrow which is pointed in the downward direction. This arrow represents the invariant mass value of the event for which the quality factor is being calculated. Also contained within each figure is a legend with the values of the parameters for each fit.

Table 5.1: A table which summarizes the parameters and functions used to fit the K^+K^- invariant mass histograms.

K^+K^- invariant mass Functions:

Function	Parameters	Initial Values	Restricted Range
Relativistic B.W.	Amplitude	10	$0-100$
	m_ϕ	1.019	$1.01-1.03$
3^{rd} Degree Polynomial	C_0	0.987354	Fixed
	C_1, C_2, C_3	$-1200, 200, 200$	Free
Gaussian	μ	0	Fixed
	σ	0.005	$0-0.05$

Fitting the $\gamma\gamma$ Invariant Mass. On top of fitting the K^+K^- invariant mass, it is also necessary to fit the $\gamma\gamma$ invariant mass. Fitting this distribution is far more simple than what was needed to describe the K^+K^- invariant mass. The η resonance sits on top of a simple background, and is far enough away from the dominant π^0 peak that further inspection of the background is not necessary. In addition, since the η resonance is nowhere near the threshold for $\gamma\gamma$, performing any type of advanced fit to include breakup momentum and resolution effects is not necessary. Therefore, the $\gamma\gamma$ invariant mass spectra was fit by utilizing the summation of a signal function and a background function. The signal function is a Voigtian (Equation 5.12), which is technically a non relativistic Breit-Wigner (Equation 5.11) convoluted with a Gaussian. This convolution is necessary because the GlueX resolution of the η resonance is much greater than the natural width of the η meson, which is on the order of a keV. In the total signal function (Equation 5.12) there is one independent variable, and three fit parameters, and one fixed parameter. The independent variable is the $\gamma\gamma$ invariant mass, and the fixed parameter is the natural width of the η meson which is listed in the PDG as $\Gamma_o = 1.31keV$. The fit parameters of the function are the amplitude, A which simply scales the function to fit the statistics, the mass value of the η for the fit parameter μ, and the resolution of the η. The limits and starting values of all parameters are summarized in Table 5.2.

$$|\Delta(m)|^2 = \frac{\Gamma_o}{(m-\mu)^2 + \frac{\Gamma_o^2}{4}} \tag{5.11}$$

$$S(m) = A \int |\Delta(m')|^2 G(m-m')dm' \tag{5.12}$$

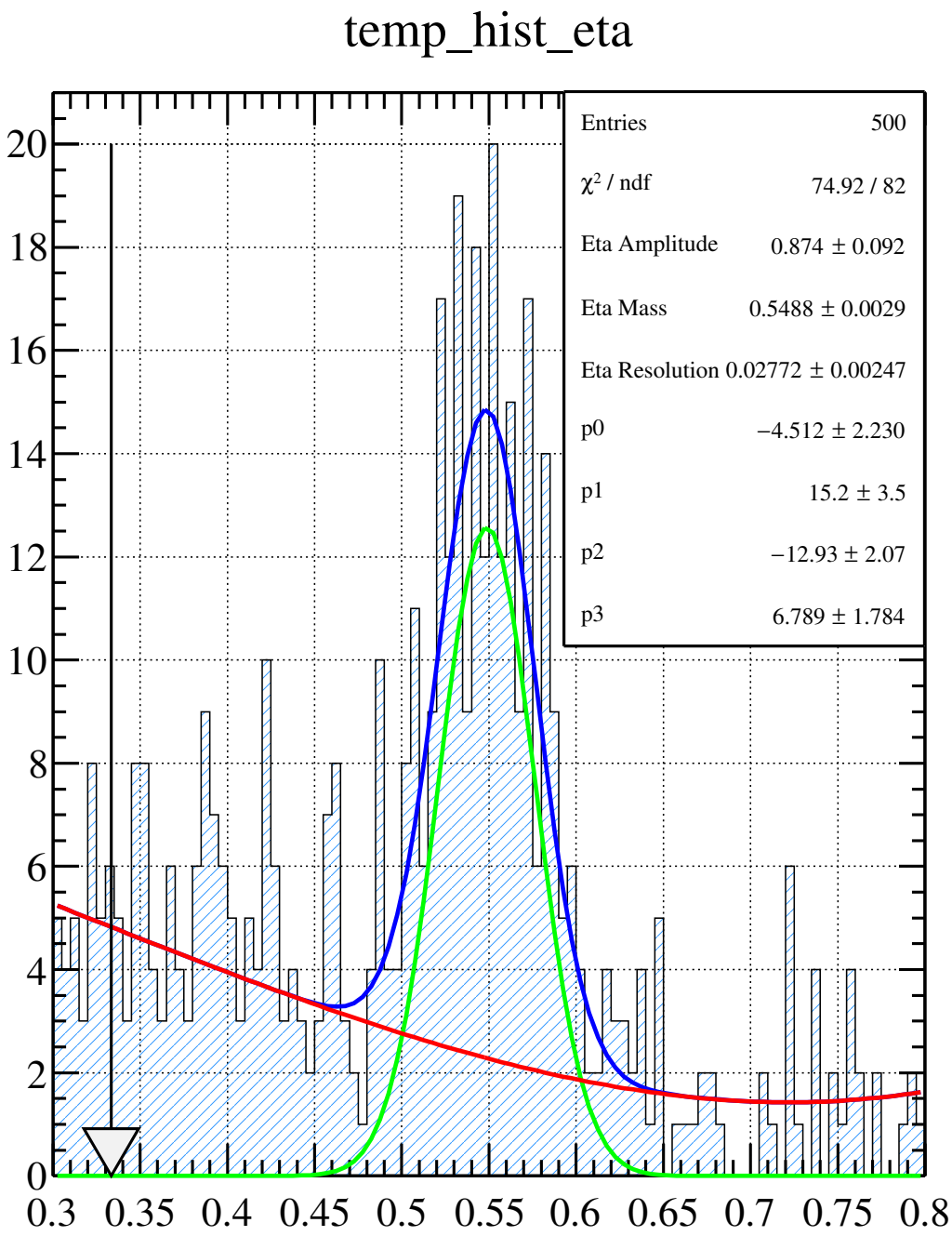

Figure 5.11: A fit which will result in an extremely low quality factor due to the very few signal events in comparison to background events at the location of the arrow, or invariant mass of the event being considered.

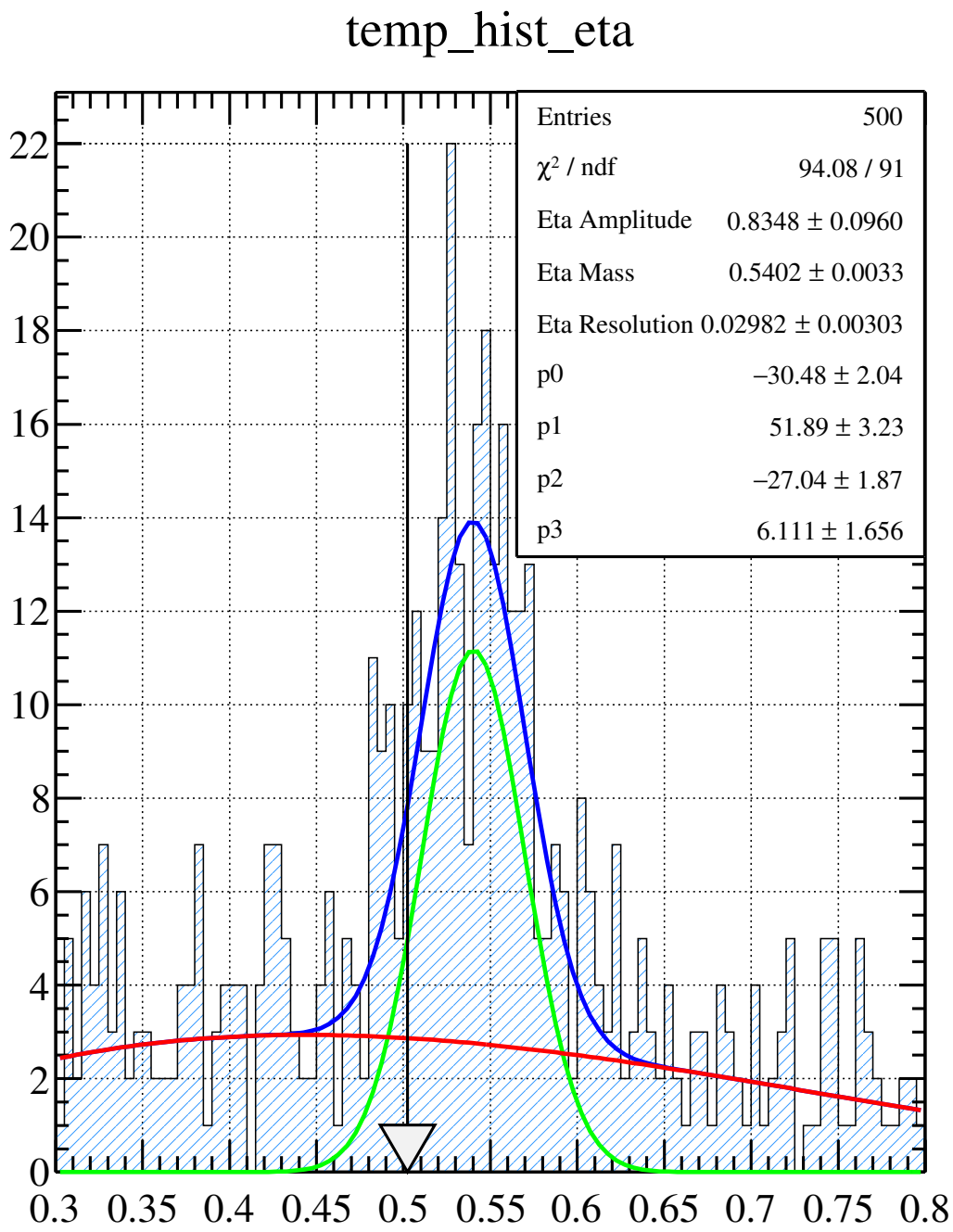

Figure 5.12: A fit which will result in a quality factor somewhat above 0.5, due to the fact that there are slightly more signal events as compared to background events at the location of the arrow, or invariant mass of the event being considered.

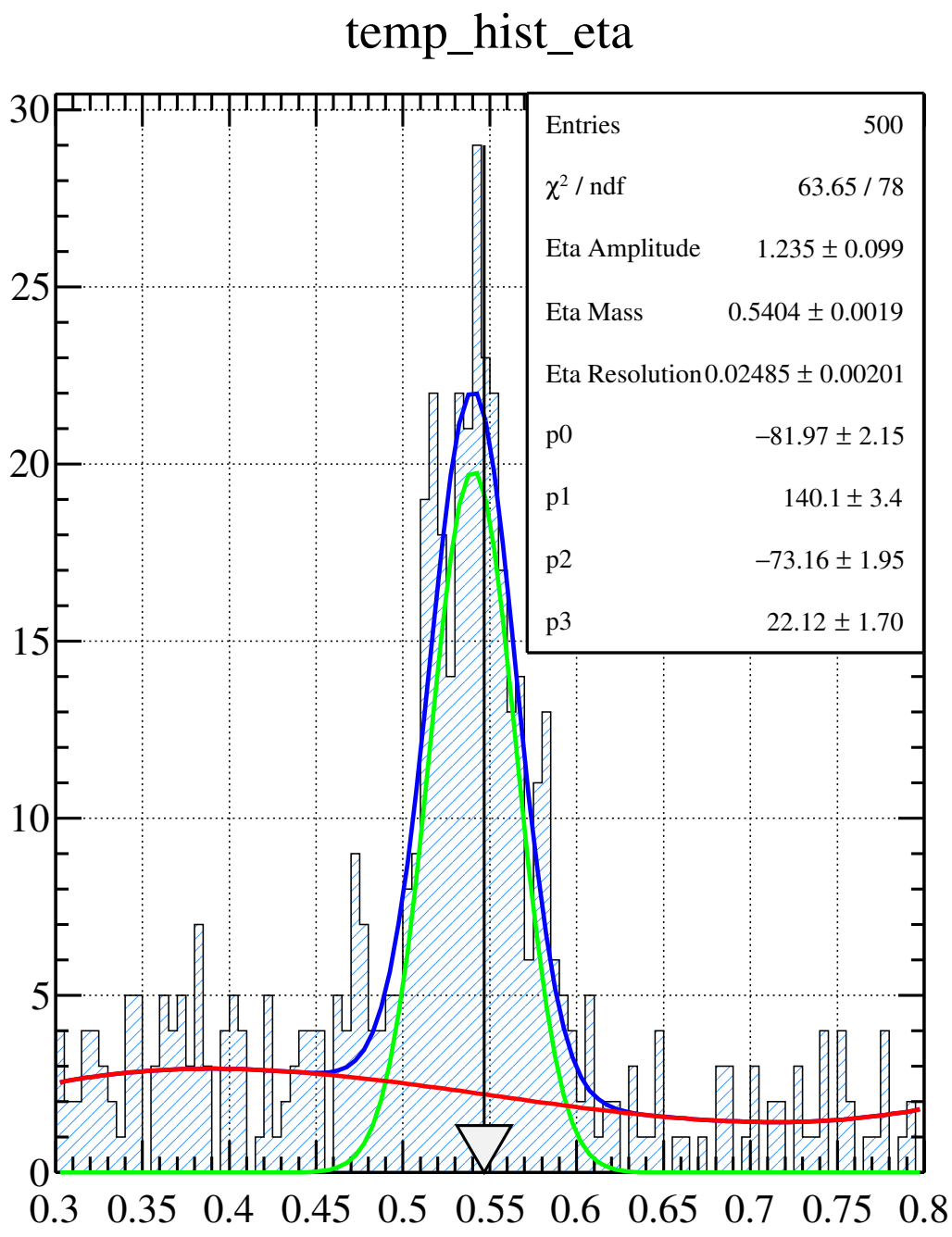

Figure 5.13: A fit which will result in a very high quality factor due to the large number signal events in comparison to background events at the location of the arrow, or invariant mass of the event being considered.

The background function that was chosen to describe the $\gamma\gamma$ background was a Chebyshev polynomial (Equation 5.13). It should be noted that the functional form of this third order polynomial is different than the one that was used to describe the K^+K^- because there is no threshold effect that has to be accounted for in the $\gamma\gamma$ invariant mass. This function has four free fit parameters with no restrictions on value due to the variability of background shapes in this analysis.

$$B(m) = C_3 * x^3 + C_2 * x^2 + C_1 * x + C_0 \tag{5.13}$$

Finally, the total function that was used to ultimately fit the $\gamma\gamma$ invariant mass distributions was the sum of Equation 5.12 and Equation 5.13. A summary of all parameters and functions used to fit the $\gamma\gamma$ invariant mass is given in Table 5.2.

Examples of different fits of the $\gamma\gamma$ invariant mass distributions have been provided in Figures[5.11][5.12][5.13]. Just like the examples given for the K^+K^- invariant mass fits, each figure contains a blue line which represents the total fit of the data. The total fit in this particular instance is simply the sum of a Voigtian and a third degree Chebyshev polynomial. The figures also contain a green line which represents the signal portion of the fit and a red line which represents the background portion of the fit. These are described by a Voigtian and third degree Chebyshev polynomial, respectively. Located within each plot is also a vertical arrow which is pointed in the downward direction. This arrow represents the invariant mass value of the event for which the quality factor is being calculated. Also contained within each figure is a legend with the values of the parameters for each fit.

Table 5.2: A table which summarizes the parameters and functions used to fit the $\gamma\gamma$ invariant mass histograms.

$\gamma\gamma$ invariant mass Functions:

Function	Parameters	Initial Values	Restricted Range
Voigtian	Amplitude	2	$0-5$
	m_η	0.547	$0.52-0.56$
	σ	0.02	$0.001-0.1$
	Γ	0.00000131	Fixed
3^{rd} Chebyshev Polynomial	C_0, C_1, C_2, C_3	None	Free

5.2.2 Three Quality Factor Methods

In order to thoroughly study the $\phi\eta$ final state, a total of three unique quality factor methods were attempted. Each of these analyses follow the standard quality factor prescription detailed in Subsection 5.2.1. Each analysis is unique because a different set of kinematic observables was used to find the set nearest neighbors for each event.

1. (ϕ Only) The first quality factor method considers the kinematic observables of the K^+K^- system, and therefore can only separate the ϕ signal from the K^+K^- background. The quality factor for this analysis will be denoted with Q_ϕ.

2. (η Only) The second quality factor method only considers the kinematics observables of the $\gamma\gamma$ system, and therefore only separates the η signal from the $\gamma\gamma$ background. The quality factor for this analysis will be denoted with Q_η.

3. ($\phi\eta$) The third and final quality factor analysis considers the kinematics observables for *both* the K^+K^- system and the $\gamma\gamma$ system. The quality factor for this analysis will be denoted with $Q_{\phi\eta}$.

The specific list of kinematic observables and how a quality factor was calculated for each analysis is detailed in Subsections 5.2.2, 5.2.2, and 5.2.2, respectively.

It should be noted that the ϕ Only analysis will use the same fit functions for the K^+K^- invariant mass distribution (Subsection 5.2.1), and it will not fit the $\gamma\gamma$ invariant mass distribution. The η Only analysis will use the same fit functions for the $\gamma\gamma$ invariant mass distribution (Subsection 5.2.1), and it will not fit the K^+K^- invariant mass distribution. Finally, the $\phi\eta$ analysis will use both the function for the K^+K^- invariant mass distribution (Subsection 5.2.1), and the function for the $\gamma\gamma$ invariant mass distribution (Subsection 5.2.1). Lastly, all three analyses only accept the 500 nearest neighbors (Subsection 5.2.1).

Calculating the Kinematic Distance Between Events. As mentioned in Subsection 5.2.2, there are a total of three unique quality factor analyses attempted in this thesis, and therefore there are three unique calculations to find the kinematic distance between events.

***ϕ* Only.** The list of kinematic observables used to identify the ϕ meson and to ultimately calculate Q_ϕ are given in Table 5.3.

Since this quality factor analysis is only attempting to separate the ϕ from K^+K^- background, there is no need to include any information about the η or its decay products, $\gamma\gamma$. Therefore,

Table 5.3: A table which summarizes the coordinates used to describe the $\gamma p \to pX$; $X \to \phi Y$ $\phi \to K^+K^-$; final state. This set of coordinates will ultimately lead to the calculation of Q_ϕ. The coordinates ξ_0 through ξ_5 are used in the kinematic distance equation, described by Equation (5.1). The last coordinate is the reference coordinate for this analysis.

ξ_k	Coordinate	Maximum Range of Coordinate
ξ_0	$K^+_{HE\cos(\theta)}$	2
ξ_1	$K^+_{HE\phi}$	2π radians
ξ_2	$GJ, \cos(\theta)$	2
ξ_3	GJ, ϕ	2π radians
ξ_4	E_{beam}	9 GeV
ξ_5	t	$3.3\frac{GeV^2}{c^4}$
ξ_r	K^+K^- invariant mass	Reference Coordinate

in order to properly identify the $\gamma p \to pX$; $X \to \phi Y$ $\phi \to K^+K^-$ final state, a total of six coordinates are needed. Two of the six coordinates come from the angular distributions of the daughter states of ϕ: $K^+_{HE\cos(\theta)}$, $K^+_{HE\phi}$; where the angles ϕ and θ are the polar coordinates in the helicity reference frame, or the rest frame of the ϕ. Two more of the eight total coordinates will come from the angular distributions of ϕ. Much like the kaons, these coordinates will be $GJ, \cos(\theta)$ and GJ, ϕ; where ϕ and $\cos(\theta)$ are polar angles in the Gottfried-Jackson frame; or the rest frame of the $K^+K^-\gamma\gamma$ parent state. The last two coordinates needed are the beam energy (E_{beam}), and the momentum transfer, t. Since t is the well known Mandelstam variable, t is related to the beam energy and the four momentum of the $\phi\eta$ parent state, such that $t^2 = (\gamma^\mu - X^\mu)^2$; where γ^μ is the energy-momentum four vector for the beam, and X^μ is the energy-momentum four vector for the $\phi\eta$ parent state. Since t, the beam energy E_{beam}, and the mass of the $K^+K^-\gamma\gamma$ parent state is known, the magnitude of the $K^+K^-\gamma\gamma$ parent state momentum is directly proportional to these measurements. Knowing the magnitude of the momentum and the mass of the $K^+K^-\gamma\gamma$ parent state allows us to fully describe the $\gamma p \to pX$; $X \to \phi Y$ $\phi \to K^+K^-$ reaction. The final detail that needs to be mentioned is the reference coordinate that is used in this quality factor analysis. Because it is imperative to have a pure ϕ signal, the reference coordinate for this procedure will be the K^+K^- invariant mass. Although this coordinate does not play a role in the calculation of the kinematic distance, it is imperative to define it as the reference coordinate which will ultimately serve as the tool to separate signal events from background events, and to calculate Q_ϕ.

***η* Only.** The list of kinematic observables used to identify the η meson and to ultimately calculate Q_η are given in Table 5.4.

Table 5.4: A table which summarizes the coordinates used to describe the $\gamma p \to pX$; $X \to \eta Y$; $\eta \to \gamma\gamma$ final state. This set of coordinates will ultimately lead to the calculation of Q_η The coordinates ξ_0 through ξ_5 are used in the kinematic distance equation, described by Equation (5.1). The last coordinate is the reference coordinate for this analysis.

ξ_k	Coordinate	Maximum Range of Coordinate
ξ_0	$\gamma_{HE\cos(\theta)}$	2
ξ_1	$\gamma_{HE\phi}$	2π radians
ξ_2	$GJ, \cos(\theta)$	2
ξ_3	GJ, ϕ	2π radians
ξ_4	E_{beam}	9 GeV
ξ_5	t	$3.3\frac{GeV^2}{c^4}$
ξ_r	$\gamma\gamma$ invariant mass	Reference Coordinate

This quality factor analysis is only attempting to separate the η from $\gamma\gamma$ background, there is no need to include any information about the ϕ or its decay products, K^+K^-. Therefore, in order to properly identify the $\gamma p \to pX$; $X \to \eta Y$; $\eta \to \gamma\gamma$ final state, a total of six coordinates are needed. Two of the six coordinates come from the angular distributions of the daughter states of η: $\gamma_{HE\cos(\theta)}$, $\gamma_{HE\phi}$; where the angles ϕ and θ are the polar coordinates in the helicity reference frame, or the rest frame of the η. Two more of the eight total coordinates will come from the angular distributions of η. Much like the photon, these coordinates will be $GJ, \cos(\theta)$ and GJ, ϕ; where ϕ and $\cos(\theta)$ are polar angles in the Gottfried-Jackson frame; or the rest frame of the $K^+K^-\gamma\gamma$ parent state. The last two coordinates needed are the beam energy (E_{beam}), and the momentum transfer, t. Since t is the well known Mandelstam variable, t is related to the beam energy and the four momentum of the $\phi\eta$ parent state, such that $t^2 = (\gamma^\mu - X^\mu)^2$; where γ^μ is the energy-momentum four vector for the beam, and X^μ is the energy-momentum four vector for the $\phi\eta$ parent state. Since t, the beam energy E_{beam}, and the mass of the $K^+K^-\gamma\gamma$ parent state is known, the magnitude of the $K^+K^-\gamma\gamma$ parent state momentum is directly proportional to these measurements. Knowing the magnitude of the momentum and the mass of the $K^+K^-\gamma\gamma$ parent state allows us to fully describe the $\gamma p \to pX$; $X \to \eta Y$; $\eta \to \gamma\gamma$ reaction. The final detail that needs to be mentioned is the reference coordinate that is used in this quality factor analysis. Because it is imperative to have

a pure η signal, the reference coordinate for this procedure will be the $\gamma\gamma$ invariant mass. Although this coordinate does not play a role in the calculation of the kinematic distance, it is imperative to define it as the reference coordinate which will ultimately serve as the tool to separate signal events from background events, and to calculate Q_η.

$\phi\eta$. The list of kinematic observables used to identify the ϕ meson and the η meson; and to ultimately calculate $Q_{\phi\eta}$ are given in Table 5.5.

Table 5.5: A table which summarizes the coordinates used to describe the $\gamma p \to pX$; $X \to \phi\eta$ $\phi \to K^+K^-$; $\eta \to \gamma\gamma$ final state. This set of coordinates will ultimately lead to the calculation of $Q_{\phi\eta}$ The coordinates ξ_0 through ξ_7 are used in the kinematic distance equation, described by Equation (5.1). The last two coordinates are the reference coordinates for this analysis.

ξ_k	Coordinate	Maximum Range of Coordinate
ξ_0	$K^+_{HE\cos(\theta)}$	2
ξ_1	$K^+_{HE\phi}$	2π radians
ξ_2	$\gamma_{HE\cos(\theta)}$	2
ξ_3	$\gamma_{HE\phi}$	2π radians
ξ_4	$GJ, \cos(\theta)$	2
ξ_5	GJ, ϕ	2π radians
ξ_6	E_{beam}	9 GeV
ξ_7	t	$3.3\frac{GeV^2}{c^4}$
ξ_r	K^+K^- invariant mass	Reference Coordinate
ξ_r	$\gamma\gamma$ invariant mass	Reference Coordinate

The final quality factor analysis is attempting to identify both the ϕ and η mesons and to also reject any background. It should be noted that the backgrounds for this analysis are different and include $\phi\gamma\gamma$, ηK^+K^-, and $K^+K{-}\gamma\gamma$. Therefore, in order to properly identify the $\gamma p \to pX$; $X \to \phi\eta$ $\phi \to K^+K^-$; $\eta \to \gamma\gamma$ final state, a total of eight coordinates are needed. Four of the eight coordinates come from the angular distributions of the daughter states of ϕ and η. More specifically, the four coordinates are $K^+_{HE\cos(\theta)}$, $K^+_{HE\phi}$, $\gamma_{HE\cos(\theta)}$, $\gamma_{HE\phi}$; where the angles ϕ and θ are the polar coordinates in the helicity reference frame. It should be noted that since the K^+ and γ particles are daughters of different parent states, they will have different helicity frames which are relative to the rest frames of ϕ and η mesons, respectively. Two more of the eight total coordinates will come from the angular distributions of ϕ and η. Much like the K^+ and γ particles, these coordinates will be $GJ, \cos(\theta)$ and GJ, ϕ; where ϕ and $\cos(\theta)$ are polar angles in the Gottfried-Jackson frame; or

the rest frame of the $\phi\eta$ parent state. The last two coordinates needed to describe the $\gamma p \to p\phi\eta$ final state is the beam energy (E_{beam}), and the momentum transfer, t. Since t is the well known Mandelstam variable, t is related to the beam energy and the four momentum of the $\phi\eta$ parent state, such that $t^2 = (\gamma^\mu - X^\mu)^2$; where γ^μ is the energy-momentum four vector for the beam, and X^μ is the energy-momentum four vector for the $\phi\eta$ parent state. Since t, the beam energy E_{beam}, and the mass of the $\phi\eta$ parent state is known, the magnitude of the $\phi\eta$ parent state momentum is directly proportional to these measurements. Knowing the magnitude of the momentum and the mass of the $\phi\eta$ parent state allows us to fully describe the $\gamma p \to p\phi\eta$ reaction. The final detail that needs to be mentioned is the reference coordinates that are used in this quality factor analysis. Because it is imperative to have a pure $\phi\eta$ signal, there will be two reference coordinates for this procedure. One of them will be the K^+K^- invariant mass, and the other will be the $\gamma\gamma$ invariant mass. Although these coordinates do not play a role in the calculation of the kinematic distance, it is imperative to define them as the reference coordinates which will ultimately serve as the tool to separate signal events from background events, and to calculate $Q_{\phi\eta}$.

Calculating the Quality Factor. Once the fits of the K^+K^- and $\gamma\gamma$ invariant mass histograms have converged, the final step of calculating a quality factor can be performed. This is done by knowing the signal and background functions, as well as their fitted parameters, for both the K^+K^- and $\gamma\gamma$ distributions. Knowing the parameters of the fit will allow the user to accurately estimate the number of signal events and the number of background events for a given invariant mass value. The invariant mass value that should be used is the one which corresponds to the event that is being studied, and the parameters are determined by the fit of the invariant mass distribution of nearest neighbors. More specifically, the quality factor associated with the K^+K^- invariant mass distribution will be Equation 5.14.

$$Q_\phi = \frac{S(m_{KK})}{S(m_{KK}) + B(m_{KK})} \tag{5.14}$$

In Equation (5.14), the function $S(m)$ is the convoluted relativistic Breit-Wigner described by Equation (5.10), and the function $B(m)$ is the convoluted third degree polynomial described by Equation (5.9). Lastly, the m_{KK} variable describes the K^+K^- mass of the event being considered. The quality factor associated with the $\gamma\gamma$ invariant mass distribution will be Equation 5.15.

$$Q_\eta = \frac{S(m_{\gamma\gamma})}{S(m_{\gamma\gamma}) + B(m_{\gamma\gamma})} \tag{5.15}$$

In Equation 5.15, the function $S(m)$ is a Voigtian function, which is the convolution of a non-relativistic Breit-Wigner with a Gaussian, described by Equation 5.12. The function $B(m)$ is the simply a third degree Chevyshev polynomial described by Equation 5.13. Lastly, the $m_{\gamma\gamma}$ variable describes the $\gamma\gamma$ invariant mass of the event being considered. The last quality factor which considers both the kinematics of the ϕ and the η is given in Equation (5.16).

$$Q_{\phi\eta} = \frac{S(m_{KK})}{S(m_{KK}) + B(m_{KK})} * \frac{S(m_{\gamma\gamma})}{S(m_{\gamma\gamma}) + B(m_{\gamma\gamma})} \tag{5.16}$$

In Equation (5.16), the signal and background functions for the K^+K^- and $\gamma\gamma$ invariant mass distributions are the same as those mentioned in Equation 5.14 and Equation 5.15, respectively.

The key difference between all three quality factor calculations comes from the fact that they are all using a different set of kinematic variables to determine a set of nearest neighbors. Therefore, the K^+K^- invariant mass distribution using the ϕ Only method will be different from the K^+K^- invariant mass distribution using the $\phi\eta$ method. Conversely, the $\gamma\gamma$ invariant mass distribution using the η Only method will be different from the $\gamma\gamma$ invariant mass distribution using the $\phi\eta$ method. This subtlety will result in different $\phi\eta$ invariant mass yields, depending on the quality factor method that is being considered.

Quality Factor Highlights. The effectiveness of the quality factor approach is highlighted in Figure 5.14 and Figure 5.15. Figure 5.14 shows what the K^+K^- invariant mass distribution looks like when plotting events with weights Q_ϕ and with weights $1 - Q_\phi$. One can clearly see that the quality factor effectively separated the signal ϕ meson from the K^+K^- background. Figure 5.15 shows what the $\gamma\gamma$ invariant mass distribution looks like when plotting events with weights Q_η and with weights $1 - Q_\eta$. One can clearly see that the quality factor effectively separated the signal η meson from the $\gamma\gamma$ background.

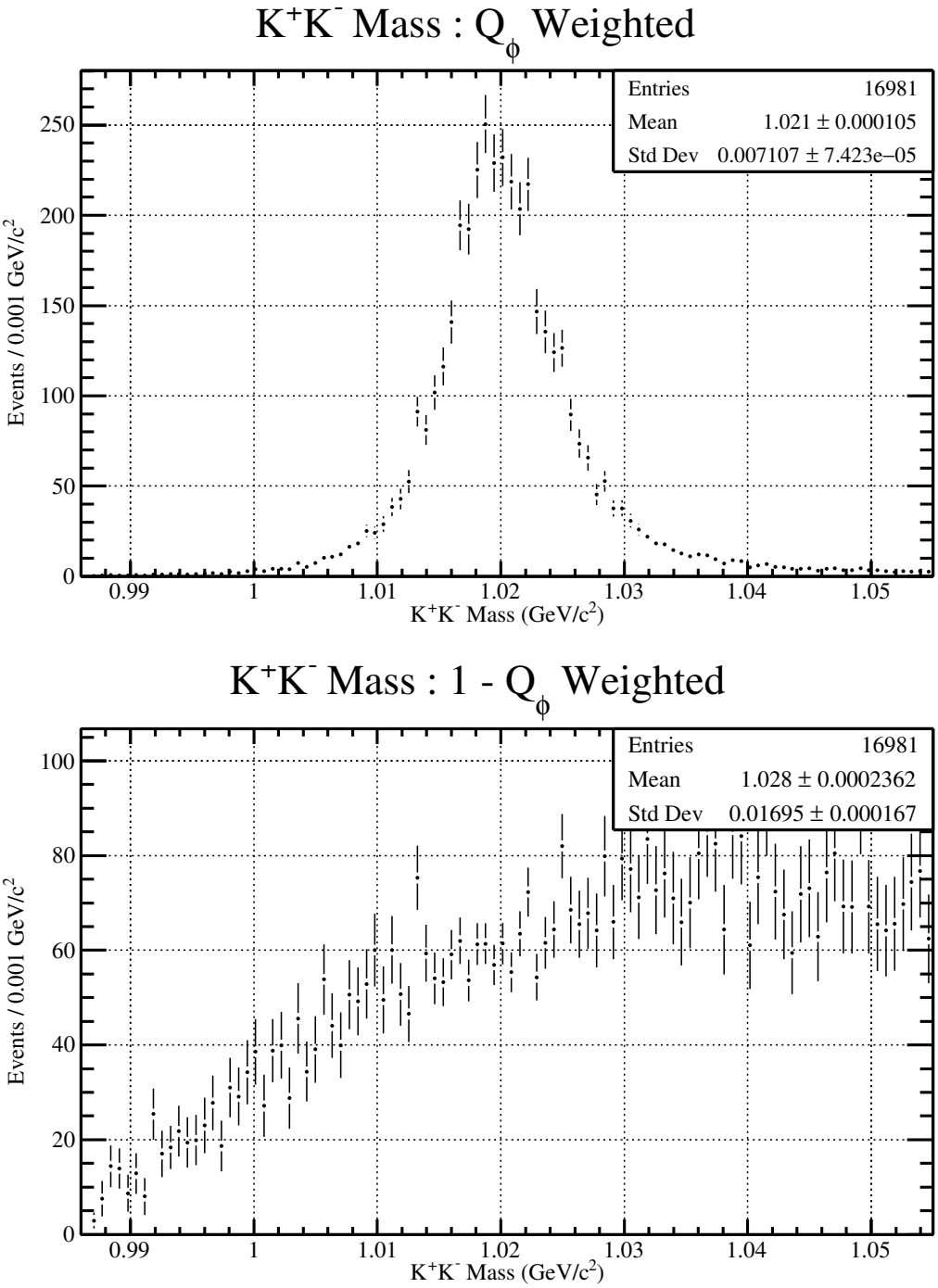

Figure 5.14: The K^+K^- invariant mass distribution plotted with the signal weight, Q_ϕ and the background weight $1 - Q_\phi$.

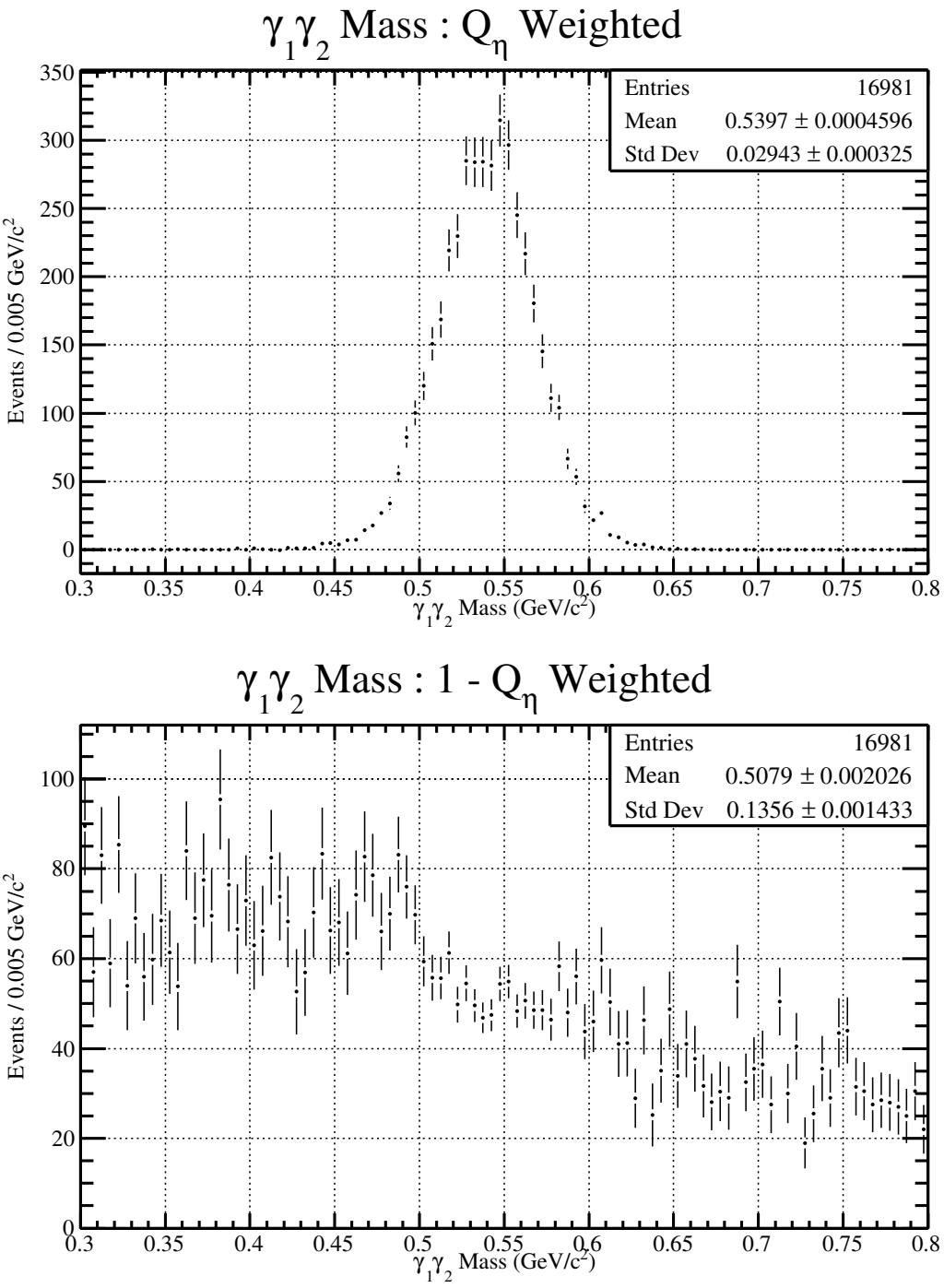

Figure 5.15: The $\gamma\gamma$ invariant mass distribution plotted with the signal weight, Q_η and the background weight $1 - Q_\eta$.

5.3 Removal of N* Background

After all particle identification cuts, selection cuts, and the determination of Quality Factors, an N* structure was found in the signal data *a posteriori* (Figure [5.16]). Also contained within the signal data were possible low mass structures in the $\phi\eta$ invariant mass (Figure [5.17]).

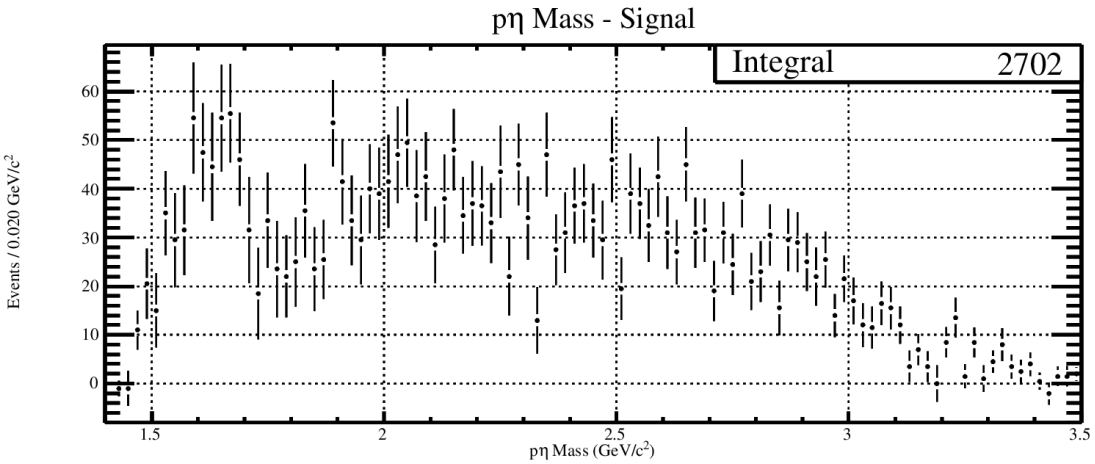

Figure 5.16: The $p\gamma\gamma$ invariant mass for the Elliptical Subtraction method (Subsec: 5.5.1). This distribution shows a possible N* structure around 1650 MeV/c^2.

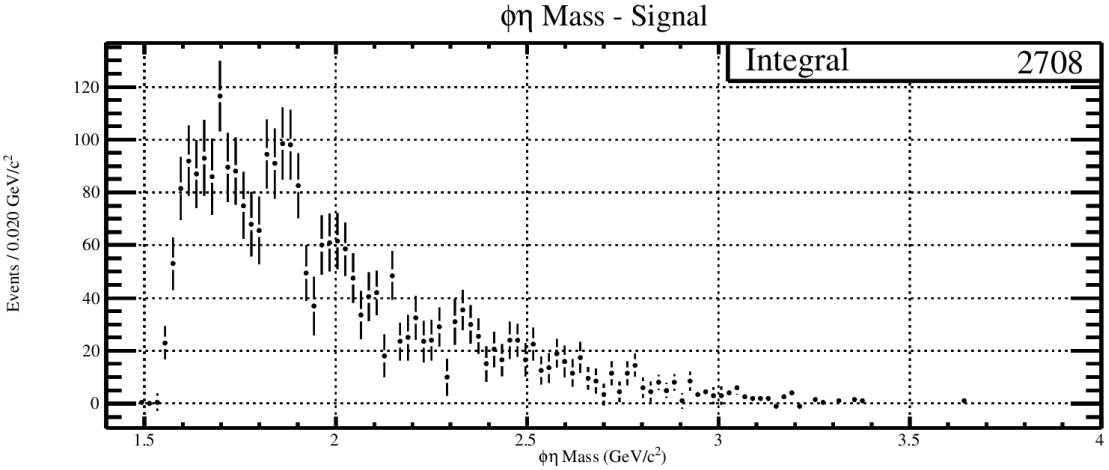

Figure 5.17: The $\phi\eta$ invariant mass for the Elliptical Subtraction method (Subsec: 5.5.1) before N* removal. This distribution shows two possible structures at lower mass.

The reason that an N* background can be seen in $\gamma p \to p\phi\eta$ data is due to the fact that an N*

can decay into a proton and η. More specifically, this background will have the reaction $\gamma p \to N^* \phi$; $N^* \to p\eta$. As you can see, this baryonic reaction has an identical final state to $\gamma p \to p\phi\eta$, but is a completely different reaction. What's worse is that this background can have a missing mass/energy that is near zero. Therefore, it is imperative to search of a method that will effectively separate this background from signal.

Many avenues were researched in order to remove the N* background; all but one were shown not to work properly. Some of the background subtraction methods that were attempted included a t cut, a beam energy cut, and a p$\gamma\gamma$ mass cut. All of these methods either did not effectively remove the N* background or removed too many signal events.

The one method which did remove the most N* background while also preserving the most signal statistics was cutting on the lab frame angle of the η meson. This cut was shown to effectively separate N* background from low mass $\phi\eta$ structures by generating three different sets of Monte Carlo data. It should be noted that these data sets are completely different from the one mentioned in Chapter 3.

1. $\gamma p \to pX(1680); X(1680) \to \phi\eta$
2. $\gamma p \to pX(1850); X(1850) \to \phi\eta$
3. $\gamma p \to N^*(1650)\phi; N^*(1650) \to p\eta$

Each of these Monte Carlo data sets were generated with a t-slope of 2.5. This slope was chosen because it closely matched the data at this stage. All three Monte Carlo data sets were also generated with a flat beam distribution. The purpose of this was to understand how certain cuts would effect the statistics at different beam energies; all of which would have roughly the same amount of statistics. An example of this is given in Figure [5.18] through Figure [5.20].

In all figures, the vertical axis is the angle the η meson and the horizontal axis is the beam energy. The angle θ is the polar coordinate in the lab frame which is the angle between the beam direction and the direction of the η. The first two figures ([5.18] and [5.19]) show similar behavior. In both Monte Carlo samples the direction of the η relative to beam direction is very shallow, and for the most part is always below 12° at higher beam energies. However, the last figure ([5.20]) shows completely different kinematic behavior. The N* Monte Carlo has very few events below

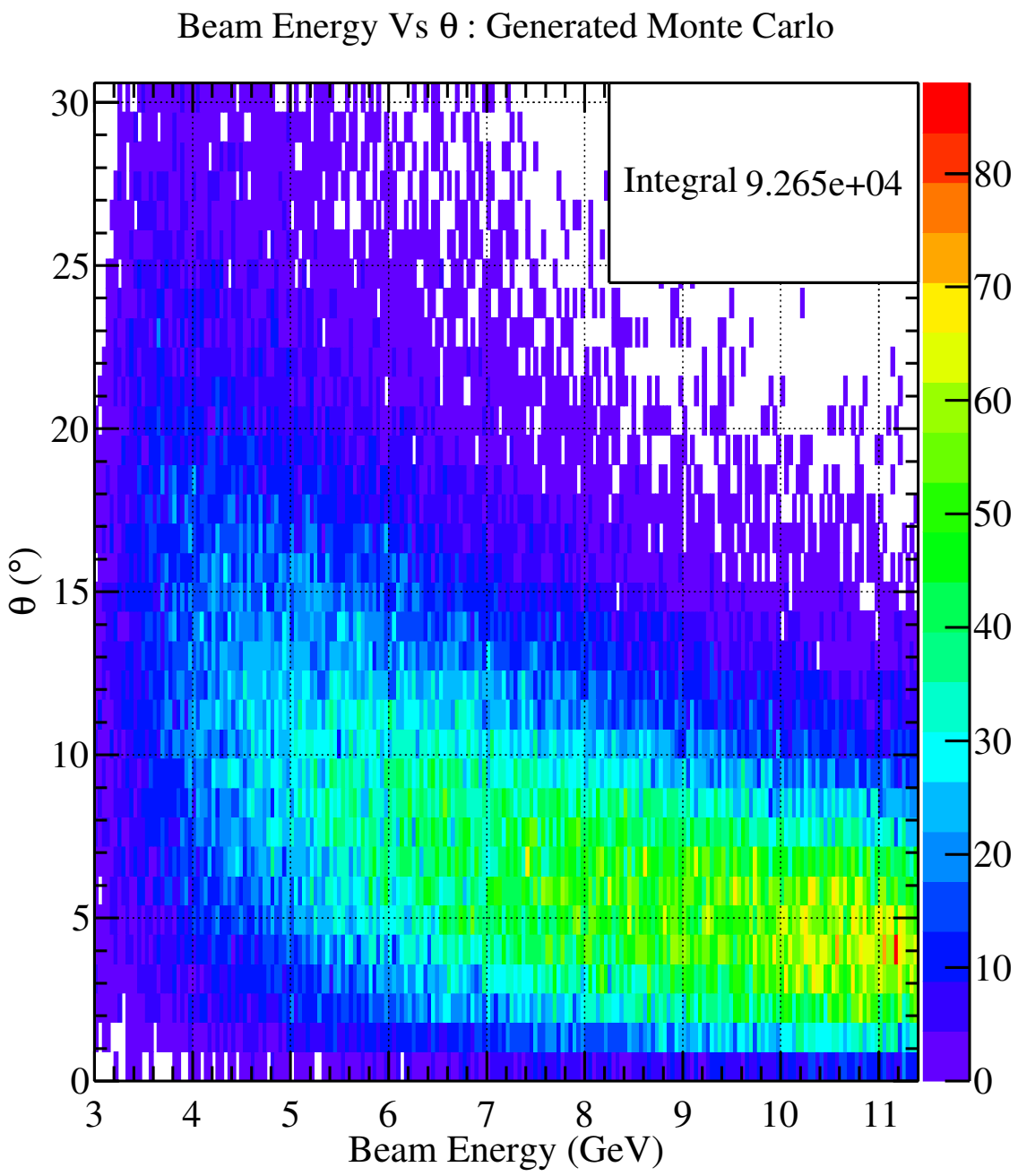

Figure 5.18: The angle of the η meson with respect to the beam direction in the lab frame versus the beam energy for $\gamma p \to pX(1680); X(1680) \to \phi\eta$ Monte Carlo sample.

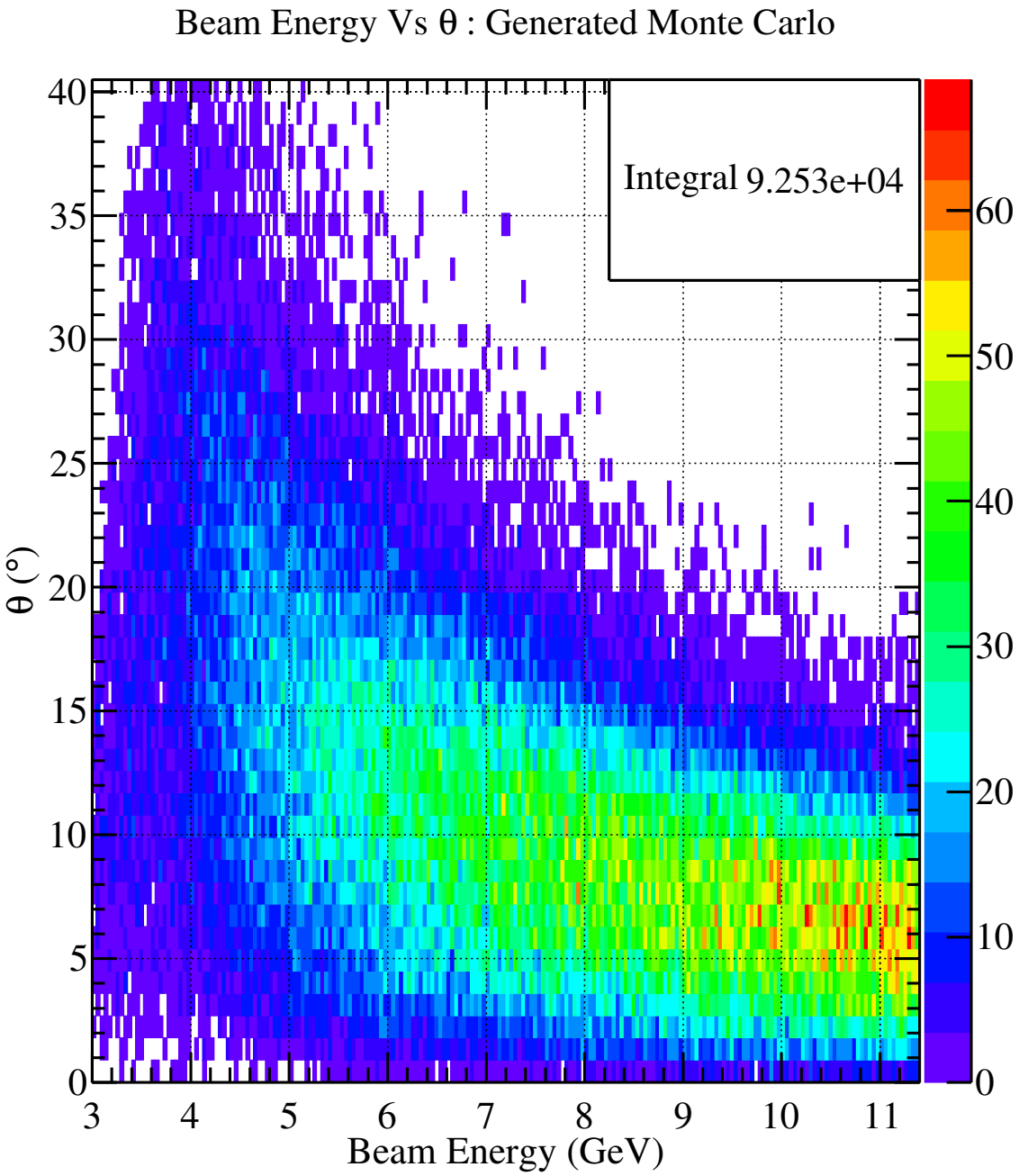

Figure 5.19: The angle of the η meson with respect to the beam direction in the lab frame versus the beam energy for $\gamma p \to pX(1850); X(1850) \to \phi\eta$ Monte Carlo sample.

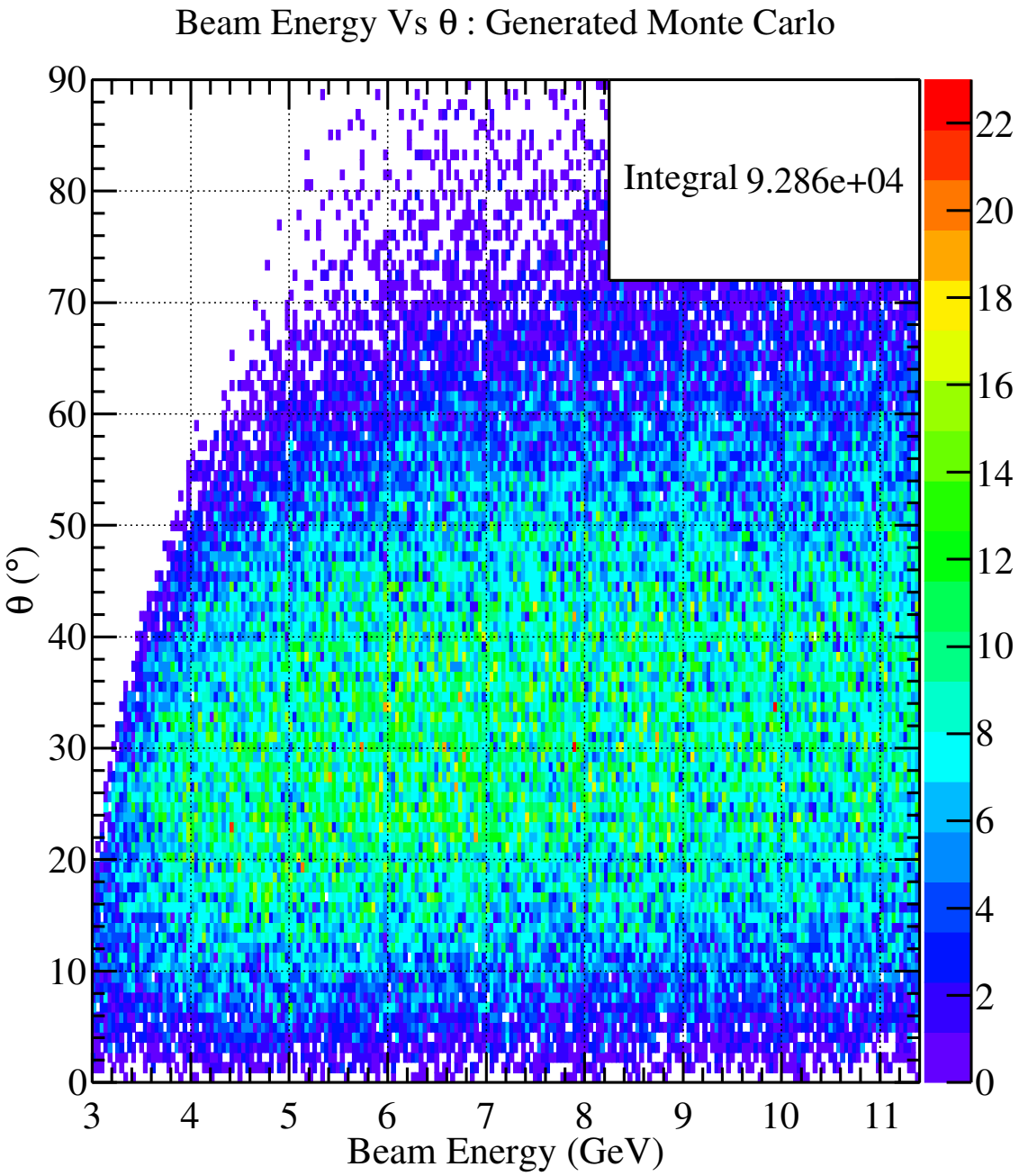

Figure 5.20: The angle of the η meson with respect to the beam direction in the lab frame versus the beam energy for $\gamma p \to N^*(1650)\phi; N^*(1650) \to p\eta$ Monte Carlo sample.

12°, and on average will decay the η at angles between 20° and 40°. Knowing this, a study of these Monte Carlo sets as a function of θ cut was performed.

Figure [5.21] provides the number of events as a function of different θ cut values for each Monte Carlo sample. This particular study looks at cut values in 1.5° increments, starting at 0° and going as high as 45°. The most important observation that this figure provides is that the number of signal events rises rapidly at lower θ cut values, whereas the N* background loses a large amount of statistics at lower θ cut values.To find the optimal θ cut value which contains the most signal events on top of background events, the same set of data is used and plotted in Figure [5.22]. The difference between Figure [5.21] and Figure [5.22] is that the N* statistics have been subtracted from all Monte Carlo data sets. This method of subtraction shows that the optimal θ cut is in the range of 15°-18°. Since the most signal statistics should be preserved, the higher cut value of 18° was chosen.

At a cut value of 18°, 10 percent of the signal Monte Carlo is lost and 82 percent of the background is removed. However, it should be mentioned again that all three Monte Carlo samples were generated with a flat beam spectrum. In order to approximate the data more accurately, the same samples were generated with a coherent beam spectrum. Since the coherent beam spectrum will force a higher density of events in the range of 8 GeV - 9 GeV, the amount of lost signal events will drop and the the amount of removed background will stay the same (Figure [5.18]-Figure [5.20]). After performing the same study with a coherent beam distribution for all Monte Carlo samples, a cut value of 18° was still optimal. At this cut, 6 percent of the signal Monte Carlo was lost and 82 percent of the background was removed.

After the completion of this Monte Carlo study, the cut of 18° θ was enforced on the data sample. The results of this cut and the effect that it has on the N* background can be seen in Figure [5.23]. The effect that it has on the $\phi\eta$ invariant mass can be seen in Figure [5.24]. Approximately 500 events were lost after the θ cut at 18°. However, the majority of these statistics were lost in the N* peak, while the apparent low mass structures in the $\phi\eta$ invariant mass remained the same.

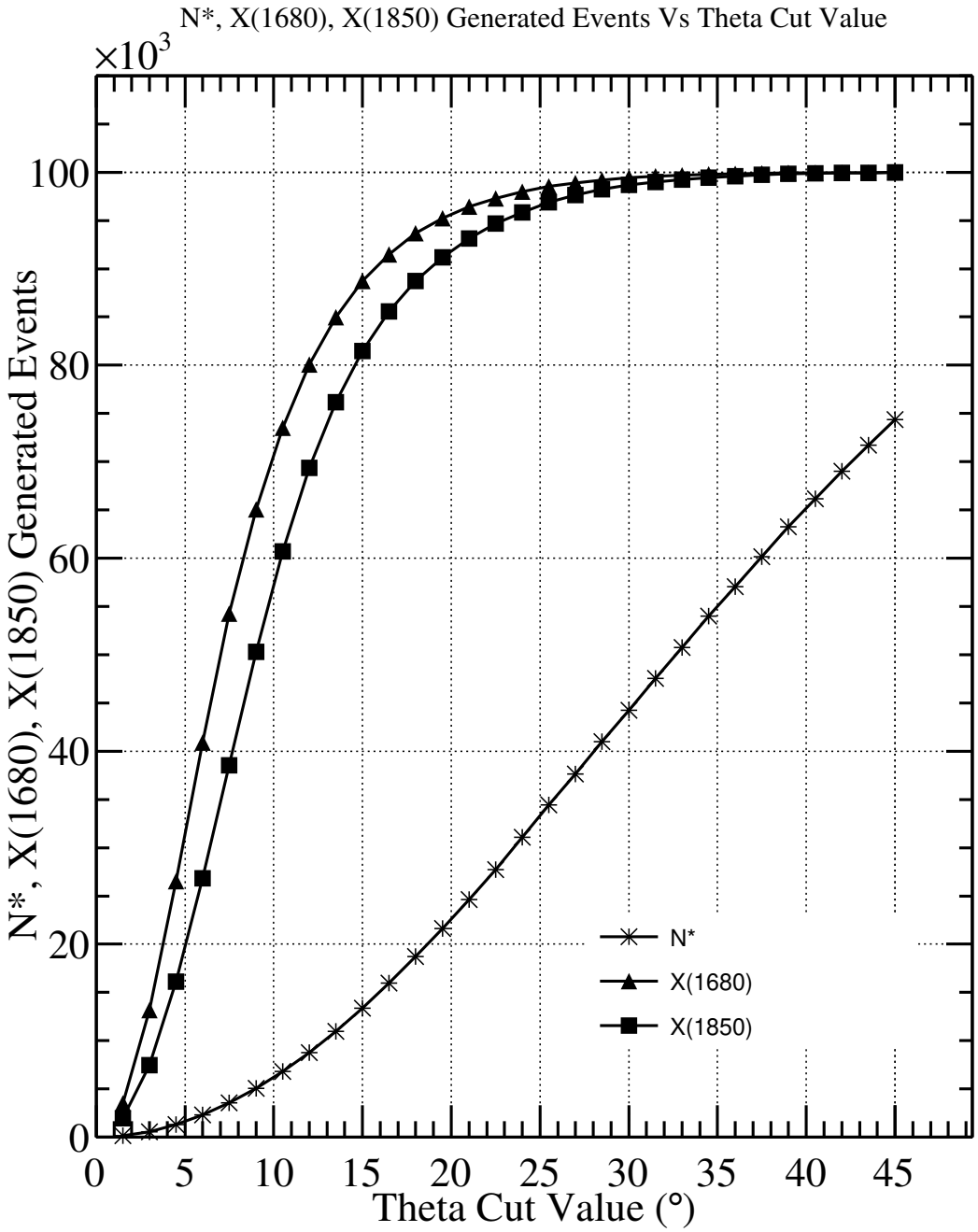

Figure 5.21: The number of N*, X(1680), and X(1850) events as a function of θ cut value.

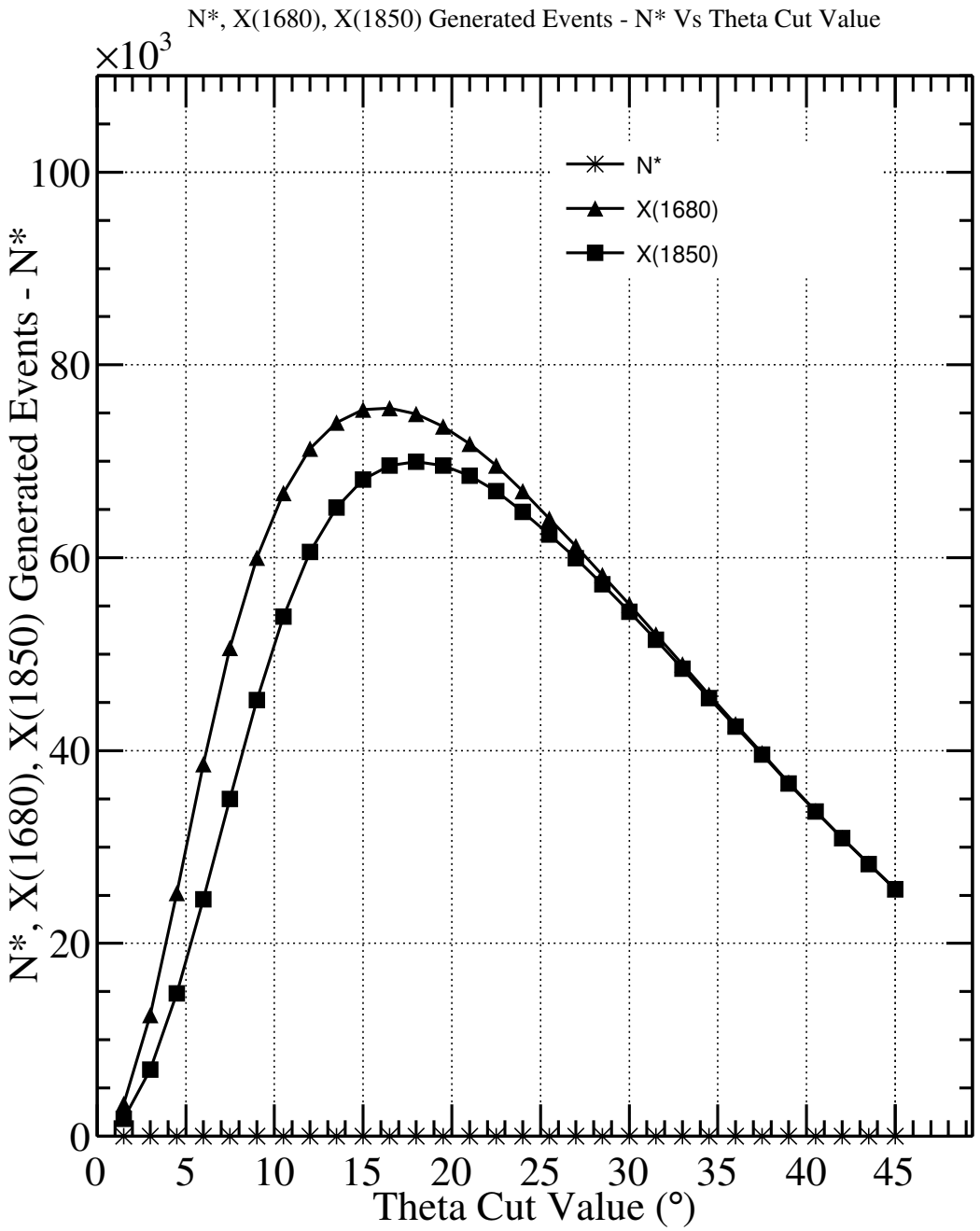

Figure 5.22: The number of N*, X(1680), and X(1850) events minus the number of N* events, as a function of θ cut value.

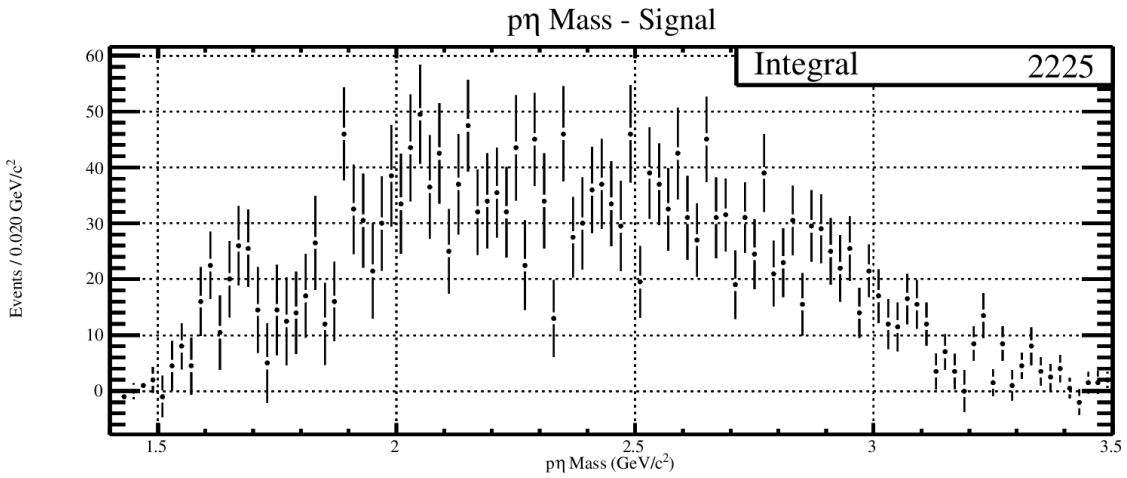

Figure 5.23: The $p\gamma\gamma$ invariant mass for the Elliptical Subtraction method (Subsec: 5.5.1) after a θ cut of 18°.

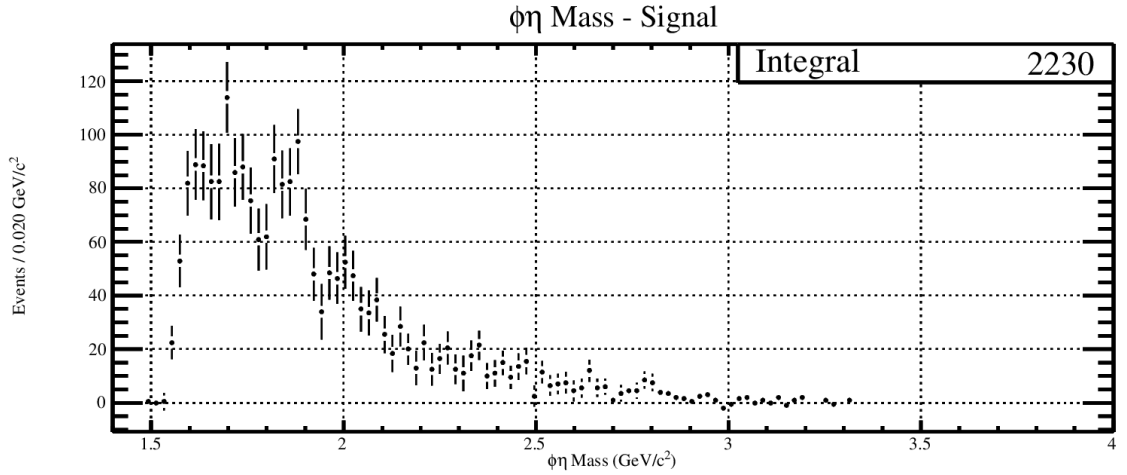

Figure 5.24: The $\phi\eta$ invariant mass for the Elliptical Subtraction method (Subsec: 5.5.1) after a θ cut of 18°.

5.4 Acceptance Corrections for $\phi\eta$ Invariant Mass and $cos(\theta)_{GJ}$

Before the final results of the $\phi\eta$ invariant mass and $cos(\theta)_{GJ}$ are shown, the acceptance corrections for each distribution are given. The acceptance corrections were found by using the generated Monte Carlo sample highlighted in Chapter 3.

This Monte Carlo sample was then simulated inside the detector using **hdgeant**, a software

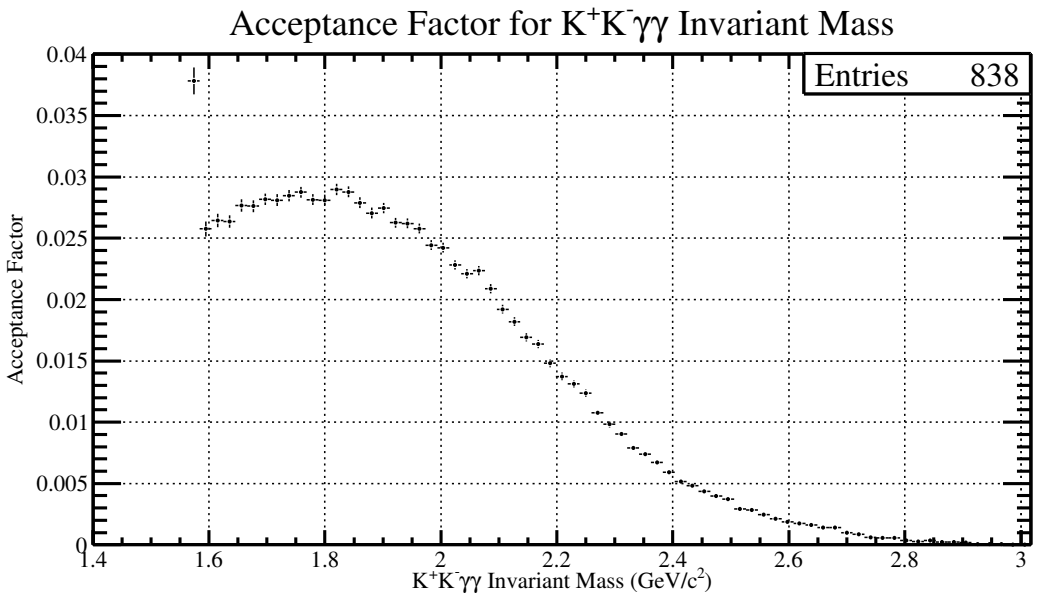

Figure 5.25: The $\phi\eta$ invariant mass acceptance factor.

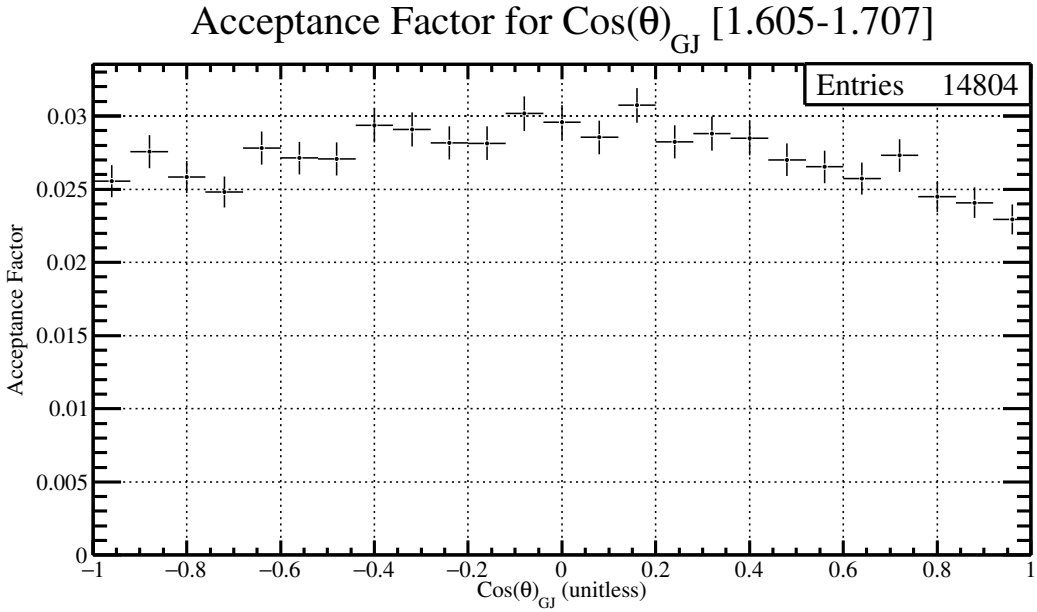

Figure 5.26: The $cos(\theta)_{GJ}$ acceptance factor for $\phi\eta$ invariant mass range between 1.605-1.707 GeV/c^2.

package inside the GlueX library which allows users to simulate what generated Monte Carlo will look like inside the detector. Once the simulation is complete, the simulated data will then be passed

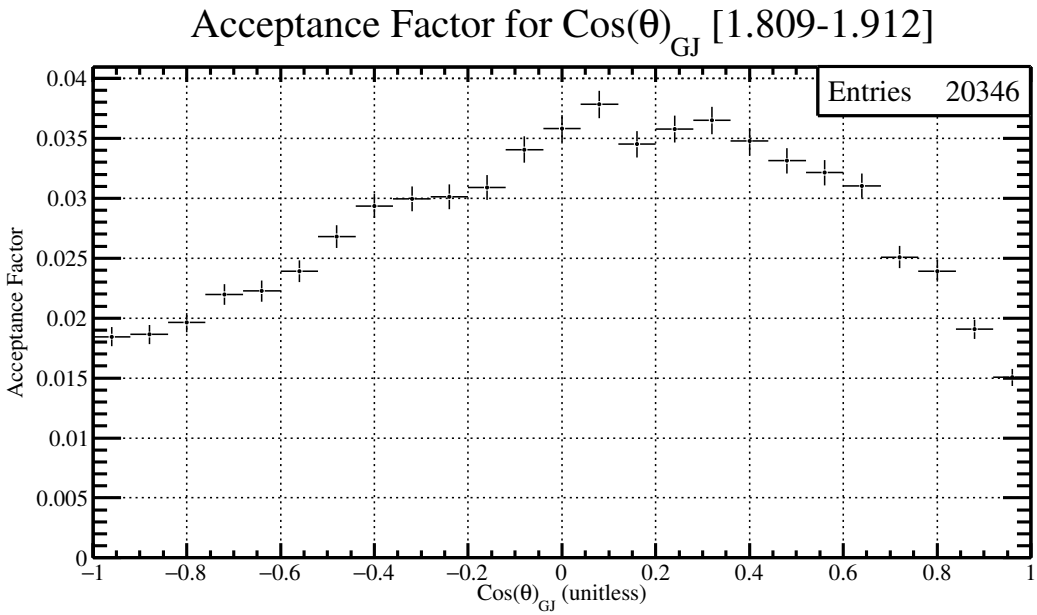

Figure 5.27: The $cos(\theta)_{GJ}$ acceptance factor for $\phi\eta$ invariant mass range between 1.809-1.912 GeV/c^2.

to **mcsmear**. Much like **hdgeant**, this is another software package inside the GlueX library which allows users to simulate the resolution of the GlueX detector after the simulation phase. After the Monte Carlo data has resolution effects added, it is then passed into the final stage, **hdroot**, which provides reconstruction to the Monte Carlo sample. After **hdroot** has completed reconstruction, a data file is reproduced which is identical to a real GlueX data file. Once this file is created, the same selection cuts that were used on the data will be enforced on the Monte Carlo sample. All Monte Carlo events that survive all phases of this simulation process are called the accepted Monte Carlo events. Finding the acceptance factors after this is very simple. To calculate the acceptance factors for a given observable, a histogram must be filled with the accepted Monte Carlo, then divided by another histogram which is filled with the generated Monte Carlo. The two observables that will be studied in this thesis are the $\phi\eta$ invariant mass and the $cos(\theta)_{GJ}$ distributions for different $\phi\eta$ invariant mass ranges. The acceptance factors for the $\phi\eta$ invariant mass are given in Figure [5.25]. There are two important results from this figure. The first observation is that there appears to be a large spike in the acceptance factor at very low $\phi\eta$ invariant mass. This is expected and is due to the $\phi\eta$ threshold being very close to this value. Since the generated Monte Carlo cannot create an invariant mass that is less than $m_\phi + m_\eta$, there are very few events in this region. However,

once the generated Monte Carlo is passed through the simulation, it is completely possible to have reconstructed events with a $\phi\eta$ invariant mass below threshold. Since the acceptance factor is defined as the number of accepted Monte Carlo divided by the number of generated Monte Carlo, the acceptance factor jumps in this region of the invariant mass. The second important observation to take away from this figure is that the acceptance factors in the region of interest is relatively smooth and well behaved. Since it appears that there may be structures from data (Figure [5.24]) in the $\phi\eta$ mass range from 1.6 to 2 GeV/c^2 it is important that the best acceptance in the Monte Carlo is also in the region.

5.5 Analysis of $\phi\eta$ Invariant Mass Plot and $cos(\theta)_{GJ}$ Distributions

After performing all cuts on the input data and establishing quality factors for three different nearest neighbor approaches, the $\phi\eta$ invariant mass can be studied. In order to study this distribution, a total of four different methods were used to identify a $\phi\eta$ final state. Each approach, along with supporting plots, are given in the subsections below.

5.5.1 Elliptical Mass Approach

There was no weighting method used for this approach. Every event has a relative weight of 1, with the exception of events which came from beam photons that were out of time. This analysis has three sets of histograms, one of them is signal plus background, another is just background and the third is the difference between the previous two, which can be interpreted at a signal distribution. An example of what the overall data set looks like is given in Figure [5.28], and an example of the signal and background selection is given in Figure [5.29].

The area which selects the $\phi\eta$ intersection can be defined using the equation for an ellipse (Equation 5.17), where the variable x will be substituted for the K^+K^- invariant mass, and the variable y will be substituted for the $\gamma\gamma$ invariant mass. Furthermore, the ellipse will need to be centered at the ϕ and η intersection. Therefore, the x variable will need to be shifted by m_ϕ, and the y variable will need to be shifted by m_η. Lastly, the semi-minor axis (a) and the semi-major axis (b) will need to be proportional to the width of the ϕ meson and the η meson, respectively. Since both resonances should have statistics which resemble that of a Gaussian distribution, a 2σ

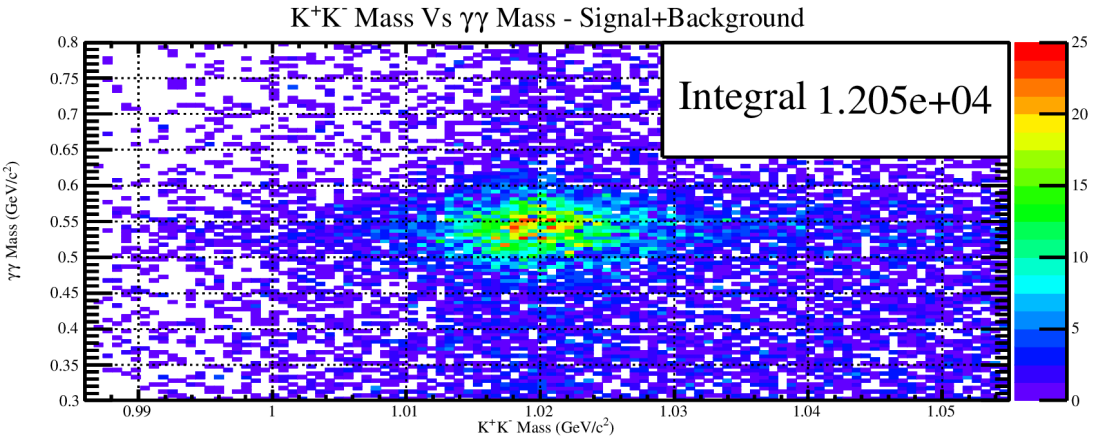

Figure 5.28: The K^+K^- invariant mass Vs $\gamma\gamma$ invariant mass before elliptical Mass selection.

width was chosen to select the signal region. This will ensure that roughly 95 percent of the signal events will be selected. Therefore, the equation which describes the $\phi\eta$ intersection in Figure [5.29] can be written as Equation 5.18.

$$1 = \frac{x^2}{a^2} + \frac{y^2}{b^2} \tag{5.17}$$

$$1 = \frac{(m_{KK} - m_\phi)^2}{(2\sigma_\phi)^2} + \frac{(m_{\gamma\gamma} - m_\eta)^2}{(2\sigma_\eta)^2} \tag{5.18}$$

The elliptical subtraction method requires that the same amount of K^+K^- vs $\gamma\gamma$ area is used to select signal and background regions. The area for an ellipse is well known, and is given in Equation 5.19. We can take the semi-major and semi-minor axis parameters from Equation 5.18 and plug it into Equation 5.19 in order to derive the total K^+K^- vs $\gamma\gamma$ signal area (Equation 5.20).

$$A = \pi ab \tag{5.19}$$

$$A_{\phi\eta} = \pi(2\sigma_\phi)(2\sigma_\eta) = 4\pi\sigma_\phi\sigma_\eta \tag{5.20}$$

Knowing that the total signal area is equal to $4\pi\sigma_\phi\sigma_\eta$, it is easy to define the background area. The first parameter that needs to be chosen is the inner radius of the background selection. Once again, it is assumed that both resonances resemble a Gaussian distribution. Therefore, an inner

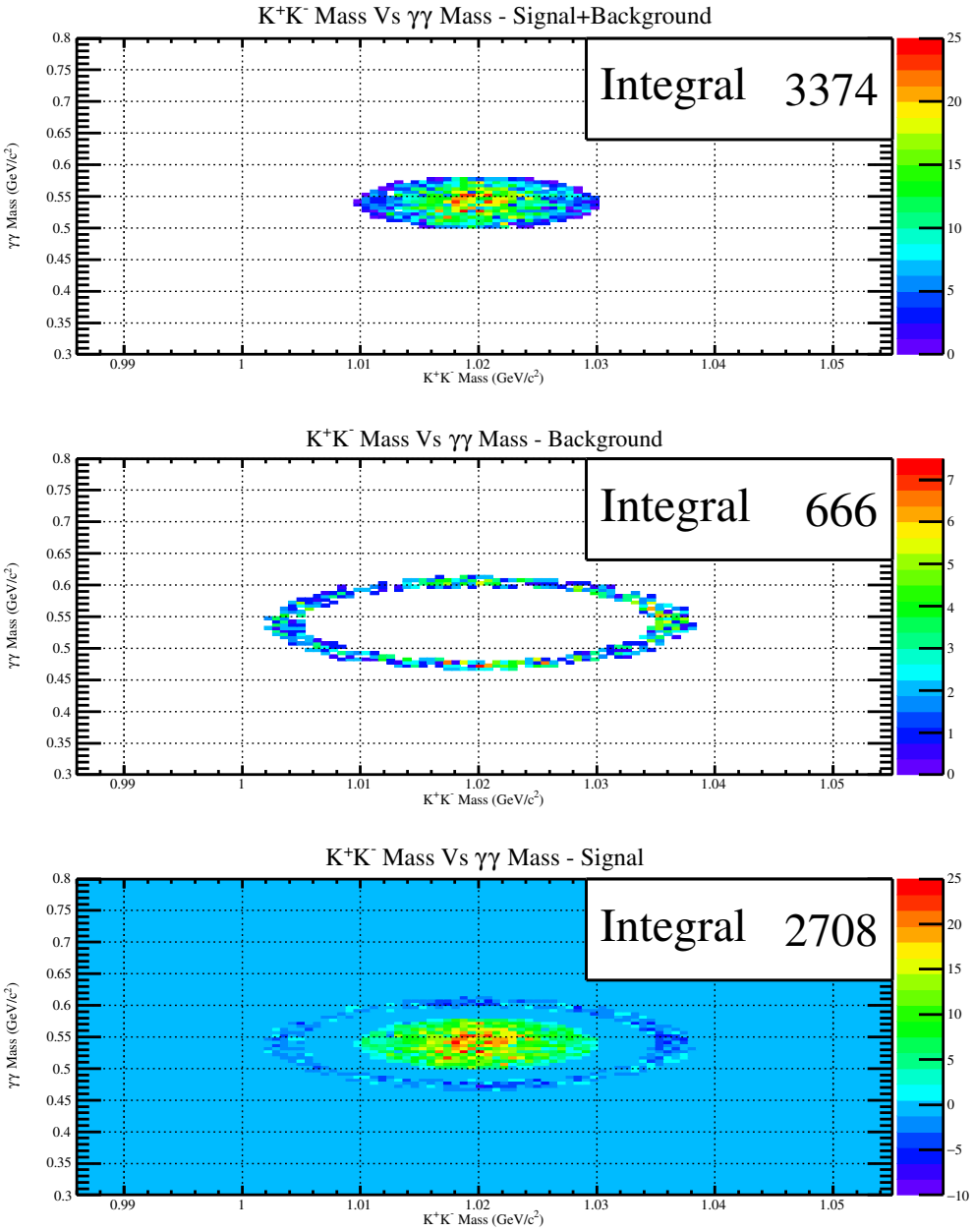

Figure 5.29: The K^+K^- invariant mass Vs $\gamma\gamma$ invariant mass showing the elliptical mass selection method. The upper most histogram shows the ellipse which selects the $\phi\eta$ intersection region, described by Equation 5.18. The middle histogram shows the ring which selects the background and is described by Equation 5.21. The bottom most histogram shows the difference between the upper and middle histograms.

radius of 3σ was chosen so that less that 1 percent of signal events would be selected, and therefore the majority of events would be background. Knowing that the inner radius will be 3σ, it is easy to derive the outer radius of the background selection. Once again, the total area of the background must be equal to the signal selection area of $4\pi\sigma_\phi\sigma_\eta$. Therefore, the outer radius of the background selection will be $\sqrt{13}\sigma$. The derivation of this area is given in Equation 5.21, and the selection is shown in the second histogram of Figure [5.29].

$$A_{BG} = \pi(\sqrt{13}\sigma_\phi)(\sqrt{13}\sigma_\eta) - \pi(3\sigma_\phi)(3\sigma_\eta) = 4\pi\sigma_\phi\sigma_\eta \tag{5.21}$$

Now that the signal and background selections have been well defined for this method, the relevant invariant mass and angular distributions can be shown. Figure [5.30] shows the $\phi\eta$ invariant mass distributions corresponding to different elliptical mass selections. The upper histogram of Figure [5.30] shows an immediate indication of two structures at lower $\phi\eta$ invariant mass. This distribution is compared to the second histogram in Figure [5.30] which is not a $\phi\eta$ selection. The histogram may show a possible structure at low invariant mass which causes the signal distribution to become slightly distorted. It should be noted that this structure is seen in other background invariant mass plots and may be an indication of a decay mode to ηKK.

The two structures seen in Figure [5.30] can be investigated by studying the angular distribution of the daughter particles in the Gottfried-Jackson frame. This distribution is important since its structure can provide an indication of what the parents spin state is. These distributions are produced by selecting $\phi\eta$ invariant mass ranges which correlate to the positions of the two structures, but do not overlap with each other. The range that was selected for the first structure is between (1.605-1.707) GeV/c^2, and the range that was selected for the seconds structure is between (1.809-1.912) GeV/c^2. The $cos(\theta)$ distribution for the first structure is given in Figure [5.31], and the $cos(\theta)$ distribution for the second structure is given in Figure [5.32]. The $cos(\theta)$ distribution for each structure does not currently provide information which may help to identify the spin state. However, it is clear that the $cos(\theta)$ distribution is different for each structure.

Using only the signal plots from Figure [5.30], [5.31], and [5.32], the acceptance corrections provided in Subsection 5.4 can be used to understand the amount of statistics that were lost due to detector acceptance. The acceptance corrected figures are provided in [5.33][5.34][5.35] below.

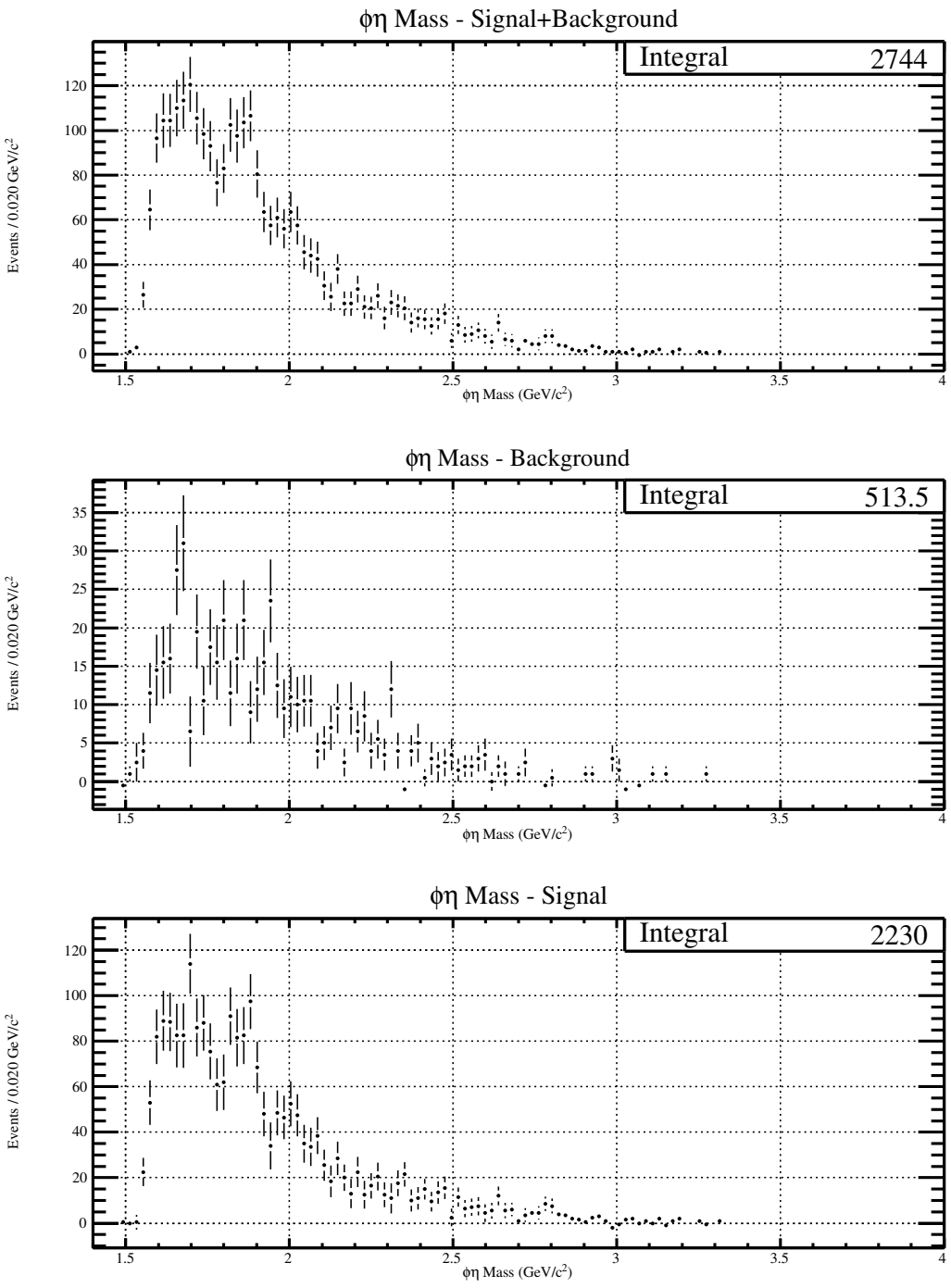

Figure 5.30: The $\phi\eta$ invariant mass for elliptical mass selection, not acceptance corrected.

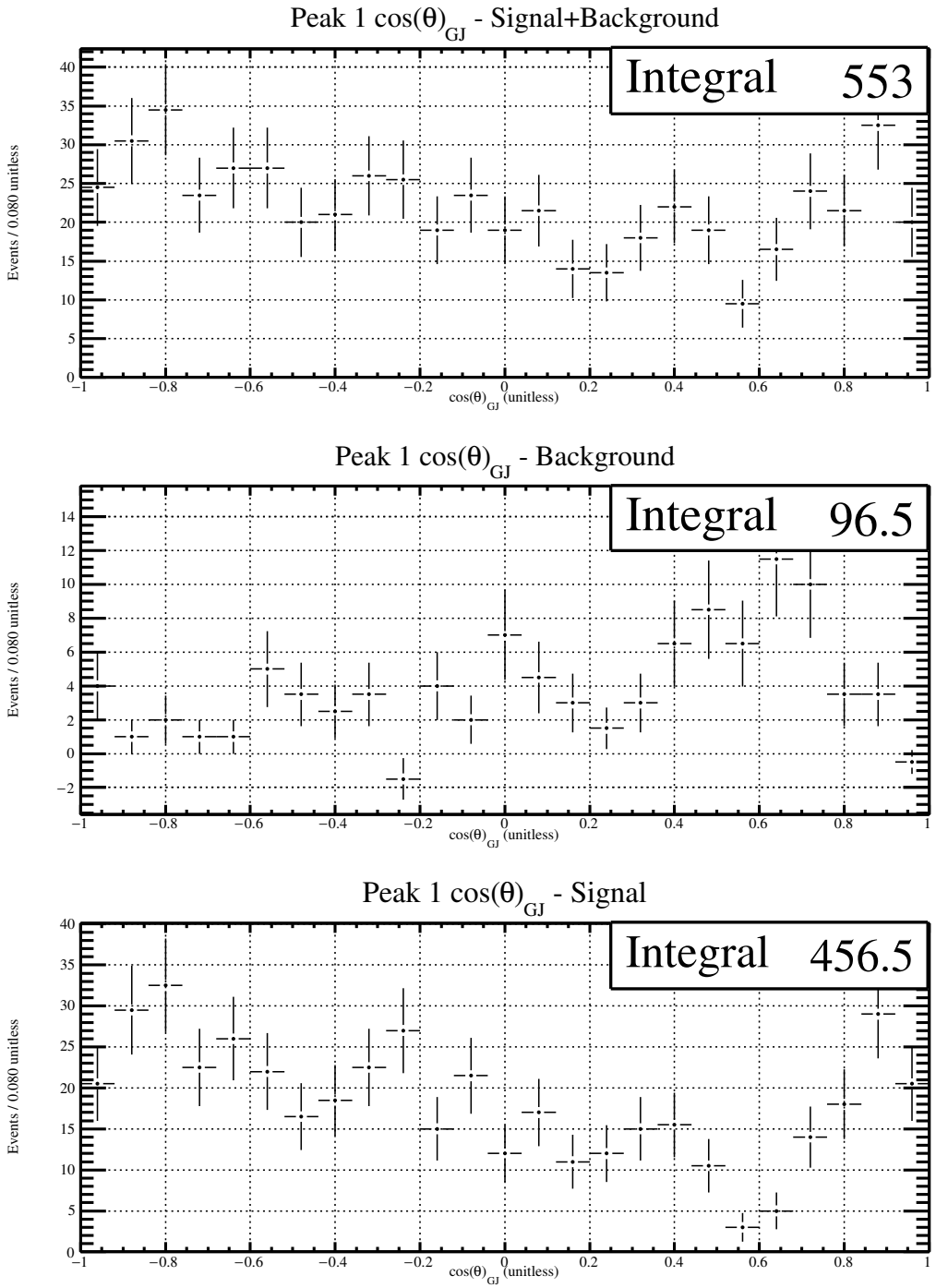

Figure 5.31: The $cos(\theta)_{GJ}$ distribution for $\phi\eta$ invariant mass between 1.605-1.707 GeV/c^2, not acceptance corrected.

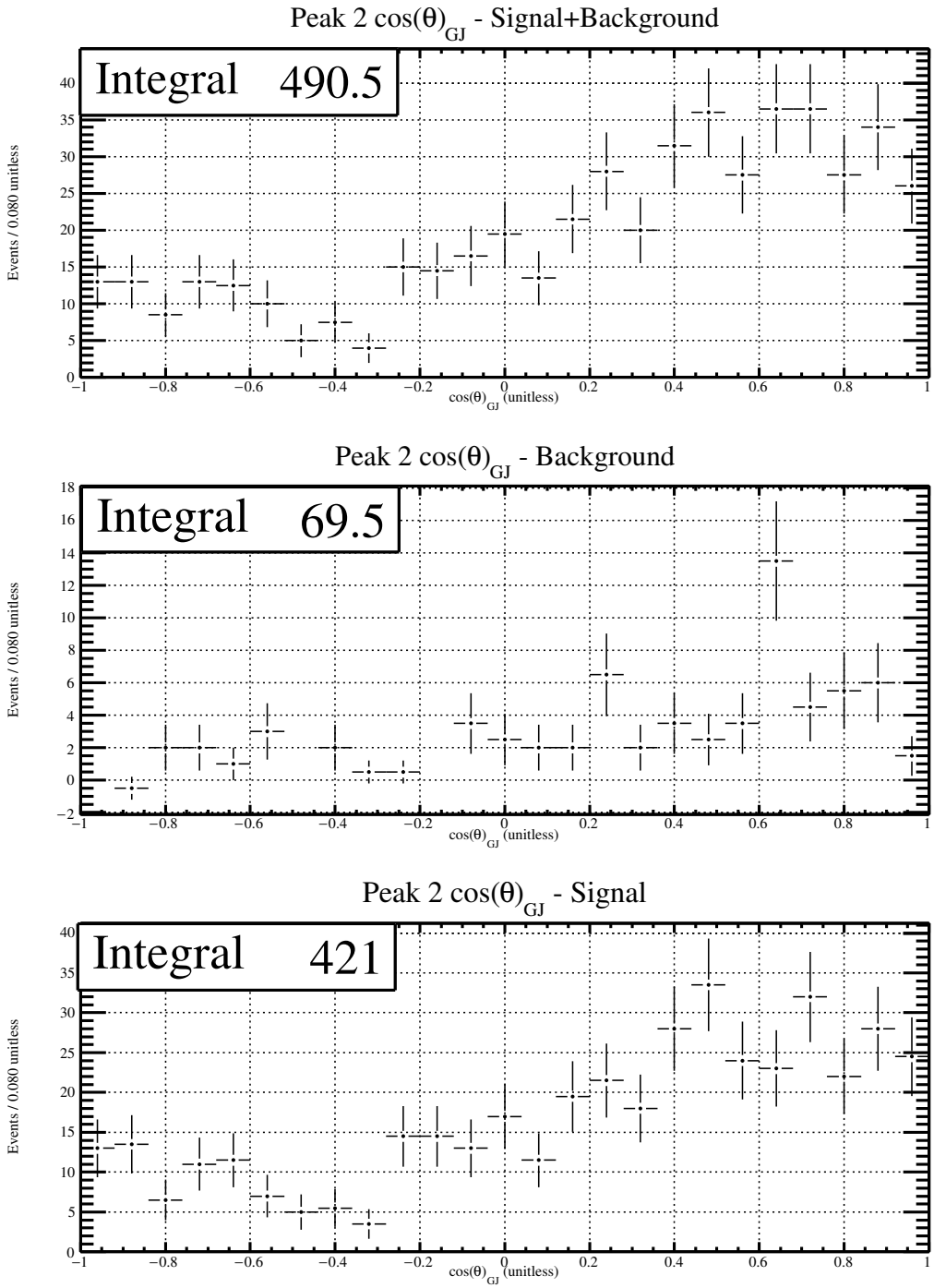

Figure 5.32: The $cos(\theta)_{GJ}$ distribution for $\phi\eta$ invariant mass between 1.809-1.912 GeV/c^2, not acceptance corrected.

Due to the mostly flat acceptance for all figures, none of the final plots presented here are greatly altered other than the amount of statistics in each bin.

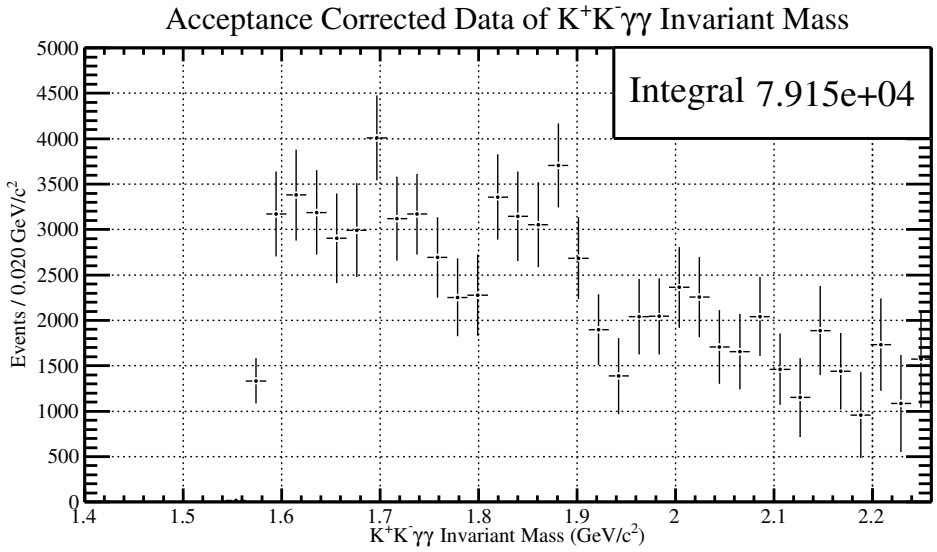

Figure 5.33: The signal $\phi\eta$ invariant mass for elliptical mass selection with the acceptance correction factors described in Figure [5.25]. The range of the distribution has been changed due to the large error bars at high $\phi\eta$ invariant mass values.

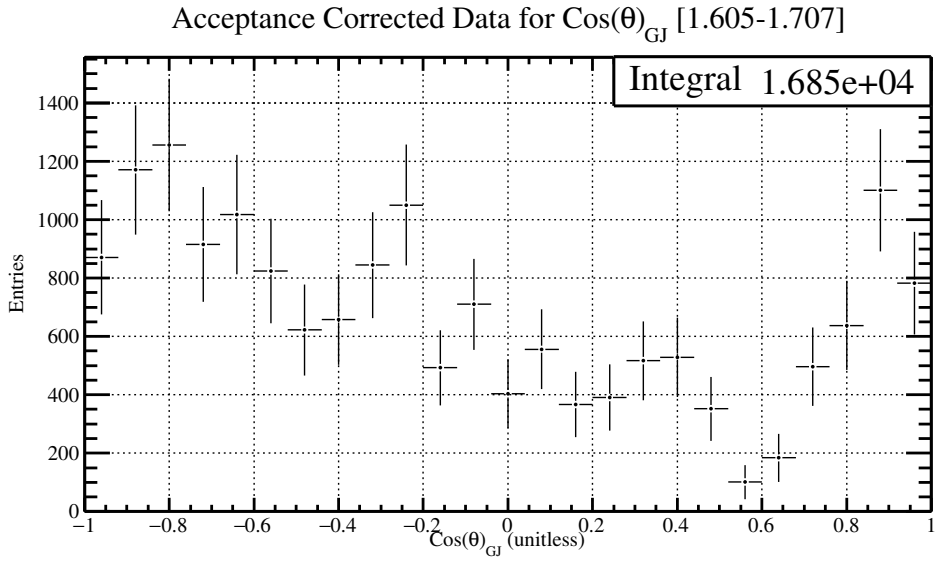

Figure 5.34: The $cos(\theta)_{GJ}$ distribution for $\phi\eta$ invariant mass between 1.605-1.707 GeV/c^2 with the acceptance correction factors described in Figure [5.26].

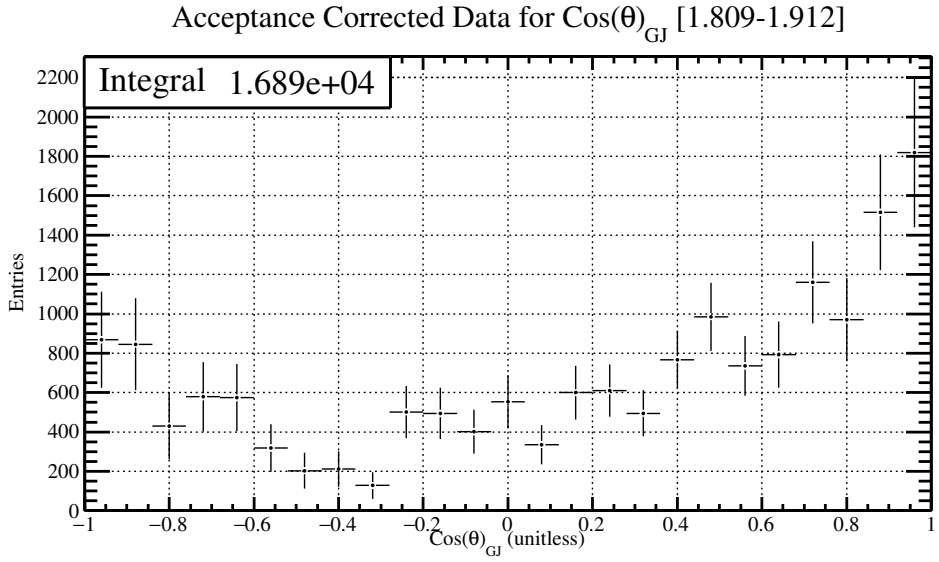

Figure 5.35: The $cos(\theta)_{GJ}$ distribution for $\phi\eta$ invariant mass between 1.809-1.912 GeV/c^2 with the acceptance correction factors described in Figure [5.27].

5.5.2 Q_ϕ Weighting, η Side-band Subtracted

This analysis uses the quality factor weights for the ϕ only method described in Subsection 5.2.2. Since this method only separates ϕ signal from K^+K^- background, it does not separate the η signal from $\gamma\gamma$ background with just Q_ϕ weighting. An example of the Q_ϕ weighted $\gamma\gamma$ invariant mass distribution is given in Figure [5.36].

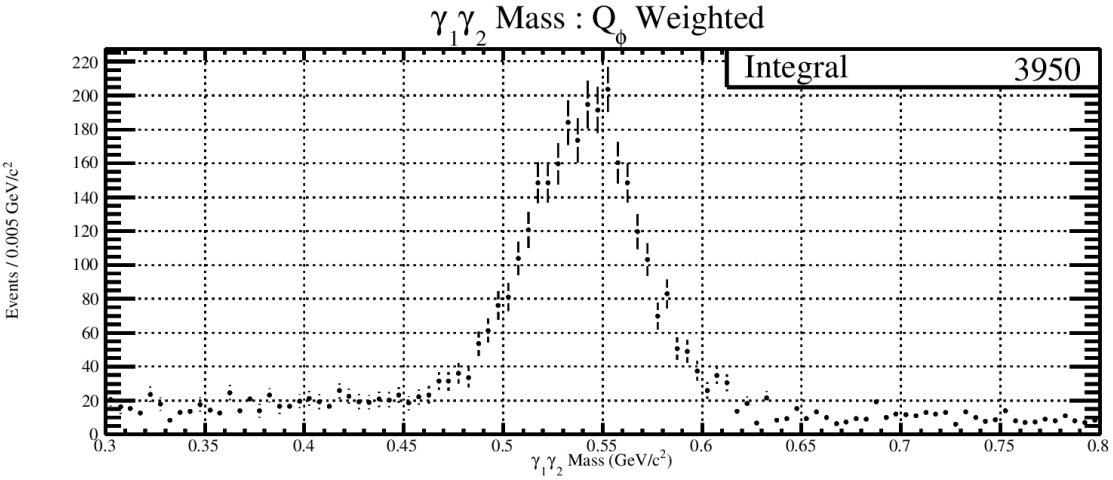

Figure 5.36: The $\gamma\gamma$ invariant mass spectrum with all events weighted by Q_ϕ.

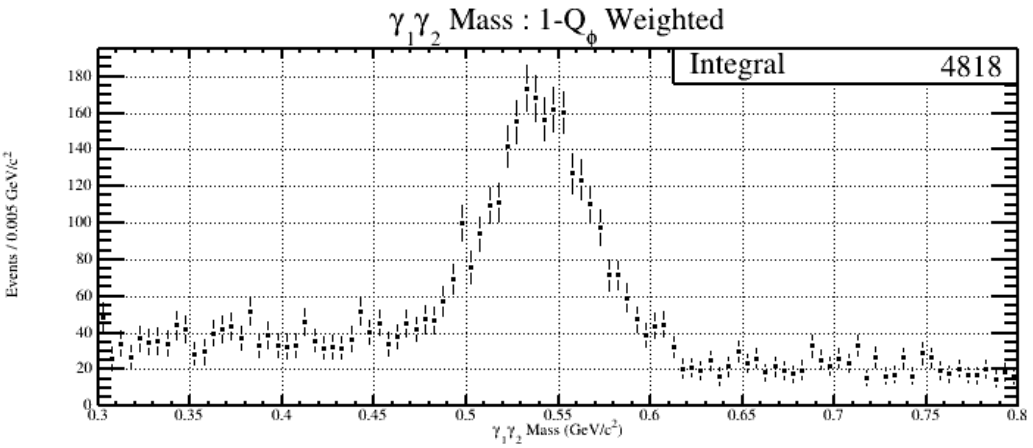

Figure 5.37: The $\gamma\gamma$ invariant mass spectrum with all events weighted by $1 - Q_\phi$.

In order to select the $\phi\eta$ final state, a $\gamma\gamma$ invariant mass cut of $\pm 2\sigma_\eta$ was enforced to select the η signal region. This selection was chosen because the η peak is assumed to have a shape which resembles a Gaussian distribution. A 2σ selection cut ensures that roughly 95 percent of the η signal will be selected. In addition to this signal selection, a side-band cut was enforced on the $\gamma\gamma$ invariant mass in order to approximate the background. One of the side-band regions ranged from $m_\eta - 5\sigma_\eta \leq m_{\gamma\gamma} \leq m_\eta - 3\sigma_\eta$, and the other side-band region ranged from $m_\eta + 3\sigma_\eta \leq m_{\gamma\gamma} \leq m_\eta + 5\sigma_\eta$. These regions were chosen for two reasons. One of which is the fact that the total $m_{\gamma\gamma}$ range used to select the η signal region must be equal to the range used to select the background region. The second reason is to ensure that less than 1 percent of data would be contained within the background selection.

Once the signal and background selections are established, the $\phi\eta$ final state can be studied with this weighting method. The $\phi\eta$ final state is found by weighting all events with Q_ϕ, then selecting the η signal region. Once this distribution is known, a second distribution is filled with the $\gamma\gamma$ side-band selection. Taking the difference between the two distributions provides a $\phi\eta$ final state. An example of what all of these distributions look like is provided in Figure [5.38]. The top histogram of Figure [5.38] is the $K^+K^-\gamma\gamma$ invariant mass weighted by Q_ϕ and a 2σ selection of the η peak. The middle histogram is the $K^+K^-\gamma\gamma$ invariant mass weighted by Q_ϕ and a $\gamma\gamma$ side-band selection. Finally, the bottom histogram is the difference between the top histogram and the middle histogram. The bottom histogram of Figure [5.38] is considered to be the $\phi\eta$ invariant mass plot

for this weighting method. The reason that this is the signal plot for this method is because the ϕ has been identified by means of the nearest neighbors approach described in Subsection 5.2.2; and the η has been identified by means of a side-band subtraction.

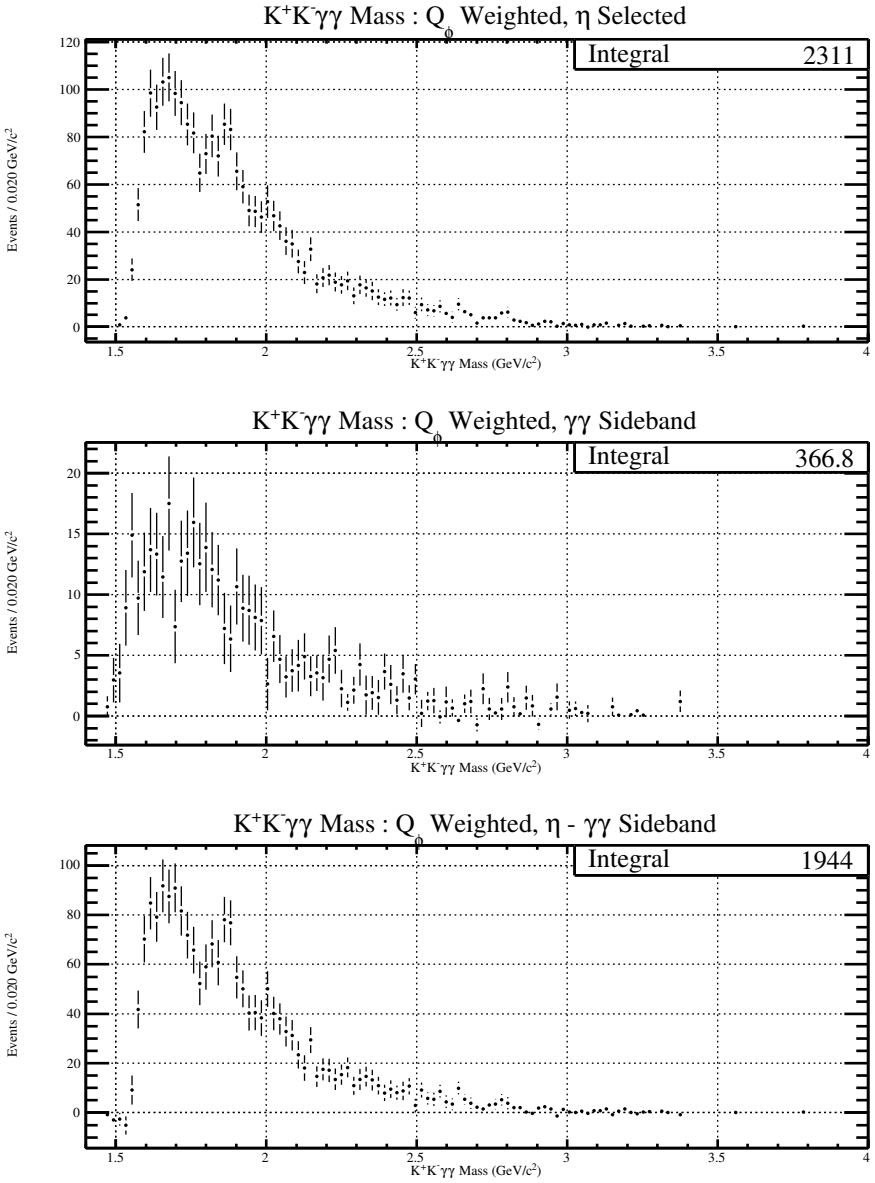

Figure 5.38: The $K^+K^-\gamma\gamma$ invariant mass spectrum with all signal events weighted by Q_ϕ, not acceptance corrected. The top histogram is the data which selects the η peak contained in Figure [5.36]. The middle histogram is the data which selects the $\gamma\gamma$ side-band data. The bottom histogram is the $\phi\eta$ signal and is the difference between the first histogram and the second histogram.

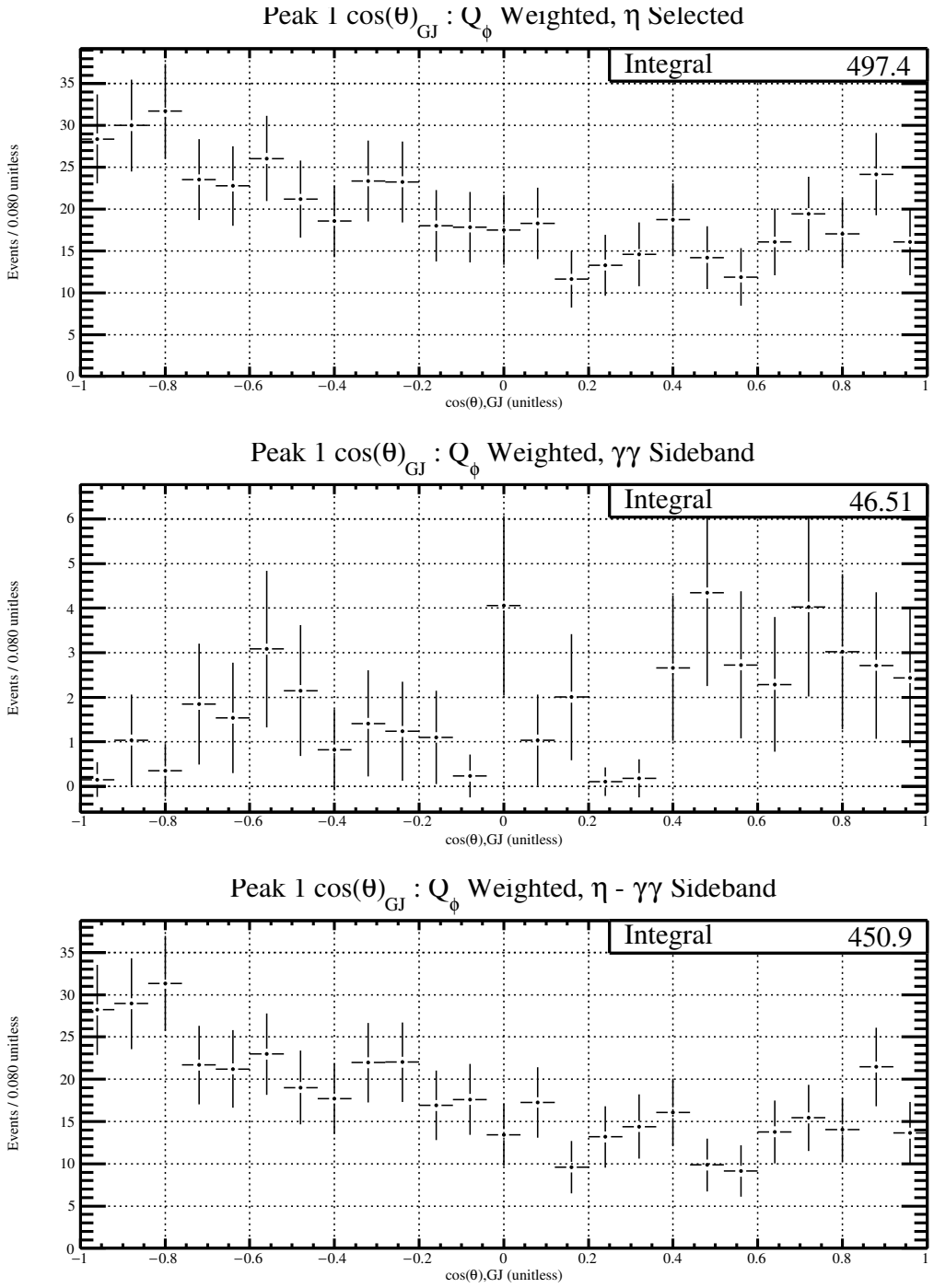

Figure 5.39: The $cos(\theta)_{GJ}$ distribution for $\phi\eta$ invariant mass between 1.605-1.707 GeV/c^2, not acceptance corrected.

Contained within the signal histogram of Figure [5.38] are two structures which resemble the

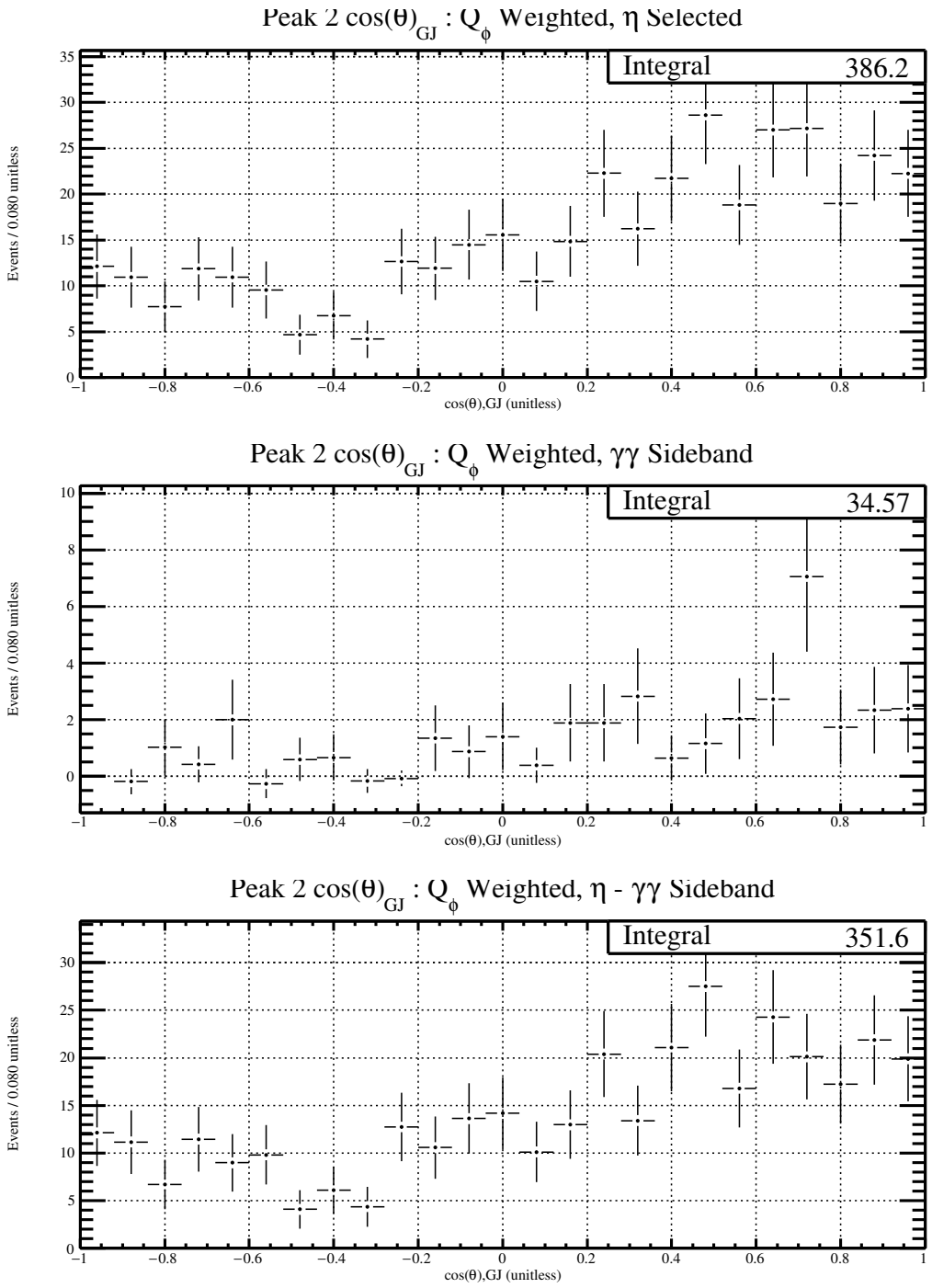

Figure 5.40: The $cos(\theta)_{GJ}$ distribution for $\phi\eta$ invariant mass between 1.809-1.912 GeV/c^2, not acceptance corrected.

structures also seen in Subsection 5.5.1. In order to better understand the nature of these structures, the $cos(\theta)_{GJ}$ angles are extracted for these regions of $\phi\eta$ invariant mass. The $cos(\theta)_{GJ}$ angles for the first structure are given in Figure [5.39] and are found by imposing a cut on the $\phi\eta$ invariant mass with a range of 1.605-1.707 GeV/c^2. The $cos(\theta)_{GJ}$ angles for the second structure are given in Figure [5.40] and are found by imposing a cut on the $\phi\eta$ invariant mass with a range of 1.809-1.912 GeV/c^2. There is no clear angular structure in Figure [5.39] or Figure [5.40]. The only clear observation that is made is that the angular distributions of each region are different from one another.

Using only the signal plots from Figure [5.38], [5.39], and [5.40], the acceptance corrections provided in Subsection 5.4 can be used to correct any detector effects. The acceptance corrected figures are provided in [5.41][5.42][5.43] below. Due to the mostly flat acceptance for all figures, none of the final plots presented here are greatly altered other than the amount of statistics in each bin.

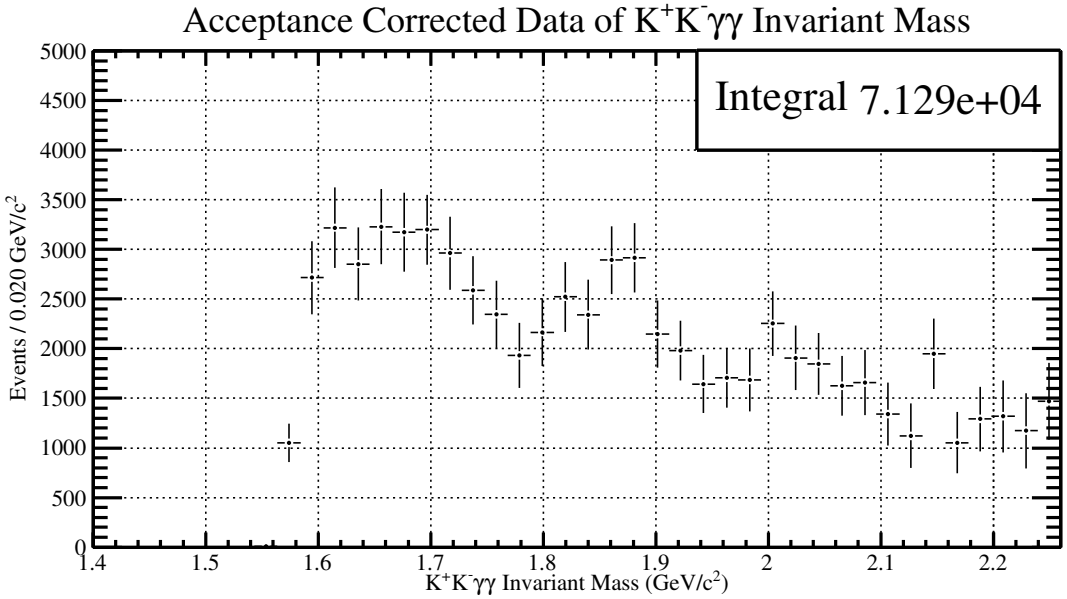

Figure 5.41: The $K^+K^-\gamma\gamma$ invariant mass spectrum with all signal events weighted by Q_ϕ, and the η is selected by side-band subtraction. The spectrum is acceptance corrected as described by Figure [5.25]. The range of the distribution has been changed due to the large error bars at high $\phi\eta$ invariant mass values.

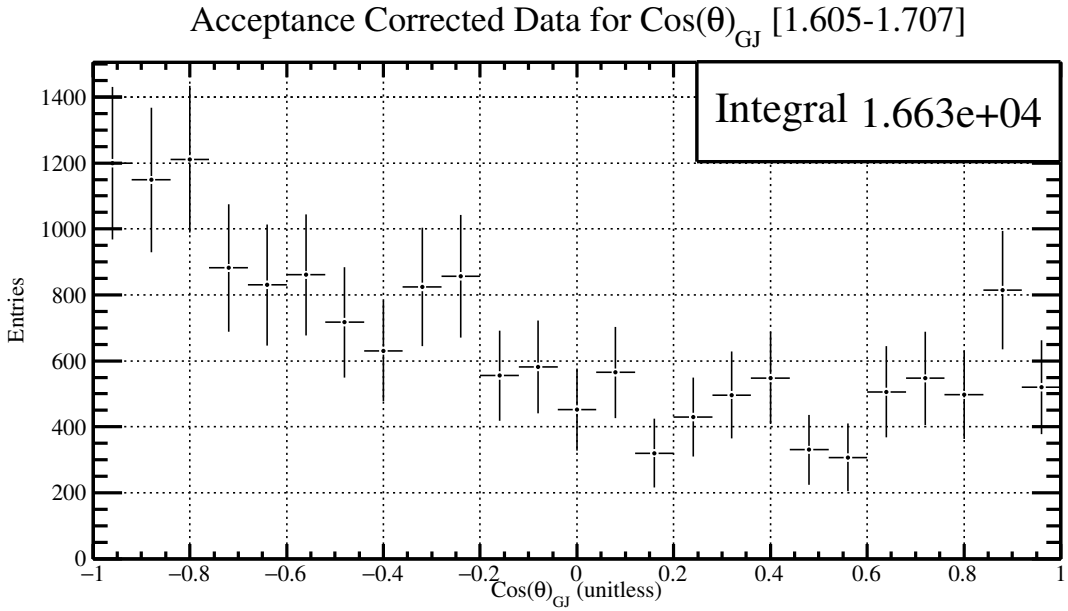

Figure 5.42: The $cos(\theta)_{GJ}$ distribution for $\phi\eta$ invariant mass between 1.605-1.707 GeV/c^2 with the acceptance correction factors described in Figure [5.26].

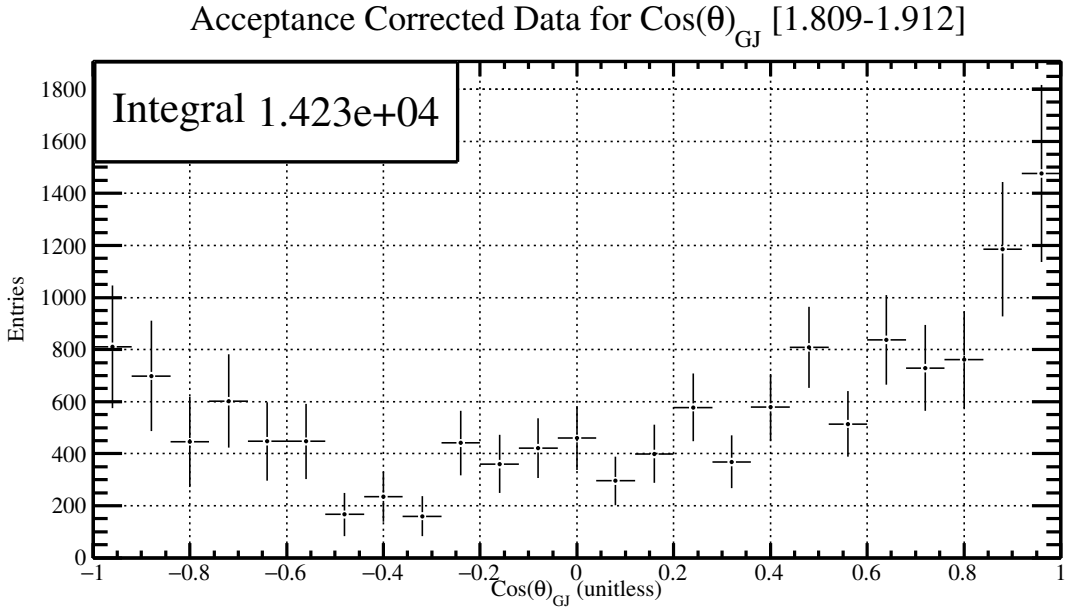

Figure 5.43: The $cos(\theta)_{GJ}$ distribution for $\phi\eta$ invariant mass between 1.809-1.912 GeV/c^2 with the acceptance correction factors described in Figure [5.27].

5.5.3 Q_η Weighting, ϕ Side-band Subtracted

This analysis uses the quality factor weights for the η only method described in Subsection 5.2.2. Since this method only separates η signal from $\gamma\gamma$ background, it does not separate the ϕ signal from K^+K^- background with just Q_η weighting. An example of the Q_η weighted K^+K^- invariant mass distribution is given in Figure [5.44].

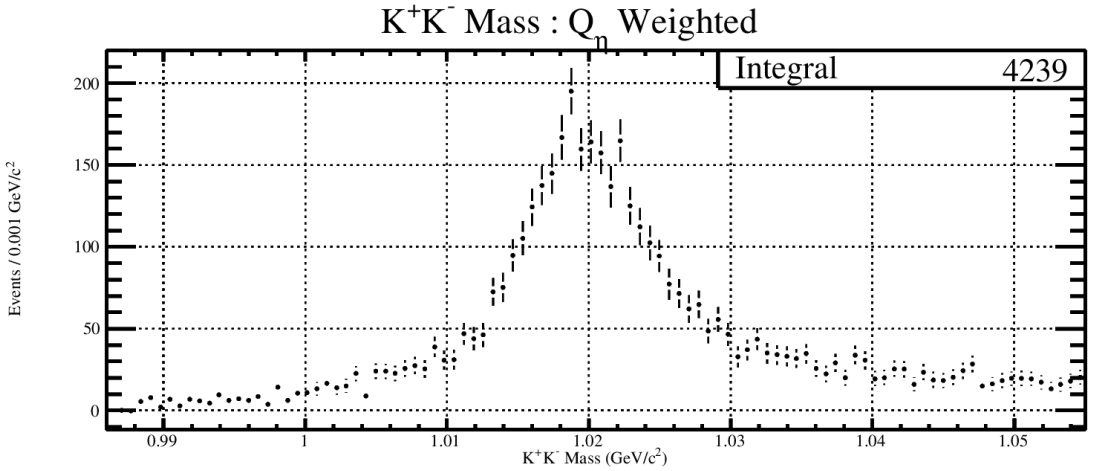

Figure 5.44: The fit of the K^+K^- invariant mass spectrum with all events weighted by Q_η.

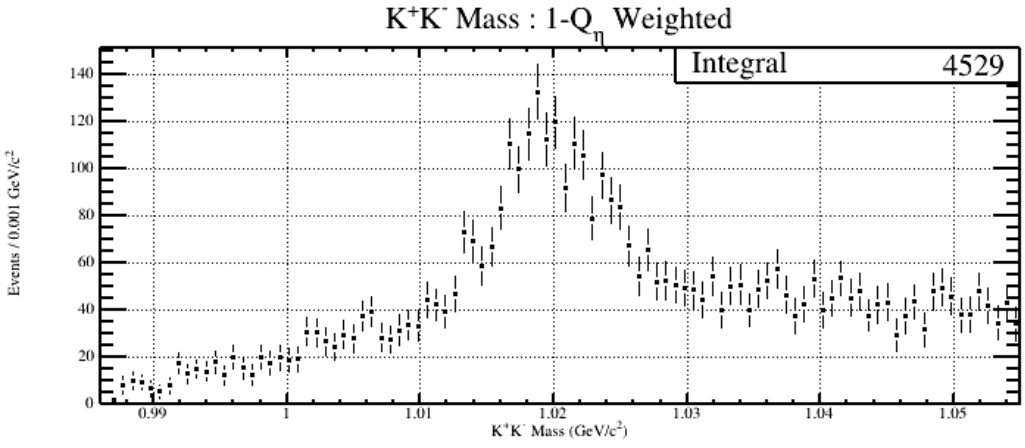

Figure 5.45: The K^+K^- invariant mass spectrum with all events weighted by $1 - Q_\eta$.

In order to select the $\phi\eta$ final state, a K^+K^- invariant mass cut of $\pm 2\sigma_\phi$ was enforced to select the ϕ signal region. This selection was chosen because the ϕ peak is assumed to have a shape which resembles a Gaussian distribution. A 2σ selection cut ensures that roughly 95 percent of the ϕ signal will be selected. In addition to this signal selection, a side-band cut was enforced on the K^+K^- invariant mass in order to approximate the background. One of the side-band regions ranged from $m_\phi - 5\sigma_\phi \leq m_{K^+K^-} \leq m_\phi - 3\sigma_\phi$, and the other side-band region ranged from $m_\phi + 3\sigma_\phi \leq m_{K^+K^-} \leq m_\phi + 5\sigma_\phi$. These regions were chosen for two reasons. One of which is the fact that the total $m_{K^+K^-}$ range used to select the ϕ signal region must be equal to the range used to select the background region. The second reason is to ensure that less than 1 percent of data would be contained within the background selection.

Once the signal and background selections are established, the $\phi\eta$ final state can be studied with this weighting method. The $\phi\eta$ final state is found by weighting all events with Q_η, then selecting the ϕ signal region. Once this distribution is know, a second distribution is filled with the K^+K^- side-band selection. Taking the difference between the two distributions provides a $\phi\eta$ final state. An example of what all of these distributions look like is provided in Figure [5.46]. The top histogram of Figure [5.46] is the $K^+K^-\gamma\gamma$ invariant mass weighted by Q_η and a 2σ selection of the ϕ peak. The middle histogram is the $K^+K^-\gamma\gamma$ invariant mass weighted by Q_η and a K^+K^- side-band selection. Finally, the bottom histogram is the difference between the top histogram and the middle histogram. The bottom histogram of Figure [5.46] is considered to be the $\phi\eta$ invariant mass plot for this weighting method. The reason that this is the signal plot for this method is because the η has been identified by means of the nearest neighbors approach described in Subsection 5.2.2; and the ϕ has been identified by means of a side-band subtraction.

One interesting result from this method and the others presented in this thesis is the ability to study backgrounds. The middle histogram of Figure [5.46] shows a clear indication that a structure is present in the ηKK invariant mass. This structure is also seen in the background histograms of Figure [5.30] and Figure [5.54]. However, this structure is *not* seen in the background histogram of Figure [5.38]. The consistency of this structure showing up in some backgrounds, but not all, provides evidence that it may have a decay mode to both $\phi\eta$ and ηKK.

Contained within the signal histogram of Figure [5.46] are two structures which resemble the structures also seen in Subsection 5.5.1, Subsection 5.5.2. In order to better understand the nature

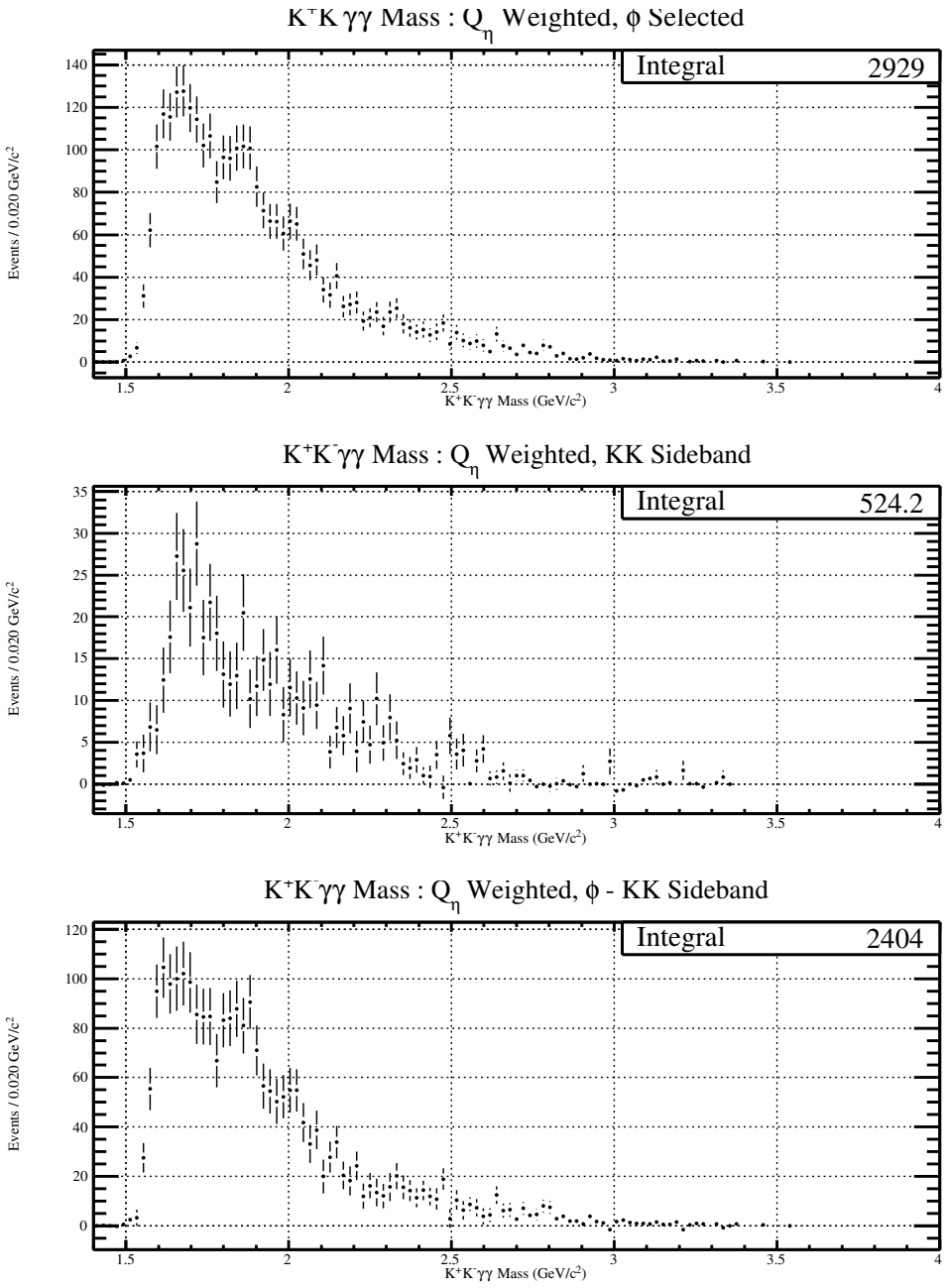

Figure 5.46: The $K^+K^-\gamma\gamma$ invariant mass spectrum with all signal events weighted by Q_η, not acceptance corrected. The top histogram is the data which selects the ϕ peak contained in Figure [5.44]. The middle histogram is the data which selects the K^+K^- side-band data. The bottom histogram is the $\phi\eta$ signal and is the difference between the first histogram and the second histogram.

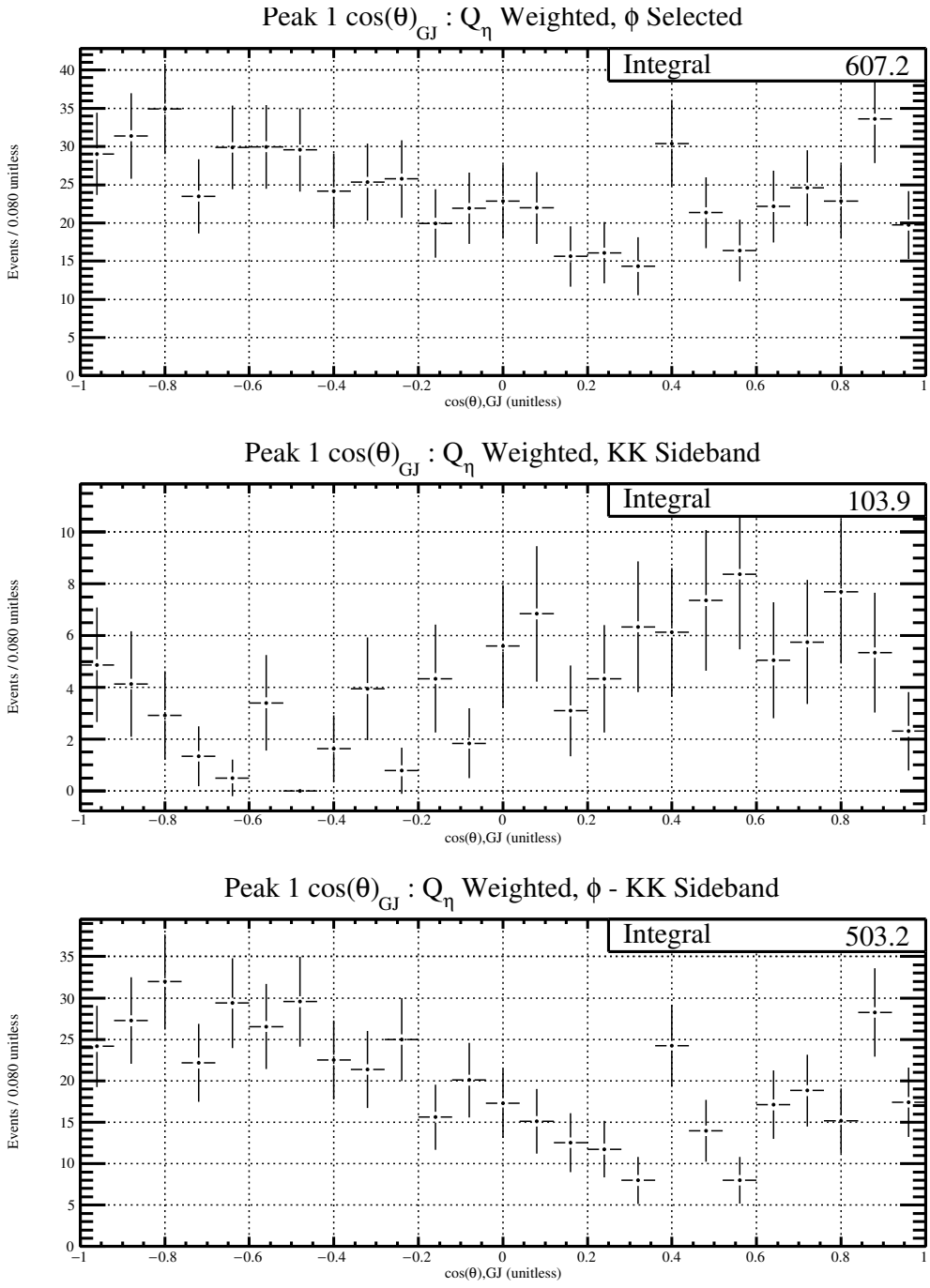

Figure 5.47: The $cos(\theta)_{GJ}$ distribution for $\phi\eta$ invariant mass between 1.605-1.707 GeV/c^2, not acceptance corrected.

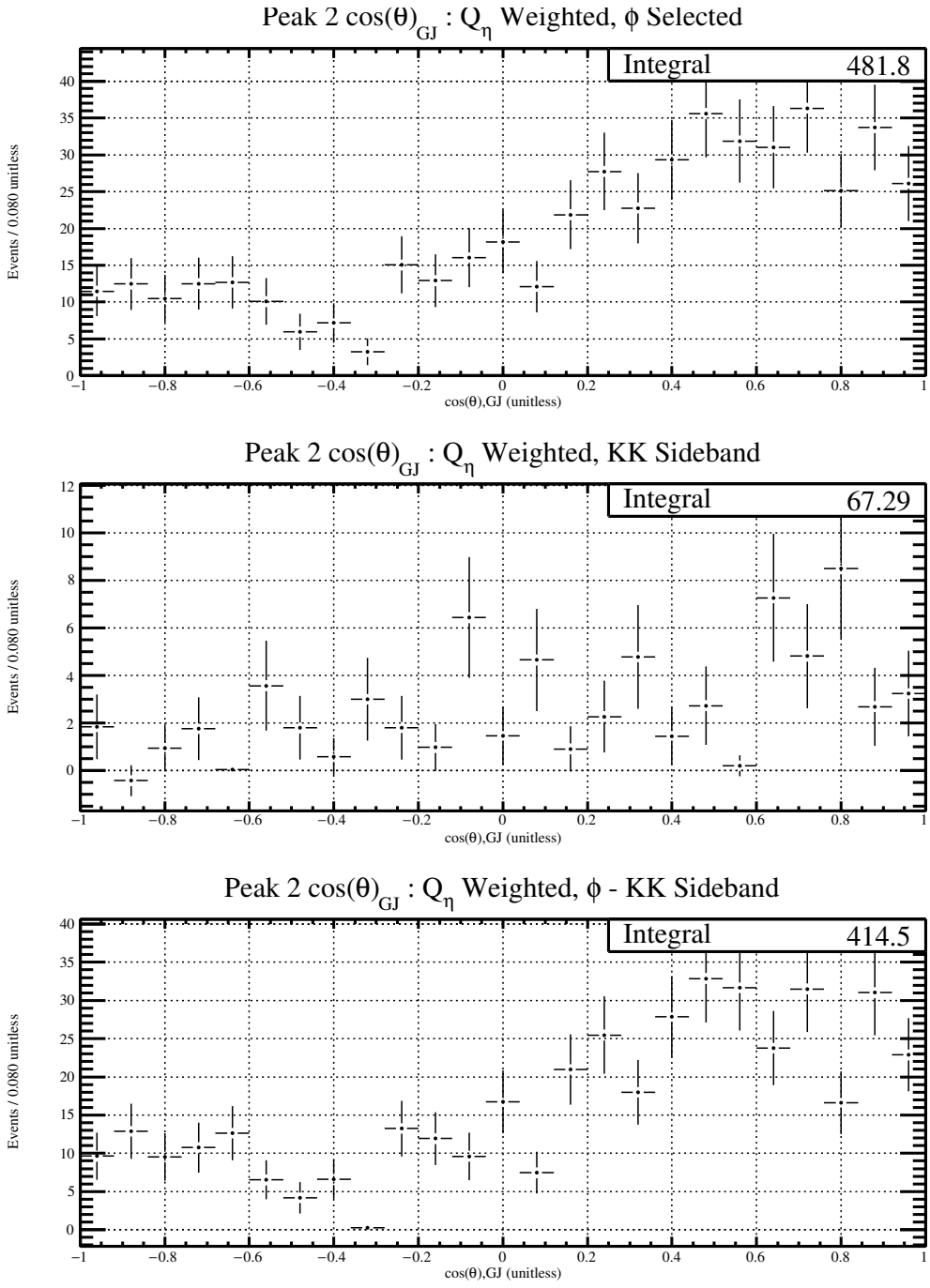

Figure 5.48: The $cos(\theta)_{GJ}$ distribution for $\phi\eta$ invariant mass between 1.809-1.912 GeV/c^2, not acceptance corrected.

of these structures, the $cos(\theta)_{GJ}$ angles are extracted for these regions of $\phi\eta$ invariant mass. The $cos(\theta)_{GJ}$ angles for the first structure are given in Figure [5.47] and are found by imposing a cut on the $\phi\eta$ invariant mass with a range of 1.605-1.707 GeV/c^2. The $cos(\theta)_{GJ}$ angles for the second structure are given in Figure [5.48] and are found by imposing a cut on the $\phi\eta$ invariant mass with a range of 1.809-1.912 GeV/c^2. There is no clear angular structure in Figure [5.47] or Figure [5.48]. The only clear observation that is made is that the angular distributions of each region are different from one another.

Using only the signal plots from Figure [5.46], [5.47], and [5.48], the acceptance corrections provided in Subsection 5.4 can be used to correct any detector effects. The acceptance corrected figures are provided in [5.49][5.50][5.51] below. Due to the mostly flat acceptance for all figures, none of the final plots presented here are greatly altered other than the amount of statistics in each bin.

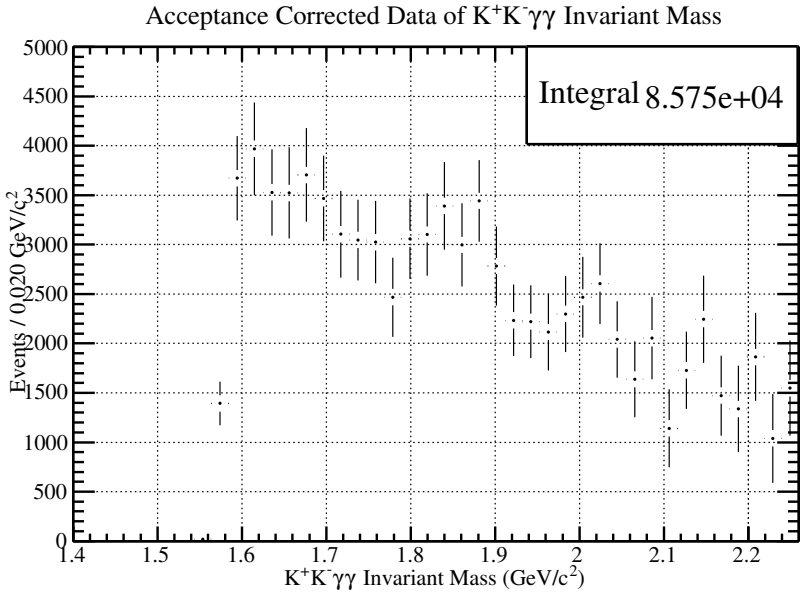

Figure 5.49: The $K^+K^-\gamma\gamma$ invariant mass spectrum with all signal events weighted by Q_η, and the ϕ is selected by side-band subtraction. The spectrum is acceptance corrected as described by Figure [5.25]. The range of the distribution has been changed due to the large error bars at high $\phi\eta$ invariant mass values.

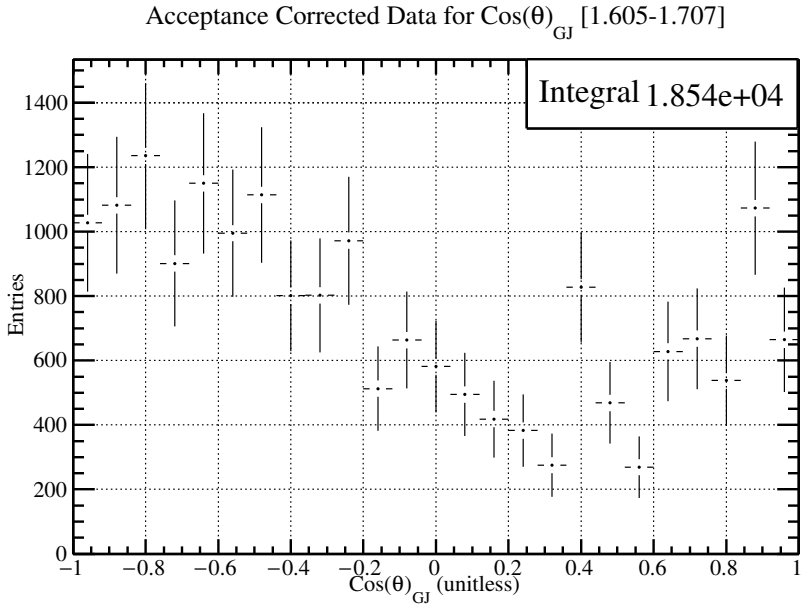

Figure 5.50: The $cos(\theta)_{GJ}$ distribution for $\phi\eta$ invariant mass between 1.605-1.707 GeV/c^2 with the acceptance correction factors described in Figure [5.26].

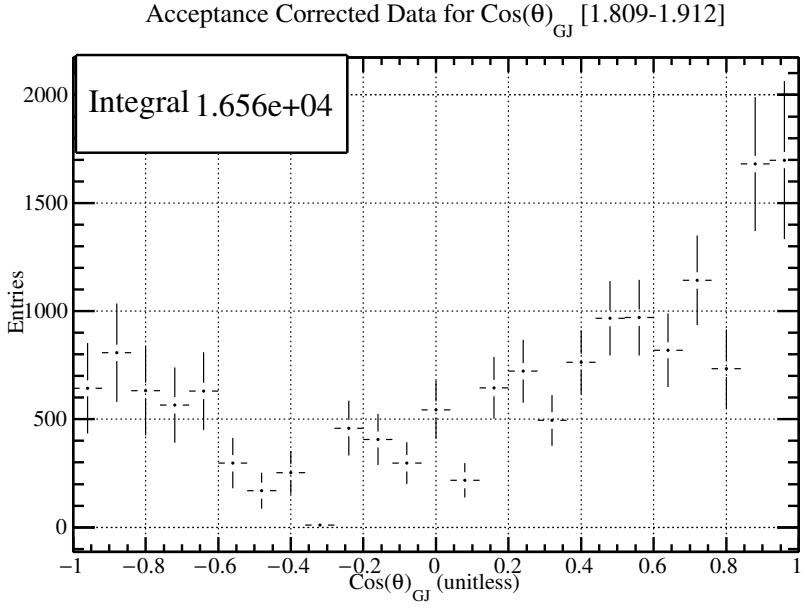

Figure 5.51: The $cos(\theta)_{GJ}$ distribution for $\phi\eta$ invariant mass between 1.809-1.912 GeV/c^2 with the acceptance correction factors described in Figure [5.27].

5.5.4 $Q_{\phi\eta}$ Weighting

This analysis uses the quality factor weights for the $\phi\eta$ only method described in Subsection 5.2.2. Since this method separates both η signal from $\gamma\gamma$ background, and ϕ signal from K^+K^- background, the only weight that is needed event by event is $Q_{\phi\eta}$. An example of the $Q_{\phi\eta}$ weighted $K^+K^-\gamma\gamma$ invariant mass distribution and the corresponding background plot is given in Figure [5.54].

One interesting result from this method and the others presented in this thesis is the ability to study backgrounds. The lower histogram of Figure [5.54] shows a clear indication that a structure is present in the $1 - Q_{\phi\eta}$ weighted invariant mass. This structure is also seen in the background histograms of Figure [5.30] and Figure [5.46]. However, this structure is *not* seen in the background histogram of Figure [5.38].

Contained within the signal histogram of Figure [5.54] are two structures which resemble the structures also seen in Subsection 5.5.1, Subsection 5.5.2, and and Subsection 5.5.3. In order to better understand the nature of these structures, the $cos(\theta)_{GJ}$ angles are extracted for these regions of $\phi\eta$ invariant mass. The $cos(\theta)_{GJ}$ angles for the first structure are given in Figure [5.55] and are found by imposing a cut on the $\phi\eta$ invariant mass with a range of 1.605-1.707 GeV/c^2. The $cos(\theta)_{GJ}$ angles for the second structure are given in Figure [5.56] and are found by imposing a cut on the $\phi\eta$ invariant mass with a range of 1.809-1.912 GeV/c^2. There is no clear angular structure in Figure [5.55] or Figure [5.56]. The only clear observation that is made is that the angular distributions of each region are different from one another.

Using only the signal plots from Figure [5.54], [5.55], and [5.56], the acceptance corrections provided in Subsection 5.4 can be used to improve the statistics in each figure as well as correct any detector effects. The acceptance corrected figures are provided in [5.57][5.58][5.59] below. Due to the mostly flat acceptance for all figures, none of the final plots presented here are greatly altered other than the amount of statistics in each bin.

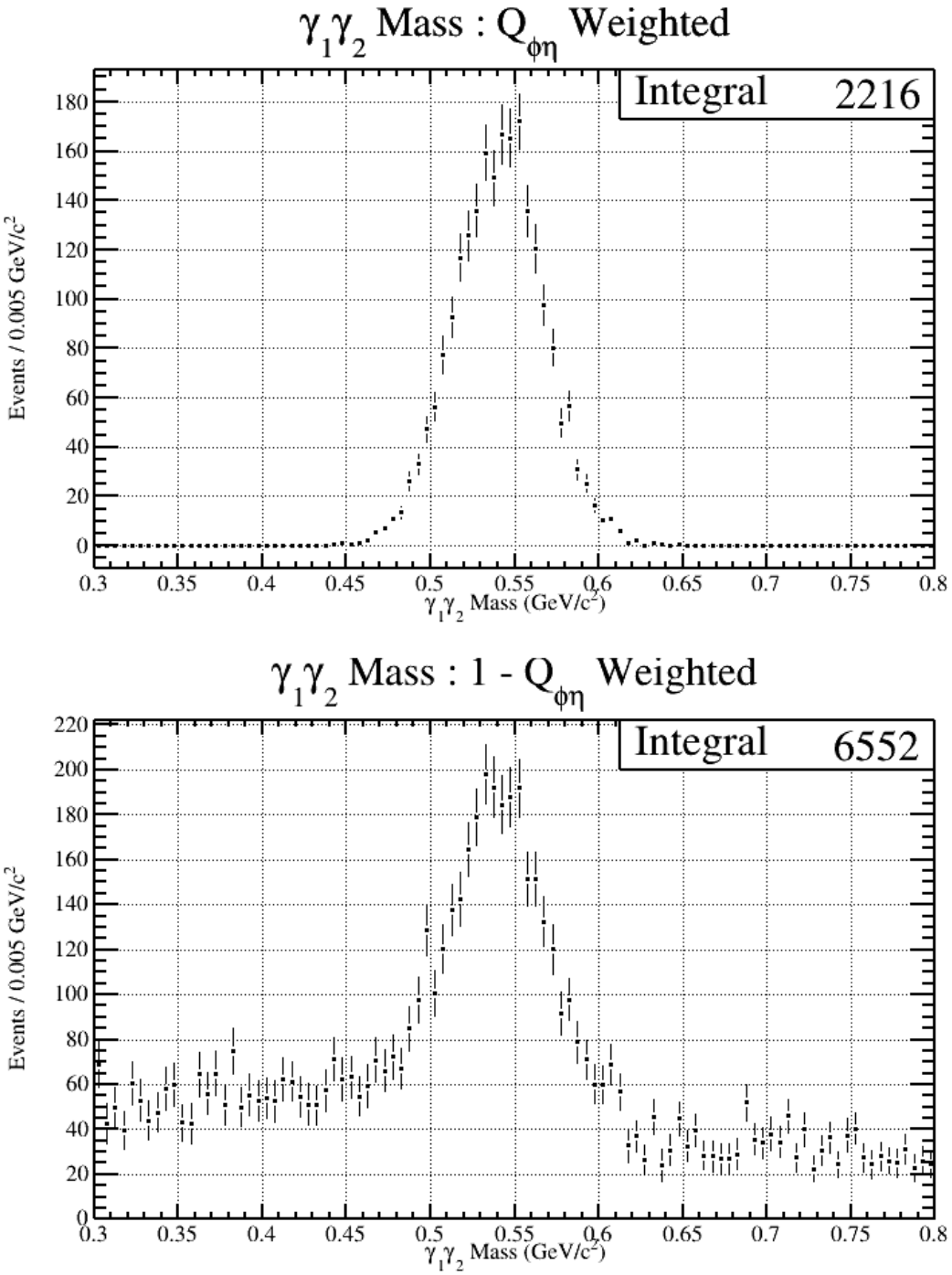

Figure 5.52: The $\gamma\gamma$ invariant mass spectrum with all signal events weighted by $Q_{\phi\eta}$, not acceptance corrected.

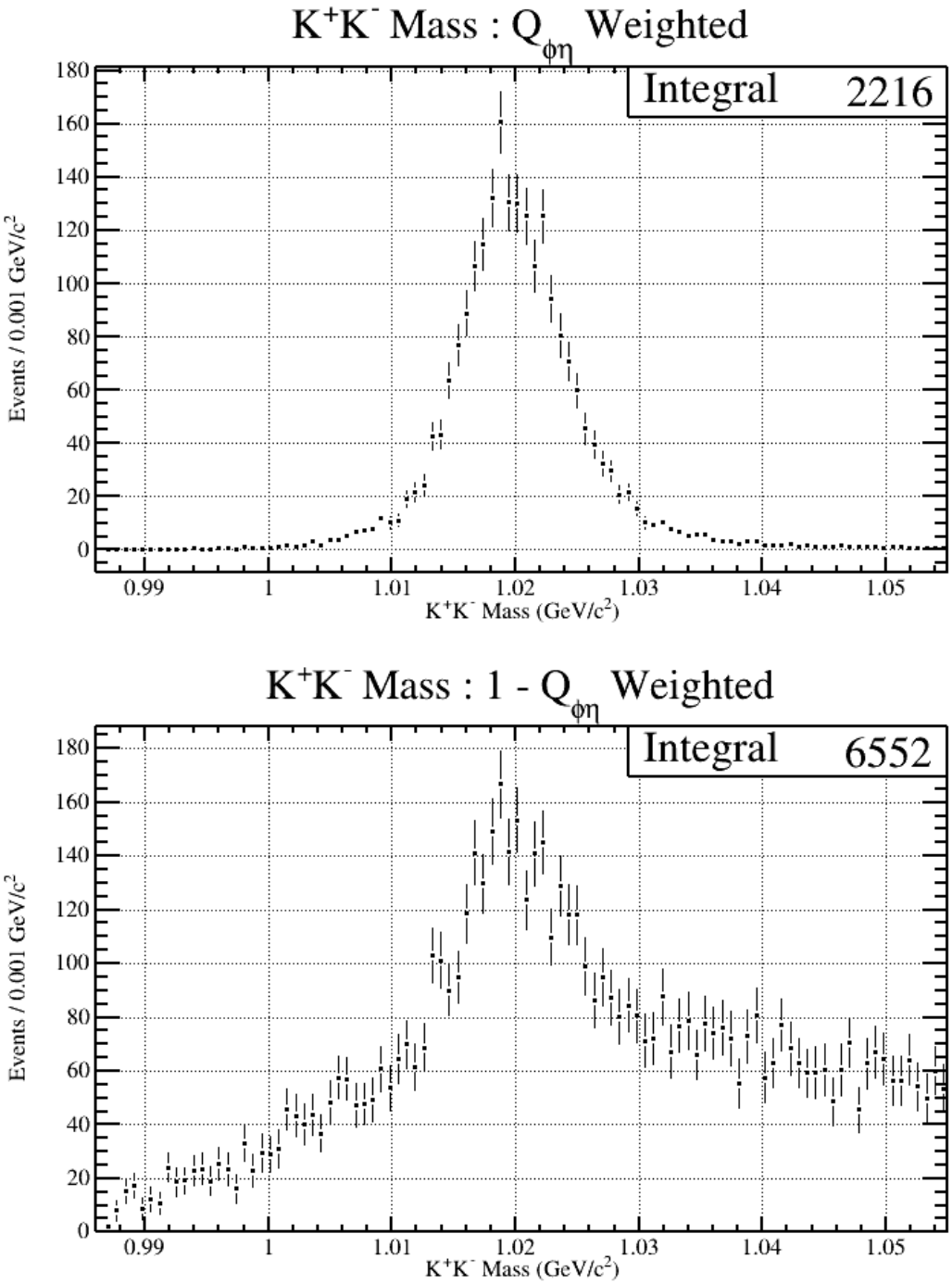

Figure 5.53: The K^+K^- invariant mass spectrum with all signal events weighted by $Q_{\phi\eta}$, not acceptance corrected.

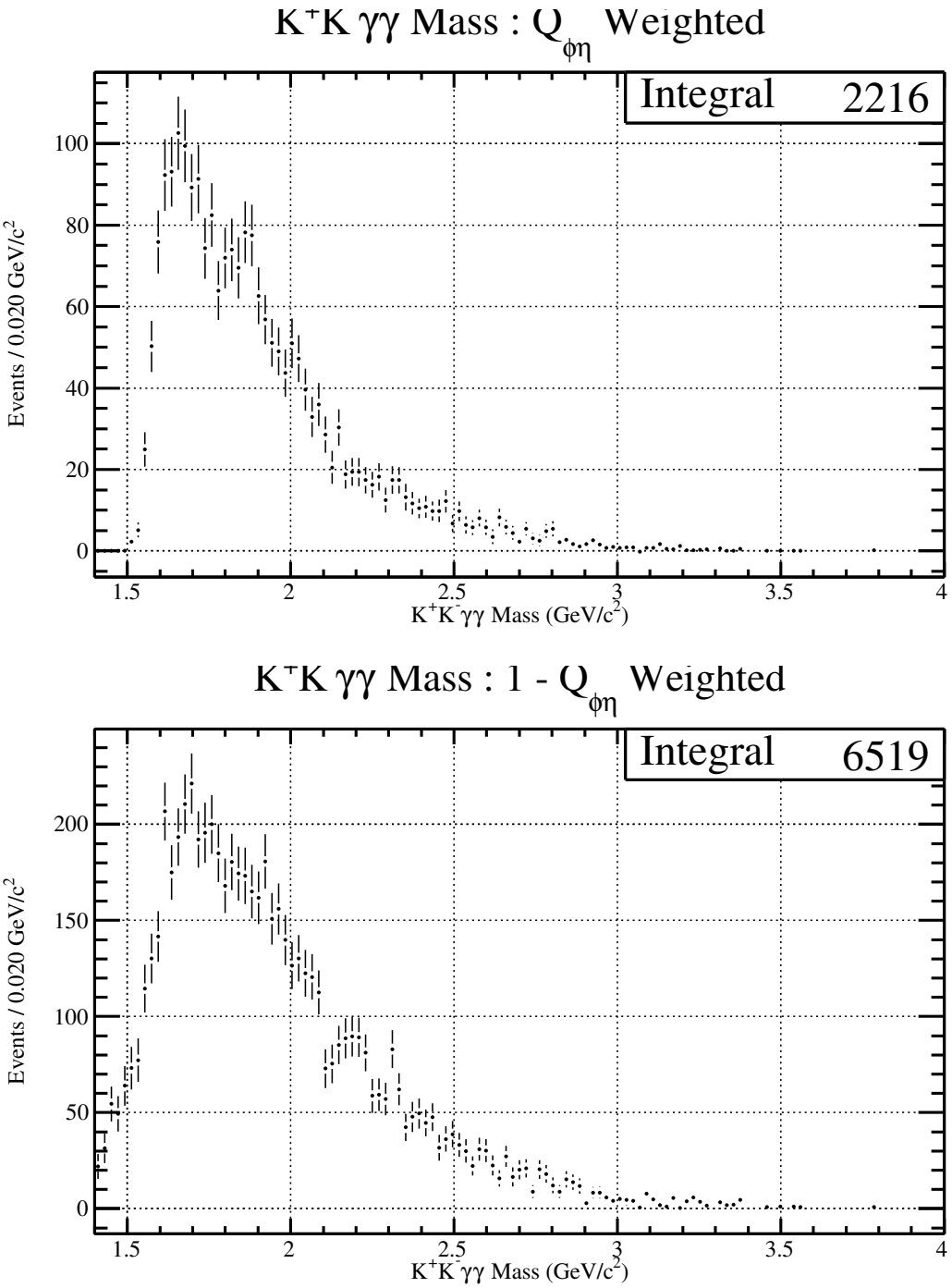

Figure 5.54: The $K^+K^-\gamma\gamma$ invariant mass spectrum with all signal events weighted by $Q_{\phi\eta}$, not acceptance corrected.

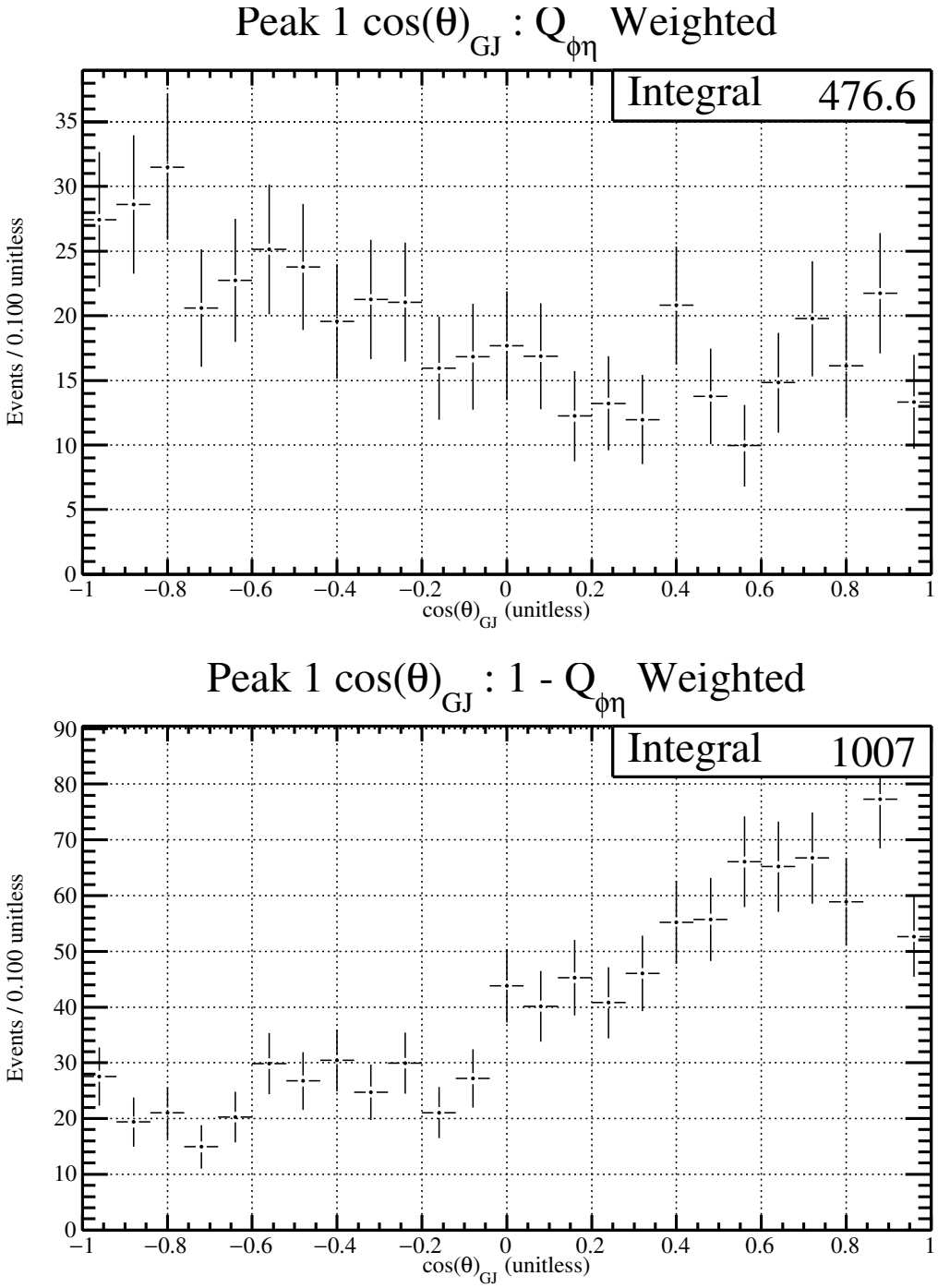

Figure 5.55: The $cos(\theta)_{GJ}$ distribution for $\phi\eta$ invariant mass between 1.605-1.707 GeV/c^2, not acceptance corrected.

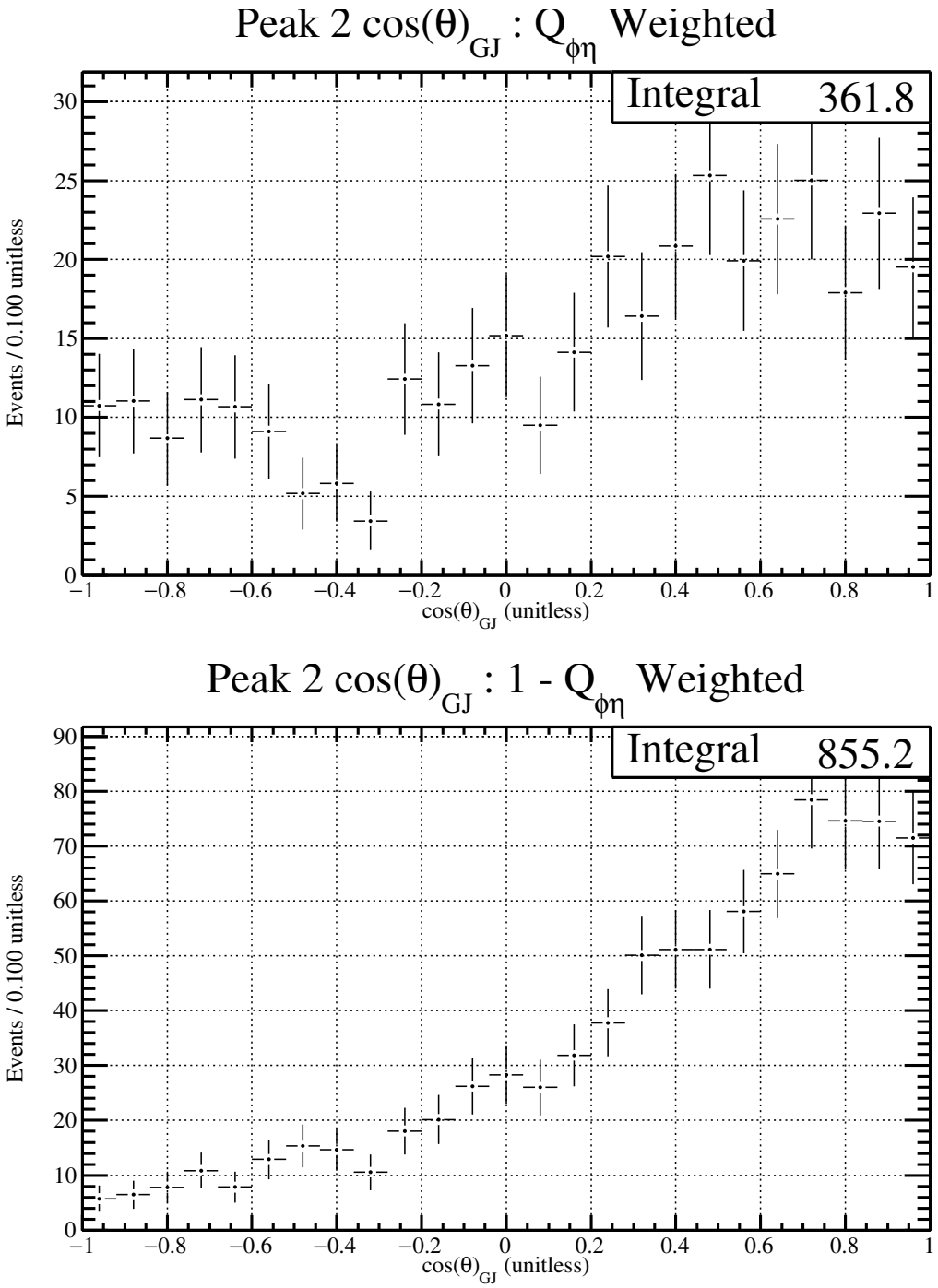

Figure 5.56: The $cos(\theta)_{GJ}$ distribution for $\phi\eta$ invariant mass between 1.809-1.912 GeV/c^2, not acceptance corrected.

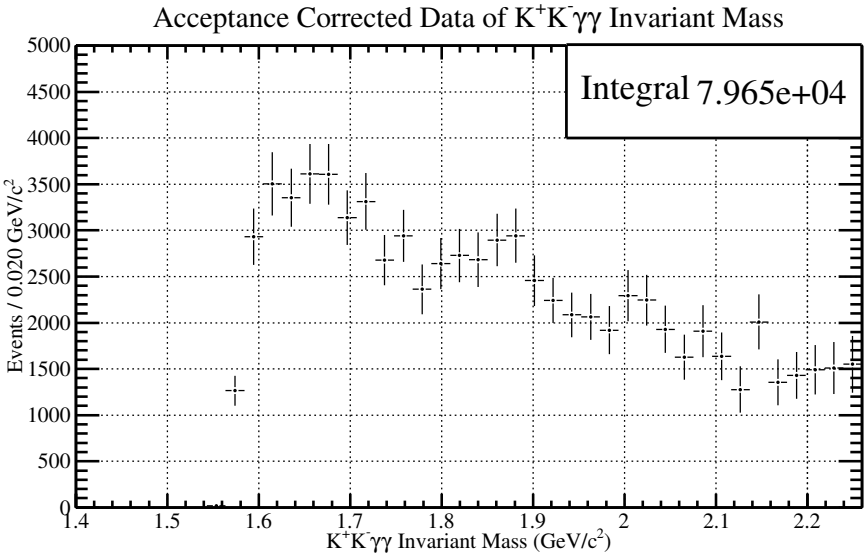

Figure 5.57: he $K^+K^-\gamma\gamma$ invariant mass spectrum with all signal events weighted by $Q_{\phi\eta}$. The spectrum is acceptance corrected as described by Figure [5.25]. The range of the distribution has been changed due to the large error bars at high $\phi\eta$ invariant mass values.

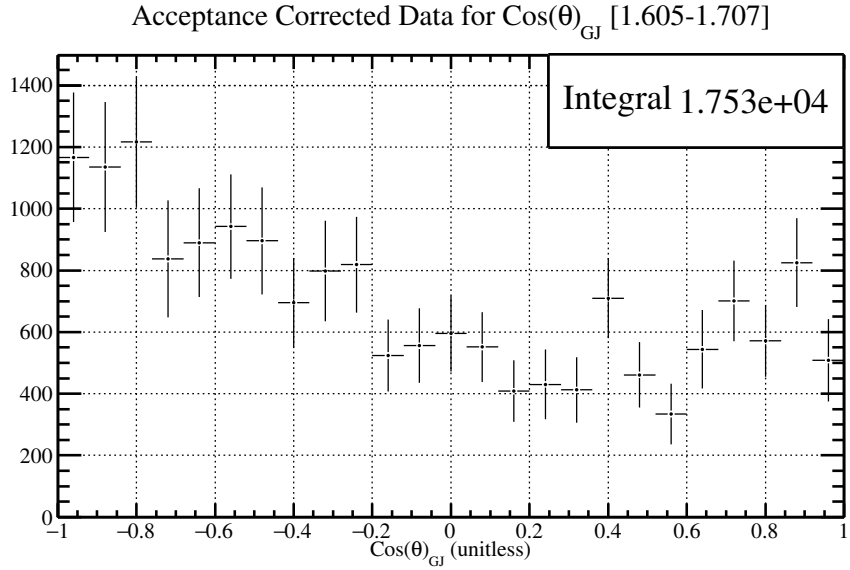

Figure 5.58: The $cos(\theta)_{GJ}$ distribution for $\phi\eta$ invariant mass between 1.605-1.707 GeV/c^2 with the acceptance correction factors described in Figure [5.26].

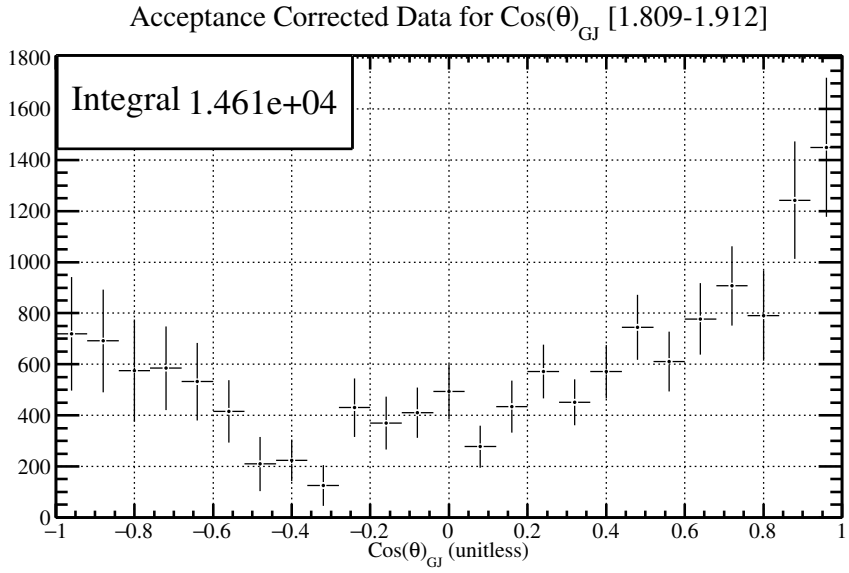

Figure 5.59: The $cos(\theta)_{GJ}$ distribution for $\phi\eta$ invariant mass between 1.809-1.912 GeV/c^2 with the acceptance correction factors described in Figure [5.27].

5.6 Fitting $\phi\eta$ Invariant Mass Plots for Signal Distributions

Since the acceptance of the $\phi\eta$ invariant mass is not reliable near threshold (Figure 5.25), the signal distributions without acceptance corrections will be fit. Using the signal distributions for all selections methods mentioned above, the $\phi\eta$ invariant mass distribution will be tested with four different functions. Each function contains accepted Monte Carlo as a background function. It should be noted that this accepted Monte Carlo sample has a t, and beam energy distribution which matches data. The four different functions are the following:

1. Two interfering relativistic Breit-Wigners as signal, plus a scaled accepted Monte Carlo distribution as background.
2. One low mass relativistic Breit-Wigner as signal, plus a scaled accepted Monte Carlo distribution as background.
3. One high mass relativistic Breit-Wigner as signal, plus a scaled accepted Monte Carlo distribution as background.
4. No signal distribution, only a scaled accepted Monte Carlo distribution as background.

The purpose of fitting the signal distributions with each function mentioned above is to test the probability of structures existing within the data set. More specifically, this method will test the

probability of observing: two structures, only one low mass structure, only one high mass structure, or no structures at all.

The signal fit that will be used for each function is described by Equation 5.22.

$$|Q(m)|^2 = A * |\frac{F_1(m)}{F_1(m_{Peak1})} * \Delta_1(m) + re^{i\varphi} * \frac{F_3(m)}{F_3(m_{Peak2})} * \Delta_3(m)|^2 \tag{5.22}$$

This equation in closely related to Equation 5.3 except that there is an additional relativistic Breit-Wigner, and the Blatt-Weisskopf centrifugal-barrier factors are normalized. This additional relativistic Breit-Wigner contains an imaginary coefficient and a Blatt-Weisskopf centrifugal-barrier factor for a spin 3 particle. The purpose of normalizing the Blatt-Weisskopf centrifugal-barrier factors is to have the fit parameter r represent the relative ratio between the amplitudes of the first peak and the second peak. The spin values of 1 and 3 for the first and second peaks were chosen because their mass and width values are comparable to known s$\bar{s}$ resonances in the PDG. The first peak has a similar mass and width to the $\phi(1680)$, which is reported as $(m_{\phi(1680)} = 1680 \pm 20, \sigma_{\phi(1680)} = 150 \pm 50) MeV/c^2$ in the PDG. The second peak has a similar mass and width to the $\phi_3(1850)$, which is reported as $(m_{\phi(1850)} = 1854 \pm 7, \sigma_{\phi(1850)} = 87^{+28}_{-23}) MeV/c^2$ in the PDG.

The signal fit for each distribution will use a total of 7 parameters, 4 of them will be the mass and width of the first and second peak, another 2 will come from the phase and ratio values contained within the complex coefficient, and the last parameter is the overall normalization. The background for each fit is simply the phase space produced by the accepted Monte Carlo multiplied by a normalization coefficient. Therefore, the total function used to fit the $\phi\eta$ invariant mass will have 8 parameters. The difference in each fitting method in terms of their free or fixed parameter values is given in Table 5.6.

The last technicality of the $\phi\eta$ invariant mass fit that needs to be addressed is the method for representing the breakup momentum, which will clearly be different than the form used in Subsection 5.2.1. Deriving the breakup momentum in the rest frame of the $\phi\eta$ parent state is straight forward and has the form given in Equation 5.23.

$$|P| = \frac{\sqrt{m^2(m^2 - 2(m_\eta^2 + m_\phi^2)) + (m_\eta^2 - m_\phi^2)}}{2m} \tag{5.23}$$

The issue with this Equation 5.23 as compared to $\sqrt{m^2 - (2m_K)^2}$ is the fact that the invariant mass values of m_η and m_ϕ have a width, whereas m_K does not. This means that the breakup

Table 5.6: A table which summarizes the parameter ranges or fixed values in rows corresponding to different fit functions for the $\phi\eta$ invariant mass. The parameters A_{sig}, and A_{bg} have units of number of events, m_{Peak1}, σ_{Peak1}, m_{Peak2}, and σ_{Peak2} have units of GeV/c^2, φ has units of radians, and r is unit less.

$\phi\eta$ Invariant Mass Parameter Ranges and Functions:

Functions	A_{sig}	m_{Peak1}	σ_{Peak1}	m_{Peak2}	σ_{Peak2}	r	φ	A_{bg}
1) 2BW + BG	0-100	1.6-1.7	0-0.3	1.8-1.9	0-0.3	0-10	-3.15-3.15	0-0.02
2) Low BW + BG	0-100	1.6-1.7	0-0.3	1.850	0	0	0	0-0.02
3) High BW + BG	0-100	1.680	0	1.8-1.9	0-0.3	1	0	0-0.02
4) BG Only	0	1.680	0	1.850	0	0	0	0-0.02

momentum for the $\phi\eta$ invariant mass cannot be represented functionally, and therefore data must be used. To do this, the breakup momentum and $\phi\eta$ invariant mass is plotted on a two dimensional color plot for each event (Figure [5.60]). All events are weighted with $Q_{\phi\eta}$ in order to use the purest sample.

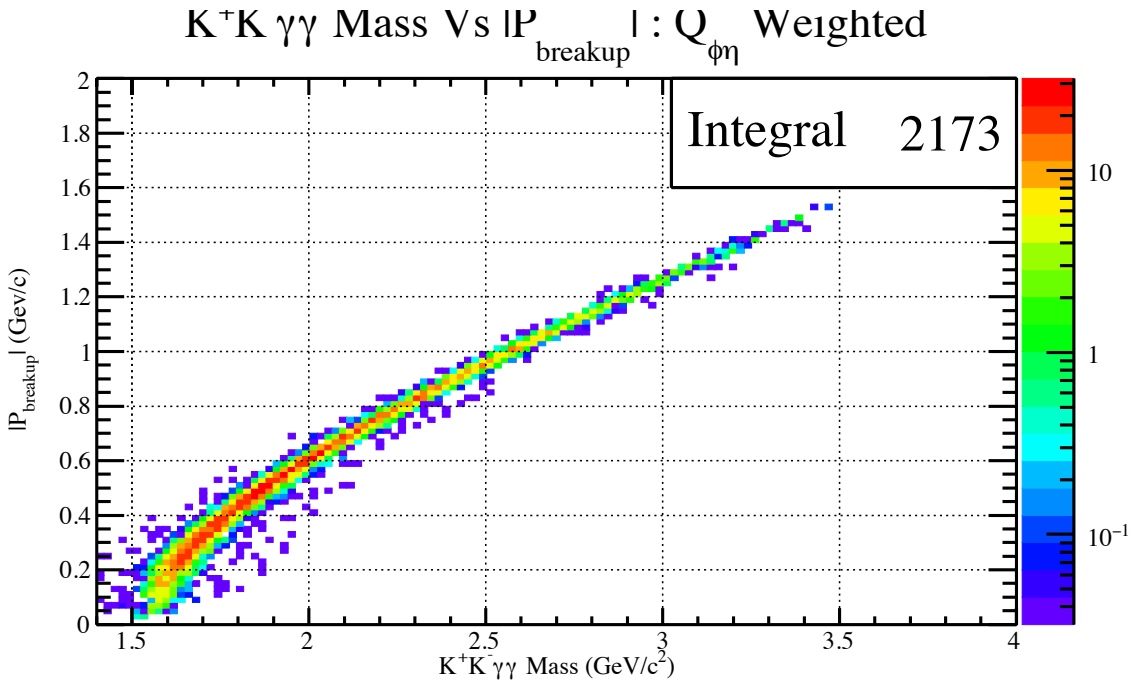

Figure 5.60: The two dimensional color plot of the $K^+K^-\gamma\gamma$ invariant mass vs the break-up momentum. All events are weighted by $Q_{\phi\eta}$.

Looping through each bin of $K^+K^-\gamma\gamma$ invariant mass from Figure [5.60] and projecting onto the vertical axis will provide the $\phi\eta$ break-up momentum spread for that mass range. Taking the mean break-up momentum value for each bin provides a data driven interpolation for Equation 5.23. More specifically, for a given $\phi\eta$ invariant mass value, a breakup momentum is assigned based on the linear fit between two points given in Figure [5.61]. Using this breakup momentum, the signal distribution for each selection method can be fit.

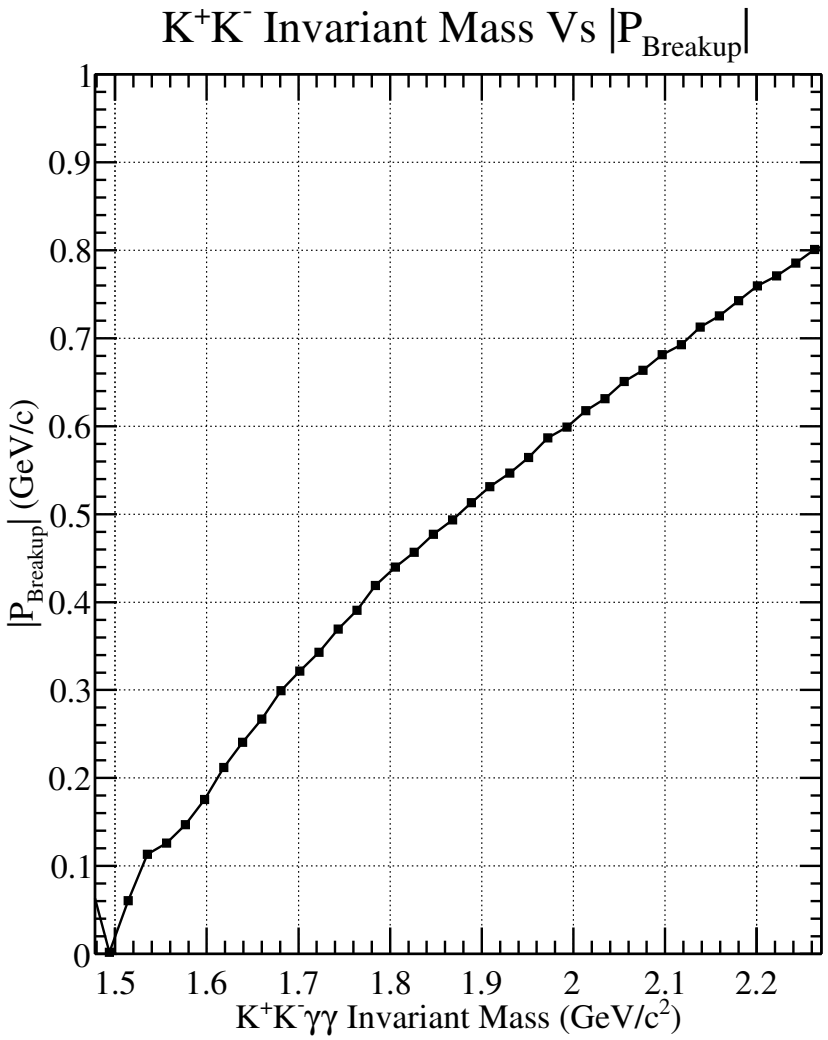

Figure 5.61: An interpolation graph, where the horizontal points are the bin values from Figure [5.60], and the vertical values are the mean values for the break-up momentum projections.

5.6.1 Elliptical Fits

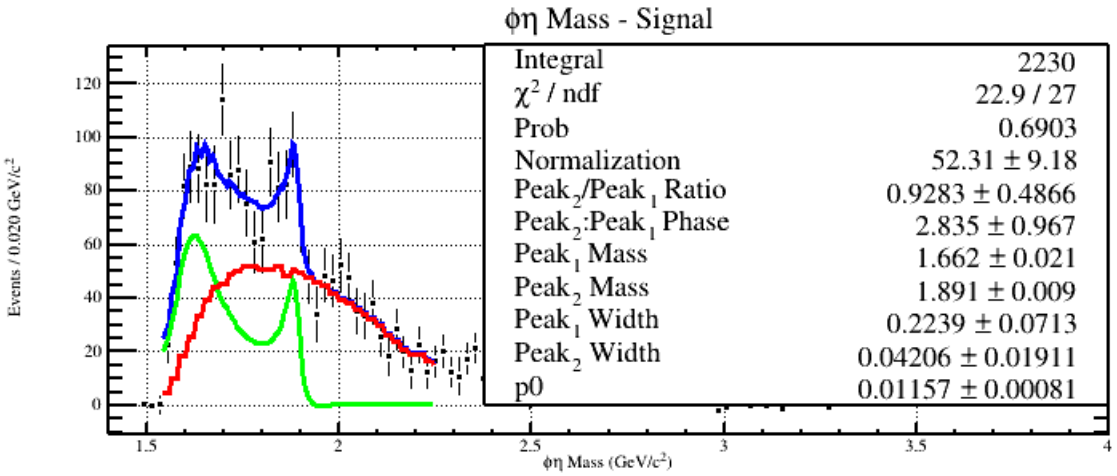

Figure 5.62: Fit of the $\phi\eta$ mass using the elliptical signal distribution in Figure [5.30]. The fit contains two interfering relativistic Breit-Wigners as signal, plus a scaled accepted Monte Carlo distribution as background. The χ^2/ndf, probability, and fit parameters are all given in the stat box.

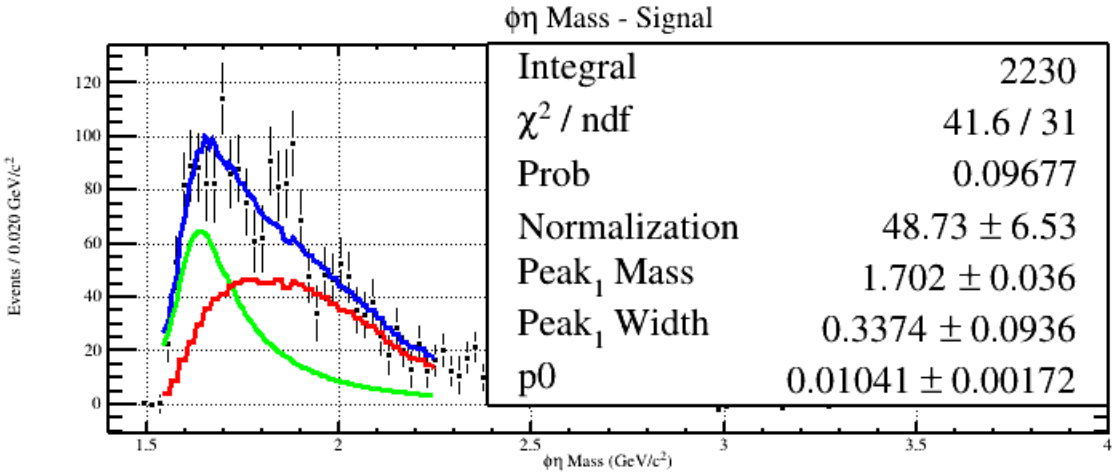

Figure 5.63: Fit of the $\phi\eta$ mass using the elliptical signal distribution in Figure [5.30]. The fit contains one low mass relativistic Breit-Wigner as signal, plus a scaled accepted Monte Carlo distribution as background. The χ^2/ndf, probability, and fit parameters are all given in the stat box.

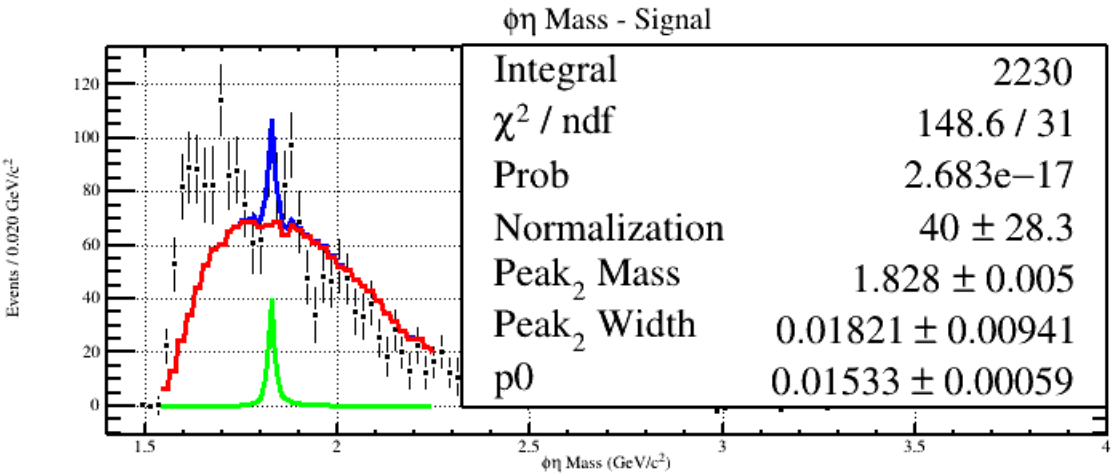

Figure 5.64: Fit of the $\phi\eta$ mass using the elliptical signal distribution in Figure [5.30]. The fit contains one high mass relativistic Breit-Wigner as signal, plus a scaled accepted Monte Carlo distribution as background. The χ^2/ndf, probability, and fit parameters are all given in the stat box.

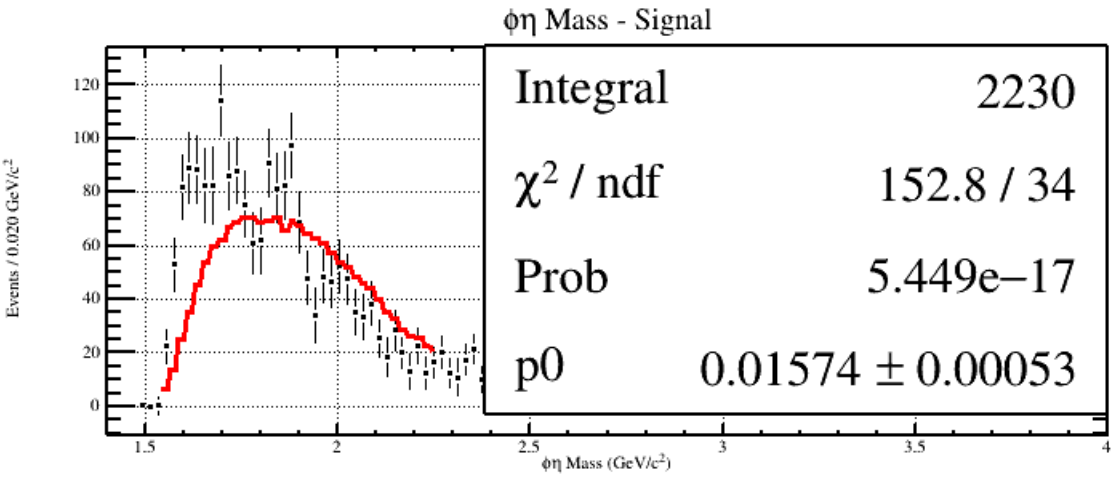

Figure 5.65: Fit of the $\phi\eta$ mass using the elliptical signal distribution in Figure [5.30]. The fit contains no signal distribution, only a scaled accepted Monte Carlo distribution as background. The χ^2/ndf, probability, and fit parameters are all given in the stat box.

5.6.2 Q_ϕ Weighting, η Side-band Subtracted Fits

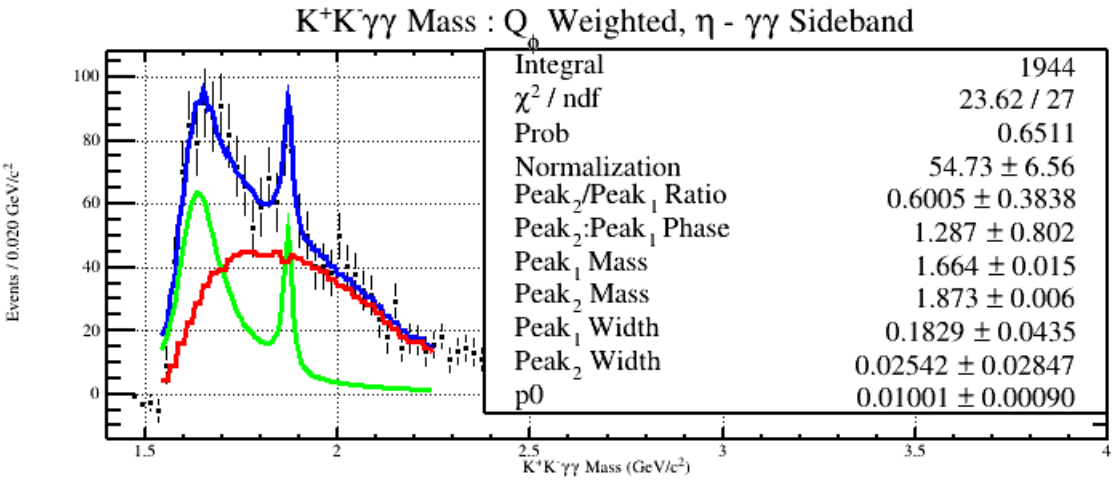

Figure 5.66: Fit of the $\phi\eta$ mass using the Q_ϕ Weighted, $\eta-\gamma\gamma$ Sideband distribution in Figure [5.38]. The fit contains two interfering relativistic Breit-Wigners as signal, plus a scaled accepted Monte Carlo distribution as background. The χ^2/ndf, probability, and fit parameters are all given in the stat box.

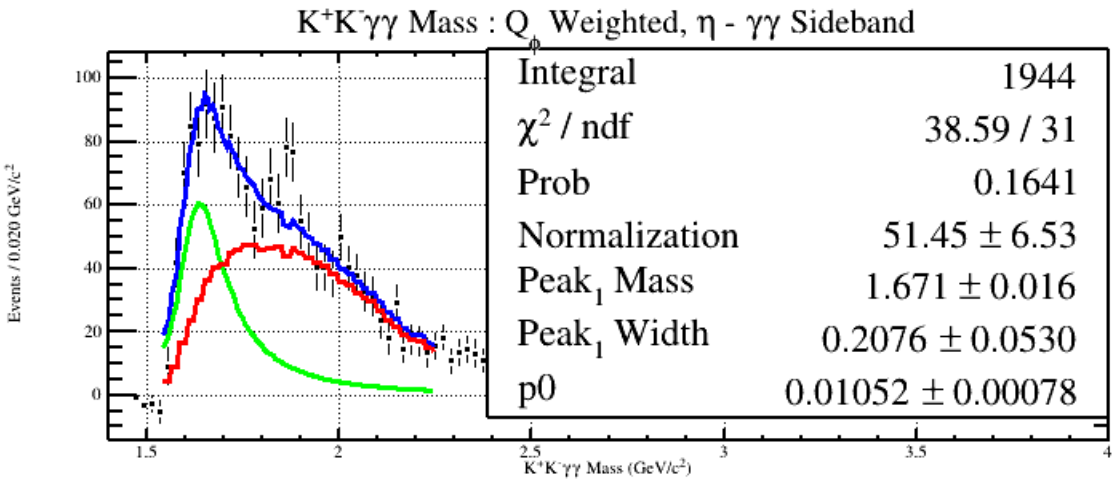

Figure 5.67: Fit of the $\phi\eta$ mass using the Q_ϕ Weighted, $\eta-\gamma\gamma$ Sideband distribution in Figure [5.38]. The fit contains one low mass relativistic Breit-Wigner as signal, plus a scaled accepted Monte Carlo distribution as background. The χ^2/ndf, probability, and fit parameters are all given in the stat box.

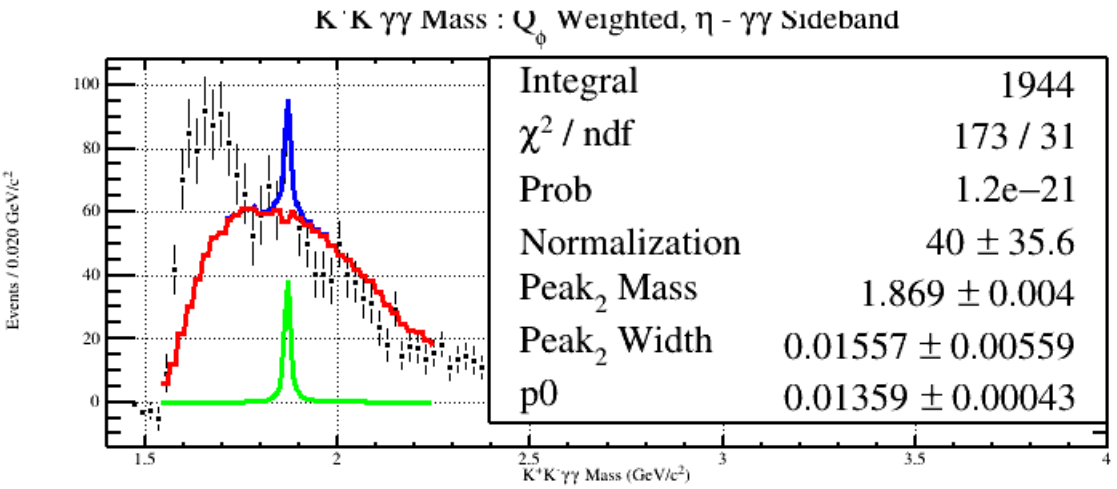

Figure 5.68: Fit of the $\phi\eta$ mass using the Q_ϕ Weighted, $\eta-\gamma\gamma$ Sideband distribution in Figure [5.38]. The fit contains one high mass relativistic Breit-Wigner as signal, plus a scaled accepted Monte Carlo distribution as background. The χ^2/ndf, probability, and fit parameters are all given in the stat box.

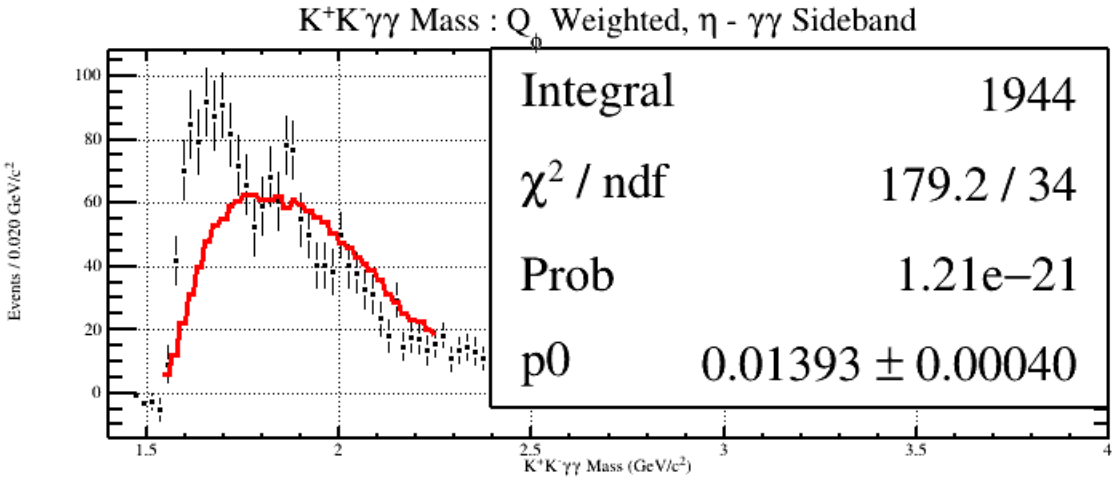

Figure 5.69: Fit of the $\phi\eta$ mass using the Q_ϕ Weighted, $\eta-\gamma\gamma$ Sideband distribution in Figure [5.38]. The fit contains no signal distribution, only a scaled accepted Monte Carlo distribution as background. The χ^2/ndf, probability, and fit parameters are all given in the stat box.

5.6.3 Q_η Weighting, K^+K^- Side-band Subtracted Fits

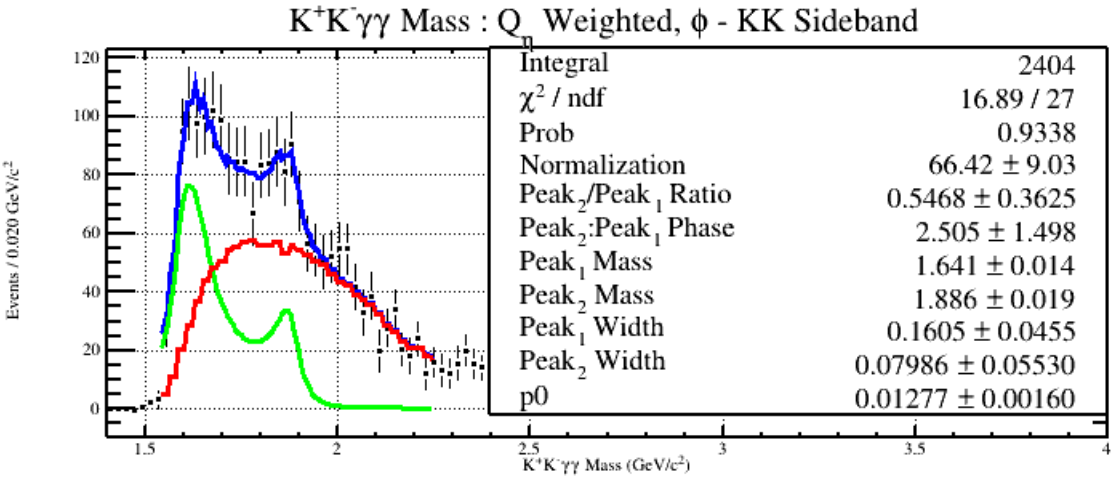

Figure 5.70: Fit of the $\phi\eta$ mass using the Q_η Weighted, $\phi-$KK Sideband distribution in Figure [5.46]. The fit contains two interfering relativistic Breit-Wigners as signal, plus a scaled accepted Monte Carlo distribution as background. The χ^2/ndf, probability, and fit parameters are all given in the stat box.

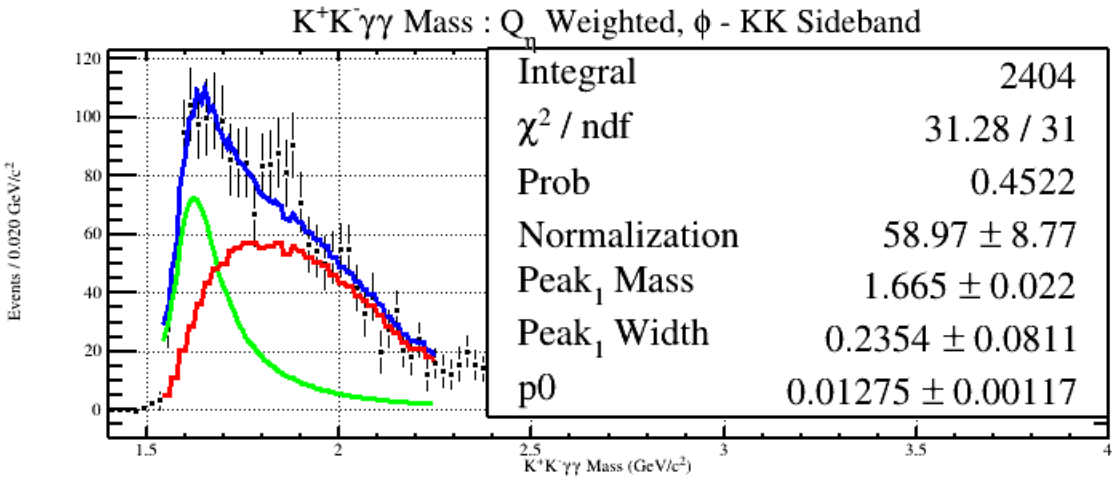

Figure 5.71: Fit of the $\phi\eta$ mass using the Q_η Weighted, $\phi-$KK Sideband distribution in Figure [5.46]. The fit contains one low mass relativistic Breit-Wigner as signal, plus a scaled accepted Monte Carlo distribution as background. The χ^2/ndf, probability, and fit parameters are all given in the stat box.

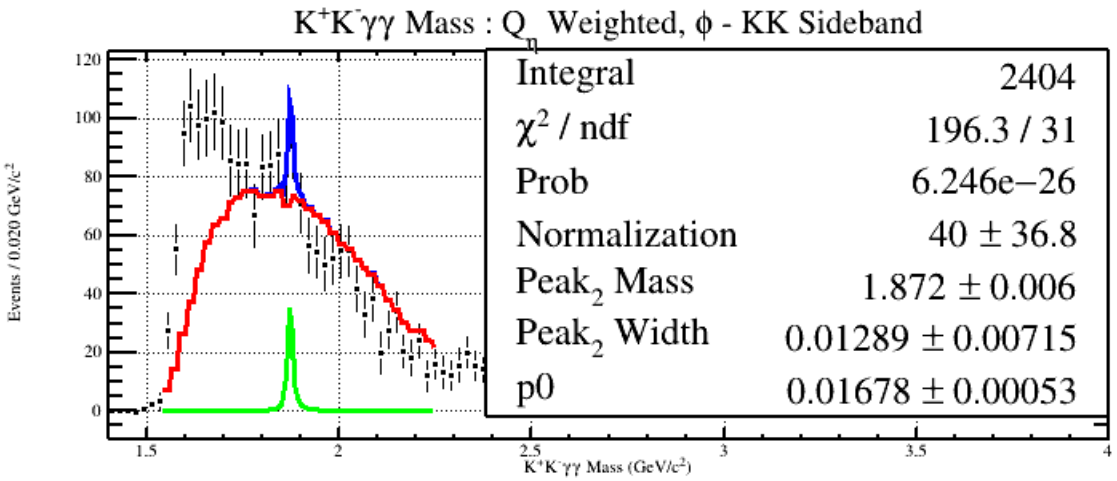

Figure 5.72: Fit of the $\phi\eta$ mass using the Q_η Weighted, $\phi-$KK Sideband distribution in Figure [5.46]. The fit contains one high mass relativistic Breit-Wigner as signal, plus a scaled accepted Monte Carlo distribution as background. The χ^2/ndf, probability, and fit parameters are all given in the stat box.

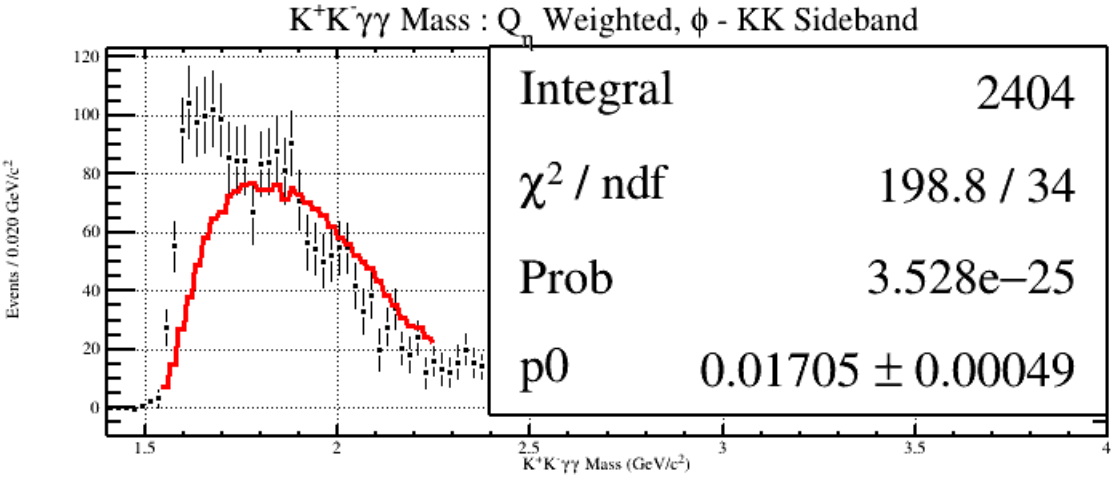

Figure 5.73: Fit of the $\phi\eta$ mass using the Q_η Weighted, $\phi-$KK Sideband distribution in Figure [5.46]. The fit contains no signal distribution, only a scaled accepted Monte Carlo distribution as background. The χ^2/ndf, probability, and fit parameters are all given in the stat box.

5.6.4 $Q_{\phi\eta}$ Weighting Fits

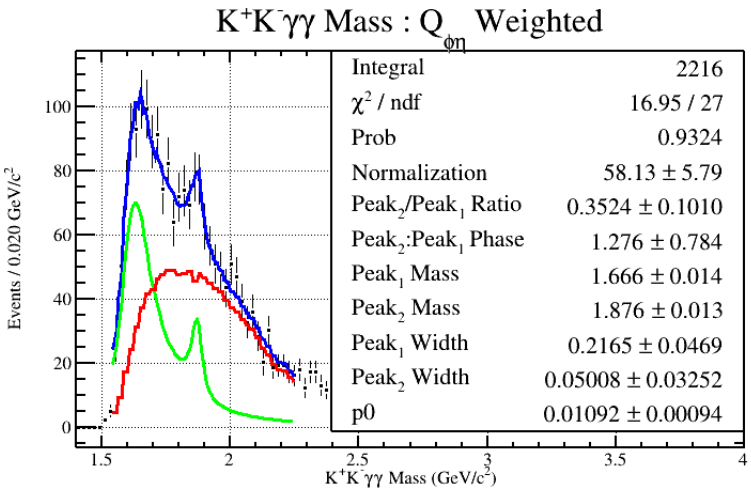

Figure 5.74: Fit of the $\phi\eta$ mass using the $Q_{\phi\eta}$ Weighted distribution in Figure [5.54]. The fit contains two interfering relativistic Breit-Wigners as signal, plus a scaled accepted Monte Carlo distribution as background. The χ^2/ndf, probability, and fit parameters are all given in the stat box.

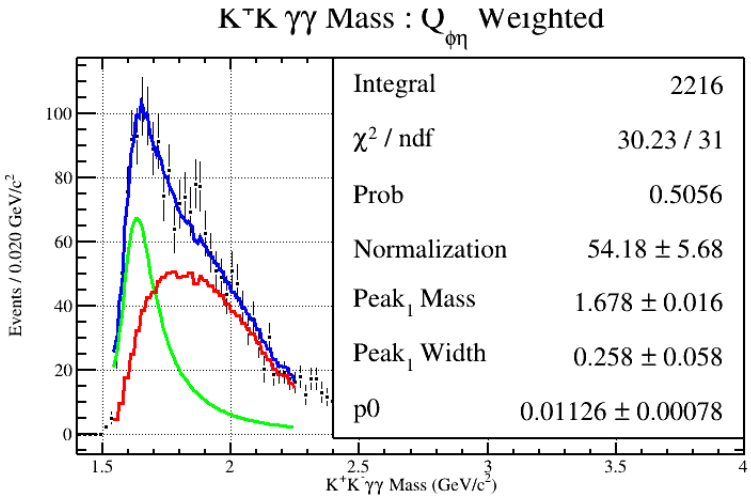

Figure 5.75: Fit of the $\phi\eta$ mass using the $Q_{\phi\eta}$ Weighted distribution in Figure [5.54]. The fit contains one low mass relativistic Breit-Wigner as signal, plus a scaled accepted Monte Carlo distribution as background. The χ^2/ndf, probability, and fit parameters are all given in the stat box.

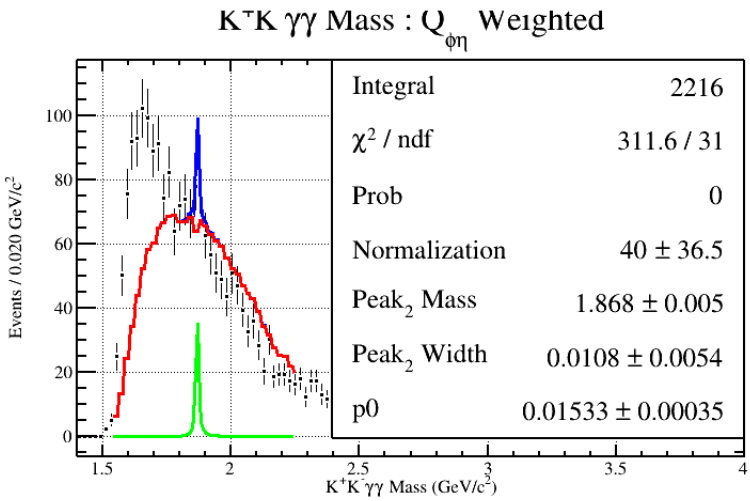

Figure 5.76: Fit of the $\phi\eta$ mass using the $Q_{\phi\eta}$ Weighted distribution in Figure [5.54]. The fit contains one high mass relativistic Breit-Wigner as signal, plus a scaled accepted Monte Carlo distribution as background. The χ^2/ndf, probability, and fit parameters are all given in the stat box.

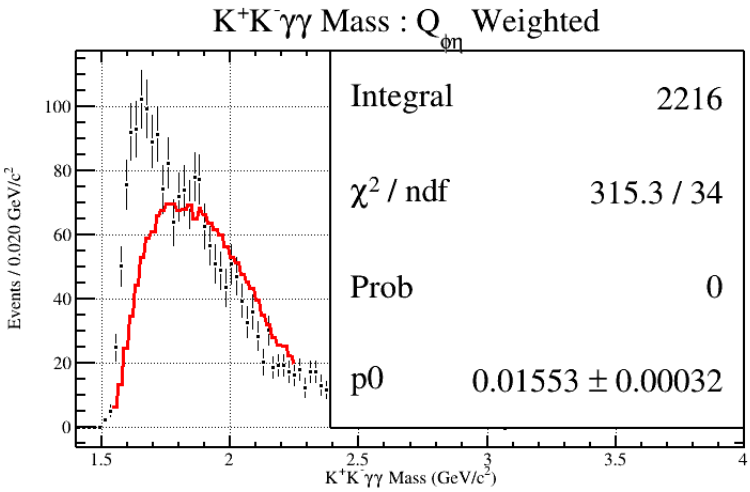

Figure 5.77: Fit of the $\phi\eta$ mass using the $Q_{\phi\eta}$ Weighted distribution in Figure [5.54]. The fit contains no signal distribution, only a scaled accepted Monte Carlo distribution as background. The χ^2/ndf, probability, and fit parameters are all given in the stat box.

5.6.5 Tabular Summary of Fit Results and Discussion

Table 5.7: A table which summarizes the fits which utilized two interfering relativistic Breit-Wigners as signal, plus a scaled accepted Monte Carlo distribution as background.

Two Interfering Relativistic Breit-Wigners + Accepted Monte Carlo:

Selection Method	Peak$_1$ Mass (GeV/c^2) Peak$_2$ Mass (GeV/c^2)	Peak$_1$ Width (GeV/c^2) Peak$_2$ Width (GeV/c^2)	Probability
Elliptical	1.662 ± 0.021 1.891 ± 0.009	0.2239 ± 0.0713 0.04206 ± 0.01911	0.6903
Q_ϕ, $\eta - \gamma\gamma$	1.664 ± 0.015 1.873 ± 0.006	0.1829 ± 0.0435 0.02542 ± 0.02847	0.6511
Q_η, $\phi-$KK	1.641 ± 0.014 1.886 ± 0.019	0.1605 ± 0.0455 0.07986 ± 0.05530	0.9338
$Q_{\phi\eta}$	1.666 ± 0.014 1.876 ± 0.013	0.2165 ± 0.0469 0.05008 ± 0.03252	0.9324

Table 5.8: A table which summarizes the fits which utilized one low mass relativistic Breit-Wigner as signal, plus a scaled accepted Monte Carlo distribution as background.

Low Mass Relativistic Breit-Wigner + Accepted Monte Carlo:

Selection Method	Peak$_1$ Mass (GeV/c^2)	Peak$_1$ Width (GeV/c^2)	Probability
Elliptical	1.702 ± 0.036	0.3374 ± 0.0936	0.09677
Q_ϕ, $\eta - \gamma\gamma$	1.671 ± 0.016	0.2076 ± 0.0530	0.1641
GeV/c^2 Q_η, $\phi-$KK	1.665 ± 0.022	0.2354 ± 0.0811	0.4522
$Q_{\phi\eta}$	1.678 ± 0.016	0.258 ± 0.058	0.5056

Table 5.9: A table which summarizes the fits which utilized one high mass relativistic Breit-Wigner as signal, plus a scaled accepted Monte Carlo distribution as background.

High Mass Relativistic Breit-Wigner + Accepted Monte Carlo:

Selection Method	Peak$_2$ Mass (GeV/c^2)	Peak$_2$ Width (GeV/c^2)	Probability
Elliptical	1.828 ± 0.005	0.01821 ± 0.00941	2.683e-17
Q_ϕ, $\eta - \gamma\gamma$	1.869 ± 0.004	0.01557 ± 0.00559	1.2e-21
Q_η, $\phi-$KK	1.872 ± 0.006	0.01289 ± 0.00715	6.246e-26
$Q_{\phi\eta}$	1.868 ± 0.005	0.0108 ± 0.0054	0

Table 5.10: A table which summarizes the fits which utilized only the accepted Monte Carlo distribution.

Accepted Monte Carlo:

Selection Method	Probability
Elliptical	5.449e-17
Q_{ϕ}	1.21e-21
Q_{η}	3.528e-25
$Q_{\phi\eta}$	0

Since each selection method appeared to contain two different structures in the $\phi\eta$ invariant mass, it was necessary study the validity of them by means of fitting with several different functions. Each function returned a different set of parameters, and a probability. Using the probability of each function, a number of deductions can be made. Given the set of probabilities presented in Table 5.10, it is clear that the signal data for each selection method is not a manifestation of $\phi\eta$ phase space. In addition, the probabilities presented in Table 5.8 as compared to Table 5.9, may indicated that the first peak carries a greater significance than the second peak. Lastly, the probabilities presented in Table 5.7 as compared to all other tables shows that the fit that contains two interfering relativistic Breit-Wigners always has a higher probability than any other function, regardless of selection method. This large difference in probability is good evidence that there are two structures in the $\phi\eta$ invariant mass.

Since Table 5.7 always contains the highest probabilities, the parameter values from that table will be used to approximate the mass and width of each peak. The weighted average for the mass, width, and errors for each peak will be calculated using Equation 5.24 and Equation 5.25.

$$\bar{x} \pm \delta\bar{x} = \frac{\Sigma_i w_i x_i}{\Sigma_i w_i} \pm (\Sigma_i w_i)^{-1/2} \tag{5.24}$$

$$w_i = 1/(\delta x_i)^2 \tag{5.25}$$

Plugging in the mass, width, and error values for each selection method in Table 5.7, it was found that the first peak had a weighted average of $(m_{Peak1} = 1.657 \pm 0.008)\frac{GeV}{c^2}$ for the invariant mass, and a weighted average of $(\sigma_{Peak1} = 0.190 \pm 0.024)\frac{GeV}{c^2}$ for the width. In addition, the second

structure had a weighted average of $(m_{Peak2} = 1.879 \pm 0.004)\frac{GeV}{c^2}$ for the invariant mass, and a weighted average of $(\sigma_{Peak2} = 0.042 \pm 0.014)\frac{GeV}{c^2}$ for the width.

The weighted mass and width values for the first peak closely resemble that of the $\phi(1680)$, which is the radially excited version of the $\phi(1020)$, and has been mentioned several times throughout this thesis. The $\phi(1680)$ is assumed to be a pure $s\bar{s}$ state according to the PDG. However, the structure observed in this data cannot be identified as the $\phi(1680)$ due to the lack of statistics and therefore the inability to perform a partial wave analysis which provides the quantum numbers of the state. The $\phi(1680)$ has been seen in photoproduction, but only from KK final states and not from $\phi\eta$. It should be noted that the $\phi(1680)$ invariant mass value reported by photoproduction experiments is significantly higher than those reported by e^+e^- collider experiments.

Furthermore, the weighted mass and width values for the second peak closely resemble that of the $\phi_3(1850)$. The $\phi_3(1850)$ is assumed to be a pure $s\bar{s}$ state according to the PDG. However, the structure observed in this data cannot be identified as the $\phi_3(1850)$ due to the lack of statistics and therefore the inability to perform a partial wave analysis which provides the quantum numbers of the state. Some interesting facts about the $\phi_3(1850)$ is that it has only been seen in KK and KK^* final states from experiments with a kaon beam. The $\phi_3(1850)$ has never been seen in photoproduction or e^+e^- collider experiments. It should also be noted that an s$\bar{s}$ triplet state of $(1^{--}, 2^{--}, 3^{--})$ is expected to be close to this invariant mass value [39]. Given Table 1.2 from Chapter 1, it is clear that all of these states, as well as the $\phi(1680)$, can decay to a $\phi\eta$ final state. However, further investigation of this final state is needed in order to properly identify the observed structures. Analyzing the Spring 2018 Physics Run and the Fall 2018 Physics run at GlueX will more than quadruple the current physics data set, and will allow for a more diverse investigation of these structures. Some of these additional investigations may include a beam asymmetry, cross section, or a partial wave analysis.

CHAPTER 6

SUMMARY

The advancement of meson spectroscopy has entered a new age with the creation and construction of the GlueX spectrometer at Thomas Jefferson National Accelerator Facility. The study of photoproduced quark-antiquark bound states will only improve as more statistics accumulate in the coming years. Past photoproduction experiments have attempted to study the $\phi\eta$ final state, but only managed to observe a few hundred events with no indication of any structures in the invariant mass spectra. The statistics presented in this thesis are well into the thousands and show good evidence that two structures are present in the final invariant mass plots. To ensure the purest signal sample, the data presented in this thesis was refined in order to remove as many sources of background as possible. These included the removal of N* baryonic backgrounds from $\gamma p \to N^*\phi; N^* \to p\eta$ as well as backgrounds from misidentified kaons.

To verify the validity of the structures, a collection of different signal and background studies were performed on the data. In each instant, the structures observed in the $\phi\eta$ invariant mass remained, with comparable values for mass and width. Furthermore, each signal distribution was fit with four different equations, each of which containing a different number of signal peaks. For each selection method, it was shown that the function which included two interfering relativistic Breit-Wigners yielded the highest probability in comparison to all other functions. Using the mass and width values from all selection methods, and only using the fit with two signal peaks, it was found that the first structure had a weighted average of $(m_{Peak1} = 1.657 \pm 0.008)\frac{GeV}{c^2}$ for the invariant mass, and a weighted average of $(\sigma_{Peak1} = 0.190 \pm 0.024)\frac{GeV}{c^2}$ for the width. In addition, the second structure had a weighted average of $(m_{Peak2} = 1.879 \pm 0.004)\frac{GeV}{c^2}$ for the invariant mass, and a weighted average of $(\sigma_{Peak2} = 0.042 \pm 0.014)\frac{GeV}{c^2}$ for the width.

Although the mass and widths of the structures observed in the $\phi\eta$ invariant mass plots are consistent with pure $s\bar{s}$ candidates in the PDG, identification of these structures is not possible with the statistics at hand. Further investigation needs to be done, including the analysis of the Spring 2018 Physics Run and the Fall 2018 Physics run at GlueX. The addition of these statistics will

more than quadruple the current physics data set, and will allow for a more diverse investigation of these structures. Some of these additional investigations may include a beam asymmetry, cross section, or a partial wave analysis.

BIBLIOGRAPHY

[1] J.J. Thomson. Nobel lecture: Carriers of negative electricity, July 2017. `http://www.nobelprize.org/nobel_prizes/physics/laureates/1906/thomson-lecture.html`.

[2] James Chadwick. Nobel lecture: The neutron and its properties, Aug 2017. `http://www.nobelprize.org/nobel_prizes/physics/laureates/1935/chadwick-lecture.html`.

[3] David Griffiths. *Introduction to Elementary Particle Physics*. WILEY-VCH, 2010.

[4] Georges Aad *et al.* Observation of a new particle in the search for the Standard Model Higgs boson with the ATLAS detector at the LHC. *Phys. Lett. B*, 2012.

[5] Murray Gell-Mann. The eightfold way: A theory of strong interaction symmetry. Technical report, California Institute of Technology, 1961.

[6] K.A. Olive *et al. (Particle Data Group)*. Chin. Phys. C, 38, 090001, (2014).

[7] M. G. Alekseev *et al.* Observation of a $J^{PC} = 1^{-+}$ exotic resonance in diffractive dissociation of 190 GeV/c π^- into $\pi^-\pi^-\pi^+$. *Phys. Rev. Lett.*, 2010.

[8] N. Black T. Barnes and P.R. Page. Strong decays of strange quarkonia. *Physical Review D*, 2003.

[9] F. Mané *et al.* Study of the reaction $e^+e^- \to K^0_S K^0_L$ in the total energy range 1.4-2.18 gev and interpretation of the K^+ and K^0 form factors. *Phys. Lett. Volume 99B, number 3*, 1981.

[10] B. Aubert *et al.* Measurements of $e^+e^- \to K^+K^-\eta$, $K^+K^-\pi^0$, and $K^0_s K^\pm\pi^\mp$ cross sections using initial state radiation events. *Phys. Rev., D*, 77:092002, May 2008.

[11] Mukesh S. Saini. *Search for new and unusual strangeonia in photoproduction using CLAS*. PhD thesis, Florida State University, 2013.

[12] D. Aston *et al.* Evidence for a high mass enhancement in K^+K^- photoproduction. *Phys. Lett. B*, 104:231–234, August 1981.

[13] M. Atkinson *et al.* Photoproduction of mesons by linearly polarized photons of energy 20–40 gev and further evidence for a photoproduced high-mass kk enhancement. *Zeitschrift für Physik C Particles and Fields*, 27(2):233–238, Jun 1985.

[14] J.M. Link *et al.* Observation of a 1750 Mev/c^2 enhancement in the diffractive photoproduction of K^+K. *Phys. Lett. B.*, 545:50–56, Oct 2002.

[15] B. Aubert *et al.* Structure at 2175 mev in $e^+e^- \to \phi f_0(980)$ observed via initial-state radiation. *Phys. Rev. D*, 74:091103, Nov 2006.

[16] Gui-Jun Ding *et al.* A candidate for 1^{--} stangeonium hybrid. *Phys. Lett. B*, 650:390–400, July 2007.

[17] S. Okubo. ϕ-meson and unitary symmetry model. *Phys. Lett.*, 5(2):165–168, Jun 1963.

[18] G. Zweig. An su3 model for strong interaction symmetry and its breaking. Technical report, CERN Geneva, 1964.

[19] K.Okada I. Iizuka and O. Shito. Systematics and phenomenology of boson mass levels. *Prog. Theor. Phys.*, 1966.

[20] Jan 2018. JLab Picture Exchange - https://www.jlab.org.

[21] Exploring the nature of matter, Jan 2018. https://www.jlab.org/about.

[22] https://www.jlab.org/accelerator-science.

[23] R. Kazimi *et al.* Cebaf injector achieved world's best beam quality for three simultaneous beams with a wide range of bunch charges. *Proceedings EPAC 2004*, 2004.

[24] Diamond on goniometer, Jan 2015. https://logbooks.jlab.org/book/halld.

[25] Hall D / GlueX Technical Construction Report, Jul 2017. `https://halldweb.jlab.org/DocDB/0025/002511/006/tcr.pdf`.

[26] H. Al Ghoul *et al.* Measurement of the beam asymmetry Σ for π^0 and η photoproduction on the proton at E_γ=9 GeV. *Phys. Rev. C*, 2017.

[27] M. Dugger *et al.* Design and construction of a high-energy photon polarimeter. *Nuclear Instruments and Methods in Physics Research Section A: Accelerators, Spectrometers, Detectors and Associated Equipment*, 2017.

[28] Nov 2013. https://gluex.phys.uregina.ca/pictures.

[29] A. Somov *et al.* Performance of the pair spectrometer of the gluex experiment. *International Conference on Particle Physics and Astrophysics*, 2015.

[30] Kapton HN general-purpose polyimide film, Sep 2018. http://www.dupont.com/products-and-services/membranes-films/polyimide-films/brands/kapton-polyimide-film/products/kapton-hn.html.

[31] C.D. Keith. HallD LH2 Cryotarget, Jan 2014. https://halldweb1.jlab.org/wiki/images/b/b8/HallD_Target_Table.

[32] E. Pooser *et al.* The GlueX Start Counter Detector. *Nuclear Instruments and Methods in Physics Research Section A: Accelerators, Spectrometers, Detectors and Associated Equipment*, 2018.

[33] Hall D Superconducting Solenoid - Technical Note, Mar 2018. https://halldweb.jlab.org/DocDB/0023/002378/005/sol_note.pdf.

[34] The GlueX / HallD Central Drift Chamber, Jul 2008. https://halldweb.jlab.org/DocDB/0009/000990/011/cdc_dr.pdf.

[35] R.R. Crittenden *et al.* A 3000 element lead-glass electromagnetic calorimeter. *Nuclear Instruments and Methods in Physics Research Section A: Accelerators, Spectrometers, Detectors and Associated Equipment*, 1997.

[36] *Modern Particle Physics.* Cambridge University Press, 2013.

[37] GlueX/Hall D Calorimeter Final Design and Safety Review, Feb 2008. https://halldweb.jlab.org/DocDB/0009/000988/001/fcal.pdf.

[38] C.A. Meyer M. Williams, M. Bellis. Separating signals from non-interfering backgrounds using probabilistic event weightings. *arXiv preprint arXiv:0804.3382*, 2008.

[39] Search for new forms of hadronic matter in photoproduction. *JLab Proposal E-04-005*, Oct 2010. http://www.jlab.org/exp_prog/proposals/04/PR04-005.pdf.

BIOGRAPHICAL SKETCH

Bradford Emerson Cannon was raised in the small and quiet town of New Boston, New Hampshire. He attended New Boston Central School for his elementary education; then continued his education in Goffstown, New Hampshire for middle school and high school. After graduating from Goffstown High School in 2009, he attended the University of New Hampshire where he earned a Bachelor of Science degree in Physics. After graduation, he immediately began his pursue of a Doctoral degree in physics at Florida State University. Upon graduation, he intends to pursue a career in Data Science or Research and Development.